WIFFEN

DOE/ET-0058/1

U.S. Department of **Energy**

Assistant Secretary for Energy Technology
Office of Fusion Energy

August 1978

Alloy Development for Irradiation Performance

Quarterly Progress Report
January-March, 1978

Weld 55°C 86
316 @ 55°C - 87
PE-16 - 92
White Unit No. - 142

Available from:

National Technical Information Service (NTIS)
U.S. Department of Commerce
5285 Port Royal Road
Springfield, Virginia 22161

Price: Printed copy: $9.50
Microfiche: $3.00

FOREWORD

This report is the first in a series of Quarterly Technical Progress Reports on *"Alloy Development for Irradiation Performance"* (ADIP) which is one element of the Fusion Reactor Materials Program, conducted in support of the Magnetic Fusion Energy Program of the U. S. Department of Energy. Other elements of the Materials Program are:

- *Damage Analysis and Fundamental* ***Studies*** *(DAFS)*
- *Plasma-Materials Interaction (PMI)*
- *Special Purpose Materials (SPM)*

The ADIP program element is a National effort composed of contributions from a number of National laboratories, universities, industrial and institutional laboratories organized by the Materials and Radiation Effects Branch, Office of Fusion Energy, DOE, and a Task Group on *Alloy Devetopment for Irradiation Performance* which operates under the auspices of that Branch. The purpose of this series of reports is to provide a working technical record of that effort for the use of the program participants, for the fusion energy program in general, and for the Department of Energy.

This report is organized along topical lines in parallel to a Program Plan of the same title (to be published) so that activities and accomplishments may be followed readily relative to that Program Plan. Thus, the work of a given laboratory may appear throughout the report. Chapters 1, 2, 7, and 8 report on topics which are generic to all of the ADIP Program: Analysis and Evaluation, Test Methods Development, Status of Irradiation Experiments, and Corrosion Testing and Hydrogen Permeation Studies, respectively. Chapters 3, 4, 5, and 6 report the work that is specific to each of the four paths of alloy development along which the program is structured - Path A: Austenitic Alloys, Path B: Fe-Ni-Cr Superalloys, Path C: Reactive and Refractory Metals and Alloys, and Path D: Innovative Concepts. The Table of Contents is annotated for the convenience of the reader.

This report has been compiled and edited under the guidance of the Chairman of the Task Group on *Alloy Development for Irradiation Performance*, E. E. Bloom of Oak Ridge National Laboratory, and his efforts, those of the supporting staff of ORNL and the many persons who made technical contributions are gratefully acknowledged. T. C. Reuther, Materials and Radiation Effects Branch, is the Department of Energy counterpart to the Task Group Chairman and has responsibility for the ADIP Program within DOE.

Klaus M. Zwilsky, Chief
Materials and Radiation
Effects Branch
Office of Fusion Energy

ALLOY DEVELOPMENT PROGRAM STRATEGY

Development of materials to withstand the hostile environment of a fusion reactor first-wall presents the most formidable challenge that materials engineers have had to face yet. The combination of temperature, stress, and radiation effects in the form of displaced atoms and transmutation products places demands on materials well beyond current capabilities. The Office of Fusion Energy, Department of Energy, has recognized the magnitude of the problem of developing structural materials for first-wall applications and has established an alloy development program to meet this challenge. The strategy for this program is summarized below.

Goals

The program is focused on development of materials for commercial reactors by the end of this century. It also is organized to provide materials data for design of the relatively low-performance devices that will be constructed in the intervening time. For the commercial reactor the goal is development of a structural material that will have a service life of *40* MWyr/m^2.

Basis of Strategy

1. There is today no single class of candidate materials that obviously will be able to meet the requirements of a commercial reactor. This means that the program must be broad in terms of the range of materials that it includes. Premature selection or rejection of a structural material could severely limit design performance options later. Performance criteria must be established early in the program, and the number of materials considered must be reduced rapidly, on the basis of properties of unirradiated materials wherever possible.

2. Several performance factors or failure mechanisms could limit the useful life of structural components. Slight design alterations could change the material properties controlling lifetime. As a consequence, a broad program aimed at defining and improving several properties concurrently is necessary.

3. The exposure goal of 40 MWyr/m^2 makes irradiation effects the dominant element in the program. There is no way to estimate the properties of materials irradiated to such high levels on the basis of properties of unirradiated materials. Final decisions on alloy choices will be based on extensive measurement of irradiated materials including the evaluation of properties during irradiation. The program will not be directed exclusively at irradiation performance, however, and much of the early identification of promising alloy systems for development will be based on measurements of properties outside the irradiation environment.

4. The ideal test environment has a fusion neutron spectrum, a flux high enough to allow accelerated testing and an experimental volume on the order of 10 liters. Such a source is not currently available or authorized, but the plan assumes that one will become available around 1990. Since materials development is such a long-term activity involving many time-consuming iterations to achieve an optimum condition, the program cannot be delayed until then. This means that in the next few years the program must rely on less-than-ideal sources (principally fission reactors), simulation techniques, and, of necessity, a strong understanding of the physical processes that occur during irradiation. The Damage Analysis and Fundamental Studies Task Group and the d-Li neutron source are essential elements of this part of the strategy.

The Parallel Path Approach

Initial studies suggest that stainless steels, nickel-base alloys, and refractory or reactive metal alloys all offer attractive properties for fusion reactor applications. Our present knowledge does not allow us to identify one of these as the most promising and to concentrate our efforts on it. A parallel path approach is essential to allow the wide range of potential candidates to be assessed fairly. The four paths included in the program represent materials that have not only different basic characteristics in terms of probable fusion reactor performance but also different levels of technology development and different degrees of risk or potential for performance and success.

These four individaul paths are identified and described in the following paragraphs.

Path A: Austenitic Alloys

Alloys in the composition range of the austenitic stainless steels represent our most established technology, including both fabrication and irradiation experience. We are in a position now to identify Prime Candidate Alloys for this class and to proceed to optimize them in terms of composition and microstructure. These materials will meet the needs of near term machines.

Path B: Fe-Ni-Cr Superalloys

Alloys in this class offer higher strength and higher temperature capabilities than the stainless steels. Our knowledge, especially of irradiation performance, is more limited, however, and we will begin by investigating a series of Base Research Alloys that are aimed at defining useful compositions for optimization. These studies will result in identification of a group of Prime Candidate Alloys and an optimization program similar to that for the Path A alloys.

Path C: Reactive and Refractory Metals and Alloys

Although the reactive (e.g., titanium) and refractory (e.g., vanadium, niobium) metals have received relatively little attention for fission reactor applications they have attractive physical and mechanical properties that suggest high potential for fusion reactors. Limited irradiation testing of vanadium alloys has shown little degradation of properties. The reactive and refractory metal alloy systems are markedly different in character, but they are both included in Path C because schedules for their development are similar. Work in this class begins with a broad series of scoping alloys that will lead first to a group of Base Research Alloys and finally to the identification of Prime Candidate Allbys that will be optimized as in the other classes.

Path D: New Concepts

Path D will address innovative and composite material options. This path is included in the program in recognition that the conventional concepts of metallurgical development that are implicit in Paths A, B, and C may not be adequate for fusion reactor application. These alternative concepts will be examined to overcome the performance limits imposed by more conventional materials engineering. This path might include novel concepts such as graded materials, fiber structures, composites, structural ceramics, unique material processes, ordered alloys, and other imaginative ideas that offer the possibility of reduction to engineering practice. It also will include ultra-low activation concepts. The development schedule will follow the steps in Path C after an initial evaluation of the concepts is completed.

Major Milestones

A schedule of major (Level 1) milestones is given in the following table. It allows an optimized alloy to be designed for each path by early in the 21st century. (OPT-A1 indicates the initial optimized alloy on Path A; the schedule allows two sequences of optimization on Path A and one on each of the others.) This is not to imply that all paths will be followed to completion; as results become available less promising approaches will be eliminated. This program presents the strategy for reaching an optimized alloy on each of the individaul paths.

ORNL-DWG 77-16242

COMPARISON OF LEVEL 1 MILESTONES ON DIFFERENT ALLOY DEVELOPMENT PATHS

YEAR	PATH A	PATH B	PATH C	PATH D
1970	SELECT PATH A PRIME CANDI-DATE ALLOYS	SELECT PATH 0 BASE RESEARCH ALLOYS	SELECT PATH C ALLOYS FOR SCOPING STUDIES	ISSUE REQUEST FOR PRO-POSALS FOR IDENTIFICATION OF PROMISING PATH D MATERIALS
1979				
1980				SELECT PROMISING PATH D CONCEPTS FOR SCOPING STUDIES
1981			SELECT PATH C BASE RESEARCH ALLOYS	
1902				
1903	IDENTIFY OPT-A1	SELECT PATH 0 PRIME CANDI-DATE ALLOYS		SELECT PATH D BASE RESEARCH MATERIALS
1984				
1985				
1986			SELECT PATH C PRIME CANDIDATE ALLOYS	
1987				
1988				SELECT PATH D PRIME CANDIOATE MATERIALS
1909				
1990				
1991	ESTABLISH ENGINEERING OATA BASE AND PERFORMANCE LIMITS	IDENTIFY OPT-0		
1992	IDENTIFY OPT-A2			
1993				
1994			IDENTIFY OPT-C	
1995				
1996				IDENTIFY OPT-D
1991				
1998				
1999	ESTABLISH ENGINEERING DATA BASE AND PERFORMANCE LIMITS FOR OPT-A2			
2000		ESTABLISH ENGINEERING DATA BASE AND PERFORMANCE LIMITS FOR OBT-B		
2001				
2002			ESTABLISH ENGINEERING DATA BASE AND PERFORM ANCE LIMITS FOR OPT-C	
2003				
2004				ESTABL Sh ENG NEERING DATABASE AND PERFORM-ANCE L M TS FOR OPT-C

HIGHLIGHTS

1.1 The Establishment of Alloy Development Goals Important to the Commercialization of Tokamak–Based Fusion Reactors (ANL and McDonnell Douglas)

Definition of the magnitude of material property improvement required to achieve an acceptable life for tokamak reactor first walls provided important guidance to alloy development. Relating material property requirements to reactor design also improves communication between the design and materials specialist necessary to reach the desired reactor performance.

1.2 Economic Impact of Using Refractory Metals for Fusion Reactors (McDonnell Douglas)

Determination that the cost of refractory metal components restricts their use to first wall/blanket/header components increase the need for defining compatibility between refractory metals, coolant and common non–refractory metal piping, pumps,, etc. Also, definition of the potential economic advantages for refractory metals helped to scope the appropriate development effort.

2.1 Determination of Fatigue Specimen Configuration for Irradiation Effects Testing (McDonnell Douglas)

Use of a sheet material fatigue specimen substantially increases the number of specimens per unit volume of reactor test space. It also eliminates the need for rod stock thereby relieving the strain on test material availability, particularly important for most path C materials.

3.5 The Influence of Irradiation on the Properties of Path A Alloy Weldments (ORNL)

Samples of type 316 stainless steel welded with 16-8-2 filler metal irradiated at about 55°C were lower in strength and comparable in ductility to the unirradiated base metal.

Evaluation of 20%–cold–worked type 316 stainless steel irradiated at about 55°C to produce up to 10 dpa and 500 at. ppm He shows that the alloy will not swell any measurable amount and that the only tensile property change of consequence for service at or near this temperature is a severe *loss* of uniform elongation. Total elongation and strength properties are relatively unaffected by this irradiation.

CONTENTS

The hydrogen permeability of Inconel 625 was measured over a range of temperatures and hydrogen pressures that included values relevant to the Doublet III experiment (Inconel 625 is being used *as* the vacuum vessel material for Doublet III). The permeation rate obeyed a half-power dependence on hydrogen pressure down to the lowest pressure studies (10^{-1} Pa). The activation energy and permeation coefficient were in good agreement with published data for other Inconel-type alloys. These results will also be useful as a standard for comparison of the effectiveness of permeation barrier methods applied to path B alloys.

1. ANALYSIS AND EVALUATION STUDIES

The designs for power-producing fusion reactors are in a very embryonic and rapidly changing state. Requirements for materials performance are thus not well defined. However, regardless of the final designs, the environment will clearly be extremely demanding on materials in regions of high neutron flux. One cannot identify a class of alloys on which the development efforts should focus — thus the parallel paths of the Alloy Development Program. The combination of reactor designs that are evolving and the necessity for including alloys with widely different physical, chemical, and mechanical properties in the program could lead to an impossibly large number of potential problems and possible solutions. Analysis and evaluation studies are an essential part of the Alloy Development Program in order to translate fusion reactor performance goals into material property requirements and to identify crucial and generic problems on which development activities should be focused. As the Alloy Development Program proceeds and a better understanding of the behavior of materials in potential fusion reactor environments is attained, these studies will also identify problems that will necessitate design solutions.

1.1 THE ESTABLISHMENT OF ALLOY DEVELOPMENT GOALS IMPORTANT TO THE COMMERCIALIZATION OF TOKAMAK-BASED FUSION REACTORS

M. Abdou, S. D. Harkness, S. Majumdar, V. Maroni, and B. Misra (Argonne National Laboratory) and B. A. Cramer, J. W. Davis, D. A. DeFreece, and D. L. Kummer (McDonnell Douglas Astronautics Company - St. Louis).

1.1.1 ADIP Task

Task number I.A.l - Define Material Property Requirements and Make Structural Life Predictions.

1.1.2 Objective

The primary objective of this study was to investigate requirements for tokamak reactor first wall material properties. In conjunction with this work other objectives were to identify appropriate wall loading and lifetime goals and to estimate the economic impact of dimensional changes caused by swelling and/or creep. These considerations are directly related to alloy development since results supply direction to the development activities.

1.1.3 Summary

Fatigue, crack growth, and creep rupture properties were investigated in the context of lithium cooled first wall structural designs for commercial tokamak reactors. The studies resulted in the definition of the physical properties for fatigue, creep-fatigue, flaw growth, creep rupture, and irradiation swelling required to meet a goal life of 10 $MW\text{-}Yr/m^2$. Fatigue and flaw growth properties were shown to need improvements over presently defined properties for annealed Type 316 stainless steel.

System study codes were used to investigate the effects of parameters such as wall loading and life on cost of electricity.

1.1.4 Progress and Status

The commercialization of magnetic fusion energy will require the use of materials under conditions for which a limited data base currently exists. This program has been directed toward developing an understanding

of material requirements in order to efficiently accomplish research and development efforts. This program is completed and the final report' is published; therefore, only the highlights will be summarized.

This work consisted of independent studies by Argonne National Laboratory (ANL) and McDonnell Douglas Astronautics Company–St. Louis (MDAC-St. Louis).

The general approach in the flaw growth, fatigue, and creep rupture studies conducted by MDAC-St. Louis was to determine the quantitative properties in order to achieve a 10 MW-Yr/m^2 life. Required property values were then compared with the values for irradiated 316 stainless steel, and the needed improvement in properties, if any, identified. Design parameters were based on the background attained in past studies which were performed using the UWMAK-I conceptual first-wall design. Sources of stress that were considered included coolant pressures, temperature gradients, swelling and dead weight. In the study, the impact of several variables was assessed. These variables, upon which required flaw growth rate properties depend, included material thickness, initial flaw depth, and flaw shape or aspect ratio.

The ANL analysis of creep-fatigue requirements was based on a lithium cooled reactor system containing cylindrical first wall cells. Thermal-hydraulic calculations were made to provide a basis for defining stresses for different materials and reactor operating conditions. The duty cycles expected for different reactor operating conditions were compared with allowable life based on unirradiated Type 316 stainless steel and vanadium alloy properties. Important variables were the geometry and amount of restraint of the first wall module, maximum temperature allowable in a system representative for both an austenitic stainless steel and a vanadium alloy, wall loading, burn time, the presence or absence of stress relaxation, and the maximum magnetic field.

Swelling requirements were addressed from the standpoint of effects on first wall growth and associated reactor cost. Wall loading and life trade studies were included in the assessment because of the close interrelationship between property requirements, first wall life, and neutron wall loading.

The ANL systems study code was used to investigate the effect on reactor economics of increasing wall loading and wall lifetime values. These variables were considered in the context of a tokamak-based reactor whose gross thermal output ranged from 3000 to 9000 MW.

In the MDAC-St. Louis systems study, wall loading and lifetime goals were established by utilizing the tokamak systems analysis and cost code (TOCCOMO) to consider a broad range of performance variables. The primary variables were wall loading and life, B_{max}, β, unit size (MW thermal), first wall material and temperature, plasma shape factor and maintenance time required for wall replacement.

1.1.5 Conclusions

Annealed 316 SS fatigue and crack growth property improvements are required to meet the goal life of 10 MW-Yr/m^2. An increase in irradiated fatigue life of approximately 500% is required at a neutron wall loading of 2.5 MW/m^2 and a peak coolant temperature of 489°C. Approximately a factor of 40 improvement (decrease) is required in annealed Type 316 SS flaw growth rates based on elastic analysis. This variation between existing data and required flaw growth data is shown in Figure 1.1.1. Irradiation and thermal creep reduce the required improvement to a factor of 15. These results include a scatter factor of 4 on life. Required properties are strongly dependent on cycle frequency (determined by burn time and down time) and temperature (relates to wall loading).

Vanadium alloys appear to have advantages over 316 stainless steel in yielding longer first wall life. A comparison is shown in Figure 1.1.2. Vanadium offers potential for a longer life first wall compared to stainless steel primarily because of reduced thermal stresses. Cyclic thermal stresses are the major contributors to life limiting failures related to fatigue and crack growth. Vanadium alloys may be able to accommodate wall loadings of ~10 MW/m^2 even without the use of a divertor. Using a maximum structural temperature limit of 600°C for stainless steel and 750°C for vanadium alloys results in wall loading limits of 3.7 and 7 MW/m respectively, based on an elastic thermal stress limit of twice the yield strength.

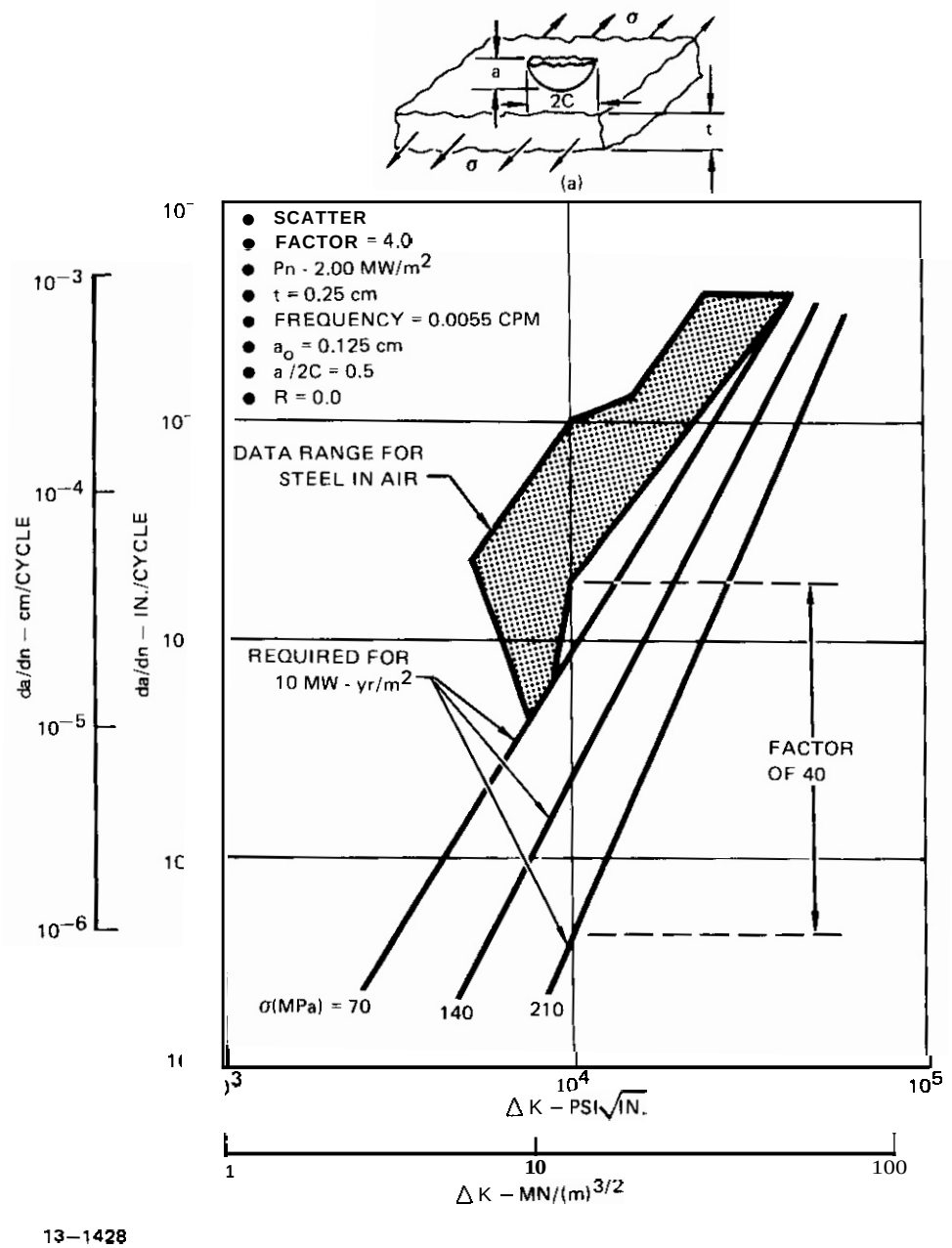

Figure 1.1.1 Dependency of Required Fatigue Crack Growth Properties (da/dn) on Stress level.

Present Type 316 stainless steel creep rupture properties are acceptable. Poorer unirradiated properties can be tolerated if detrimental effects of irradiation can be reduced.

Swelling should be limited to an end–of life value of 10%.

The McDonnell-Douglas Astronautics Company - St. Louis studies indicate that a wall loading of *2-4* MW/m^2 is **near** optimum for minimum

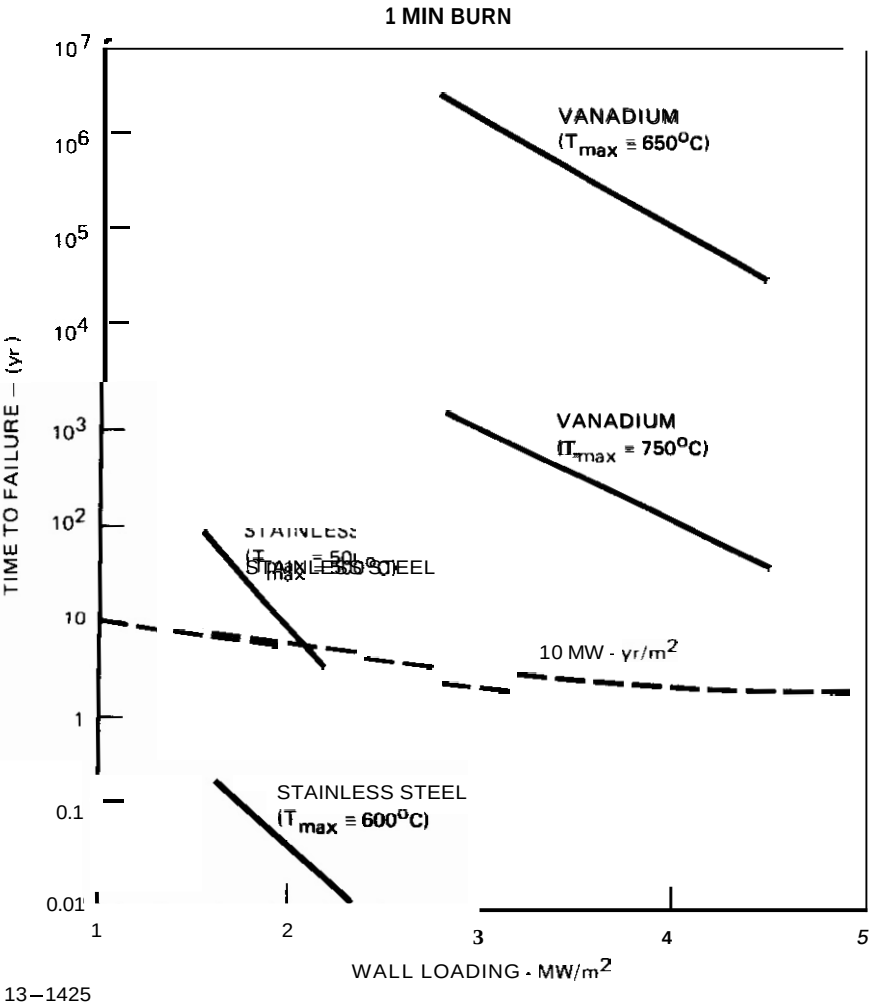

Figure 1.1.2 Variation of Fatigue Life for a Clamped First Wall (Assuming No Stress Relaxation)

cost of electricity for a plant capacity below 7000 MW_t and that small economic incentives exist for achieving a wall life greater than 10–15 MW-Yr/m^2. ANL studies indicate that there is strong economic incentive to achieve lifetimes of 30 MW-Yr/m^2 at wall loadings of 6 MW/m^2 for tokamak-based reactors if the utilities can accept large plant sizes on the order of 9000 MW_t.

1.1.6 Reference

1. Abdou, M., Harkness, S. D., Majumdar, S., Maroni, V., Misra, B. (ANL), Cramer, B. A., Davis, J. W., DeFreece, D. A., and Kummer, D. L., (McDonnell-Douglas Astronautics Company - St. Louis), The Establishment of Alloy Development Goals Important to the Commercialization of Tokamak-Based Fusion Reactors, ANL/FPP/TM-99, MDCE-1743, November 1977.

1.2 ECONOMIC IMPACT OF USING REFRACTORY METALS FOR FUSION REACTORS - J. W. Davis (McDonnell Douglas Astronautics Company - St. Louis).

1.2.1 ADIP Task

Task Number I.A.1 - Define critical material properties and quantify their relative importance to guide alloy selection and development.

1.2.2 Objective

To determine if the refractory metals offer economic and/or technical advantage for major use in commercial fusion reactors.

1.2.3 Summary

This study was performed to determine the relationship between the cost of fabricated hardware, coolant temperature, life and the cost of electricity. Five materials were involved, stainless steel, titanium, vanadium, niobium and molybdenum. The reactor used in these studies was sized to 5000 MW_{th}, used a noncircular plasma (aspect ratio of 2), lithium as a coolant, and steam for electrical power generation. Using this reactor design and the computer cost and modeling code TOCOMO, the costs of electricity associated with using these various metals was determined.

The results of this study indicate that the use of refractory metals in the first wall, blanket, and header region of a fusion reactor offer economic advantage over stainless steel and titanium, provided they have modestly longer life or permit a moderately higher peak coolant temperature. If this use is expanded beyond the header, out through the primary coolant loop, the cost of electricity is significantly increased. This increase in cost is only recovered, relative to the use of stainless steel or titanium for a very narrow set of operating conditions. These conditions require the stainless steel or titanium structure to operate with a 400°C coolant have a component life <5 MW yrs/m^2 and the refractory metals to operate at 650°C and have a life of >10 MW yrs/m^2. Therefore, it appears that the use of refractory metals should be restricted to the first wall, blanket, and header region only and stainless steel or titanium be used for the primary coolant loop.

1.2.4 Progress and Status

A complete report on this portion of the study has been issued[1], therefore, only the highlights will be presented. The initial thrust of this study was directed at an examination of the economic impact of using refractory metals. Since the current conceptual fusion reactor designs are in a state of flux, it was decided not to marry these analyses to any particular reactor design. As a result, a generic tokamak type of reactor was developed using the computer modeling code TOCOMO which combined the best features of a variety of designs into a self-consistent commercial fusion reactor definition. This reactor was sized for 5000 MW of thermal power, had an elliptical plasma shape with a height-to-width ratio of 2 and a major radius of 7.89 meters and a minor radius of 2.5 meters. Lithium was used as the primary coolant together with a steam power conversion system. The average neutron wall loading was 2.6 MW/m^2. Using this reactor design and the computer cost and modeling code TOCOMO, the costs associated with using the refractory metals was determined. The metals that were studied were the refractory metals Nb-1Zr, V-20Ti, and Mo-0.5Ti-0.08Zr (TZM) and the reactive metal Ti-6Al-2Sn-4Zr-2Mo-0.25Si (Ti-6242s). In this study these materials were sequentially introduced first into the first wall/blanket/header and next into the primary coolant loop. The resultant cost of electricity was compared to using stainless steel or titanium for these components.

In general the cost of fabricating a refractory metal structure is significantly higher than for either stainless steel or titanium. This cost delta is primarily due to the higher cost of raw material. The relationship between the cost of electricity and the cost of a fabricated first wall/blanket component is shown in Figure 1.2.1 for various wall lives. This figure shows that for a life of 10 MW yrs/m^2, the cost of electricity changes 2 mills/kW-hr for a $100/kg change in the fabricated component cost. The cost spread between stainless steel and the most expensive refractory metal, vanadium, is $155/kg, or in terms of reactor system performance, about 2.5 mills/kW-hr. Therefore, it can be concluded that the fabricated first wall and blanket component cost has a moderate impact upon the commercial fusion reactor performance (cost of electricity).

As will be discussed later, the higher cost of refractory metal components can be offset by longer life or higher operating temperature.

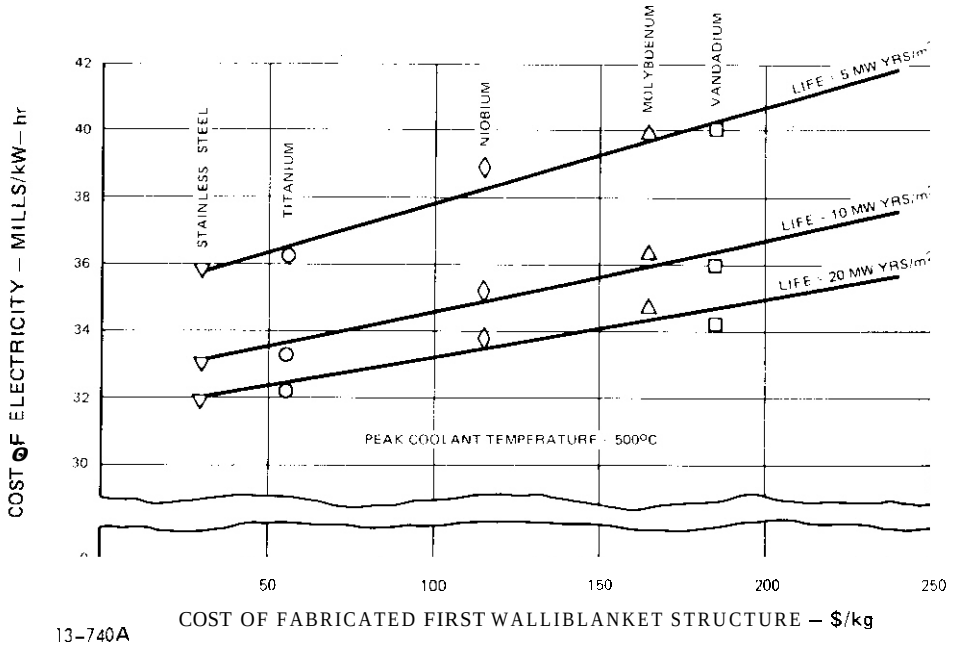

Figure 1.2.1 Effect of Fabricated First Wall/Blanket Structure Cost on Electricity Cost

The relationship between component life and coolant temperature is shown in Figure 1.2.2 for various materials in the first wall, blanket, and header region. For all materials there is a strong economic incentive for increased wall life, if life is short. However, after 10–15 MW yrs/m^2 the benefit of additional wall life increases are greatly diminished. This cost of electricity to wall life relationship is essentially independent of the peak coolant temperature. For the refractory metals (Nb-1Zr, V-20Ti, and TZM), the benefit of increasing life continues to a higher fluence limit or life than for either stainless steel or titanium.

With respect to wall life, the refractory metals were found to be economically competitive with stainless steel under certain constraints. For example, at a peak coolant temperature of 500°C, if the life of the stainless steel or titanium is 7 MW yrs/m^2 or less, the life of the refractory metals would have to be about twice that of the stainless steel or titanium for equal costs of electricity, again at a fixed peak coolant temperature of 500°C. If the life of stainless steel or titanium

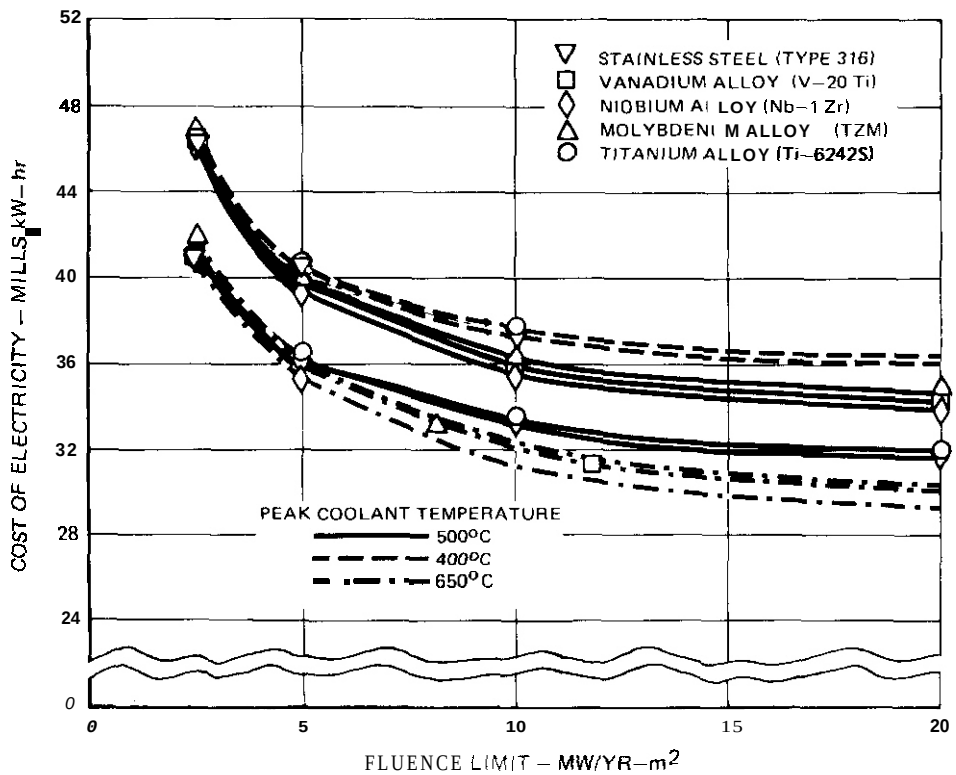

Figure *1.2.2* Life and Coolant Temperature Effects on Cost of Electricity for Material Changes in 1st Wall and Blanket Only

is about 10 MW yrs/m^2 or greater, the refractory metals will never become economically competitive at a fixed peak coolant temperature of 500°C. A change in the peak coolant temperature can alter some of these conclusions. For example, if the stainless steel or titanium is limited to a peak coolant temperature of 400°C, the refractory metals at a peak coolant temperature of *500°C* would be economically competitive at any life greater than 3 MW yrs/m^2 and the economic margin increases with increasing life. A similar relationship exists if the coolant temperature for stainless steel and titanium could be increased to *500°C* and the refractory metals could operate with a peak coolant temperature of *650°C.* For a maximum contrast case, vanadium, operating at a peak coolant temperature of *650°C* and having a life of *20* MW yrs/m^2 would provide a savings of 21% or 7 mills/kW-hr in the cost of electricity as compared to stainless steel or titanium operating with a peak coolant temperature of *400°C* and having a life of 10 MW yrs/m^2.

The previous figures showed the relationship between life, peak coolant temperature, and the cost of electricity for various structural materials used in the first wall, blanket, and header region only. Outside of this region, low cost materials such as titanium or stainless steel were used. However, because of the possibility of contamination or corrosion due to dissimilar metals being used in the same coolant loop, it may be necessary to use the same structural material throughout the primary coolant loop which includes the first wall, blanket, piping, first heat exchanger, pumps, dump tanks, valves, etc. Figure 1.2.3 shows this extended use of refractory metals significantly increases the cost of electricity. This increased cost is only recovered, relative to the use of stainless steel or titanium for a very narrow set of operating conditions. These conditions require that stainless steel or titanium structures operate with a 400°C coolant and have a component life of <5 MW yrs/m^2 and the refractory metals operate at 650°C and have a life of >10 MW yrs/m^2.

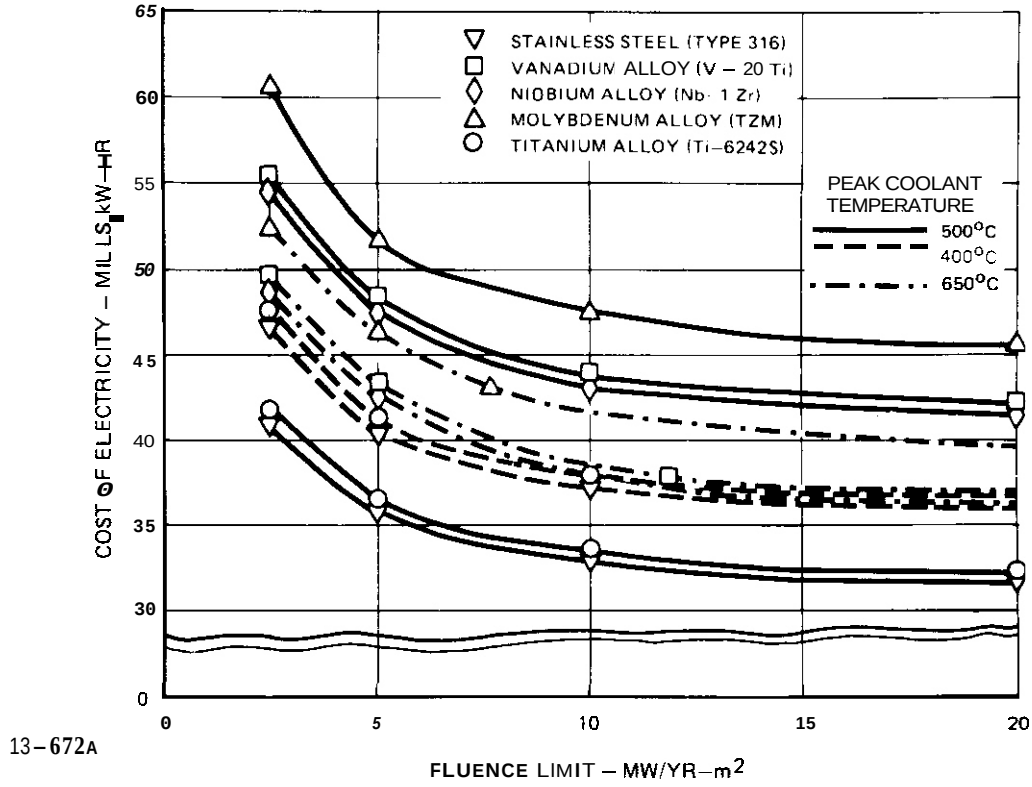

Figure 1.2.3 Life and Coolant Temperature Effects on Cost of Electricity for Material Changes in Blanket. Piping and Heat Exchanger/Storage System

1.2.5 Conclusions

The use of refractory metals in the first wall, blanket, and header region of a fusion reactor offer potential economic advantage over stainless steel and titanium provided they have a longer life or permit a higher peak coolant temperature. If the use of refractory metals is extended past the header region throughout the primary coolant loop, it is doubtful the refractory metals would offer economic advantage except for a very narrow set of conditions.

1.2.6 References

1. J. W. Davis, Economic Impact of Using Refractory Metals for Fusion Reactors, McDonnell Douglas, COO-4247-1, 1977.

1.3 ALLOYS FOR THE FUSION REACTOR ENVIRONMENT - A TECHNICAL ASSESSMENT

- D. L. Kummer, B. A. Cramer, D. A. DeFreece, J. W. Davis (McDonnell Douglas Astronautics Company - St. Louis), and ADIP Task Group.

1.3.1 ADIP Task

Task Number I.A.1 - Define Material Property Requirements and Make Structural Life Predictions.

1.3.2 Objective

The objective was to perform a technical assessment of the structural materials for the first wall/blanket component of a fusion reactor.

1.3.3 Summary

Primary and backup materials were selected for an Experimental Power Reactor (EPR), Demonstration Power Reactor (DPR) and Commercial Power Reactor (CPR). Testing and manpower requirements for establishing the material property data needed for design was defined. Natural resources and industrial capability necessary to satisfy a fusion economy were examined. Structural material life, failure modes and radioactivity considerations were among the factors evaluated.

1.3.4 Progress and Status

This activity is completed and a final report is published.] Therefore only the highlights will be summarized.

First wall/blanket structure was emphasized in the technical assessment of materials subject to intense irradiation. This is believed to be the most critical major component that is significantly damaged by irradiation from the plasma.

The assessment approach was to first define the most important factors that determine the acceptability of the first wall/blanket material. Then the material properties that significantly influence the ability of the candidate materials to satisfy these important factors were examined. Testing requirements to measure the material properties

were then explored. Some material properties and structural responses were examined in light of reactor system parameters in order to identify system/material trades that lead toward an improved reactor. Quantitative descriptions of material performance, testing, or important material/system factors were not possible in many cases because of the limited state-of-development of reactor design and of irradiated material properties. However, an attempt was made to quantify factors as much as possible knowing that future revisions to the assessment will be required as more information becomes available. In reality, reactor systems definition and materials requirements are mutually dependent on each other and both will be subject to considerable change as the evolution of fusion reactors takes place.

Performance of the first wall/blanket structure was judged to be more important than the environmental or safety issues that are affected by the first wall/blanket component. Perforance relates to the cost of electricity produced by a commercial reactor or the ability to satisfy the goals of an EPR or DPR. The major factors that affect performance were found to be life, maintenance time, peak coolant temperature and fabricated part cost. Resources could be an important factor for commercial power reactors (CPR's) depending upon the material availability and price, if controlled by foreign sources.

Increasing life beyond 10 to 15 MW yrs/m^2 caused only small additional reductions in the cost of electricity. However, the time required to change-out the first wall/blanket has a significant bearing on the desired life and this time is not accurately known. Therefore, striving for a long life is desirable until the change-out time and cost are better defined.

With regard to repair/maintenance, it may not be possible to achieve acceptable welds in radiation damaged material (high helium content). Also, a cooldown to low temperature (RT to 100°C) may cause very high stresses due to creep distortions that occurred during high temperature operation. The material may also be less ductile at low temperatures. These considerations may require a complete change-out during refurbishment rather than periodic replacement of portions of the first wall.

Design changes could also be made to accommodate these considerations.

Systems analysis of a typical reactor showed that a peak coolant temperature of 400°C could cause as much as a 21% increase in the cost of electricity compared to a peak coolant temperature of 650°C. Although it is acceptable to use relatively low coolant temperatures and consequently modest first wall/blanket operating temperatures, there is a significant conversion efficiency penalty. This penalty is reduced; however, if very expensive materials must be used to accommodate the high temperature or if life is shortened.

The cost of fabricated first wall/blanket structure was found to be important for a CPR within the range of $29 to $184/kg. This is the cost range between stainless steel and vanadium, the most expensive refractory metal considered. An increase in allowable peak coolant temperature (∿50 to 150°C depending on life) or life (generally a 2 fold increase at 500°C) offset this large increase in the cost of fabricated hardware. This means that: (1) the more expensive materials can be used with potentially little or no cost penalty, (2) higher prices can be paid for raw materials thereby improving resource availability, and (3) advanced manufacturing and inspection procedures can be used to assure high reliability. On the other hand, if expensive refractory metals have to be used throughout the blanket coolant loop (piping, heat exchanger, etc.) to avoid embrittlement, an economic advantage for refractory metals is difficult to achieve.

Failure modes for the first wall/blanket structure were found to include: (1) leak, (2) rupture, (3) deformation, and (4) instability. The first two are of greatest concern. One very small opening (crack) that permits air or coolant to enter the plasma chamber will introduce sufficient contamination to prevent acceptable plasma performance and cause a reactor shutdown. Unfortunately, crack formation and propagation has been a common event in structural materials in a variety of applications including power plants of all types. Rupture is a more catastrophic event and will likely be associated with the low elongation of radiation damaged material. Therefore, material properties such as crack growth rate, fracture toughness, fatigue life and embrittlement are important

for the first wall/blanket structural material. Any detrimental effect of irradiation on these properties, of course, is undesirable.

The reduction in elongation associated with radiation damage is expected to be detrimental to life; more so than swelling. Swelling is *not* a direct failure mode as it is for LMFBR which requires a minimum gap between fuel pins. For a fusion reactor, swelling is a source of stress the magnitude of which is controlled by irradiation creep and this relationship currently is not well understood.

A chief source of stress, including cyclic stresses that cause fatigue, is the temperature change associated with the pulse type operating conditions representative of tokamak or theta pinch reactors. Such cyclic operation accelerates failure by almost all failure modes and is the origin of fatigue failures. The magnitude of resultant stresses is a function of design and material. To minimize these thermal stresses, the material should have a low thermal expansion coefficient, high thermal conductivity and low modulus of elasticity. In this regard, the refractory metals, and to a lesser extent titanium, are superior to stainless steel and the nickel base 'alloys.

Another potential way to increase life, is to operate the material at a temperature below where helium has a significant effect on the fracture mechanisms. This allowable temperature is a function of the material melting point and again the refractory metals and perhaps titanium have an advantage over stainless steel and nickel alloys. However, the refractory metals also have major potential shortcomings. Niobium and vanadium are very sensitive to interstitial embrittlement from impurities in the coolant and molybdenum has fabrication, particularly welding, shortcomings.

Design of a reliable (no leaks for life of part) long life first wall/blanket structure will require precise structural analysis and testing of representative hardware. Precise structural analysis requires a complete mechanical property data base for irradiated material. Establishing this data is one of the most difficult problem areas. The reasons are the lack of high test volume, high flux, fast neutron sources. To obtain mechanical properties on a large number of specimens

requires much larger test volumes than available in d-Li and INS accelerator devices. For the next decase, only fission reactors will be available for such testing. This includes mixed spectrum reactors such as ORR, ATR, General Electric Test Reactor, HIFR and the High Flux Beam Reactor. Such reactors can duplicate the dpa to helium ratio in nickel-containing materials and therefore seem to be appropriate test facilities for these materials although correlation with the fusion reactor neutron spectrum is not yet completed.

Fast'fission reactors such as EBR-II and FFTF provide high dpa's and large test volumes but may not be available to the fusion program. They may be acceptable for testing non nickel bearing materials if helium effects on mechanical properties can be eliminated as an area of concern. This may be possible if the material is operated at a relatively low temperature, i.e., <400°C for SS, <500°C for Ti and <600°C for V.

If mixed spectrum and fast fission reactors can be used as the principal irradiation test facilities for fusion materials, the neutron source limitations will be greatly reduced, especially if mixed spectrum fission reactors are acceptable.

The first fusion reactor facilities contemplated per published DMFE plans are a FERF (operate about 1986) and a Materials Test Reactor (MTR) that would operate about 1994. A FERF, of modest flux, would be marginally adequate for establishing the data base for DPR but is compatible with CPR dates.

An attempt was made to define the testing requirement for establishing the material property data base needed for high reliability design. Crack growth and fatigue property measurements dominated the number of specimens required. Even with only 3 specimens per data point, a classical test matrix involves over 13,000 specimens. Application of statistical experiment test techniques will reduce this number. However, it appears that a large number of specimens will have to be subjected to a significant neutron fluence in order to establish a reasonable data base. Remembering that the first wall/blanket structure is a leak critical, inaccessible pressure vessel, the need for reliability, and consequently a good data base, seems warranted.

Assuming that 5000 specimens per alloy must be tested and that 1 ORR reactor is needed over a 10-year period, the testing cost will be $25M to $35M per specific material. Use of an FFTF would greatly increase cost because the operating cost is estimated to be $60M/year. If 5000 specimens were tested over a 10-year period using 10%of the FFTF, the testing cost will be $70M to $80M per alloy.

The questions of the scope of testing required and needed test facilities are very important and need additional study immediately. A "bootstrapping" method of building EPR with a minimum of material property data and then using the knowledge gained in operating EPR for design of DPR has been suggested. This may work but has risk and schedule shortcomings.

It seems clear that austenitic stainless steel or a nickel base alloy are the only viable candidates for EPR. Major reasons include: (1) knowledge of performance in a fast neutron environment (from LMFBR program), (2) ability to use fission reactors for irradiation testing, (3) mill product availability and industrial manufacturing experience, and (4) apparent ability to meet performance requirements.

If the required irradiation'testing to obtain the necessary material property data and to perform design verification testing is similar to the scope previously discussed, it will be difficult to use any material other than the EPR material for DPR. It appears that the number of materials that are submitted to characterization testing will have to be very few because of the expense and time for irradiation testing. Making a decision on the alloy for EPR and DPR at the earliest possible date will conserve the limited manpower and irradiation test resources available. This will improve the probability of successful development of an improved material for CPR.

Material choices for the CPR cannot be accurately made at this time. Vanadium and titanium appear more promising than stainless steel or nickel alloys because of lower thermal stresses, a greater probability of operation below the critical helium embrittlement temperature, low activity, and domestic resources. Niobium and molybdenum are resource limited. Stainless steel and nickel alloys appear to have limited life potential (1-4 MW yrs/m^2).

The case for low induced radioactivity first wall/blanket structural materials was examined. The potential advantage of hands-on maintenance outboard of the shield is not enhanced by low activity of the first wall/blanket. Only the materials in the shield are important. The possibility of hands-on maintenance inboard of the shield appears unlikely. Therefore, the radioactivity of the first wall/blanket structural material has little, if any, effect on the important hands-on maintenance possibilities. For accident and releases to the atmosphere considerations, tritium dominates. This leaves reduced storage of activated components removed from the reactor as the only payoff for use of low activity first wall/blanket structural materials. Although storage is not technically difficult, low residual activity may be important for public acceptance. If the material can be reused in a reasonable period of time, economic and resources advantages exist.

Vanadium and titanium will have a very low activity level after about 50 years and some believe recycling is possible after 50 years of decay. These two materials seem to be the only first wall/blanket structural materials for which there is a payoff due to low activity. Also they appear promising from other standpoints and their use would not likely impose any significant performance penalties.

1.3.5 Conclusions

One of the most pacing problems is irradiation testing to support alloy development and property characterization. Establishing a material property data base to enable the design of high reliability first wall/blanket structures will require a large instrumented test volume. Establishing this data base is complicated by the need for extensive fatigue and crack growth property data. Fatigue and crack growth are likely failure modes and difficult to measure properties particularly on irradiated material. Also testing to determine the performance of designs is needed which also requires high volume test facilities. Therefore, ways to permit the use of mixed spectrum and fast fission reactors should be emphasized. Complete development and characterization of alloys/designs for reliable operation in a CPR appears to

require a fusion reactor suitable for materials/structures testing. Use of fission reactors is appropriate for nickel bearing alloys and perhaps for non-nickel bearing alloys if they are operated at a temperature where helium does not contribute to the fracture process. Operation at such a temperature may also be desirable to maximize life.

The number of materials that can be sufficiently characterized by irradiation testing in the next 20 years to permit reliable design is limited. Therefore, selection of the candidates at an early date is desirable to conserve resources and meet schedules. A stainless steel or nickel alloy appears to be the only viable candidate for EPR and probably DPR. Exploratory development of an optimum CPR material should begin with emphasis on vanadium and titanium alloys. The EPR/DPR alloy would be the backup for CPR. Vanadium and titanium are clearly the most attractive candidates for CPR from low activity and resources standpoints. Niobium and molybdenum both appear to have resource limitations. Refractory metals have a longer potential life than stainless steel and nickel base alloys, particularly if operated at modest temperatures of 500 to 600°C. Systems studies showing that a peak coolant temperature of 500 to 600°C and modest ($2-3$ MW/m^2) wall loadings are acceptable for efficient power generation improves the outlook for achieving long life materials. Also, the systems studies have shown that use of the high cost refractory metals for first wall/blanket structure only has modest impact on the cost of electricity, depending upon the life and allowable coolant temperature improvements offered. However, if the refractory metals are also used for piping, valves, heat exchanger, etc., it is difficult for them to be cost competitive. The factors considered for selection of the materials for EPR, DPR and CPR seem appropriate but the weight to apply to each remain uncertain particularly for CPR.

Additional integrated design, structural analysis, materials and maintenance studies need to be conducted to better define the options and the best approaches. Until structural design philosophies are established and risk assessments made, the scope of the irradiation test program required to establish design data cannot be accurately defined. Likewise, designs that permit rapid and reliable changeout of a first wall module

that fails prematurely need to be developed so that this option can be traded against the needed design reliability and life.

1.3.6 References

1. U.S. Department of Energy, Alloys for The Fusion Reactor Environment, DOE/ET-0007 (January 1978).

1.4 RECYCLING POTENTIAL OF TITANIUM ALLOYS - J. W. Davis (McDonnell-Douglas), G. L. Kulcinski (University of Wisconsin), and T. Y. Sung (Brookhaven).

1.4.1 ADIP Task

Task Number I.A.l.l - Select initial representative designs, obtain property data, establish analysis procedures and complete initial analysis.

1.4.2 Objective

To determine if the radioactive decay of titanium is sufficiently short to allow reprocessing in a reasonable time (<50 years) and how the common alloying elements of titanium effect that reprocessing.

1.4.3 Summary

This study examines just how long one must contain radioactive titanium before it can be safety reprocessed. It was assumed that the spent first wall and blanket structural material would be completely reprocessed in a standard manufacturing facility capable of both primary and secondary fabrication.

It was found that reprocessing could occur when the chemical hazard associated with inhalation was greater than the hazard associated with inhalating the same amount of radioactive species. This conclusion allowed the use of the threshold limiting value (TLV) to set a limit on the airborne concentration of the elements. Then by calculating the time required for that amount of material to decay to the same diluent factor indicated by the biological hazard potential (BHP) in air, the time for reprocessing was determined. Based on these assumptions it was determined that it is feasible to think of titanium, and some of its alloying elements as being recyclable in a relatively short time period (<50 years).

1.4.4 Progress and Status

Some of the criteria that has been identified for the selection of first wall/blanket structural material are low cost, fabricability, availability, resistance to radiation damage, coolant compatibility,

temperature capability, and low long-term radioactivity. To date the materials that have received the most attention and have been identified as partially satisfying these criteria are the austenitic stainless steels, nickel base alloys, refractory metals (niobium and vanadium), the aluminum alloys, and in some cases the nonmetals such as carbon and SiC. An additional class of materials, referred to as the reactive metals (titanium) was added to the list based on the results of a McDonnell Douglas study.' This study revealed that titanium appeared to offer advantage over stainless not only on strength-to-weight and thermal stress bases, but also from a radioactivity standpoint. The radioactivity of the titanium alloy Ti-6Al-4V in comparison to other candidate structural materials is shown in Figure 1.4.1. This figure reveals that the short term radioactivity is high (as it is for all the potential structural materials), while the intermediate term radioactivity (a few weeks to a few months after shutdown) is comparable to most candidate structural materials. However, it is in the area of long term radioactivity (which drops to very low levels after roughly 10 years of storage), that titanium appears to offer a distinct advantage because it presents the possibility of reprocessing the material in a standard manufacturing facility. The ability to reuse critical materials is not only environmentally beneficial, but it can also reduce the demand on mineral resources.

This study was designed to explore the potential for early reprocessing of titanium alloys. Since alloying elements can affect the radioactivity, it is necessary to know their affect on the desirable short lived radioactivity of titanium. To accomplish this, we calculated the radioactivity, BHP, and afterheat of several of the common alloying elements of titanium (i.e., Si, Al, V, Cr, Mo, Zr, Mn, and Sn) using the blanket model described in Reference 1, the cylindrical calculations (P_3 S_8) and the computer codes of Sung.' The results of these calculations are shown in Figure 1.4.2 and are based on a reactor with a thermal power level of 5000 MW and a neutron wall loading of 1.25 MW/m^2. This figure shows that the addition of Si, Sn, Cr, or V to titanium does not increase the BHP above that due to titanium for times >1 year.

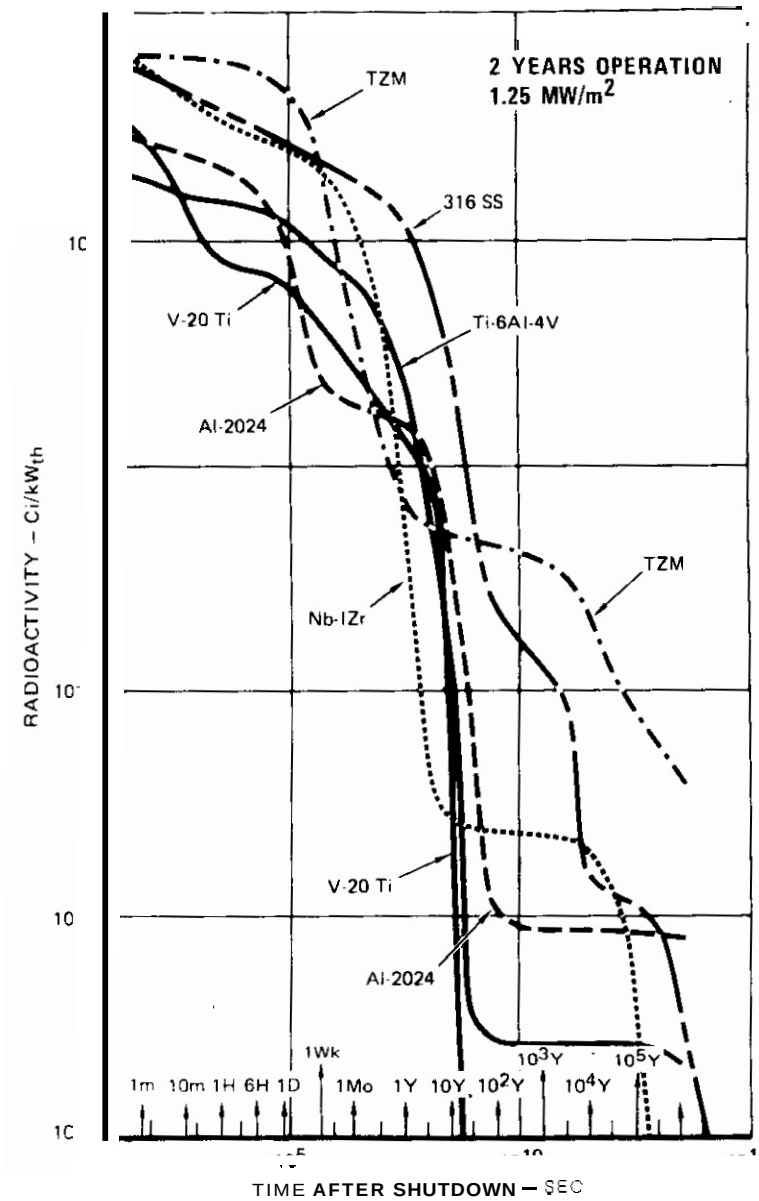

Figure 1.4.1 **Radioactivity of Fusion Reactor Blankets After Shutdown**

The BHP for these elements drops to insignificant levels in approximately 10-20 years. The addition of Mn has a significant effect on the near term BHP but it decays to insignificant levels after about 30 years. The addition of Al, Zr, and Mo increases the BHP above titanium and they would take several thousand years to decay to insignificant levels.

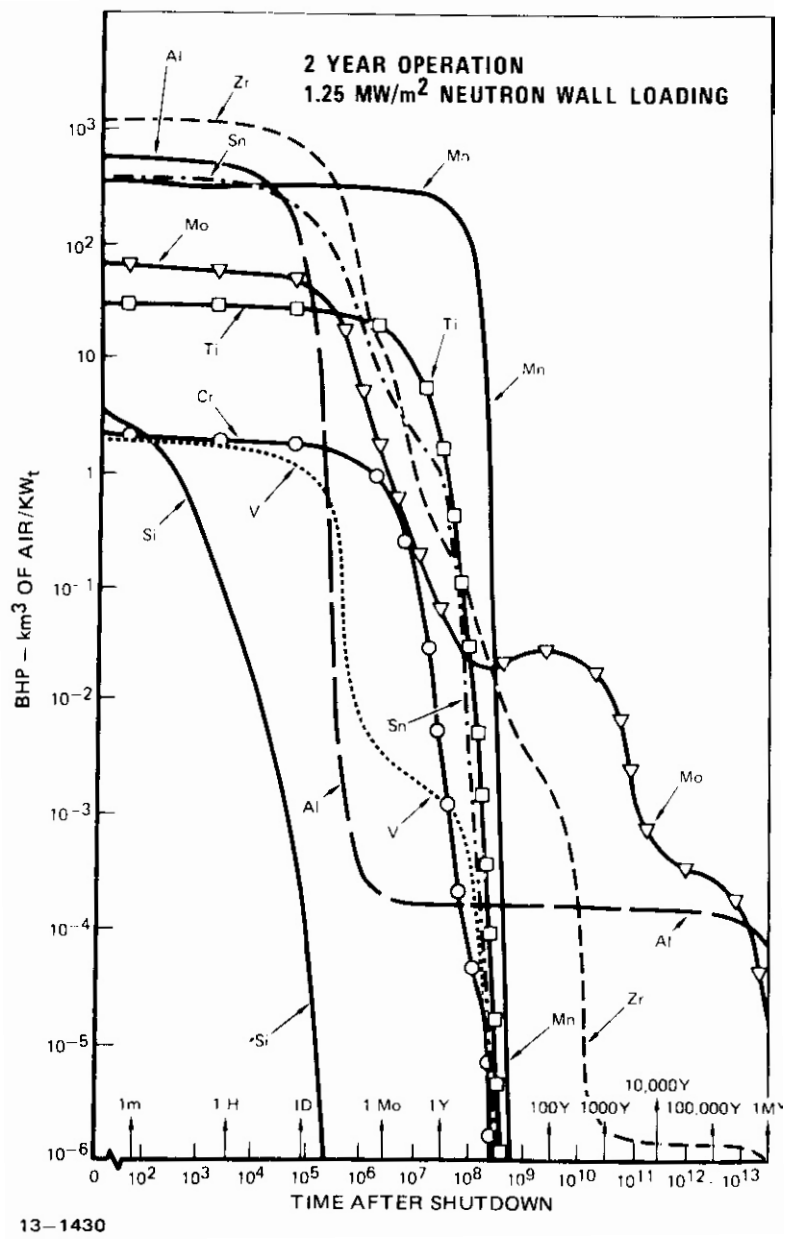

Figure 1.4.2 First Wall BHP For Several Elements

Therefore, from a radioactivity standpoint, the alloying elements for titanium in order of increasing desirability are:

Increasing desirability

Mo, Al, Zr, Mn, Cr, V, Sn, Si

Once the desired alloying elements for titanium were known, the next step was to determine how long one must contain such radioactive material before it can be safely released to the environment. Because any analysis of this type must rely on some subjective assessment of "how safe is safe," we have tried to error on the conservative side so as to not overstate the case for titanium. In addition, it was assumed that the spent first wall and blanket structural material would be reprocessed in a standard manufacturing facility which would completely reprocess the material (i.e., primary and secondary fabrication). It was also assumed that reprocessing could occur when the chemical hazard associated with inhalation is greater than that due to the hazard associated with inhaling the same amount of radioactive species. This allows one to use the threshold limiting value (TLV) to set a limit on the airborne concentration of elements and then to calculate the time required for that amount of material to decay to the same diluent factor indicated by the BHP in air. In other words, when the limiting value of the BHP in (km^3/kW_{th}) equals the mass of the first wall (g/km^3) then the materials can be reprocessed in a standard plant.

The implications of this can be illustrated by a simple calculation for titanium. The TLV for titanium is 10^1 g/km^3 and the mass of a titanium first wall in a UWMAK-I type of reactor is 10 g/kW_{th}. Therefore, when the BHP (air) reaches 10^{-6} $km^3/kWth$, titanium could be reprocessed. Referring to Figure *1.4.3*, which is a replot of the information presented in Figure *1.4.2* on a linear scale, it is seen that this level is achieved for titanium in roughly 10 years. Table 1.4.1 summarizes the results of calculations for several other common alloying elements of titanium and reveals that with the exception of aluminum and manganese, certain alloying elements for titanium would reach the industrial threshold limits in less than 10 years. It might be argued that with a "small" amount of reprocessing constraints and some extra cost, one might be able to tolerate somewhat higher BHP values. However, in examining Figure *1.4.3*, one can see that even factors of 10 to 100 times the limiting BHP would make, at the most, only a few years difference for all except Al and does not change the general conclusion for Ti significantly. Included in Table 1.4.1 is the approximate radiation level of various

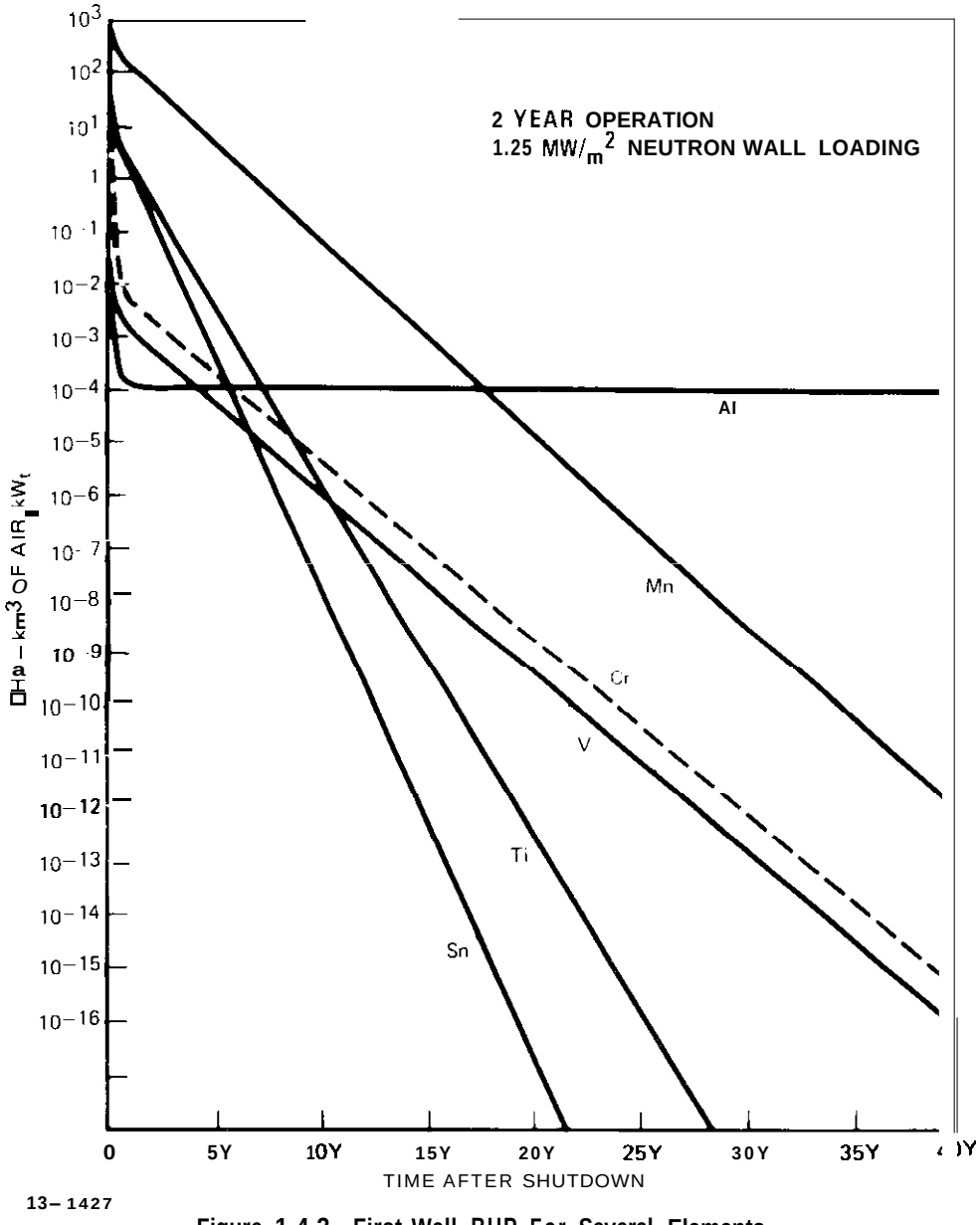

Figure 1.4.3 First Wall BHP For Several Elements

first wall elements after decaying for the time required for BHP to equal the industrial hazard index (IHI). The radiation levels from all of the elements are well below the background level of 0.01 mrem/hr except for aluminum. This means that the industrial hazard index (IHI) appears to be the most restrictive criterion on which to judge the time of reprocessing. Therefore, it is completely reasonable to think about neutron-irradiated titanium and certain of its alloying elements as being recyclable in a relatively short time period (<50 years).

Table 1.4.1 Approximate Time For Fusion Reactor Elements to Decay to Hazard Levels Comparable to Industrial Threshold Limits

Element	TLV (g/km^3)	Mars of 1st Wall (g/kWt)	Time For BHP to Decay to IHI Limit – Yr	Radiation Level MREM/Hr (a)
Ti	10^7 •	10.2	10	$8x10^{-9}$
Sn	$2x10^6$	16.5	7	$<10^{-10}$
V	$5x10^5$ (Dust)	13.7	6	$2x10^{-8}$
	$5x10^4$ (Fume)	13.7	3	-
Mn	$5x10^6$	16.7	22	$7x10^{-3}$
Al	107	6.1	> 100.000	$8x10^{-2}$
Cr	$5x10^5$	16.0	7	$<10^{-10}$

(a) The value shown is the radiation level at 30 cm (1 foot) from an isotropic source based on a unit volume of $1 cm^3$ of 1st wall material at the time to decay to the industrial hazard index (IHI)

13–1426

1.4.5 Conclusion

Based on the results of this study, it appears feasible to develop a titanium alloy that could be recycled in less than 50 years. Ideally this alloy should be composed of Cr, V, Sn, or Si for low radioactivity, however, with these elements the titanium would be essentially a beta alloy and unstable at the elevated temperatures *(400-500°C)* required for efficient power generation. To improve the elevated temperature stability along with properties such as elevated temperature strength, creep resistance, weldability, and toughness requires the addition of elements such as aluminum or tin. Of these two elements aluminum is preferred because it is a more potent strengthener, even though it does increase the radioactivity. However, if it is used in small concentrations (<6 w/o) it should not significantly impair the reuse potential even though some special procedures would be required at a processing facility.

1.4.6 References

1. J. W. Davis and G. L. Kulcinski, Assessment of Titanium for Use in The First Wall/Blanket Structure of Fusion Power Reactors, Electric Power Research Institute, EPRI ER-836, April 1977.

2. T. Y. Sung, PhD Thesis, University of Wisconsin, 1977.

1.5 CALCULATION OF IRRADIATION RESPONSE RATES FOR FISSION REACTORS USED BY THE ADIP IRRADIATION PROGRAMS — T. A. Gabriel, B. L. Bishop, and F. W. Wiffen (ORNL)

1.5.1 ADIP Task

ADIP Task I.A.2, Define Test Matrices and Test Procedures.

1.5.2 Objective

Previously we obtained' the calculated irradiation response in displacements per atom (DPA) and gas production values of a number of elements and metal alloys for a fusion reactor first-wall neutron spectrum. These sets of values allowed a self-consistent evaluation of the effect of alloy modification on DPA and gas production. In this work similar calculated values are presented for various locations within the fission reactors ORR, HFIR, and EBR-II. The purpose is to provide better information to experimentalists €or planning and evaluating fission reactor experiments in the light of fusion reactor needs.

1.5.3 Summary

Planning radiation damage experiments in fission reactors such as ORR, HFIR, and EBR-II in support of fusion reactor materials development requires for these facilities DPA and gas production rates for many potential materials. This report summarizes some of the calculations currently under way.

1.5.4 Progress and Status

Previously developed' irradiation response rates calculated for alloys of interest in a fusion reactor first-wall spectrum are summarized in Table 1.5.1. Details of the calculations and more extensive analysis of the results are given in the referenced report.

Presented in Table 1.5.2 are the DPA and gas production rates for several elements commonly found in many of the alloys under consideration for application in fusion reactors. The values are for the horizontal midplane positions of **ORR-C3,** HFIR-peripheral target position; and EBR-II, Row 2.

Table 1.5.1. Rates of Displacement and Gas Production in the Elemental Constituents of Candidate Alloys in a Fusion Reactor First-Wall Neutron Spectrum at a Neutron Wall Loading of 1 Mw/m^2

Element	Effective Displacement Threshold Energy (eV)	Displacement Damage (dpa/s)	Gas Production Rates, (at. ppm/s)	
			Helium	Hydrogen
		$\times 10^{-7}$	$\times 10^{-7}$	$\times 10^{-7}$
Fe	40	3.62	34.9	151.
Ni	40	3.87	130.	397.
Cr	40	3.58	32.6	100.
Mn	40	3.58	26.7	100.
V	40	3.63	15.0	78.2
Nb	60	2.31	9.18	33.3
Mo	60	2.38	14.8	21.5
Ti	30	5.03	33.5	49.7
Zr	50	2.54	2.93	25.2
Al	25	4.63	101.	94.5
Mg	25	4.48	147.	148.
Cu	30	4.88	31.8	173.
co	40	3.60	23.1	73.7

The methods used to calculate the irradiation response of elements of interest have been described in detail.' All reactions – elastic, inelastic, charged particle, $(n,2n)$, capture, etc., – that are considered in ENDF/B-IV have been included in this analysis. Nuclear data are taken from the ENDF/B-IV file, and displacement damage calculations follow the recommendations of the IAEA working group.[2] For elements other than iron, effective displacement energies recommended by Doran and Graves[3] were used.

The neutron fluxes for the three reactors were taken from 2-D transport calculations. The total flux values for the ORR, HFIR, and EBR-II locations used are 8.0×10^{18}, 5.5×10^{19}, and 2.14×10^{19} n/m^2s, respectively. As can be seen from the tables, gas production rates differ significantly for the elements that normally compose path A and path B alloys, although the displacement rates for these elements are nearly identical.

Table 1.5.2. Rates of Production of Displacements and Gas in the Elemental Constituents of Fusion Candidate Alloys for Three Reactor Spectra

Element	Effective Displacement Threshold Energy (eV)	Values for ORR C-3			Values for HFIR Peripheral Target Position			Values for EBR-II Row 2		
		Displacement Damage (dpa/s)	Gas Production Rates, (at. ppm/s)		Displacement Damage (dpa/s)	Gas Production Rates, (at. ppm/s)		Displacement Damage (dpa/s)	Gas Production Rates, (at. ppm/s)	
			Helium	Hydrogen		Helium	Hydrogen		Helium	Hydrogen
Fe	40	2.13×10^{-7}	6.23×10^{-8}	1.07×10^{-6}	1.02×10^{-6}	2.84×10^{-7}	5.24×10^{-6}	9.93×10^{-7}	2.80×10^{-7}	5.53×10^{-6}
Ni	40	2.25×10^{-7}	$(8.88 \times 10^{-7})^a$	1.36×10^{-5}	1.10×10^{-6}	$(4.25 \times 10^{-6})^a$	6.71×10^{-5}	1.10×10^{-6}	$(2.97 \times 10^{-6})^b$	4.24×10^{-5}
Cr	40	2.41×10^{-7}	2.27×10^{-8}	3.14×10^{-7}	1.16×10^{-6}	9.90×10^{-8}	1.49×10^{-6}	1.14×10^{-6}	1.32×10^{-7}	1.17×10^{-6}
Mn	40	2.65×10^{-7}	2.46×10^{-8}	2.47×10^{-7}	1.33×10^{-6}	1.07×10^{-7}	1.16×10^{-6}	1.18×10^{-6}	1.36×10^{-7}	1.05×10^{-6}
V	40	2.65×10^{-7}	4.68×10^{-9}	1.90×10^{-7}	1.28×10^{-6}	1.82×10^{-8}	9.08×10^{-7}	1.24×10^{-6}	3.98×10^{-8}	7.28×10^{-7}
Nb	60	1.43×10^{-7}	1.55×10^{-8}	1.10×10^{-7}	6.77×10^{-7}	7.15×10^{-8}	5.14×10^{-7}	7.51×10^{-7}	6.85×10^{-8}	4.23×10^{-7}
Mo	60	1.63×10^{-7}	1.54×10^{-8}	2.99×10^{-8}	7.81×10^{-7}	6.77×10^{-8}	1.36×10^{-7}	8.20×10^{-7}	8.11×10^{-8}	1.40×10^{-7}
Ti	30	3.45×10^{-7}	3.11×10^{-8}	5.06×10^{-8}	1.68×10^{-6}	1.37×10^{-7}	2.21×10^{-7}	1.49×10^{-6}	1.69×10^{-7}	2.74×10^{-7}
Zr	50	1.63×10^{-7}	4.32×10^{-10}	6.13×10^{-8}	7.70×10^{-7}	1.40×10^{-9}	2.92×10^{-7}	9.01×10^{-7}	6.12×10^{-9}	2.38×10^{-7}
Al	25	4.28×10^{-7}	1.42×10^{-7}	7.31×10^{-7}	2.02×10^{-6}	6.16×10^{-7}	3.52×10^{-6}	2.38×10^{-6}	7.38×10^{-7}	2.40×10^{-6}
Mg	25	4.35×10^{-7}	5.40×10^{-7}	2.37×10^{-7}	2.05×10^{-6}	2.54×10^{-6}	1.06×10^{-6}	2.59×10^{-6}	2.01×10^{-6}	2.13×10^{-6}
Cu	30	2.92×10^{-7}	6.11×10^{-8}	3.25×10^{-6}	1.41×10^{-6}	2.74×10^{-7}	1.60×10^{-5}	1.45×10^{-6}	2.89×10^{-7}	1.05×10^{-5}
Co	40	2.50×10^{-7}	3.18×10^{-8}	5.35×10^{-7}	1.35×10^{-6}	1.42×10^{-7}	2.56×10^{-6}	1.10×10^{-6}	1.57×10^{-7}	1.89×10^{-6}

[a] This is the helium production from direct processes only; it does not include the two-step helium production from ^{58}Ni.

[b] For EBR-II this is the full helium production rate; the two-step reaction from ^{58}Ni does not make a significant contribution because of lack of thermal energy neutrons in this reactor.

1.5.5 Conclusions and Future Work

Displacement and gas production rates are being calculated for various fission reactors so that experiments directed at fusion reactor applications can be planned.

Much more complete tabular and graphical presentations are being developed to give response rates as a function of position in ORR, HFIR, and EBR-II.

1.5.6 References

1. T. A. Gabriel, B. L. Bishop, and F. W. Wiffen, *Calculated Irradiation Response of Materials Using a Fusion-Reactor First-Wall Neutron Spectrum*, ORNL/TM-5956 (June 1977); to be published in *Nuclear Technology*.
2. "Recommendations for Displacement Calculations for Reactor/Accelerator Studies in Austenitic Steel," (Report of IAEA Specialists Meeting on Radiation Damage Units in Ferritic and Austenitic Steel), *Nucl. Eng. Design 33:* 91 (1975).
3. D. G. Doran and N. J. Graves, "Neutron Displacement Damage Cross Sections for Structural Metals," p. *463* in *Irradiation Effects in the Microstructure and Properties of Metals*, ASTM STP 611, American Society for Testing and Materials, Philadelphia, 1976.

2. TEST MATRICES AND TEST METHODS DEVELOPMENT

An important part of the alloy development effort is the definition of test matrices and development of test methods. The alloy development strategy will proceed through stages requiring tests of generally increasing difficulty and complexity.

1. Scoping tests will be used to make relative judgments between materials and metallurgical conditions and to identify critical properties. Such tests, which will be used where large numbers of variables are involved, must be rapid, simple, and decisive.

2. Developmental tests will be used for optimization of the Prime Candidate Alloys. They will be broader and more extensive than the scoping tests. In-reactor testing will be an important part of this work.

3. Engineering property tests will be devised to provide the broad data base needed for reactor design.

2.1 DETERMINATION OF FATIGUE SPECIMEN CONFIGURATION FOR IRRADIATION EFFECTS TESTING - B. A. Cramer and J. W. Davis (McDonnell-Douglas Astronautics Company - St. Louis).

2.1.1 ADIP Task

Task Number I.A.2 - Define Test Matrices and Test Procedures.

2.1.2 Objective

The objective of this effort was to establish configurations for tensile and fatigue test specimens, fabricated from sheet material, for application in irradiation testing.

2.1.3 Summary

The geometry of a small fatigue specimen for irradiation testing has been defined. This specimen is fabricated from thin sheet material, occupies the same test volume as the SS-1 sheet tensile specimen, and increases the number of fatigue tests per unit volume of test space by a factor of 4 to 5.

2.1.4 Progress and Status

Limited reactor space is available for irradiation testing of potential fusion reactor materials. In the latter half of 1977 a titanium test matrix was developed for irradiation experiments in MFE #1. In defining the fatigue tests it was determined that using the standard rod specimen would not allow a sufficient number of tests for the 4 alloys and the various heat treatments to be evaluated. Therefore a smaller specimen, fabricated from sheet material was defined.

The specimen configuration is shown in Figure 2.1.1. This specimen has a constant width test section with a Grodzinski elliptical fillet.[1] This configuration results in an acceptable low stress concentration factor (K_t) of approximately 1.02 in the test section. The stress concentration factor is a function of b/a and b/d for the Grodzinski fillet configuration. However, the stress concentration factor is relatively insensitive to variations about the dimensions shown. This specimen,

although smaller than specimens typically used, conforms to configurations used in the aircraft industry for sheetmetal fatigue testing. Guidelines used in establishing specimen grip dimensions are: (1) the specimen grip width (D) should be at least three times the net test section width (d), and (2) the pin diameter should be at least equal to the net test section width.

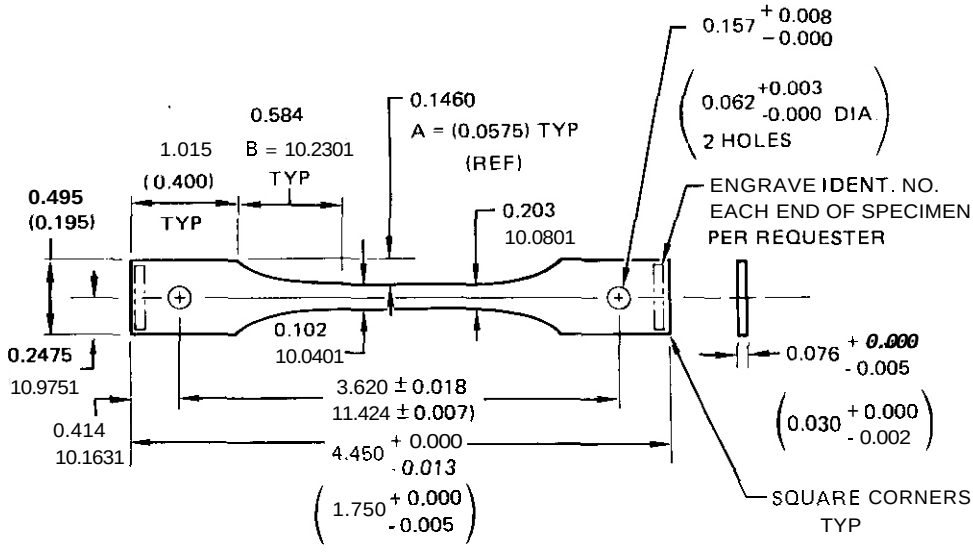

NOTE:

1. ALL DIMENSIONS ARE IN CENTIMETERS (INCHES)
2. BREAK ALLSHARPEDGES.
3. SURFACE FINISH ROUGHNESS HEIGHT RATING OF .8 μm RMS 132 MICROINCH) OR BETTER ALL OVER.
4. POLISH REDUCED AREA LONGITUDINALLY TO REMOVE ALL WORK MARKS VISIBLE AT APPROXIMATELY 20X MAGNIFICATION UNDER A LIGHT MICROSCOPE,
5. ALLTOLERANCES ±0.0025 (±0.001) EXCEPT WHERE OTHERWISE SPECIFIED.
6. ALL SPECIMENS AND MATERIALS MUST BE IDENTIFIED AT ALL TIMES WITH HEAT NUMBER.
7. A & B DIMENSIONS DEFINE MINOR & MAJOR RADII FOR ELLIPTICAL FILLET.

13–1431 **Figure 2.1.1 Fatigue Specimen Configuration**

Use of small specimens represents a departure from standard fatigue testing (typical minimum test section widths are usually .5 inches). Generally higher fatigue life (as much as a factor of 2) is obtained with relatively smaller specimens due to the reduced possibility of the specimen containing a flaw. However, in the case of the very small specimen widths being proposed for irradiation testing, the machining of the

specimen edges will become a critical factor since a burr or flaw would cause premature fatigue failure. With larger sheet widths, this is generally precluded by shot peening the edges to produce an initial compression stress along the edges. This will not he possible with the small specimens because shot peening might significantly affect the specimen fatigue properties. Therefore special consideration will have to he given to machining of these specimens.

2.1.5 Conclusions

The sheet specimen defined for irradiation testing represents a step toward obtaining increased test data from existing test facilities. Because of the critical nature of the specimen edge machining as well as the effects of tolerances (such as the position of the loading hole with respect to the test section), a larger amount of scatter is expected with these specimens than with standard fatigue specimens. This may be acceptable, however, because of the comparative nature of irradiated and unirradiated testing. A relatively large number of unirradiated specimens needs to be tested to establish the expected scatter.

2.1.6 Reference

1. Peterson, R., Stress Concentration Design Factors, John Wiley & Sons Inc., 1953.

3. PATH A ALLOY DEVELOPMENT — AUSTENITIC STAINLESS STEELS

Path A alloys are those alloys generally known as austenitic stainless steels. The most common U.S. designations are AISI types 304, 316, 321, and 347. Primary considerations for selecting this class of alloys for further development are:

1. state-of-the-art production and fabrication technology;
2. extensive data on the effects of neutron irradiation on properties, which show the potential of these alloys for MFR applications;
3. compatibility with proposed coolants and breeding fluids;
4. evidence that for MFR conditions (He, dpa, temperatures) the properties are sensitive to composition and microstructure — thus showing potential for further development.

The strategy for development of these alloys has two related objectives:

1. to determine for a reference alloy the effects of irradiation on those properties most important to fusion reactor design;
2. to develop a path A alloy that is optimized for fusion reactor applications.

The first objective will provide a data base for near-term reactor design and, most important, guidance as to which properties limit performance of this type alloy. Work on the reference alloy will provide direction for the actual alloy development efforts of the second objective. Type 316 stainless steel in the 20%-cold-worked condition appears to be the best choice as a reference alloy. It is the present reference cladding and duct alloy in the breeder reactor programs, and there are extensive data on the unirradiated mechanical properties, effects of heat treatment on properties, structure, and phase stability, and the effects of fast neutron irradiation on properties. The present technology of austenitic stainless steels, including understanding of the physical and mechanical properties and irradiation response, is such that alloy development efforts can move to optimization for use in fusion reactor applications. A Prime Candidate Alloy (PCA) (Fe—16% Ni—14% Cr—2% Mo—2% Mn—0.5% Si—0.2% Ti—0.05% C) has been selected by the ADIP task group. Efforts will now focus on optimizing the composition and microstructure of the PCA leading towards the selection of OPT-A1 (Program Plan designation of first optimized path A alloy).

3.1 COMPARISON OF TITANILTM-MODIFIED AND STANDARD TYPE 316 STAINLESS STEEL IRRADIATED IN HFIR — SWELLING AND MICROSTRUCTURE — P. J. Maziasz and E. E. Bloom (ORNL)

3.1.1 ADIP Task

ADIP Task I.C.2, Microstructure and Swelling in Austenitic Alloys.

3.1.2 Objective

The objective of this work is to examine the effect of titanium additions on the microstructural development and swelling behavior of austenitic stainless steels irradiated in a mixed-spectrum fission reactor to produce helium and displacements in approximately the same amounts as in a fusion reactor.

3.1.3 Summary

Swelling in annealed type 316 stainless steel irradiated in HFIR at 580 to 780°C to fluences producing 1850 to 3300 at. ppm He and 30 to 47 dpa is reduced by the addition of 0.23 wt % Ti. Microstructural examination shows that small helium bubbles are encrusted on finely dispersed intragranular TiC precipitate particles. The TiC particles are preferred sinks for accommodating helium over dislocations and other precipitate phases. Irradiation of the titanium-modified alloy in HFIR at 600°C, forms $M_{23}C_6$ and Ti(C,N)S at the grain boundaries. This precludes formation of large grain boundary cavities. At higher temperatures, grain boundary cavities form in the alloy with 0.23 wt % Ti, but the cavities are much smaller than in annealed type 316 irradiated under similar conditions. At higher temperatures, the swelling of the annealed alloy with 0.23 wt % Ti approaches that of type 316 stainless steel because the TiC precipitate coarsens and large portions of the matrix are too far from the precipitate to be affected. Finally, in the 20%-cold-worked condition, the addition of 0.23 wt % Ti to type 316 stainless steel reduces swelling and retards recrystallization for irradiation in HFIR at 580 to 590°C to fluences producing 1.5 to 3.0 dpa and 30 to 80 at. ppm He.

3.1.4 Progress and Status

Samples of annealed type 316 stainless steel with and without 0.23 wt % Ti have been irradiated in HFIR at temperatures from 600 to 780°C to fluences producing 30 to 60 dpa and 1850 to 4000 at. ppm He. The compositions of these steels are given in Table 3.1.1. Swelling values are given in Table 3.1.2 and plotted as a function of temperature in Fig. 3.1.1. These swelling values are cavity volume fractions as determined by electron microscopy. In the temperature range 600 to 780°C, the swelling is clearly reduced by the titanium addition. This can be understood from the microstructural examination.

Table 3.1.1. Composition of Type 316 Stainless Steel Irradiated in HFIR

Alloy	Content, wt %[a]										
	Cr	Ni	Mo	Mn	C	Ti	Si	P	S	N	B
Standard	18.0	13.0	2.58	**1.90**	*0.05*	***0.05***	*0.80*	**0.013**	**0.016**	0.05	*0.0005*
Ti Modified	17.0	12.0	2.50	**0.5**	*0.06*	**0.23**	*0.40*	**0.01**	**0.013**	**0.0055**	**0.0007**

[a] Balance iron.

The precipitate phases observed after irradiation of annealed type 316 stainless steel in HFIR at *550* to 680°C to fluences producing 2000 to 3300 at. ppm He and 30 to 47 dpa are discussed in Sect. 3.3 of this report. They are also summarized in Table 3.1.3. If results for annealed type 316 stainless steel with 0.23 wt % Ti, also summarized in Table 3.1.2, are compared with those for standard type 316, the addition of titanium has obviously caused intragranular precipitation of TiC. Figures 3.1.2 and 3.1.3 show, respectively, unmodified type 316 stainless steel and the alloy containing 0.23 wt % Ti after irradiation at 600°C to fluences producing 1850 to 2000 at. ppm He and **30** dpa. Both samples have intragranular Laves phase. The unmodified type 316 has sigma phase and large cavities at the grain boundaries, while the alloy with 0.23 wt % Ti has $M_{23}C_6$, Ti(C,N)S, and very few cavities at the grain boundaries. Most importantly, the alloy with 0.23 wt % Ti has fine TiC particles dispersed

Table 3.1.2. Swelling and Cavity Statistics for Type 316 Stainless Steel With and Without 0.23 wt % Ti

Alloy	Condition	Irradiation Temperature (°C)	Helium (at. ppm)	Displacement Damage (dpa)	Immersion Density Change (%)	Cavity Content, vol %			Cavity Concentration		Average Diameter, nm	
						Matrix	Grain Boundary	Total	Matrix (m^{-3})	Grain Boundary (m^{-2})	Matrix	Grain Boundary
									$\times 10^{20}$	$\times 10^{13}$		
Std	Annealed	550	2990	42		8.5 ± 2.5		8.5 ± 2.5	4.4 ± 1.3	[a]	50 ± 3.7	335
		600	2000	30	3.90	1.6 ± 0.3	0.1 ± 0.05	1.7 ± 0.3	1.6 ± 0.5	1.65	58 ± 10	140
		680	4140	61	14.0	4.0 ± 1.0	2.8 ± 1.6	6.8 ± 2.6	0.46 ± 0.12	0.14	108 ± 9.5	640
+Ti	Annealed	580	3156	45	2.40	1.30 ± 0.4	0.1 ± 0.05	1.4 ± 0.5	0.96 ± 0.30	4.0 ± 1.0	57 ± 3	78
		600	1850	29	2.20	0.9 ± 0.3		0.9 ± 0.3	9.3 ± 2.3		22 ± 3	
		680	3290	47	2.50	2.70 ± 0.7	0.3 ± 0.7	3.0 ± 1.0	0.30 ± 0.10	1.5	97 ± 20	184
		780	3420	48	7.40	8.2 ± 2.5	1.0 ± 0.2	9.0 ± 3.0	0.060 ± 0.015		270 ± 20	4000
+Ti	10% CW	600	3600	57		4.5 ± 1.0			2.7 ± 1.5		52 ± 15	
Std	20% CW	590	86	3.3	0.47	0.06 ± 0.03		0.06 ± 0.03	25 ± 7		7.1 ± 0.6	
+Ti	20% CW	580	70	3.0	0.21	0.022 ± 0.006		0.022 ± 0.006	2.0 ± 0.5		12 ± 0.8	

[a] Large cavities are on intragranular Laves phase; density is $1.2 \times 10^{18}/m^3$.

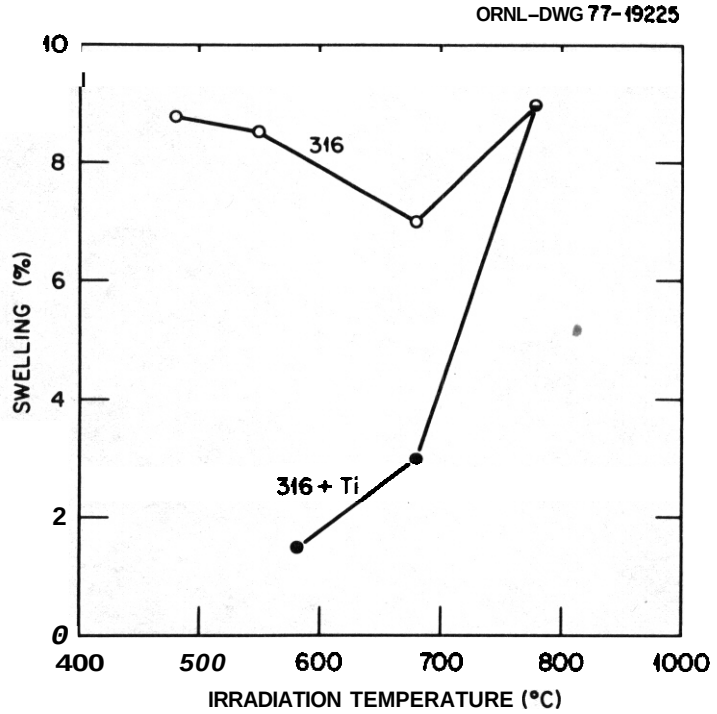

Fig. 3.1.1. Swelling as Determined by Cavity Volume Fraction as a Function of Irradiation Temperatures for Type 316 Stainless Steel With and Without 0.23 wt % Ti Irradiated to Fluences Producing 3000 to 4200 at. ppm He and *40* to ***60*** dpa.

Table **3.1.3.** Precipitate Phases Observed After HFIR Irradiation of Type 316 Stainless Steel Unmodified and Modified with 0.23 wt % Ti

Irradiation Temperature (°C)	Precipitate Phases Observed					
	Annealed Type 316		Annealed with Ti		10%Cold Worked with Ti	
	Intergranular	Intragranular	Intergranular	Intragranular	Intergranular	Intragranular
550	$M_{23}C_6$	$M_{23}C_6$ M_6C Laves				
600	Sigma	Laves	$M_{23}C_6$ Ti(C,N)S	Laves TiC	Sigma $M_{23}C_6$	$M_{23}C_6$ M_6C Laves Chi TiC
680	Sigma	Chi	Sigma $M_{23}C_6$	Chi TiC		

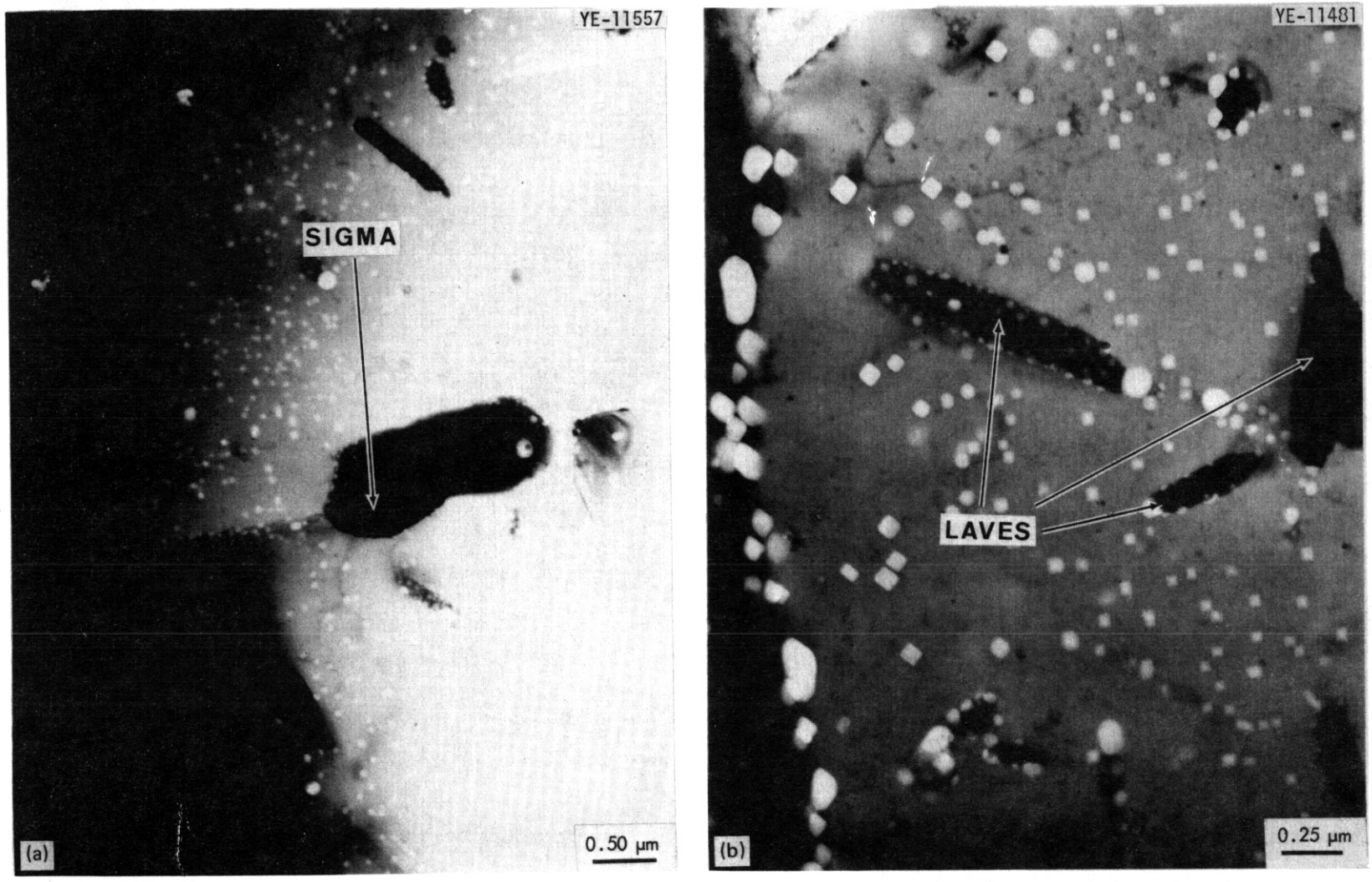

Fig. 3.1.2. Annealed Type 316 Stainless Steel Irradiated in HFIR at 600°C to a Fluence Producing 2000 at. ppm He and 30 dpa. (a) Grain boundary with large isolated sigma particle and grain boundary cavities. (b) Matrix with intragranular Laves phase coated with cavities similar to those in the matrix.

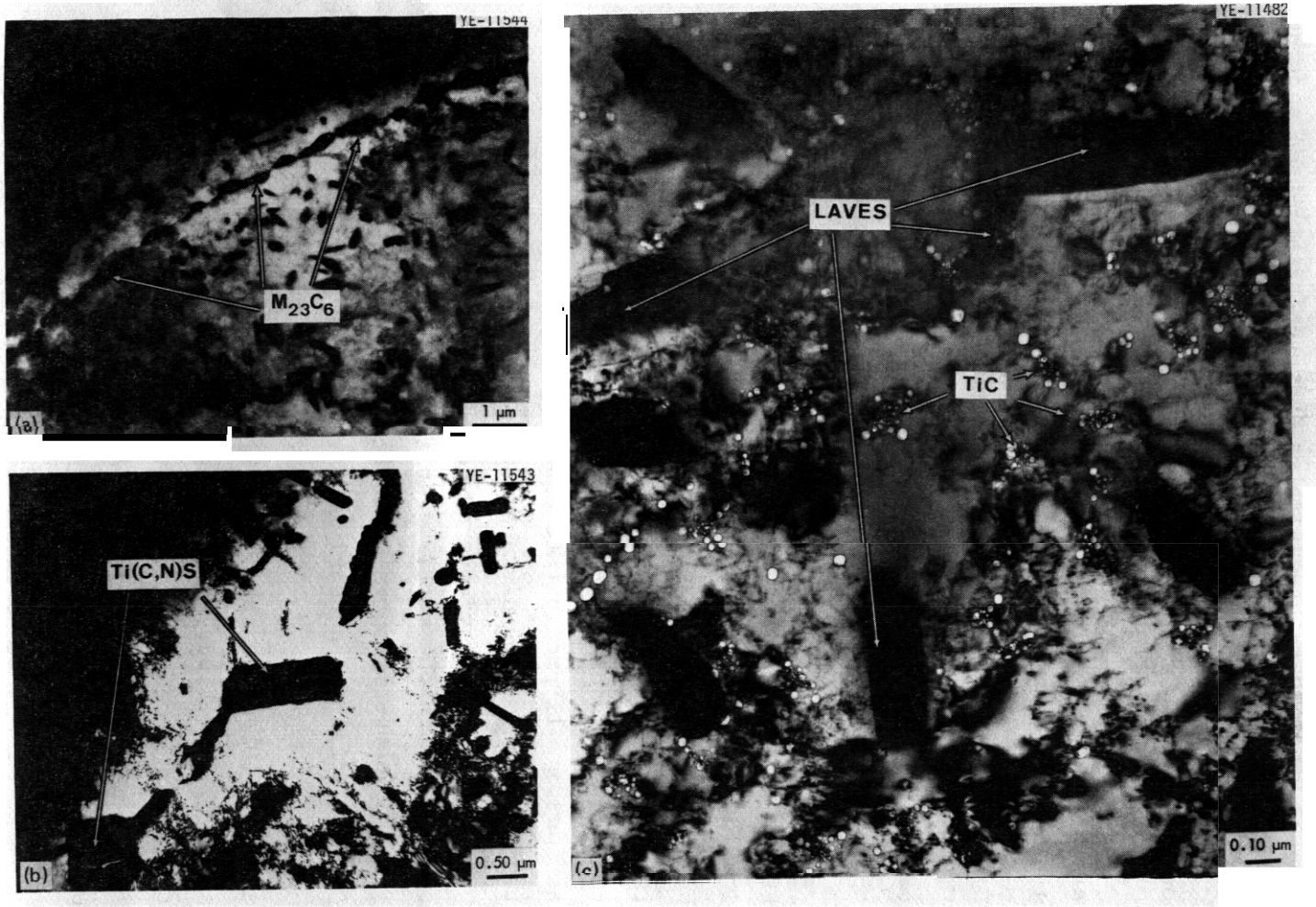

Fig. 3.1.3. Annealed Type 316 Stainless Steel with 0.23 wt % Ti Irradiated in HFIR at 600°C to a Fluence Producing 1850 at. ppm He and 30 dpa. (a) Grain boundary with nearly continuous $M_{23}C_6$ particles and no large grain boundary cavities. (b) Occasional Ti(C,N)S at the grain boundaries. (c) Intragranular coarse Laves phase and finely dispersed TiC precipitate. Note the tiny cavities adjacent to the precipitate particles and the virtually denuded zone surrounding each cluster of precipitate particles and cavities.

throughout the sample, and these particles are encrusted with small helium bubbles. The effect of this uniformly distributed precipitation can be realized when the Laves phase precipitates and precipitate-free portions of the matrix are compared for the two materials. In the annealed type 316 stainless steel, the Laves phase and the matrix have cavities that are about 58 nm in diameter on the average. The Laves phase precipitate particle density is $3 \times 10^{18}/m^3$. Thirty percent of the cavities in the sample are associated with this precipitate (the total cavity concentration is $1.6 \times 10^{20}/m^3$). In the annealed type 316 stainless steel with 0.23 wt % Ti, the average cavity diameter is about 22 nm. The cavities found in the matrix are 50 to 60 nm in diameter, but the cavities at the interface of the TiC particles are 5 to 20 nm in diameter. The TiC particle density is $1 \times 10^{20}/m^3$ and the Laves density is $1.5 \times 10^{19}/m^3$, nearly five times the density of Laves phase precipitate particles in annealed type 316 stainless steel. Nearly 90% of the total cavity density of $1 \times 10^{21}/m^3$ is associated with the TiC precipitate. The result of this nearly exclusive accommodation of this helium by the TiC precipitate results in 1.0% swelling in the alloy with 0.23 wt % Ti as opposed to 1.6% in standard type 316 stainless steel.

Cavities form on all precipitate phases present in annealed type 316 stainless steel, as well as on dislocations in the matrix and on grain boundaries. These can all be viewed as competing sinks for helium that cannot be accommodated in the matrix. In the case of nearly everything other than TiC, the competition is quite equal, but when a TiC precipitate is present, its interfaces are nearly the exclusive sink for accommodating the helium

Examination of 10%-cold-worked type 316 stainless steel with 0.23 wt % Ti irradiated at 600°C to a fluence producing 3600 at. ppm He and 57 dpa helps show the effectiveness of TiC competing for helium with the other possible precipitate phase sinks in type 316 stainless steel. Table 3.1.3 shows the phases present, and the microstructural features are shown in Fig. 3.1.4. The phases present are $M_{23}C_6$, M_6C, sigma, chi, and Laves in addition to TiC. No phase except TiC exhibits the interface encrusted with small cavities.

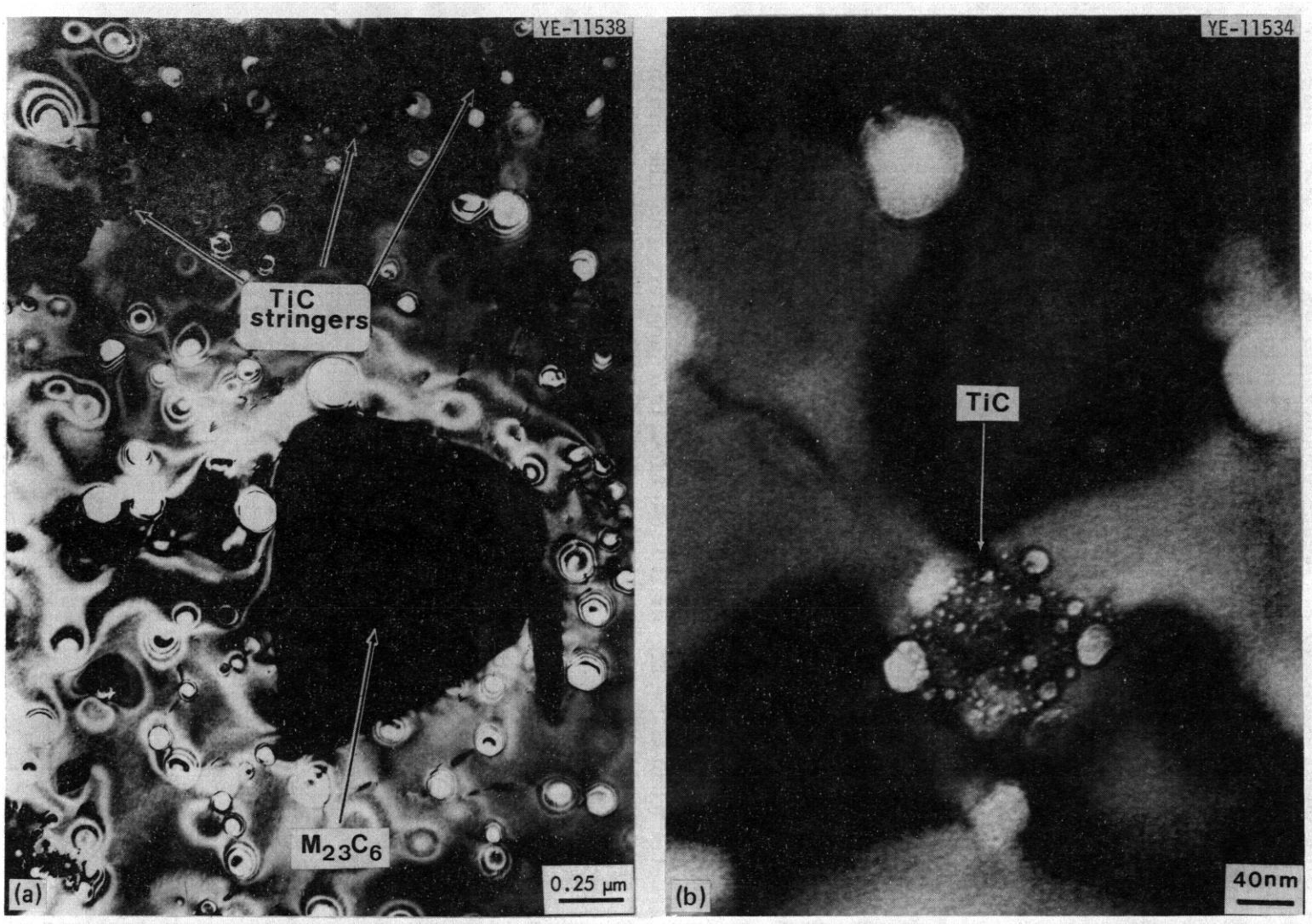

Fig. 3.1.4. Microstructures of 10%-Cold-Worked Type 316 Stainless Steel with 0.23 wt % Ti Irradiated in HFIR at 600°C to a Fluence Producing 3600 at. ppm He and 57 dpa. (a) Intragranular stringers of fine TiC precipitate. Note large cavities and other phases in between TiC stringers. (b) Intragranular small TiC precipitate particle, showing the normal clustering of small cavities at its interface.

Examination of annealed type 316 stainless steel with 0.23 wt % Ti after irradiation at 680°C to a fluence producing 3300 at. ppm He and 47 dpa shows higher swelling and the onset of grain boundary cavitation with the increase in temperature. The phases present are shown in Table 3.1.3 and the microstructural features in Fig. 3.1.5. Sigma, occasional $M_{23}C_6$, and cavities are observed at the grain boundaries. Intragranularly, TiC and large plates of chi phase are observed. The TiC behaves as before; cavities are encrusted about the precipitate particles. However, the cavities associated with the precipitate range from about 10 nm to about the average cavity diameter of 97 nm. Furthermore, the TiC precipitate particle density has been reduced to $2 \times 10^{18}/m^3$ and the size has increased. Much larger regions of matrix are unaffected by TiC, and in these regions the cavity size and density are similar to those in annealed type 316 stainless steel irradiated under the same conditions (see Table 3.1.2). The grain boundary cavities, however, are about 185 nm in diameter in annealed type 316 with 0.23 wt % Ti and 640 nm in annealed unmodified type 316 stainless steel after irradiation at 680°C. This is greater than a factor of 3 reduction in diameter, and the grain boundary component of swelling in Table 3.1.2 reflects this. Through these effects, primarily the coarsening of the TiC precipitation, the effect of TiC is reduced with increasing temperature until finally, as shown in Fig. 3.1.1, both alloys swell similarly at 780°C.

The fact that the effectiveness of TiC is reduced by coarsening of its distribution is dramatically demonstrated by again considering the microstructure of 10%-cold-worked type 316 stainless steel with 0.23 wt % Ti irradiated at 600°C. The distribution of fine TiC particles is artificially coarsened by the formation of stringers of TiC precipitate as shown in Fig. 3.1.4. The precipitate exhibits its normal encrustment with small cavities ranging from 3 to 20 nm in diameter, but the regions of matrix unaffected by TiC show cavities ranging from 50 to 150 nm in diameter, resulting in 4.5% matrix swelling. Furthermore, the regions of the matrix unaffected by TiC show many more precipitate types than annealed material that exhibits only Laves phase in addition to TiC. Whether this clustering of TiC was induced by the fabrication procedure or the recrystallization of the specimen during irradiation is not clear, but the consequences of an inhomogeneous distribution of TiC are clear.

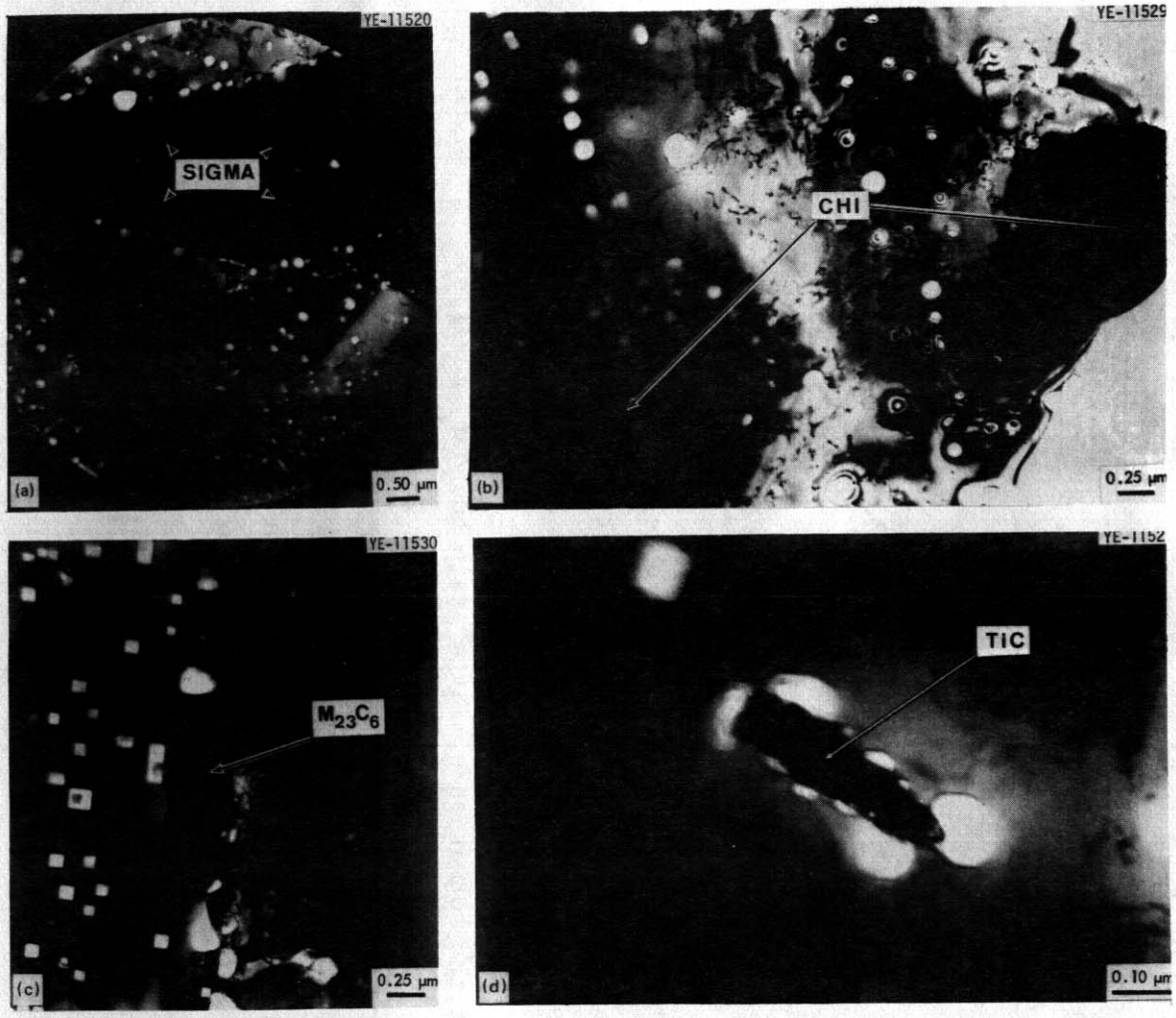

Fig. 3.1.5. Annealed Type 316 Stainless Steel with 0.23 wt % Ti Indicated in HFIR at 680°C to a Fluence Producing 3300 at. ppm He and 57 dpa. (a) Large sigma phase precipitate particle at grain boundary triple point. (b) Large plates of intragranular chi phase. (c) Isolated grain boundary $M_{23}C_6$ precipitate particle and grain boundary cavities. (d) Intragranular TiC precipitate particle. Many small cavities are associated with the interface, but also several large cavities.

Finally, 20%-cold-worked type 316 stainless steel with and without 0.23 wt % Ti have been examined after irradiation at 580 to 590°C to fluences producing 30 to 80 at. ppm He and 1.5 to 3.0 dpa. The swelling results are included in Table 3.1.2, and the microstructures are shown in Figs. 3.1.6 and 3.1.7. The swelling of the alloy with 0.23 wt % Ti is less than that of the unmodified alloy because the increase in cavity size (12 and 7.5 nm, respectively) was overcome by the decrease in cavity density by an order of magnitude (2.0×10^{20} and $2.5 \times 10^{21}/m^3$, respectively). Furthermore, many of the small cavities in the type 316 stainless steel with 0.23 wt % Ti are clustered about small TiC precipitate particles. Finally the type 316 stainless steel appears to be about 10% recrystallized, and the alloy with 0.23 wt % Ti shows no recrystallization.

3.1.5 Conclusions

1. Swelling in annealed type 316 stainless steel in the temperature range 580 to 780°C is reduced by the addition of 0.23 wt % Ti.

2. The reduction in swelling can be related to the preferential accommodation of helium in small cavities at TiC interfaces.

3. After irradiation of annealed type 316 stainless steel with 0.23 wt % Ti at 600°C intergranular $M_{23}C_6$ and Ti(C,N)S are observed and these prevent the formation of large grain boundary cavities. At higher temperatures, where grain boundary cavities form, the cavities are much smaller in the alloy with 0.23 wt % Ti than in unmodified type 316 stainless steel.

4. At higher temperatures the swelling characteristics of both alloys approach each other as the TiC particles coarsen and large portions of the matrix are unaffected by TiC. This effect can also be induced if a fine TiC precipitate is inhomogeneously distributed in stringers.

5. The addition of 0.23 wt % Ti to 20%-cold-worked type 316 stainless steel reduces swelling and retards recrystallization after irradiation at 580 to 590°C to low fluences.

This work indicates that alloy optimization in terms of composition and preirradiation microstructure should include development of fine distribution of TiC to maximize the surface area for a given volume of precipitate. This should also be combined with the precipitation of

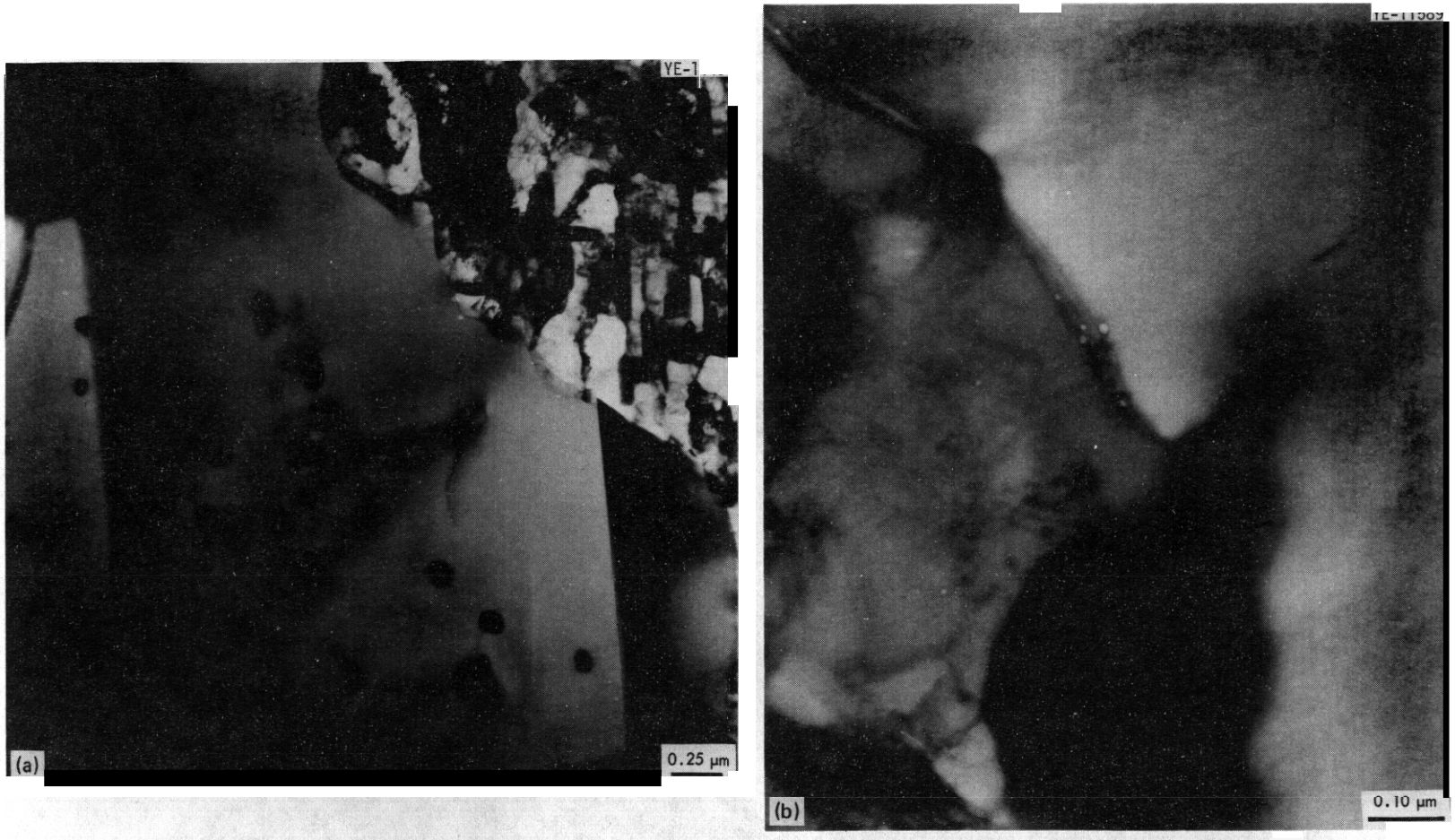

Fig. 3.1.6. Microstructures of 20%-Cold-Worked Type 316 Stainless Steel Irradiated in HFIR at 590°C to a Fluence Producing 86 at. ppm He and 3.3 dpa. (a) Low-magnification structure showing recrystallized portion of sample. The adjacent area has recovered into a small cell structure. (b) High magnification, showing the small cavities in both the recrystallized portion and the recovered portions of the grains.

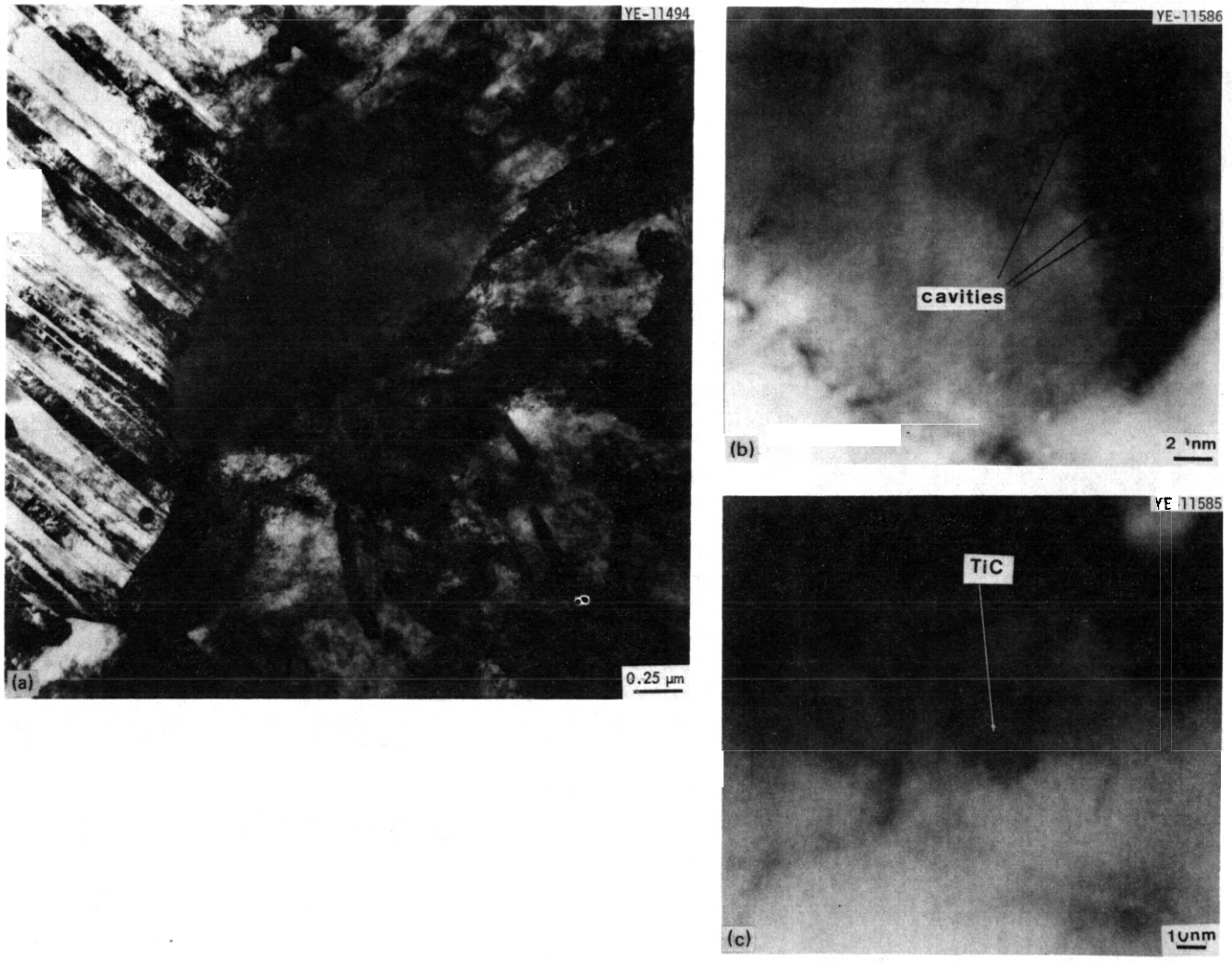

Fig. 3.1.7. Microstructures of 20%-Cold-Worked Type 316 Stainless Steel Irradiated in HFIR at 580°C to a Fluence Producing 70 at. ppm He and 3.0 dpa. (a) Low magnification, showing cold-worked portions of grains with a high dislocation density and an isolated sigma phase particle. (b) and (c) High magnification, showing cavities on deformation faults and cavities clustered about a small TiC precipitate particle, respectively.

grain boundary $M_{23}C_6$ to prevent formation of large grain boundary cavities. A stable solid solution with alloying additions to promote recombination and prevent nucleation may not be the optimum alloy for fusion applications. The ultimate goal for fusion applications may be intragranular accommodation of helium.

3.2 MECHANICAL PROPERTIES OF TYPE 316 AND TITANIUM-MODIFIED TYPE 316 STAINLESS STEEL IRRADIATED IN HFIR — P. J. Maziasz and E. E. Bloom (ORNL)

3.2.1 ADIP Task

ADIP Task 1.B.13, Tensile Properties of Austenitic Alloys.

3.2.2 Objective

Previous studies have shown that titanium additions to types 304 and 316 stainless steel produce an alloy with increased resistance to grain boundary fracture and improved ductility after irradiation to modest helium levels (<50 at. ppm). The objective of this work is to determine if these improvements are retained after irradiation to high dpa levels and helium contents typical of those expected in high-flux regions of fusion reactors.

3.2.3 Summary

Postirradiation tensile strength and ductility of annealed type 316 stainless steel are improved by the addition of 0.23 wt % Ti over the test temperature range 575 to 750°C for neutron fluences producing 1850 to 4000 at. ppm He and 30 to 60 dpa: This improvement may be correlated well with the formation of a fine intragranular TiC precipitate, which accommodates helium in small cavities at its surfaces and with smaller grain boundary cavities in titanium-modified material. A dramatic improvement in properties results at 600°C when large grain boundary cavities are replaced by the formation of intergranular $M_{23}C_6$ in addition to the intragranular TiC. The 575°C postirradiation tensile strength and ductility of 20%-cold-worked type 316 stainless steel irradiated at 580 to 600°C and low fluences producing 30 to 80 at. ppm He and 1.5 to 3.4 dpa are improved by the addition of 0.23 wt % Ti. The fracture mode of the 20%-cold-worked material is also changed from brittle intergranular to ductile transgranular by the titanium additions. Recrystallization of the 20%-cold-worked structure begins between fluences producing 50 to 60 at. ppm He and 2.5 to 2.8 dpa in type 316 stainless steel and results in a sharp drop in strength and ductility. The addition of titanium retards recrystallization of the cold-worked structure for irradiation under these conditions.

3.2.4 Progress and Status

Samples of annealed type 316 stainless steel and type 316 with 0.23 wt % Ti were irradiated in HFIR at temperatures from 600 to 780°C to fluences producing 1850 to 4000 at. ppm He and 30 to 60 dpa. The compositions of the steels are given in Table 3.1.1. Tensile data are given in Table 3.2.1, and total elongation is plotted as a function of test temperature in Fig. 3.2.1. The uniform and total elongations, which in the case of brittle intergranular fracture are equal, are improved by the addition of 0.23 wt % Ti. Table 3.2.1 also shows that the strength quantities are improved by the addition of titanium. The properties of both alloys are nearly equal after irradiation at 785°C. The strength

Table 3.2.1. Engineering Tensile Properties[a] of Type 316 Stainless Steel With and Without 0.23 wt % Ti

Temperature, °C		Helium Level (at. ppm)	Displacement Damage (dpa)	Strength, MPa		Elongation, %	
Irradiation	Test			Ultimate	Yield	Uniform	Total
			Annealed 316				
600	575	4070	60	254	211	0.82	0.82
685	650	3200	45	179	179	0.20	0.20
680	650	4200	61	57	57	0.0	0.0
785	750	3400	48	70	70	0.14	0.14
			Annealed 316 + 0.23 wt % Ti				
600	575	1850	30	414	285	4.17	4.43
680	650	3300	47	208	170	1.03	1.03
710	650	2450	40	179	161	0.66	0.66
680	700	3300	47	209	189	1.10	1.10
710	750	2200	34	155	155	0.80	0.80
785	750	3400	48	69	69	0.0	0.0
			20%-Cold-Worked 316				
	575[b]			810	770	0.90	6.00
590	575	34.0	1.5	590	530	2.50	2.50
600	575	50	2.5	580	496	2.90	2.90
600	575	60	2.8	541	507	0.50	0.50
580	575	80	3.5	435	416	0.53	0.53
			20%-Cold-Worked 316 + 0.23 wt % Ti				
	575			725	678	2.00	6.80
590	575	30	1.5	710	655	2.00	5.60
590	575	70	3.0	483	443	3.10	5.10

[a] All tests run at 0.002 in./min crosshead speed.

[b] Interpolated from tests run at 550 and 600°C.

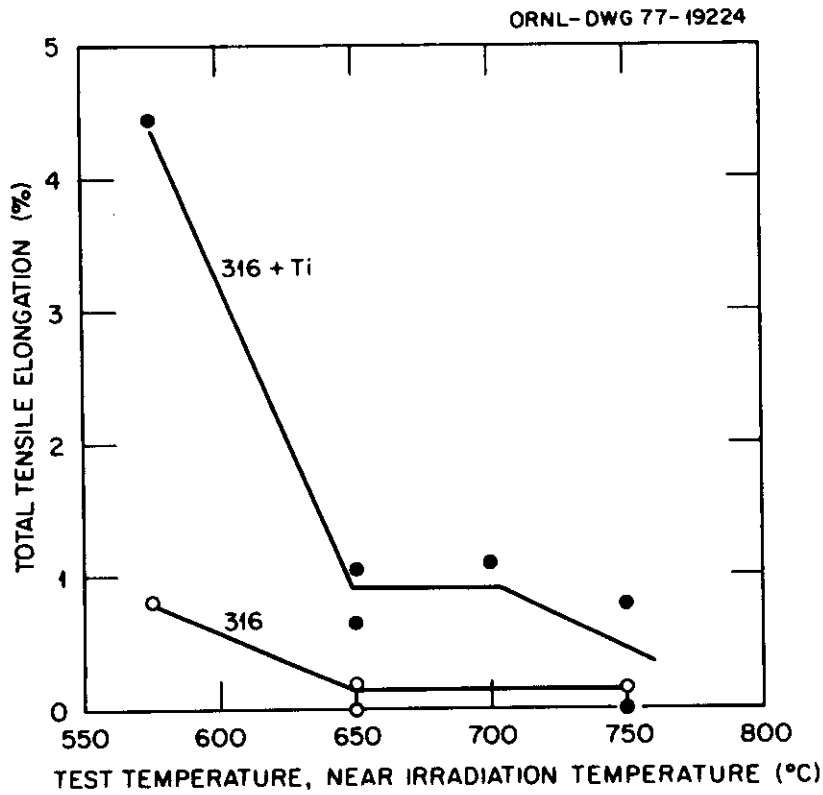

Fig. 3.2.1. Total Tensile Elongation of Annealed Type 316 Stainless Steel With and Without 0.23 wt % Ti as a Function of Test Temperature for Tensile Testing at or Near the Irradiation Temperature After Irradiation in HFIR to Fluences Producing 1850 to 4000 at. ppm He and 30 to 60 dpa.

and ductility changes observed are consistent with the microstructural changes discussed in Sect. 3.1. The precipitation of intragranular TiC, which accommodates a large fraction of the total helium in small cavities at the precipitate surface, and the smaller grain boundary cavities would be expected to reduce the effect of helium on the ductility.

An increase in the 575°C total elongation is realized for the annealed alloy with 0.23 wt % Ti irradiated at 600°C to a fluence producing 1850 at. ppm He and 30 dpa. Microstructural examination revealed that in addition to the previously mentioned trapping of helium within the grains by TiC, the grain boundaries contain intergranular $M_{23}C_6$, a few Ti(C,N)S precipitate particles, and no large cavities. Examination of the fracture by scanning electron microscopy indicates intergranular failure. Important, however, is the inequality of the total and uniform elongations. The increase in total elongation with grain boundary

precipitation of $M_{23}C_6$ has been observed' in annealed type 316 stainless steel irradiated at 530°C in HFIR to a fluence producing 4000 at. ppm He and 57 dpa. In this case the sample was tested at 500°C and the total elongation was 2.6%, anomalously high for annealed material, but not inconsistent with continuous $M_{23}C_6$ precipitated at the grain boundaries instead of large grain boundary cavities.

The ultimate strength of the annealed type 316 stainless steel with 0.23 wt % Ti irradiated at 600°C is higher than that of annealed unmodified alloy irradiated under similar conditions. The high dislocation density observed after testing indicates significant intragranular deformation before failure.

Samples of 20%-cold-worked type 316 stainless steel with and without 0.23 wt % Ti have been irradiated in HFIR at 580 to 600°C to low fluences producing 30 to 80 at. ppm He and 1.5 to 3.4 dpa. The specimens were tensile tested at 575°C after irradiation, and the tensile properties are given in Table 3.2.1. The tensile curves of several samples are shown in Fig. 3.2.2. At this temperature and fluence the addition of

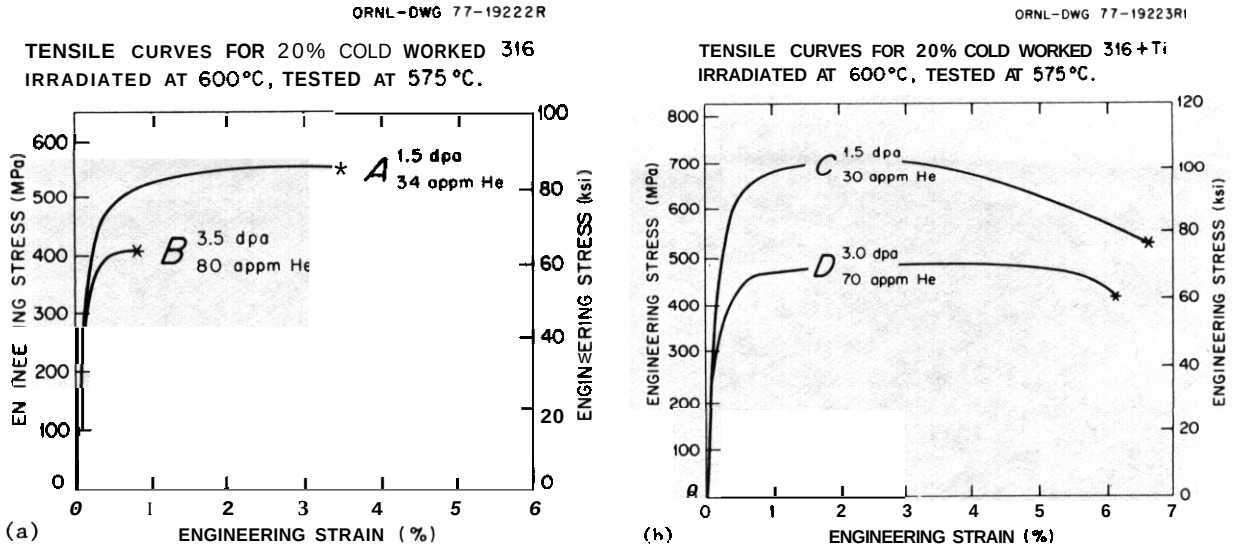

Fig. 3.2.2. Engineering Tensile Stress as a Function of Engineering Strain for 20%-Cold-Worked Type 316 Stainless Steel Irradiated in HFIR to Fluences Producing the Helium and dpa Levels Indicated, (a) Unmodified alloy. Note the sharp reduction in strain with increased fluence. (b) Alloy with 0.23 wt % Ti. The strength is reduced with fluence, but the elongation remains about the same.

titanium increases ductility and strength. The uniform elongation is equal to the total elongation for 20%-cold-worked type 316 stainless steel having from 1.5 to 3.4 dpa. This is shown in curve A of Fig. 3.2.2 and is consistent with the intergranular failure shown by the fracture surface in Fig. 3.2.3. Irradiation of 20%-cold-worked titanium-modified type 316 stainless steel to similar conditions results in the uniform elongation being much less than the total elongation, as shown in curve C in Fig. 3.2.2. This behavior is indicative of ductile transgranular failure, as shown in the 45° fracture surface in Fig. 3.2.4.

For 20%-cold-worked type 316 stainless steel irradiated at 580 to 600°C, the ductility dropped sharply after a fluence producing 60 at. ppm He and 2.8 dpa and then decreased more slowly until it reached about zero elongation at 4000 at. ppm He and 60 dpa.[2] Microstructural examination shows that this drop coincides with the beginning of recrystallization of the cold-worked structure. This can be seen in Fig. 3.2.5. If we compare similarly irradiated 20%-cold-worked type 316 stainless steel with 0.23 wt % Ti, we can see in Fig. 3.2.6 that the cold-worked structure

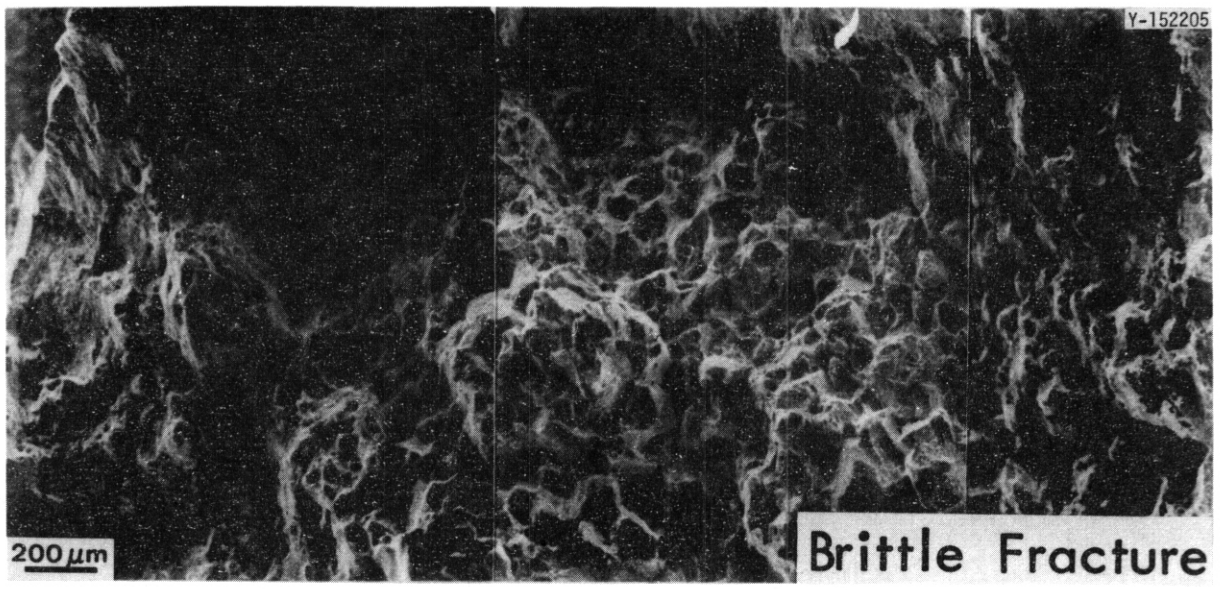

Fig. 3.2.3. Fracture Surface of 20%-Cold-Worked Type 316 Stainless Steel After Irradiation in HFIR at 590°C to a Fluence Producing 34 at. ppm He and 1.5 dpa and Tensile Testing at 575°C. The fracture surface shows brittle intergranular failure.

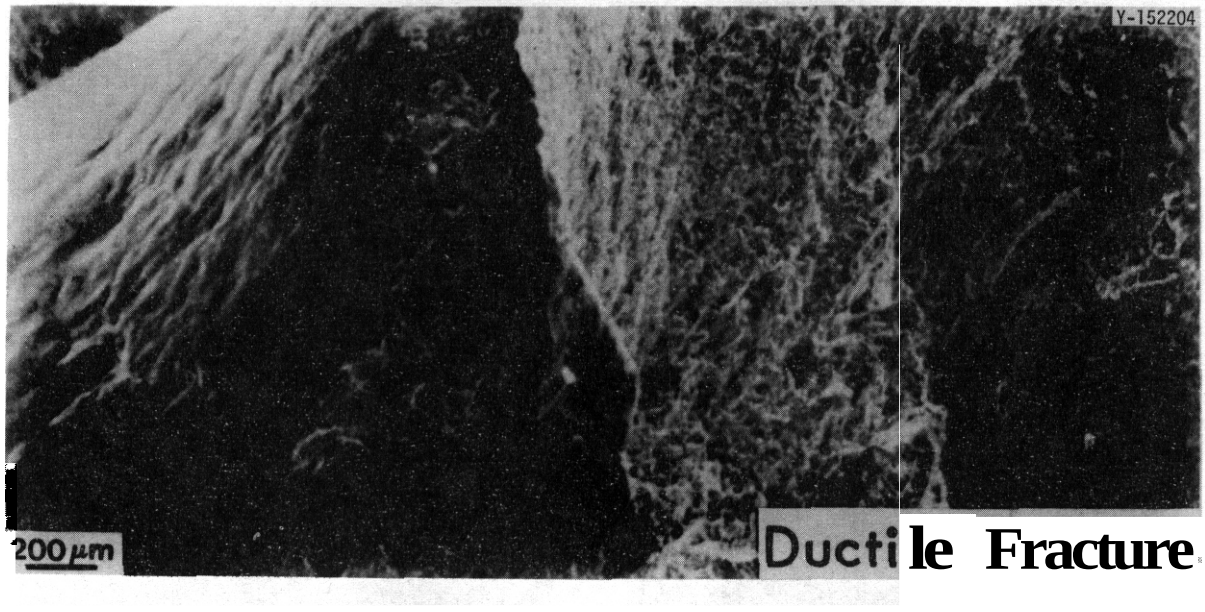

Fig. 3.2.4. Fracture Surface of 20%-Cold-Worked Type 316 Stainless Steel with 0.23 wt % Ti After Irradiation in HFIR at 590°C to a Fluence Producing 30 at. ppm He and 1.5 dpa and Tensile Testing at 575°C. The fracture surface shows classic 45" ductility transgranular failure.

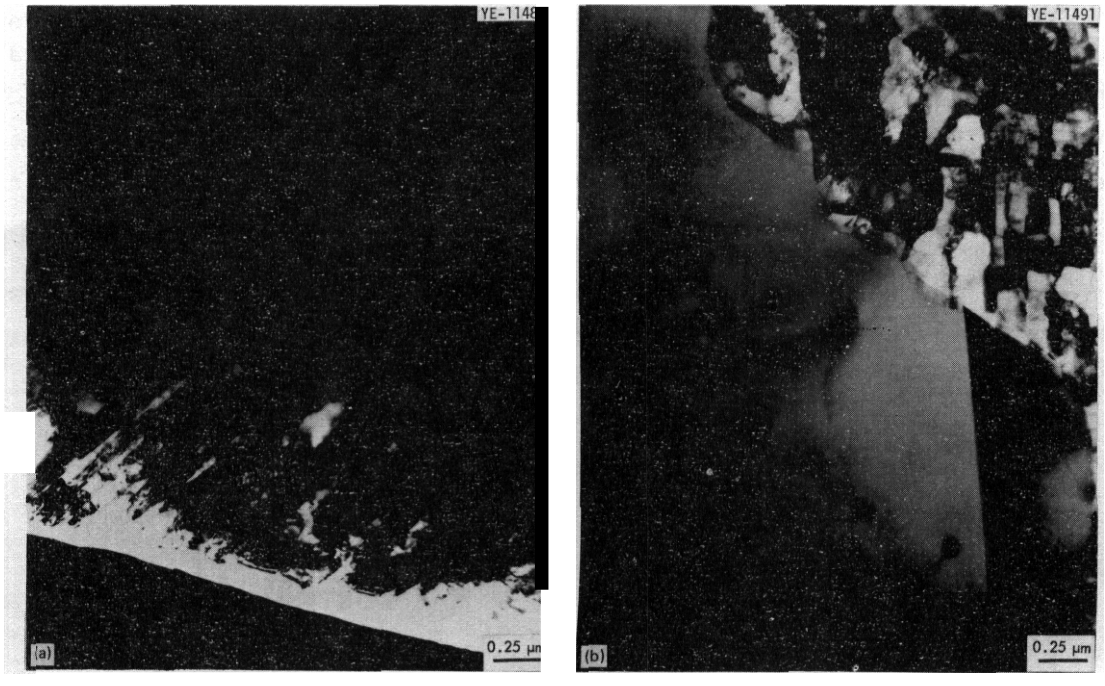

Fig. 3.2.5. Microstructure of 20%-Cold-Worked Type 316 Stainless Steel Irradiated at 580 to 590°C in HFIR. (a) Irradiated to a fluence producing 34.0 at. ppm He and 1.5 dpa. The cold-worked structure is retained. (b) Irradiated to a fluence producing 80 at. ppm He and 3.5 dpa. A large recrystallized grain is adjacent to a region recovered into cells.

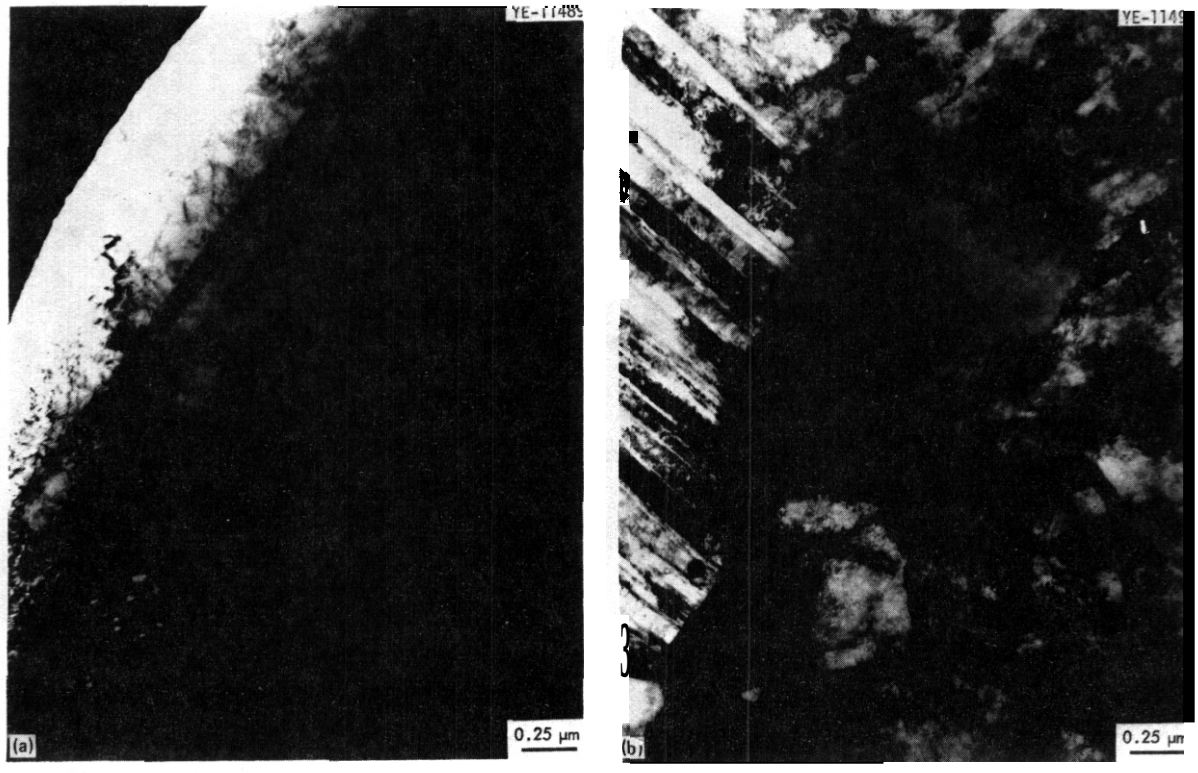

Fig. 3.2.6. Microstructures of 20%-Cold-Worked Type 316 Stainless Steel with 0.23 wt % Ti Irradiated at 590°C in HFIR. Irradiated to fluences producing (a) 30 at. ppm He and 1.5 dpa and (b) 70 at. ppm He and 3.0 dpa. The cold-worked structure is retained in both.

is retained to 70 at. ppm He and 3.0 dpa, and the corresponding mechanical properties reflect this. In this limited fluence range, the titanium addition retards recrystallization and prevents the corresponding severe degradation of properties associated with it. Section 3.1 showed that a fine TiC precipitate is observed in the 20%-cold-worked material and that it accommodates helium in small cavities at its interface as in annealed material. This improved helium accomodation is probably partly responsible for the improved irradiation resistance of titanium-modified alloy.

3.2.5 Conclusions and Future Work

1. The postirradiation tensile strength and ductility of annealed type 316 stainless steel are improved in the test temperature range 575 to 750°C by the addition of 0.23 wt % Ti for tests near the irradiation temperatures to fluences producing 1850 to 4000 at. ppm He and 30 to 60 dpa.

2. The improvement in mechanical properties with titanium addition correlates well with the formation of a fine intragranular TiC precipitate that accommodates helium in small cavities at its interfaces and with smaller grain boundary cavities than in unmodified material. A significant increase in strength and ductility coincides with the formation of an intergranular $M_{23}C_6$ precipitate instead of large grain boundary cavities, in addition to the fine TiC precipitate, at 600°C.

3. The postirradiation tensile strength and ductility of 20%-cold-worked type 316 stainless steel are improved at a test temperature of 575°C by the addition of 0.23 wt % Ti for irradiation at 580 to 600°C to fluences producing 30 to 80 at. ppm He and 1.5 to 3.4 dpa. The fracture mode for these conditions is changed from brittle intergranular to ductile transgranular by titanium addition.

4. Ductility and strength of 20%-cold-worked type 316 stainless steel are sharply reduced upon recrystallization of the cold-worked microstructure. This occurs after irradiation at 590 to 600°C to a fluence producing 50 to 60 at. ppm He and 2.5 to 2.8 dpa, and the properties remain approximately constant up to fluences producing 4000 at. ppm He and 60 dpa. The addition of 0.23 wt % Ti retards recrystallization for the low fluence conditions.

5. Fine intragranular TiC precipitate particles that behave similarly to those observed in annealed material are found after titanium addition to 20%-cold-worked type 316 stainless steel. They are probably partially responsible for the improvement in properties.

Future work will investigate the fluence dependence of the recrystallization retardation in titanium-modified alloys. If the improvement is related to TiC formation, the lower temperature irradiation response of 20%-cold-worked type 316 stainless steel with 0.23 wt % Ti needs to be examined. If TiC does not form, treatments to produce it before irradiation may be considered. The effect of grain boundary precipitation and fine intragranular TiC precipitation appears beneficial, and control of microstructure to optimize this behavior should be pursued.

3.2.6 References

1. E. E. Bloom and F. W. Wiffen, "The Effect of Large Concentrations of Helium on the Mechanical Properties of Stainless Steel," *J. Nucl. Mater.* 58: 171–84 (1975).
2. P. J. Maziasz and E. E. Bloom, "Comparison of 316 + Ti with 316 Stainless Steel Irradiated in a Simulated Fusion Environment," *Trans. Am. Nucl. Soc.* 27: 268–69 (1977).

3.3 PRECIPITATION RESPONSE OF ANNEALED TYPE 316 STAINLESS STEEL IN HFIR IRRADIATIONS AT 550 to 680°C — P. J. Maziasz (ORNL)

3.3.1 ADIP Tasks

ADIP Tasks 1.C.1, Microstructural Stability, and 1.C.2, Microstructures and Swelling in Austenitic Alloys.

3.3.2 Objective

The objective of this work is to characterize the precipitation response of annealed type 316 stainless steel to irradiation in HFIR to simultaneously produced high levels of dpa and helium. This response is compared with thermal aging and with fast-reactor irradiation precipitation response in order to determine how helium production during irradiation changes the damage structure produced.

3.3.3 Summary

The precipitation response of annealed type 316 stainless steel irradiated in HFIR is studied and compared with previously observed thermal aging and fast-reactor irradiation responses. Irradiation in HFIR produces high levels of helium and displacement damage simultaneously and thus partially simulates a fusion environment. Samples have been irradiated at temperatures from 550 to 680°C to fluences producing up to 3300 at. ppm He and 47 dpa. If the precipitation response after HFIR irradiation is compared with that after thermal aging on a time-temperature-precipitation diagram, HFIR irradiation results in similar phase combinations, but shifted to lower temperatures and shorter times relative to thermal aging. The shifts range from 70 to 200°C and are different for different phase combinations. The phase regions resulting from fast-reactor irradiation require little or no shift in temperature or time relative to thermal aging. Therefore, HFIK irradiation also results in shifting the phase regions to shorter times and lower temperatures relative to fast-reactor irradiation. When simultaneous helium production is added to the irradiation environment by HFIR irradiation, the unidentified rod-shaped precipitate particles are absent and M_6C and Laves phases are present in contrast with reactor irradiation at similar

temperatures and fluences. Most voids produced by irradiation in a fast reactor are heterogeneously nucleated on the rod-shaped precipitate particles or $M_{23}C_6$. After HFIR irradiation only a fraction of the cavities are attached to precipitate particles, with Laves being the most preferred and $M_{23}C_6$ the least preferred. Helium has been shown to change the swelling, mechanical properties, and cavity response of annealed type 316 stainless steel relative to fast-reactor irradiation. Helium is shown to change the precipitate response as well and is important in understanding and anticipating fusion environment materials response.

3.3.4 Progress and Status

3.3.4.1 Experimental

The composition of the type 316 stainless steel used in this investigation is given in Table 3.3.1. The final sample preparation involved a 50% reduction in area by swaging, machining into tensile specimens, and annealing for 1 hr at 1050°C, before irradiation in HFIR. The irradiation conditions are given in Table 3.3.1. We examined three annealed type 316 stainless steel samples irradiated in HFIR from 550 to 680°C to 2000 to 3300 at. ppm He and 30 to 47 dpa, as well as two unirradiated samples aged for 10,000 hr at 600 and 650°C.

Table 3.3.1. Conditions for Irradiation of Annealed Type 316 Stainless Steel in HFIR

Irradiation Temperature (°C)	Neutron Flux, >0.1 MeV (n/m^2 s)	Neutron Fluence, >0.1 MeV (n/m^2)	Displacement Damage (dpa)	Helium Content (at. ppm)
550	0.95×10^{19}	6.18×10^{26}	42	3000
600	1.40	4.21	30	2000
680	1.38	6.91	41	3300

3.3.4.2 Results

The experimental conditions and phases observed are presented in time-temperature-precipitation (TTP) diagrams in Fig. 3.3.1 and are summarized in Table 3.3.2. The orientation relations of the precipitate phases relative to the austenite (face-centered cubic) matrix are presented in Figs. 3.3.2 and 3.3.3 and summarized in Table 3.3.3.

The phase boundaries on the TTP curve determined by data taken by Weiss and Stickler' have been extended to longer aging times to represent data taken in this work at 600 and 650°C after aging for 10,000 hr. In some cases the curves were slightly altered, within the scope of Weiss and Stickler's data points, to be consistent with the phase reaction scheme proposed by them (see Fig. 3.3.4). In particular, the phase region of M_6C was added, because Weiss and Stickler indicate observing trace amounts of M_6C after aging at 650°C for 1500 hr and longer but did not include it in their TTP diagram. The data of Weiss and Stickler were taken for type 316 stainless steel that had been annealed at 1260°C to produce a large grain size (average grain diameter ≈560 μm). Our data were taken for type 316 stainless steel annealed at 1050°C for 1 hr as the final step in the fabrication procedure established to produce an order of magnitude smaller grain size (average grain diameter ≈55 μm). Our fabrication steps, however, included solution annealing for 1 hr at 1200°C followed by 40 to 50% reduction in area by swaging at room temperature before the final cold work and solution anneal mentioned above. It is, therefore, reasonable to assume that the amount of carbide in solution and the homogeneity of its distribution within the grains were about the same as in Weiss and Stickler's specimens, *so* that comparison of our data with their data is legitimate. Furthermore, Spruiell et al.[2] found little difference in precipitation behavior for solution anneals of 1050 and 1200°C.

In this work, aging at 600°C for 10,000 hr produced $M_{23}C_6$ (see Fig. 3.3.5) Aging at 650°C for 10,000 hr produced $M_{23}C_6$, Laves occasional sigma particles, and a small amount of M_6C (see Fig. 3.3.6). These observations are consistent with Weiss and Stickler's reaction scheme for these temperatures and, therefore, warrant extension of their TTP diagram to include these data. These samples were the control samples for the annealed type 316 stainless

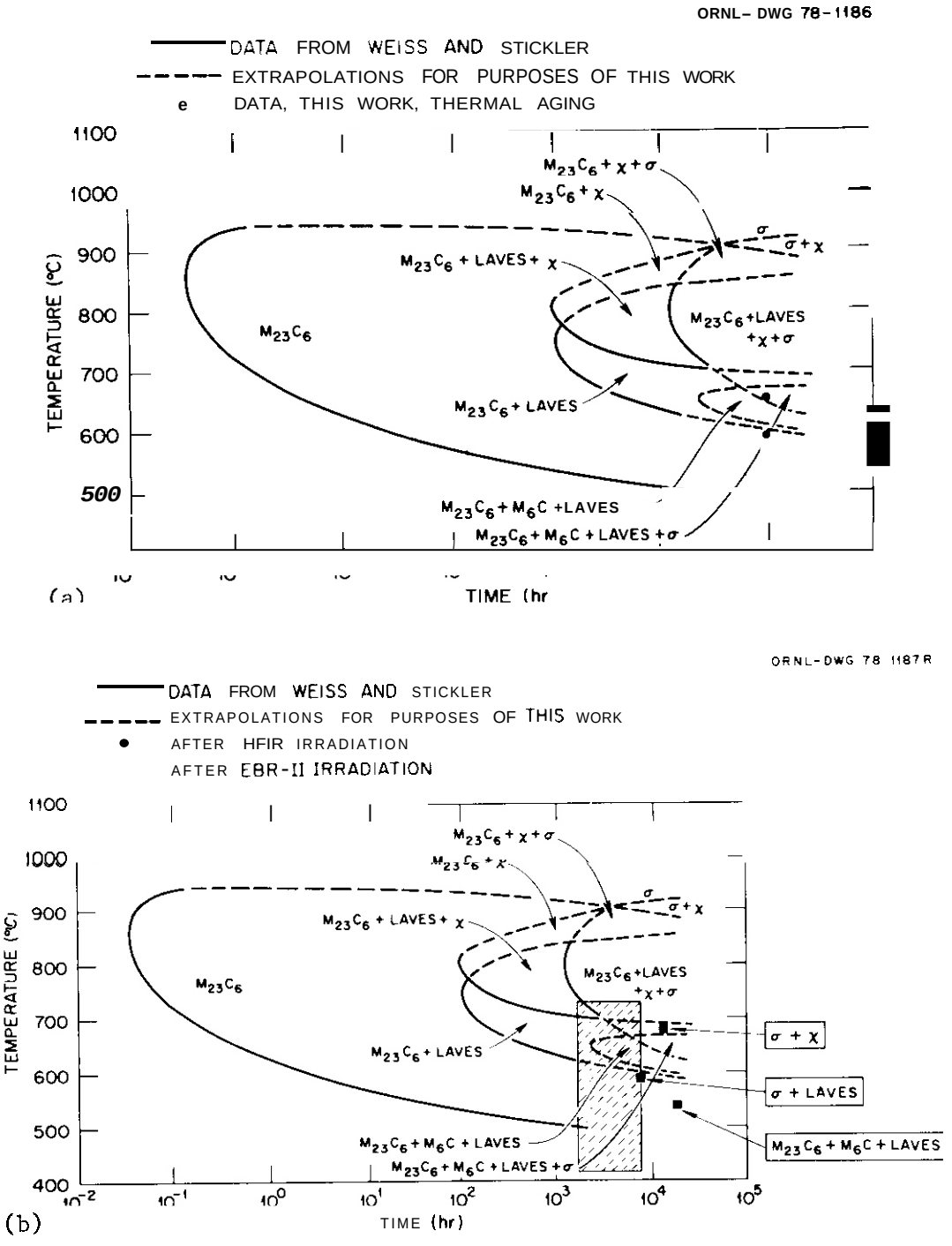

Fig. 3.3.1. A TTP Diagram for Annealed Type 316 Stainless Steel. (a) The boundaries of the phase regions taken from data by Weiss and Stickler are extended to longer aging times and to include thermal aging data from this work. (b) Data obtained after HFIR and EBR-II irradiation. The data are plotted at the irradiation temperatures and times and the phases observed are indicated.

Table 3.3.2. Summary of Precipitate Analysis on Aged or Irradiated Type 316 Stainless Steel

Exposure Temperature (°C)	Exposure Time (hr)	Intergranular Phases[a]	Intragranular Phases	Cavity Association with Intragranular Phase	Cavity Volume Fraction (%)
			Aged Samples		
600	10,000	$M_{23}C_6$ Type I	$M_{23}C_6$ Type I		
650	10,000	$M_{23}C_6$ Type I Sigma Type II	$M_{23}C_6$ Type I M_6C Type II Laves Types I, II		
			Irradiated Samples		
550	~16,000	$M_{23}C_6$ Type I	$M_{23}C_6$ Type I M_6C Type I, II Laves Types I, II	Little or None Some One large cavity per precipitate	8.5 ± 2.5
600	~7,800	Sigma Type I	Laves Types I, II	High	1.5 ± 0.3
680	~13,000	Sigma[b]	Chi Type I	Some	7.0 ± 2.5

[a]Orientation relationships are defined in Table 3.3.3 and illustrated in Figs. 3.3.2 and 3.3.3.

[b]Orientation relation was undetermined.

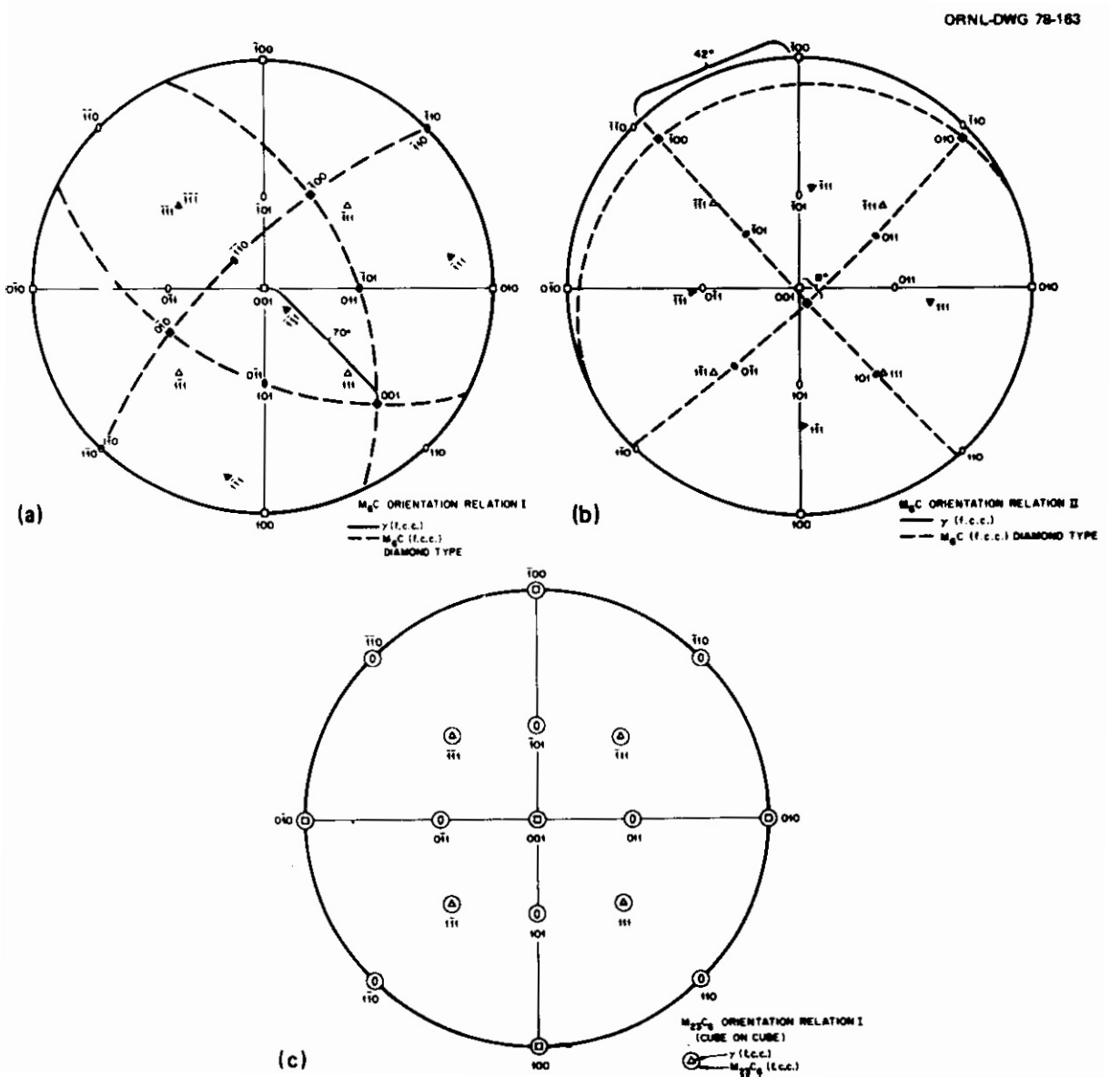

Fig. 3.3.2. Stereographic Projections of Orientation Relations (ORs) **Between γ Matrix and Carbide Precipitate Planes as Determined from Electron Diffraction.**

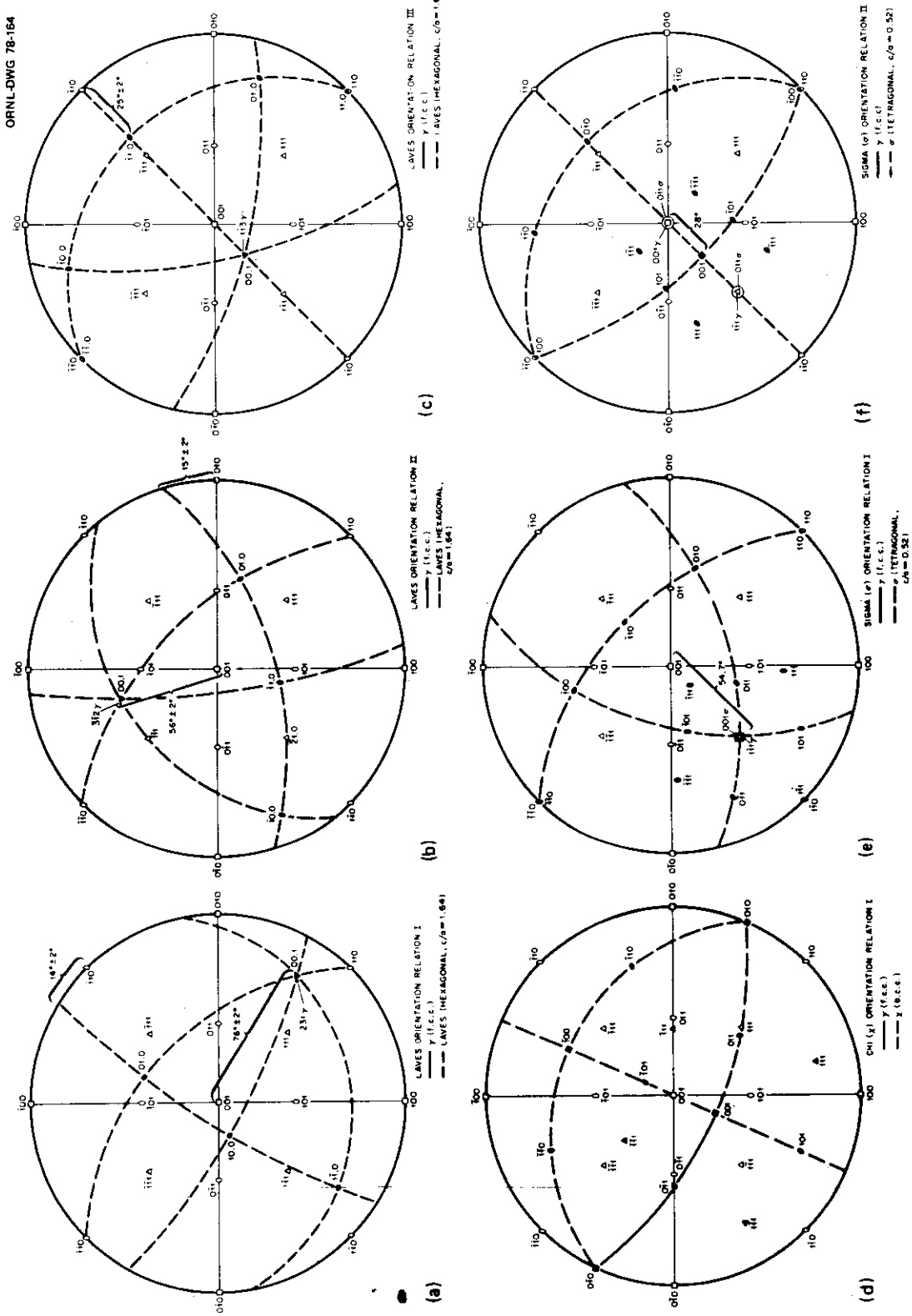

Fig. 3.3.3. Stereographic Projections of Orientation Relations (ORs) Between γ Matrix and Intermetallic Precipitate Planes as Determined from Electron Diffraction.

Table 3.3.3. Orientation Relations of Precipitate Phases

Precipitate Phase	Orientation Relation Type	Parallel Planes	Ratio of Interplanar Spacings,[a] $d'_{ppt.}/d_{\gamma}$
$M_{23}C_6$	I	[100] $M_{23}C_6$ ‖ [100]γ	$d'_{100}/d_{100} = 2.95$
		[110] $M_{23}C_6$ ‖ [110]γ	$d'_{110}/d_{110} = 2.95$
M_6C	I	(111) M_6C ‖ $(\bar{1}\bar{1}\bar{1})\gamma$	$d'_{111}/d_{\bar{1}\bar{1}\bar{1}} = 3.08$
		(110) M_6C ‖ $(1\bar{1}0)\gamma$	$d'_{\bar{1}10}/d_{1\bar{1}0} = 3.08$
	II	(101) M_6C ‖ $(111)\gamma$[b]	$d'_{101}/d_{111} = 3.08$
Laves[c]	I	(00.1)Laves ‖ $(231)\gamma$[b]	$d'_{00.1}/d_{231} = 8.04$
	II	(00.1)Laves ‖ $(\bar{3}\bar{1}2)\gamma$[b]	$d'_{00.1}/d_{\bar{3}\bar{1}2} = 8.04$
		(21.0)Laves ‖ $(1\bar{1}1)\gamma$	$d'_{21.0}/d_{1\bar{1}1} = 1.14$
	III	(00.1)Laves ‖ $(1\bar{1}3)\gamma$	$d'_{00.1}/d_{1\bar{1}3} = 7.13$
		(11.0)Laves ‖ $(110)\gamma$	$d'_{11.0}/d_{110} = 0.93$
Chi[d]	I	$(011)\chi$ ‖ $(111)\gamma$[e]	$d'_{011}/d_{111} = 3.02$
		$(1\bar{1}1)\chi$ ‖ $(01\bar{1})\gamma$[e]	$d'_{111}/d_{011} = 2.01$
		$(0\bar{1}1)\chi$ ‖ $(01\bar{1})\gamma$[e]	$d'_{0\bar{2}2}/d_{011} = 5.0$
SigmaS	I	$(001)\sigma$ ‖ $(1\bar{1}\bar{1})\gamma$	$d'_{001}/d_{1\bar{1}\bar{1}} = 2.21$
		$(1\bar{1}0)\sigma$ ‖ $(1\bar{1}0)\gamma$	$d'_{220}/d_{110} = 4.91$
		$(1\bar{1}\bar{1})\sigma$ ‖ $(1\bar{1}0)\gamma$	$d'_{2\bar{2}\bar{2}}/d_{1\bar{1}0} = 2.90$
	II	$(110)\sigma$ ‖ $(1\bar{1}\bar{1})\gamma$	$d'_{110}/d_{1\bar{1}1} = 3.0$
		$(100)\sigma$ ‖ $(1\bar{1}0)\gamma$	$d'_{100}/d_{1\bar{1}0} = 3.46$

[a] γ is fcc with $a_0 = 0.36$ nm.

[b] Not exactly parallel, a slight angular displacement.

[c] Laves d values of interplanar spacing are taken from Andrews et al., *Interpretation of Electron* Diffraction Patterns, 2nd ed., Hilger, 1971.

[d] Fe, Cr, Mo, chi phase, with d calculated from $a_0 = 0.888$ nm, from Weiss and Stickler.

[e] Several degrees from not being parallel.

[f] Fe, Cr, Mo sigma phase, with d calculated from $a_0 = 0.888$ nm, $c_0 = 0.46$ nm from Weiss and Stickler.

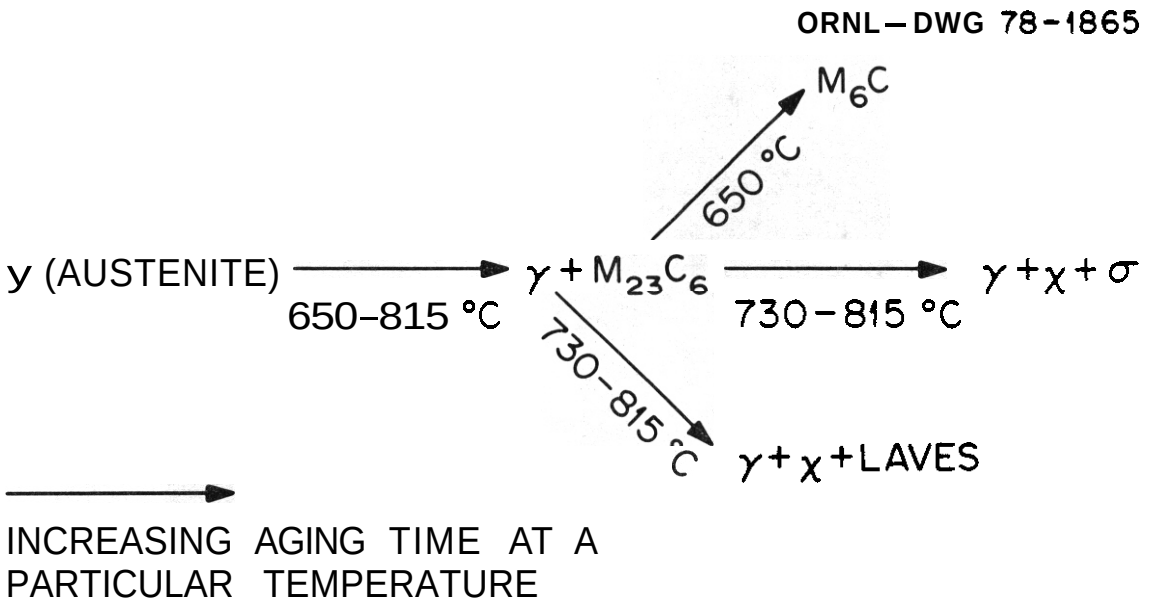

Fig. 3.3.4. Phase Reaction Sequence Proposed by Weiss and Stickler for Annealed Type 316 Stainless Steel During Aging.

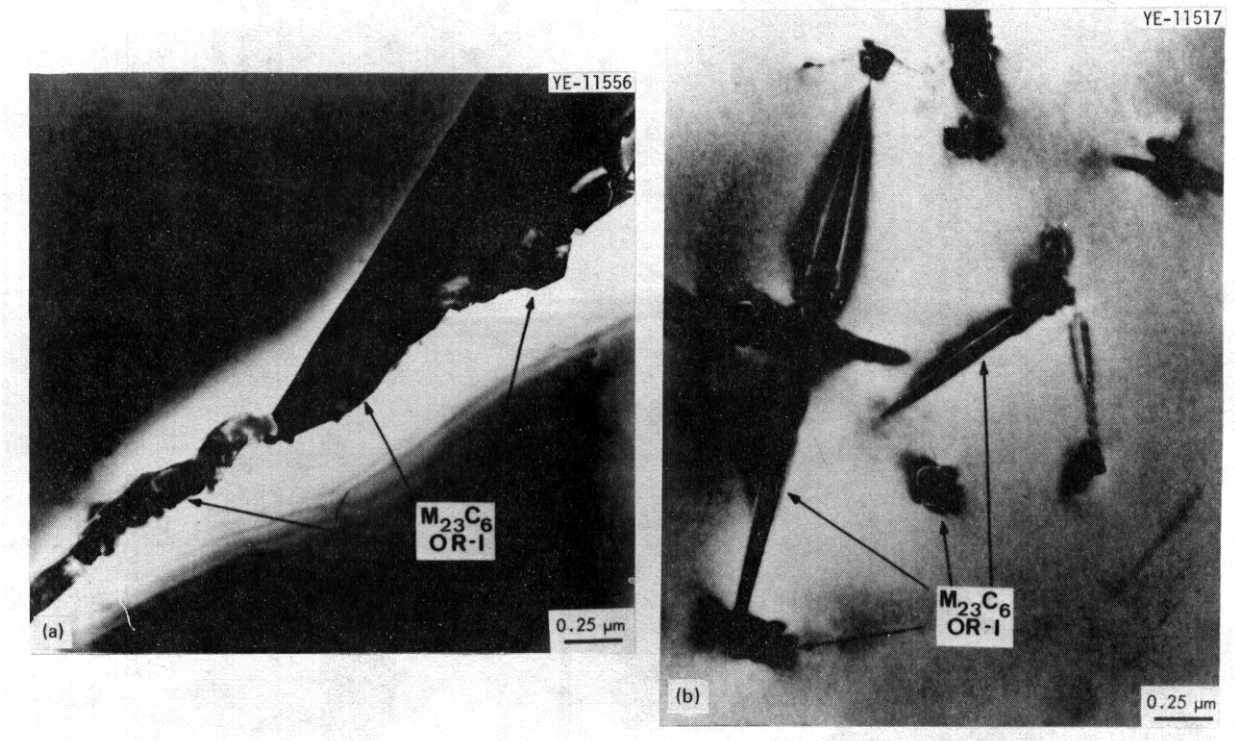

Fig. 3.3.5. Type 316 Stainless Steel Annealed 1 hr at 1050°C and Aged for 10,000 hr at 600°C. (a) High-angle grain boundary precipitation of $M_{23}C_6$. Each precipitate particle is cube on cube with either one grain on the other. (b) Sword-like intragranular $M_{23}C_6$. Precipitate particle density is about $2 \times 10^{19}/m^3$.

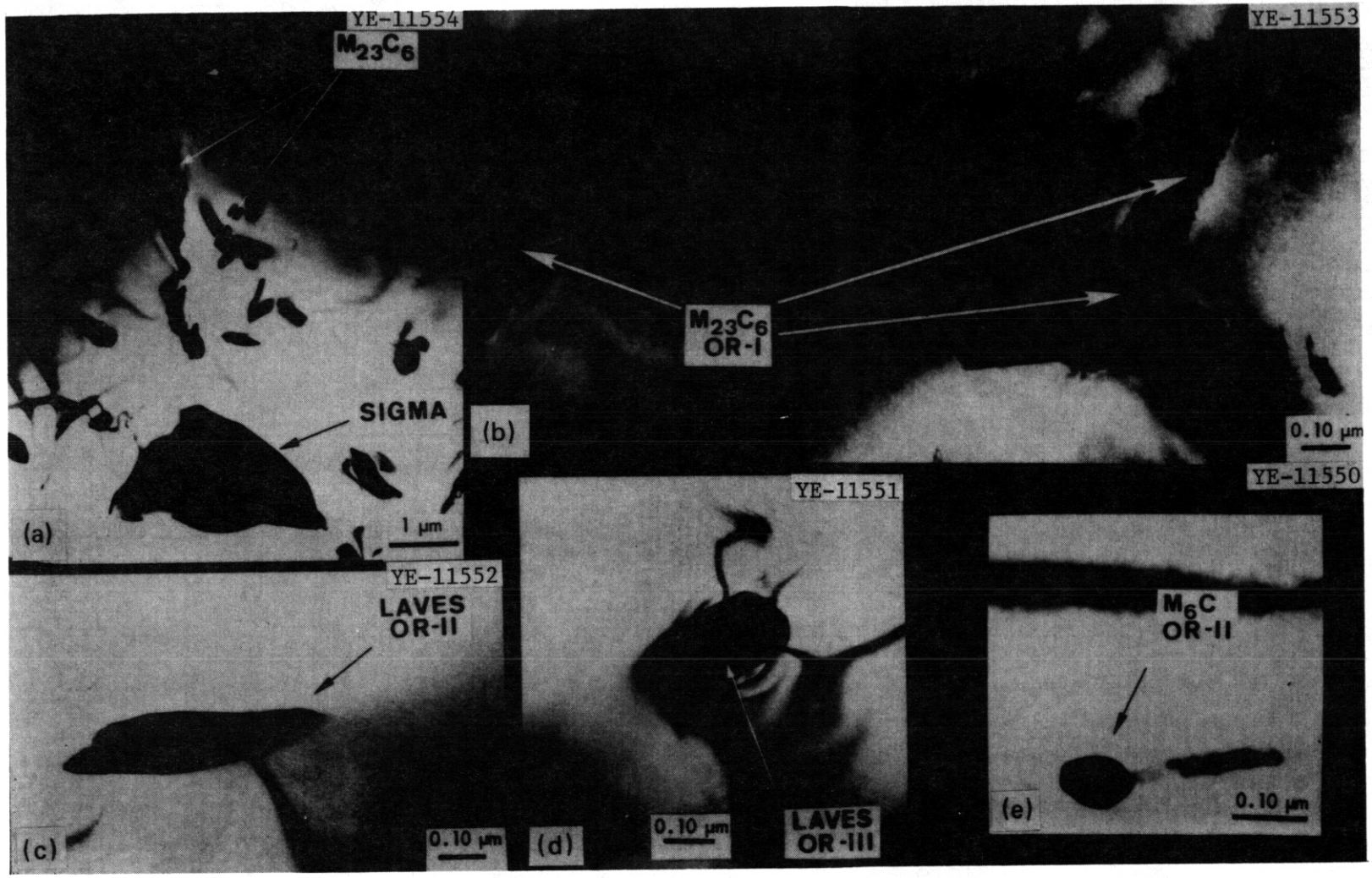

Fig. 3.3.6. Type 316 Stainless Steel Annealed 1 hr at 1050°C and Aged for 10,000 hr at 650°C. (a) Grain boundary with nearly continuous $M_{23}C_6$ and occasional sigma phase particle. (b) $M_{23}C_6$ particles, laths or plates. Beam direction is several degrees from $[1\bar{1}2]$ with $\bar{g} = [\bar{1}11]$, $s = 0$ in the γ matrix. Precipitate particle density is about $5 \times 10^{18}/m^3$. (c) Laves phase, thin lath. Precipitate is oriented on a $[1\bar{2}.1]$ Laves zone axis. Precipitate particle density is about $2 \times 10^{18}/m^3$. (d) Laves phase, rectangular chunk. Precipitate is oriented on a $[1\bar{2}.1]$ Laves zone axis. (e) Small isolated particle of M_6C oriented on a $[0\bar{1}1]$ precipitate zone axis.

steel samples irradiated in HFIR. Their compatibility with the TTP diagram justifies comparison of the HFIR-irradiated samples with this diagram.

The precipitation response of annealed type 316 stainless steel irradiated in HFIR has been examined for irradiation at 550 to 680°C to fluences producing 30 to 47 dpa and 2000 to 3300 at. ppm He. After irradiation in HFIR at 550°C to 42 dpa and 3000 at. ppm He (~16,000 hr), $M_{23}C_6$ was found at the grain boundaries and intragranularly; Laves and M_6C were also found intragranularly (see Fig. 3.3.7). After irradiation

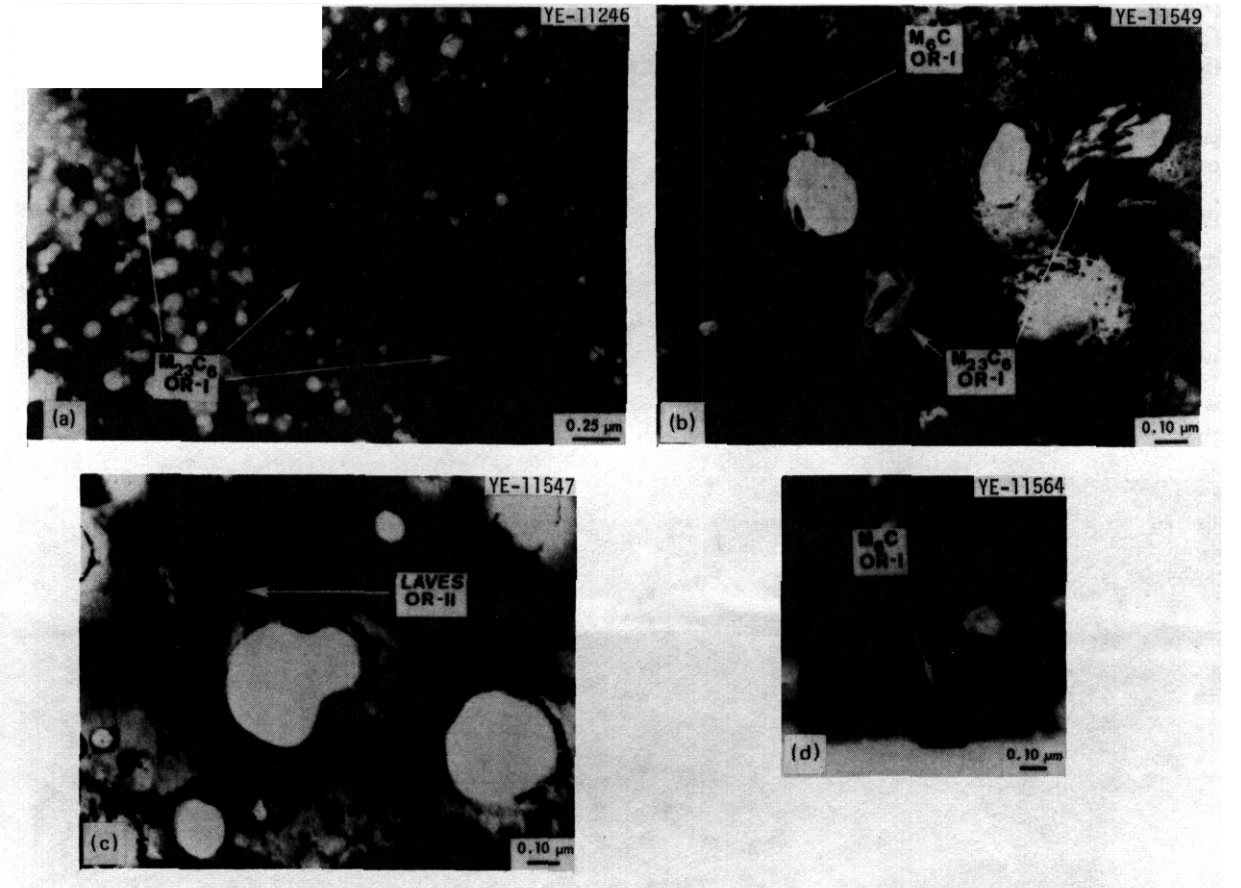

Fig. 3.3.7. Type 316 Stainless Steel Annealed 1 hr at 1050°C and Irradiated in HFIR at 550°C to 3000 at. ppm He and 42 dpa (~16,000 hr). (a) Grain boundary with nearly continuous $M_{23}C_6$. (b) Intragranular plates of $M_{23}C_6$ and M_6C; both are oriented near [0il] precipitate zones, which are coincident with a γ matrix [011] zone axis. Precipitate particle densities are about 4 and $6 \times 10^{19}/m^3$, respectively. (c) Laves phase, thin lath. Precipitate is oriented in a $[1\bar{2}.0]$ precipitate zone axis. Precipitate particle density is about $2 \times 10^{19}/m^3$. (d) Large, isolated M_6C precipitate particle, eriented on a $[1\bar{3}4]$ precipitate zone axis.

at 600°C to 30 dpa and 2000 at. ppm He (~7800 hr), large isolated intergranular sigma phase particles were observed, and Laves phase particles were distributed intragranularly (see Fig. 3.3.8). After irradiation at 680°C to 47 dpa and 3300 at. ppm He (~13,000 hr), large isolated intergranular sigma phase precipitate particles were found, and chi phase was found within the grains (see Fig. 3.3.9).

The phase combinations observed in the samples after HFIR irradiation are compared with the phase regions of the TTP diagram in Fig. 3.3.1(b). The most significant point is that the TTP diagram contains phase regions that predict the same phase combinations as observed after HFIR irradiation. However, coincidence of the points and the appropriate regions on the TTP diagram requires a shift of the points both upward in temperature and outward in time relative to thermal aging results. The shifts are different for the different samples. For the sample irradiated at 550°C, a shift of about 70°C upward is needed to obtain the appropriate phase region on the TTP diagram. The sample irradiated at 600°C requires consideration of both the TTP diagram and Weiss and Stickler's reaction scheme. If $M_{23}C_6$ is a metasable phase, then from Weiss and Stickler's

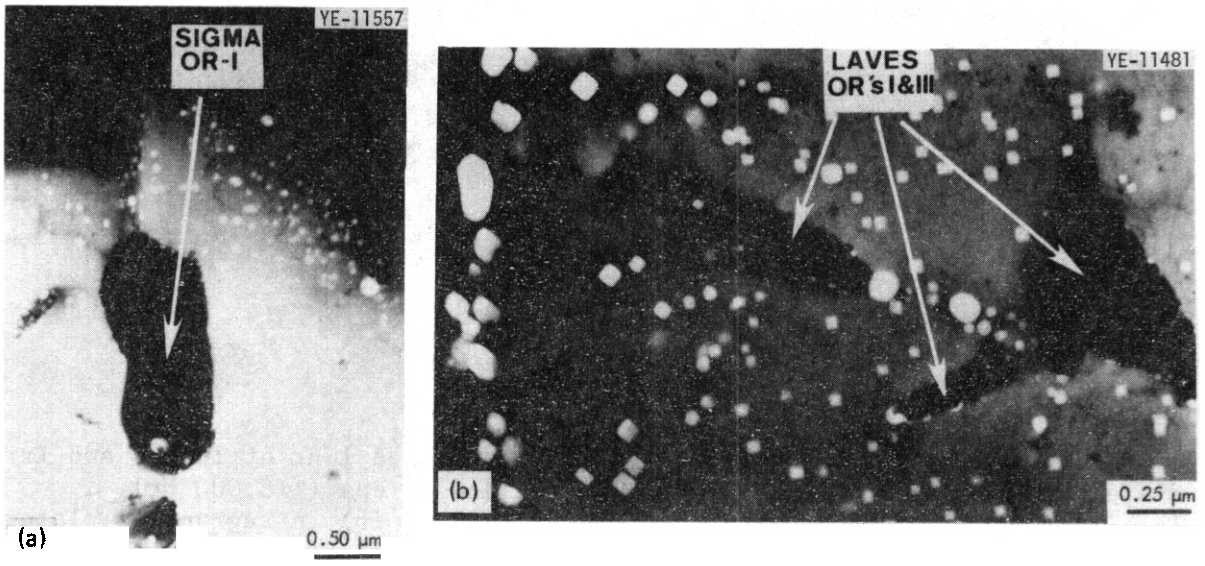

Fig. 3.3.8. Type 316 Stainless Steel Annealed 1 hr at 1050°C and Irradiated in HFIR at 600°C to 2000 at. ppm He and 30 dpa (~7800 hr). (a) Large, isolated sigma phase particle oriented near a [001] precipitate zone axis that is coincident with a $[1\bar{1}1]$ γ matrix zone axis. (b) Cavity-coated laths of Laves phase, several of which are oriented near a [00.1] precipitate zone axis. Precipitate particle density is about $3 \times 10^{18}/m^3$.

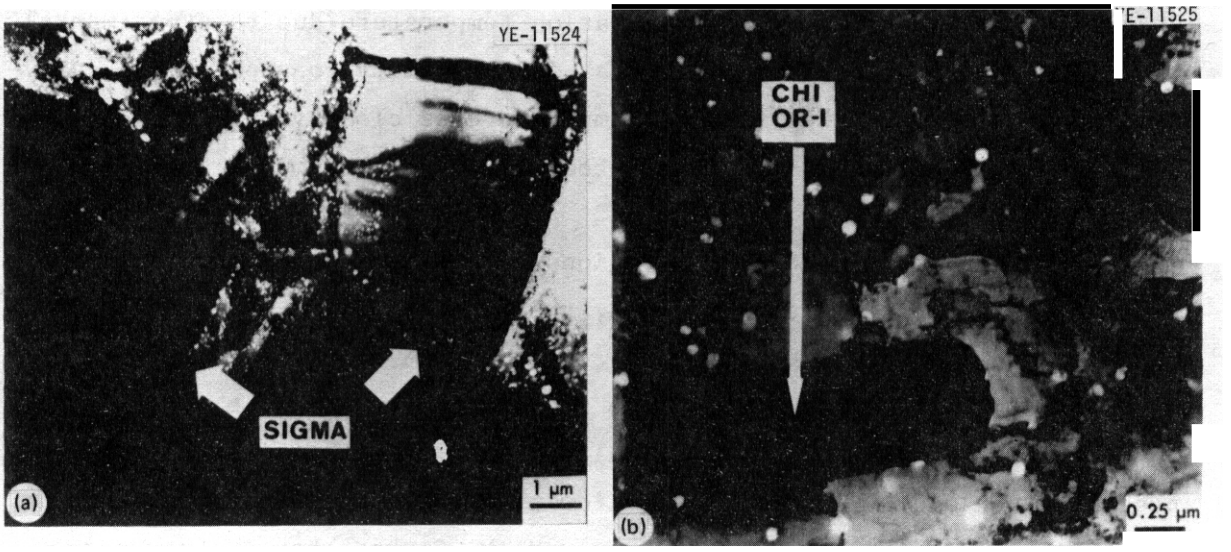

Fig. 3.3.9. Type 316 Stainless Steel Annealed 1 hr at 1050°C and Irradiated in HFIR at 680°C to 3300 at. ppm He and 47 dpa (~13,000 hr). (a) Massive sigma phase at the grain boundaries. (b) Large intragranular plates of chi phase. The dark chi phase is oriented on a [$\bar{6}81$] precipitate zone axis.

reaction scheme it is logical to assume that at some time the transformation will be complete. This means that the sigma + $M_{23}C_6$ + Laves phase region in the TTP curve will cross a boundary signifying the end of the transformation of $M_{23}C_6$ to sigma, giving a sigma + Laves phase region. Thus, the sample irradiated at 600°C would require a shift of about 90°C upward and a shift outward in time to get to an appropriate phase region on the TTP diagram. The sample irradiated at 680°C requires an upward shift of about 200°C on the TTP diagram to coincide with the appropriate phase region.

The net result of simulated fusion irradiation at these temperatures and fluences seems to be shifting the phase regions similar to those observed after thermal aging on the TTP diagram to some lower temperature and shorter time. This is in contrast to fast-reactor irradiation, where phases not observed under any aging conditions are found after irradiation, but little or no temperature shift for otherwise similar phase regions is required. The temperature shifts are approximate and are of course based upon the assumption that the calculated irradiation temperatures are correct. Until experiments with more accurate temperature control are

available, some shifts in the irradiation temperature due to experimental uncertainty must also be considered as a possibility to explain the data. A uniform shift in either time or temperature is clearly insufficient to bring coincidence of all the irradiated samples with similar phase regions on the TTP diagram.

If we compare similar phase regions on the TTP diagram for aged samples and those irradiated in HFIR, the morphology and number density of a particular phase are different. Compare the sample aged 10,000 hr at 650°C (Fig. 3.3.6) and the sample irradiated for about 16,000 hr at 550°C (Fig. 3.3.7). Figures 3.3.6(a) and 3.3.7(a) show similar $M_{23}C_6$ precipitation at the grain boundary for the aged and irradiated samples, respectively. Within the grains, however, $M_{23}C_6$ has changed from narrow laths to square plates or chunks after irradiation [Figs. 3.3.6(b), 3.3.7(b), and 3.3.7(d)]. Laves appears similar in both conditions, except that the laths are narrower after irradiation [Figs. 3.3.6(c) and 3.3.7(c)]. Irradiation produces nearly an order of magnitude greater precipitate particle densities of $M_{23}C_6$ and Laves than does thermal aging. The amount of M_6C relative to $M_{23}C_6$ and Laves also seems to have increased as a result of irradiation.

The association between cavities and the various precipitate phases is shown in Figs. 3.3.7 through 3.3.9. The cavities have previously been shown to be consistent with equilibrium helium bubbles.[3] There seems to be some cavity association with nearly every intra- or intergranular phase, but the highest cavity association in annealed type 316 stainless steel is clearly with Laves phase at 600°C [Fig. 3.3.8(b)]. The behavior of Laves has changed from association of several large cavities per precipitate particle at 550°C to the association of many smaller cavities with each precipitate particle at 600°C [Fig. 3.3.7(c) compared with 3.3.8(b)]. Intragranular $M_{23}C_6$ seems to have the lowest cavity association [Fig. 3.3.7(b)].

The orientation relations (ORs) for the phases observed after thermal aging and after HFIR irradiation were obtained from the electron diffraction patterns necessary to identify a particular phase type. These orientation relationships are plotted in terms of coincident stereographic projections of each precipitate phase relative to the standard (001) matrix projection

in Figs. 3.3.2 and 3.3.3. They can usually be summarized in terms of several low-order matrix and precipitate planes being parallel. The orientation relations for $M_{23}C_6$, chi, and sigma OR-I are consistent with data reported by others. The other relationships observed have not been reported. Laves OR-I and M_6C OR-I were found only after HFIR irradiation. Laves OR-I11 was found only after thermal aging. All other orientation relationships were unaffected by irradiation in the HFIR.

3.3.4.3 Discussion

The results, summarized briefly, show that HFIR irradiation of annealed type 316 stainless steel at temperatures from 550 to 680°C results in the precipitation of phases similar to those produced by thermal aging if compared with samples aged at higher temperatures and, in some cases, longer times. This is not the case after fast-reactor irradiation, which produces phases that do not occur under any thermal aging conditions. Figure 3.3.1(b) shows a crosshatched region of the TTP diagram corresponding to times and temperatures observed after fast-reactor irradiation. For fast reactor irradiation of annealed type 316 stainless steel, Ni_3Si[4,5] and the unidentified rod shaped precipitate[6-9] are observed. These phases are not observed after thermal aging to any time and temperature. The phases $M_{23}C_6$, sigma, and chi are observed[6-9] after fast-reactor irradiation and after thermal aging, with little shift in temperature or time relative to the TTP diagram. Laves and M_6C phases are not reported. If they are absent, it is significant because then not only has irradiation caused the presence of new phases, but it has also resulted in the absence of phases normally observed after thermal aging.

Compare irradiation in HFIR and EBR-II at 550°C. Intra- and intergranular $M_{23}C_6$ are observed in both. Intragranular M_6C and Laves phases are observed after HFIR irradiation but not after EBR-II irradiation. An unidentified rod-shaped precipitate is observed after EBR-II irradiation but not after HFIR irradiation. Compare irradiation in HFIR and EBR-II at 600°C. After fast-reactor irradiation, $M_{23}C_6$ is observed within and between grains along with the unidentified rod-shaped phase. After HFIR irradiation intergranular sigma and intragranular Laves phase are observed. Finally, compare irradiation in HFIR with that in EBR-II at 680°C. Again,

intra- and intergranular $M_{23}C_6$ and the rod-shaped precipitate are observed after irradiation in EBR-II, and sigma and chi phases are found along with these phases at 750°C. After irradiation in HFIR, only sigma is observed at the grain boundaries and chi phase is observed within the grains. For EBR-II irradiation, the phases $M_{23}C_6$, sigma, and chi appear at times and temperatures consistent with equivalent thermal aging. In HFIR, as mentioned previously, a shift in temperature and/or time is required for coincidence of similar phase regions. Since irradiation temperatures in both reactors are calculated without the benefit of verifying measurements, these comparisons are not absolute but rather assume correctness of the irradiation temperatures. But the differences are great enough to justify the conclusion that the production of helium during the irradiation has changed the precipitation response of annealed type 316 stainless steel.

Not only has the precipitation response changed, but the cavity association with precipitates is also different after irradiation in HFIR as compared with EBR-II. Voids are associated with the unidentified rods and $M_{23}C_6$ after irradiation in EBR-II. Both Brager and Straalsund,[5] and Bloom and Stiegler[6] indicate that nearly all voids are attached to precipitate particles. After HFIR irradiation, cavities are attached to nearly all precipitate phases, but only a fraction of the cavities is attached to precipitates rather than dislocations in the matrix of annealed type 316 stainless steel. Since in HFIR-irradiated material the cavities are probably equilibrium helium bubbles, the cavity association is an index of the helium accommodation of the various phases. Laves phase has several large cavities per precipitate particle at 550°C [see Fig. 3.3.6(c)] and many smaller cavities per particle at 600°C [see Fig. 3.3.7(b)] after HFIR irradiation. Apparently, of the phases present in annealed type 316 stainless steel, Laves accommodates helium most effectively. However, Maziasz and Bloom[7] have shown that even in the presence of Laves phase, nearly exclusive association of very small cavities with TiC occurs when 0.23 wt % Ti is added to annealed type 316 stainless steel. Laves is not the best possible, but the best available phase to accommodate helium in annealed unmodified type 316 stainless steel.

3.3.5 Conclusions

1. Curves drawn from the data of Weiss and Stickler on a TTP diagram for annealed type 316 stainless steel have been extrapolated to longer aging times. The shapes of portions of their curves have been altered slightly as well as extended, and M_6C phase region has been included to be consistent with their phase reaction scheme and their data. These curves were then extended to longer aging times; no unreasonable changes were necessary to include our data for aging at 600 and 650°C for 10,000 hr.

2. The precipitates identified in samples of annealed type 316 stainless steel irradiated in HFIR are compared with the TTP diagram for aging at similar times and temperatures. Phase regions consistent with the phase combinations observed after HFIR irradiation can be obtained by considering the extended TTP diagrams and Weiss and Stickler's phase reaction scheme. The appropriate phase regions on the TTP diagram are shifted upward in temperature and/or to longer times relative to HFIR irradiation times and temperatures. The shifts appear to be different for different phases.

3. If similar phase regions are compared for thermal aging and HFIR irradiation, HFIR seems to change the morphology, to increase the particle number density by nearly an order of magnitude, and to change the relative amounts of some phases as compared with thermal aging.

4. The orientation relationships for the crystal structure of precipitate phases relative to the matrix have been determined for both aged and HFIR-irradiated samples. The orientation relationships are plotted stereographically relative to the (001) projection of the matrix. The orientation relationships for sigma, chi, and $M_{23}C_6$ have been entirely or partially reported in the literature. We found M_6C OR-I and Laves OR-I only after irradiation in HFIR. Laves OR-I11 was found only after thermal aging. The other orientation relations were unaffected by irradiation in HFIR.

5. Samples of annealed type 316 stainless steel irradiated in HFIR are compared with samples irradiated for similar times and temperatures in fast reactors. Irradiation in HFIR results in the occurrence of M_6C and Laves phase but not the unidentified rod-shaped phase found in

fast-reactor irradiatior. If both irradiations are compared with similar phase regions on the TTP diagram, the HFIR results seem shifted to higher temperatures relative to the fast-reactor results.

6. The changes in precipitate response coincide with the inclusion of simultaneous helium production during the irradiation. The cavity interaction and association with the precipitate phases also change with the addition of helium. After fast reactor irradiation almost all voids are associated with either the rod-shaped phase or $M_{23}C_6$. After HFIR irradiation only a fraction of the cavities are associated with the precipitates, but there is some association with nearly every particle present. Laves phase shows the highest cavity association and $M_{23}C_6$ the least in annealed type 316 stainless steel irradiated at 550 to 580°C for up to 16,000 hr.

3.3.6 References

1. B. Weiss and R. Stickler, "Phase Instability During High Temperature Exposure of 316 Austenitic Stainless Steel," *Metall. Trans.* 3: 851 (April 1972).
2. J. E. Spruiell et al., "Microstructural Stability of Thermal-Mechanically Pretreated Type 316 Austenitic Stainless Steel," *Metall. Trans. 4:* 1533 (June 1973).
3. P. J. Maziasz, F. W. Wiffen, and E. E. Bloom, "Swelling and Microstructure Changes in Type 316 Stainless Steel Irradiated under Simulated CTR Conditions," *Radiation Effects and Tritium Technology for Fusion Reactors,* CONF-750989, Vol. I, pp. 259–88 (March 1976).
4. C. Cawthorne and C. Brown, "The Occurrence of an Ordered fcc Phase in Neutron Irradiated M316 Stainless Steel," *J. NucZ. Mater.* 66: 201 (1977).
5. H. R. Brager and F. A. Garner, "Swelling as a Consequence of Gamma Prime (γ') and M(C,Si) Formation in Neutron Irradiated 316 Stainless Steel," to be published in *Journal of Nuclear Materials.*
6. E. E. Bloom and J. O. Stiegler, "Effect of Irradiation on the Microstructure and Creep-Rupture Properties of Type 316 Stainless Steel," pp. 360–82 in *Effects of Radiation on Substructures and Mechanical Properties of Metals and Alloys, ASTM Spec. Tech. Publ.* 529, American Society for Testing and Materials, Philadelphia, September 1973.

7. J. M. Leitnaker, E. E. Bloom, and J. O. Stiegler, "The Effect of Minor Constituents on Swelling in Stainless Steel," *J. Nucl. Muter.* **49: 57–66 (1973).**

8. H. R. Brager and J. L. Straalsund, "Defect Development in Neutron Irradiated Type **316** Stainless Steel," *J. Nucl. Muter.* **46: 134–58 (1973).**

9. **P.** J. Barton, B. L. Eyre, and D. A. Stow, "The Structure of Fast-Reactor Irradiated Solution-Treated AISI Type **316** Stainless Steel," *J. Nucl. Muter.* **67: 181–97 (1977).**

10. P. J. Maziasz and E. E. Bloom, "Comparison of **316** + Ti with **316** Stainless Steel Irradiated in **a** Simulated Fusion Environment," *Trans. Am. Nucl. Soc.* **27: 268–69 (1977).**

3.4 THE SWELLING OF 20%-COLD-WORKED TYPE 316 STAINLESS STEEL IRRADIATED IN HFIR TO HELIUM LEVELS OF 200—3700 at. ppm — M. L. Grossbeck and P. J. Maziasz (ORNL)

3.4.1 ADIP Task

ADIP Task 1.C.2, Microstructures and Swelling in Austenitic Alloys.

3.4.2 Objective

The purpose of this study is to measure swelling in 20%-cold-worked type 316 stainless steel with high levels of helium and compare it with swelling in similar material containing little or no helium.

3.4.3 Summary

Specimens of 20%-cold-worked type 316 stainless steel were irradiated in the High Flux Isotope Reactor (HFIR). The mixed spectrum of this reactor results in simultaneous production of helium from a thermal neutron reaction with nickel' and displacement damage from the fast portion of the spectrum.

The amount of swelling was determined by liquid immersion density measurements. Swelling was greater than in samples containing only trace quantities of helium irradiated in EBR-II. Swelling as high as 1.6 vol % at a fluence of 7×10^{26} n/m^2 (>0.1 MeV) was found in material irradiated at 380°C. This contrasts with slight densification in material irradiated in EBR-II. Of the three temperatures investigated — 375, 475, and 575°C — lowest swelling occurred at 475°C and highest at 375°C. Low-helium, EBR-11-irradiated type 316 stainless steel exhibits' maximum swelling at about 585°C.

3.4.4 Progress and Status

Unlike an LMFBR, a fusion reactor will not experience coolant flow restriction if excessive swelling occurs in structural materials. However, since a Tokamak is such a large structure, even modest swelling could result in shape distortions and excessive stresses, especially at points of support or constraint. Swelling must, therefore, be known and should be minimized or allowed for. Since helium is known to have

a major effect on swelling, it is necessary to characterize and hopefully understand its effect and to have swelling data available to designers.

The specimens for this investigation were primarily intended for tensile property measurement. They were machined from type 316 stainless steel of composition as follows:

Element	Cr	Ni	Mo	Mn	Ti	Si	C	P	S	N	B	Fe
wt %	18.0	13.0	2.58	1.9	0.05	0.8	0.05	0.013	0.016	0.05	0.0005	Bal

The specimen material was solution annealed at 1150°C for 1 hr, then cold swaged to 50% reduction in area. This was followed by annealing at 1050°C for 1 hr followed by similar cold swaging and annealing, after which the rod was cold swaged to 20% reduction in area. The material was then machined into tensile specimens 31.7 mm long with a gage diameter of 2.0 mm.

The specimens were irradiated in HFIR in a peripheral target position. The mixed fast and thermal spectrum results in a simultaneous high displacement damage rate and high helium production rate in alloys containing nickel.[1] Seven capsules were irradiated, providing a fluence range of 0.6×10^{26} to 8×10^{26} n/m^2 (>0.1 MeV). Corresponding helium levels range from 200 to 3700 at. ppm He. Irradiation temperatures from 285 to 620°C were achieved by surrounding the specimens with helium gas gaps. No instrumentation was provided.

Densities were measured by liquid immersion using water or ethyl phthalate. Liquid temperature was controlled to within ±0.05°C, and liquid density was calibrated against a quartz standard.

Preliminary results are shown in Fig. 3.4.1. The helium-containing material has higher swelling within the fluence and temperature ranges observed than does EBR-11-irradiated material.[3] Densification observed at low fluence values in both materials results from precipitation.[4] The temperature dependence of swelling in the HFIR-irradiated material is unusual in that material irradiated at 375°C exhibits slightly greater swelling than that irradiated at 575°C, and the lowest swelling occurred

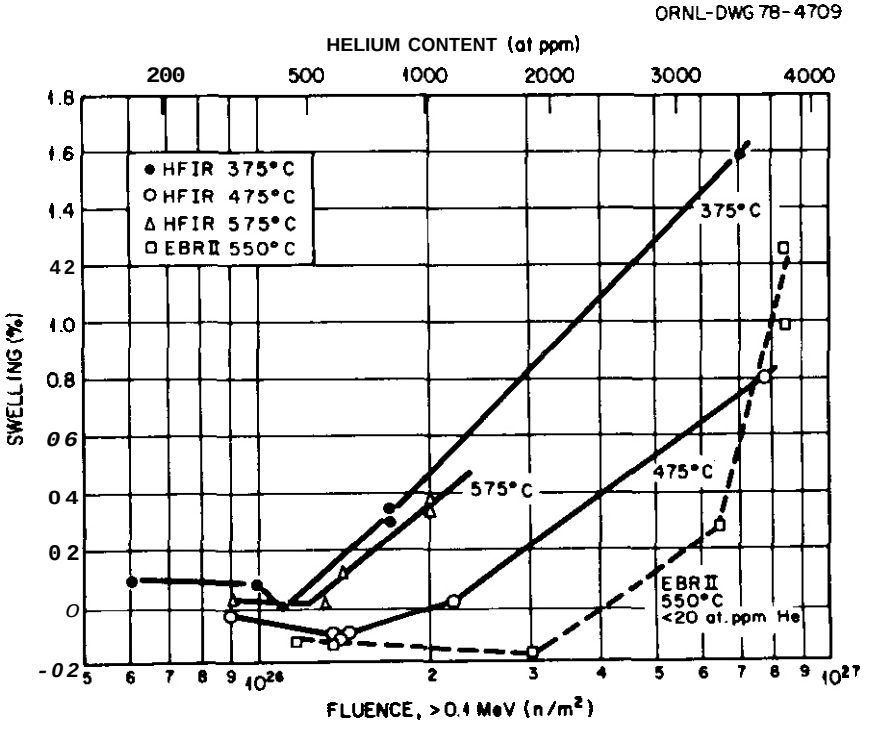

Fig. 3.4.1. Swelling as a Function of Fluence and Helium Content for HFIR-Irradiated 20%-Cold-Worked Type 316 Stainless Steel. Data on the swelling produced in a different heat of type 316 stainless steel by irradiation in EBR-II are shown for comparison.

for irradiation at 475°C. A different effect is observed' in EBR-II irradiated 20%-cold-worked type 316 stainless steel, which shows a swelling maximum at 585°C.

The high swelling at 375°C is consistent with microscopy studies by Maziasz et a1.,[4] which show a slight decrease in swelling as temperature is increased from 380 to 550°C, above which swelling increases substantially with increasing temperature. That investigation also found that at 380°C, among the numerous small cavities are a few large cavities, which are not formed at 450 and 550°C, and these seem to contribute to the larger swelling. The phenomena associated with the large cavities are not clear at present. The interactions of the cavities with helium and precipitation are undergoing further investigation.

Microstructural examination of 20%-cold-worked type 316 stainless steel irradiated at 600°C to fluences producing 1.5 to 3.0 dpa and 30 to 80 at. ppm He indicates cavity densities of $2.5 \times 10^{21}/m^3$ and

diameter of 7 to 12 nm. The microstructure of the same material irradiated in EBR-II to similar conditions shows precipitation but few or no cavities until greater than 15 to 20 dpa. Thus helium is responsible for earlier and more rapid nucleation than expected from previous observations.[4]

3.4.5 Conclusions

Swelling in 20%-cold-worked type 316 stainless steel containing greater than 2000 at. ppm He and irradiated between 375 and 575°C is significantly greater than in similar material irradiated in a fast neutron spectrum. Below a fluence of 8×10^{26} n/m^2 (>0.1 MeV), material containing less than 20 at. ppm He[5] densifies by 0.1 to 0.2% or swells by less than 0.3%, whereas irradiated material containing greater than 200 at. ppm He swells as much as 1.6%.

A swelling maximum near 375°C was found in the helium-containing material. This is in addition to the continuously increasing swelling above 550°C that was reported previously.[4]

3.4.6 References

1. J. Weitman, N. DåverNög, and S. Farvolden, "Anomalous Helium Production in Nickel," *Trans. Am. Nucl. Soc.* 13: 557–58 (1970).
2. W. K. Appleby, E. E. Bloom, J. E. Flinn, and F. A. Garner, "Swelling in Neutron-Irradiated 300-Series Stainless Steels," pp. 509–27 in *Radiation Effects in Breeder Reactor Structural Materials*, The Metallurgical Society of AIME, New York, 1977.
3. J. F. Bates et al., *An Empirical Relationship for Swelling in 20% Cold Worked 316 Stainless Steel*, HEDL-TME 76-96 (1977).
4. P. J. Maziasz, F. W. Wiffen, and E. E. Bloom, "Swelling and Microstructure Changes in Type 316 Stainless Steel Irradiated Under Simulated CTR Conditions," *Radiation Effects and Tritium Technology for Fusion Reactors*, CONF-750989, Vol. I, pp. 259–88 (March 1976).
5. N. D. Dudey and S. D. Harkness, "Helium Production in EBR-IT. Irradiated Stainless Steel," *Nucl. Appl. Technol.* 9: 700–09 (1970).

3.5 THE INFLUENCE OF IRRADIATION ON THE PROPERTIES OF PATH A ALLOY WELDMENTS — F. W. Wiffen, D. P. Edmonds, J. F. King, and J. A. Horak (ORNL)

3.5.1 ADIP Task

ADIP Task 1.B.13, Tensile Properties of Austenitic Alloys.

3.5.2 Objective

This work scopes the response of welds and weld-affected zones to irradiation over a range of temperatures and fluences. Welds with type 316 or 16-8-2 stainless steel filler metal joining 20%-cold-worked type 316 base metal are being irradiated in the ORR and HFIR. Tensile tests on the irradiated specimens will be supplemented by fractography, metallography, and microscopy to determine the effects of irradiation on the mechanical properties.

3.5.3 Sumnary

Weld-containing samples irradiated in HFIR at about 55°C exhibited large increases in the 35°C tensile strength but only modest loss of ductility. The strength of the weld-containing samples remained below the strength of the base metal, and all tested samples failed within the weld metal.

3.5.4 Progress and Status

Five rod samples made from 20%-cold-worked type 316 stainless steel welded with 16-8-2 filler metal were included in experiment HFIR-CTR-16, designed to investigate irradiation effects at about 55°C, the lower bound operating temperature for a separately cooled fusion reactor first wall. The sample geometry and orientation with respect to the weld are shown in Fig. 3.5.1. These samples were irradiated in direct contact with the reactor coolant water at a temperature of about 55°C. The experiment was in a peripheral target position in HFIR for five standard cycles, equivalent to a total of 11,466 MWd at full power of 100 MW. After irradiation these samples were tensile tested in air on an Instron machine.

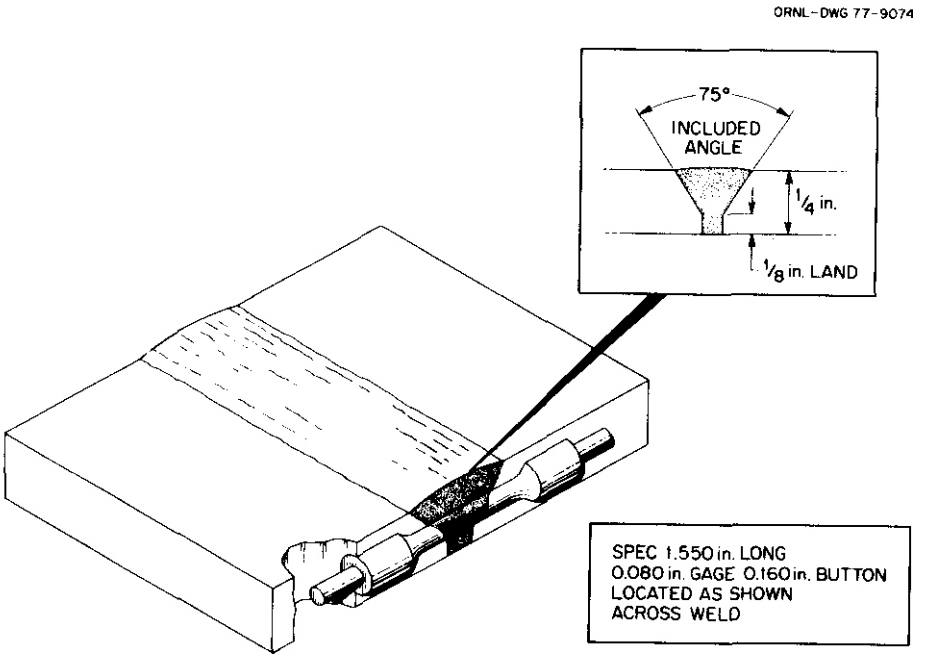

Fig. 3.5.1. Orientation of Tensile Sample with Respect to the Weld for Samples Used in the HFIR Irradiation of Weldments. The reduced gage section of the sample is 18 mm long and 2 mm diam. To convert dimensions shown on drawing, 1 in. = 25.4 mm.

Tensile test results are given in Table 3.5.1, along with results representative of the unirradiated base metal. Comparison of the control data on base metal and weld-containing specimens showed that the weld-containing samples failed at much lower stresses than samples of only base metal, and with higher uniform elongation but comparable total elongation. The irradiated samples tested at about 35°C showed higher strengths and lower ductilities than the control values. The strength values increased with increasing fluence for the three samples available, but the ductility values were approximately the same for the three tests. Although the yield strength was approximately double the control value, and the ultimate tensile strength increased approximately 40%, these strength values were still below the values for unirradiated base metal: Strength and ductility values of the irradiated sample were lower in tests at 300 and 700°C than in tests at 35°C. At both these elevated temperatures the strength values were lower for base metal tested at the same temperature.

Table 3.5.1. Tensile Properties of Welds Made with 16-8-2 Filler Metal Joining Type 316 Stainless Steel Base Metal

Irradiation Parameters[a]		Test Temperature (°C)	Strength, MPa		Elongation, %	
dpa	Helium (at. ppm)		0.2% Yield	Ultimate	Uniform	Total
		Weld Specimens				
0		-35	354	547	14.0	19.0
0		-35	333	510	12.9	16.5
-4.5	100	-35	680	735	6.8	12.0
8.7	250	-35	701	739	5.8	11.8
10.8	340	-35	727	759	1.2	13.0
10.8	340	300	565	598	3.1	6.7
5.5	130	700	214	247	1.4	1.7
		20%-Cold-Worked Type 316 Stainless Steel				
0		35	836	864	7.9	17.8
0		300	708	747	1.4	6.0
0		700	399	410	0.9	15.9

[a]Irradiation temperature about 55°C.

Location of fracture positions on post-test macrophotographs and comparison with weld locations determined by ferrite zone locations before irradiation showed that all weld specimens tested had failed within the weld metal. Fracture surfaces and microstructures have not yet been examined.

3.5.5 Conclusions and Future Work

Irradiation of weld-containing samples at about 55°C to fluences producing 4 to 11 dpa and 100 to 340 at. ppm He resulted in large strength increases in tensile tests at about 35°C but had little effect on the ductility. The strength of 16-8-2 welded specimens remained lower than the strength of the 20%-cold-worked base metal, with all tested samples failing in the weld zone.

Similar specimens containing welds with 16-8-2 and type 316 stainless steel filler metal have been irradiated at temperatures in the range 280 to 620°C. These samples will be tensile tested during the next reporting period. A related set of weld-containing and all-weld-metal sheet samples are under irradiation in ORR-MFE-1.

3.6 THE EFFECTS OF IRRADIATION AT ABOUT 55°C ON TYPE 316 STAINLESS STEEL — F. W. Wiffen (ORNL)

3.6.1 ADIP Task

ADIP Task 1.B.13, Tensile Properties of Austenitic Alloys.

3.6.2 Objective

This work was directed at establishing the effect of irradiation at about 55°C on the swelling and tensile properties of type 316 stainless steel. This experiment will provide data that can be used to project the service performance of separately cooled reactor first walls operating at temperatures well below the main blanket temperature.

3.6.3 Summary

Irradiation of 20%-cold-worked type 316 stainless steel at about 55°C to produce 4.5 to 10.5 dpa and 180 to 520 at. ppm He reduces the uniform elongation to near zero but has little effect on the total elongation or strength properties for tensile tests at 35°C. Tests in the temperature range 200 to 300°C show the same trends as for 35°C tests. Tests at *400* to 600°C show elongation and strength very close to the control values. Tensile testing at 700°C after holding the sample 30 min at temperature shows low ductility but strength values equal to the control values. This appears to be the onset of helium embrittlement. No measurable swelling was produced by this range of irradiation conditions.

3.6.4 Progress and Status

3.6.4.1 Experiment

Irradiation experiment HFIR-CTR-16 was a three-pin experiment with 42 rod tensile samples irradiated in direct contact with about 55°C reactor cooling water. The experiment was irradiated in the HFIR peripheral target position for five standard cycles, 114.66 full-power days. The method of specimen loading is shown schematically in Fig. 3.6.1.

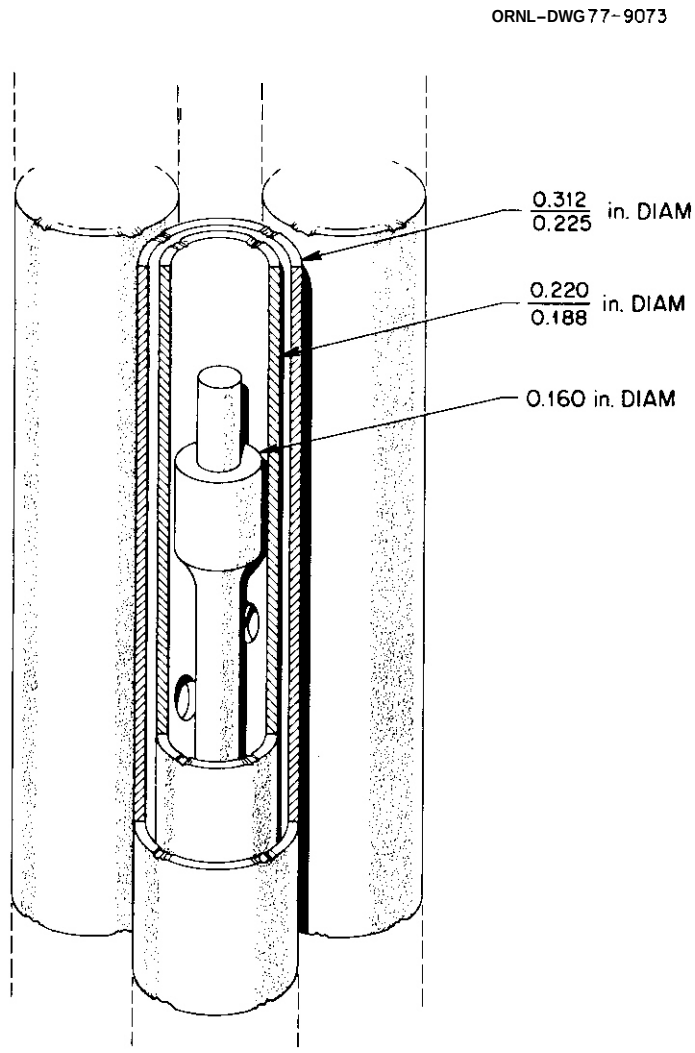

Fig. 3.6.1. Schematic Diagram of the Specimen Loading for the HFIR Water Temperature Irradiation Experiment, HFIR-CTR-16.

Specimens of 20%-cold-worked type 316 stainless steel were made from the DO heat of steel. The composition of this steel in weight percent is 18.0 Cr—13.0 Ni—2.58 Mo—1.9 Mn—0.8 Ni—0.05 C—bal Fe. Irradiation of type 316 stainless steel with 13 wt % Ni in this experiment produced from 4.5 to 10.5 dpa and from 180 to 520 at. ppm He in the samples.

All tensile tests were run in air on an Instron. In elevated-temperature tests, the samples were held at the test temperature for 30 min before the start of tests. Strain values were calculated from the chart-recorded crosshead motion during the test.

3.6.4.2 Results

Comparison of preirradiation and postirradiation specimen lengths indicated little or no swelling due to irradiation. Immersion density measurements on a few specimens confirmed little or no swelling. The combination of all measurements suggests that the 180 to 520 at. ppm He produced during the irradiation at about 55°C is accommodated in the 20%-cold-worked type 316 stainless steel without producing measurable swelling.

The tensile results are given in Table 3.6.1, and shown as a function of test temperature in Fig. 3.6.2. For the range of conditions investigated, the tensile properties at about 35°C are relatively insensitive to dpa, helium level, and strain rate during test. The yield strength and ultimate strength at about 35°C were raised about 17 and 13%, respectively, by the irradiation but were not sensitive to variations in the dpa or helium level. The uniform elongation was reduced from above 3% to about 0.4% by the irradiation, but the total elongation was little affected.

Tensile tests at temperatures above the irradiation temperature showed little or no effect on the strength values for the test temperatures from 200 *to* 700°C. The total elongation of irradiated specimens was approximately equivalent to control values for tests in the range 200 to 600°C, but dropped below 1% for tests at 700°C. The uniform elongation of irradiated samples remains near zero for tests up *to* 300°C, rises to values equivalent to the value for control tests for tests at 400 to 600°C, and returns to near zero for tests at 700°C.

Fracture surfaces have not yet been examined for the determination of fracture mode.

3.6.5 Conclusions and Future Work

Irradiation of 20%-cold-worked type 316 stainless steel at about 55°C to produce 4.5 to 10.5 dpa and 180 to 520 at. ppm He reduces the uniform elongation to near zero but has little effect on the total elongation or strength properties for tensile tests at 35°C. Tests

Table 3.6.1. Tensile Properties of 20%-Cold-Worked Type 316 Stainless Steel After HFIR Irradiation[a]

Irradiation Parameters			Test Temperature (°C)	Strength, MPa		Elongation, %	
Fluence >0.1 MeV ($\times 10^{26}$ n/m^2)	dpa	Helium (at. ppm)		0.2% Yield	Ultimate	Uniform	Total
			Control Samples				
			-35	785	817	4.1	12.3
			-35	836	864	7.9	17.8
			-35	818	862	3.3	11.2
			100	708	747	1.4	4.0
			300	682	719	1.7	6.4
			450	760	814	2.2	6.7
			500	475	132	3.4	7.7
			700	399	410	0.9	15.9
			Samples Irradiated in HFIR-CTR-16 at -55°C				
0.5	4.5	180	-35	960	967	0.4	5.1
1.13	8.8	380	-35	943	950	0.4	14.7
1.35	10.8	520	-35	948	954	0.4	12.0
1.13	8.8	380	-35[b]	945	949	0.3	11.1
1.09	8.7	370	~35[c]	1045	1054	0.6	9.5
1.27	10.2	470	200	844	847	0.3	6.7
1.30	10.5	490	300	783	783	0.2	5.5
0.73	5.5	200	300	802	802	0.2	5.6
1.27	10.2	470	400	731	763	2.7	7.5
1.27	10.2	470	500	634	708	3.6	8.2
1.24	10.0	450	600	563	634	5.3	9.6
1.24	10.0	450	700	415	419	0.3	0.4
0.69	5.4	200	700	398	407	0.4	0.9

[a] Strain rate 0.0028/min except as noted.

[b] Strain rate 0.00028/min.

[c] Strain rate 0.28 min.

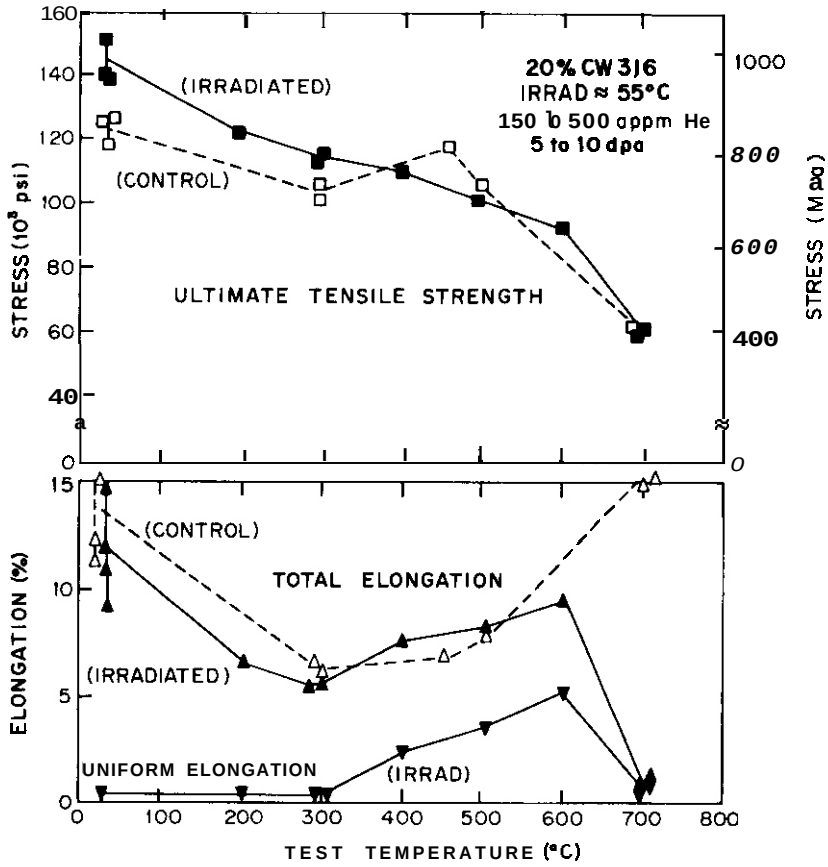

Fig. 3.6.2. Tensile Properties of 20%–Cold–Worked Type 316 Stainless Steel Irradiated at about 55°C in Experiment HFIR–CTR–16.

in the temperature range 200 to 300°C show the same trends as 35°C tests. Tests at 400 to 600°C produce elongation and strength parameters very close to the control values. Tensile testing at 700°C after holding the sample 30 min at temperature produces low ductility but strength values equal to the control values. This appears to be the onset of helium embrittlement.

Irradiation under these conditions did not produce any measurable swelling.

Fracture surface examination and limited microstructural examination will complete this work. The data will be included in the full matrix of irradiation conditions on this alloy in defining the properties of type 316 stainless steel under fusion reactor operating conditions. No further irradiation experiments are currently planned.

4. PATH B ALLOY DEVELOPMENT — HIGHER STRENGTH Fe–Ni–Cr ALLOYS

Path B alloys are the Fe–Ni–Cr "superalloys" in which tensile, creep–rupture, and fatigue strength levels higher than attainable in the austenitic stainless steels are achieved by precipitation of one or more phases. Many alloys in this class exhibit low swelling in fast-reactor irradiations. The technology for use of path B alloys in neutron radiation environments is not as advanced as for path A alloys. A basis to select a specific alloy type for further development is lacking. Accordingly, the ADIP task group has selected five base research alloys that are representative of the basic systems of path B alloys and deserve consideration for fusion reactor applications. The systems under investigation include γ' strengthened–molybdenum modified, γ' strengthened–niobium modified, $\gamma'\gamma''$ strengthened, and a high–nickel precipitation–strengthened alloy (–75%Ni).

Near–term activities are focused on evaluating the effects of a fusion reactor neutron spectrum on key mechanical and physical properties. Damage created by the fusion reactor neutron spectrum is approximated by fission reactor irradiation. Data are presently being obtained on a limited number of commercial alloys on which scoping studies were initiated two to three years ago. The emphasis will shift to the base research alloys as they become available. For those properties that are either inadequate or degraded to an unacceptable level, the influence of composition and microstructure on the response will be examined. The research program will be oriented toward determination of mechanisms responsible for the observed property changes and the effects of metal-lurgical variables on the response. The objective is to develop a basis for selection of the path B prime candidate alloy(s).

4.1 THE MICROSTRUCTURE OF NIMONIC PE-16 IRRADIATED TO PRODUCE HIGH HELIUM CONTENTS — D. N. Braski and F. W. Wiffen (ORNL)

4.1.1 ADIP Task

ADIP Task 1.C.3, Microstructures and Swelling in Higher Strength Fe-Ni-Cr Alloys.

4.1.2 Objective

The objective of this work is to characterize the microstructure and measure the swelling produced by irradiation of Nimonic PE-16 in the HFIR. The data will be used to predict the swelling that would occur in PE-16 in fusion reactor service and will be correlated with mechanical property and fracture mode work on the same samples to establish the physical processes controlling the property changes. The range of parameters included are irradiation temperatures that bracket the possible range of application temperatures, 55 to 700°C, and fluences producing 2 to 22 dpa and 100 to 5600 at. ppm He.

4.1.3 Summary

Initial experiments have begun on the effects of HFIR irradiation of PE-16, where large amounts of helium are produced in the alloy. Irradiation at 400 and 650°C produced cavities coated with the γ' precipitate phase. After irradiation at 400°C and a helium content of 370 at. ppm, the average cavity size was 16.5 nm; at 650°C and a helium content of 1030 at. ppm, a bimodal cavity distribution was created with average sizes of 31.3 and 124.0 nm. Faulted loops were formed at 400°C but not at 650°C. A new observation for irradiated PE-16 was the precipitation of $M_{23}C_6$ in the grain boundaries at 650°C. Experiments under way should help explain many of the microstructural changes in these exploratory PE-16 specimens.

4.1.4 Progress and Status

During this reporting period we have examined several solution annealed and tensile tested specimens as well as two irradiated specimens. The test conditions for these specimens bracket a large

portion of the PE-16 test matrix. The microstructural characterization of these specimens by transmission electron microscopy indicated what to expect in PE-16 after irradiation in HFIR. Examination of the next series of specimens should show, in detail, the effect of irradiation temperature from about 55 to 700°C on the microstructure and swelling of PE-16 with a helium content of about 900 at. ppm.

The composition of PE-16 (heat NNW-2282) used in this investigation is:

Element:	Ni	Cr	Fe	Mo	Al	Ti	Si	C	Mn
wt %:	43.1	16.5	bal	3.2	1.24	1.18	0.21	0.05	0.04

This composition produces an austenitic alloy that can be hardened by the precipitation of γ' phase. The γ' phase has a composition of $Ni_3(Al,Ti)$ and an ordered fcc structure with $L1_2$ symmetry. A control sample that had been solution annealed for 4 hr at 1080°C but not aged showed isolated inclusions throughout the microstructure and no γ'. This was the starting solution annealed microstructure. A second specimen of PE-16 was solution annealed for 2 hr at 1121°C and tensile tested at 500°C. Selected area electron diffraction (SAD) produced very faint (110) γ' super lattice reflections, but it was very difficult to image the particles under either bright field or dark field conditions, apparently because so little precipitate was present.

Two additional PE-16 specimens were annealed for 2 hr at 1121°C and irradiated in HFIR under the conditions listed in Table 4.1.1. Irradiation at 400°C produced a cavity concentration of $1.49 \times 10^{21}/m^3$, with an average diameter of 16.5 nm (see Table 4.1.1). The measured distribution of cavity sizes is given in Fig. 4.1.1. The cavities were quite uniformly distributed throughout the microstructure and were often found on grain boundaries. Figure 4.1.2 shows some of the small, elongated cavities lining a grain boundary. The γ' phase had precipitated on the cavities during irradiation, as shown by the bright field-dark field series shown in Fig. 4.1.3 We also found some isolated γ' particles on dislocation segments. A large number of faulted loops were created during the irradiation and were most clearly imaged under weak-beam dark-field conditions. Figure 4.1.4 shows some of these faulted loops

Table 4.1.1. Irradiation Conditions, Swelling, and TEM Results for Irradiated Nimonic PE-16[a]

Irradiation Conditions				Microstructural Results from TEM			Immersion Density Decrease (%)
Irradiation Temperature (°C)	Fluence >0.1 MeV (n/m^2)	dpa	Helium (at. ppm)	Cavity Concentration (m^{-3})	Av Cavity Diam (nm)	Cavity Volume (%)	
400	0.56×10^{26}	4.4	370	1.49×10^{21}	16.5	0.35	0.32
650	1.06×10^{26}	≅ 7	1030[b]	1.75×10^{20} small[c]	31.3	0.28	0.51
				$\geq 31 \times 10^{19}$ large[c]	124.0	2.31	≥ 2.59

[a] All samples solution annealed 2 hr at 1120°C, not aged.

[b] Measured value, used for normalization of other calculated values.

[c] Bimodal distribution of cavities.

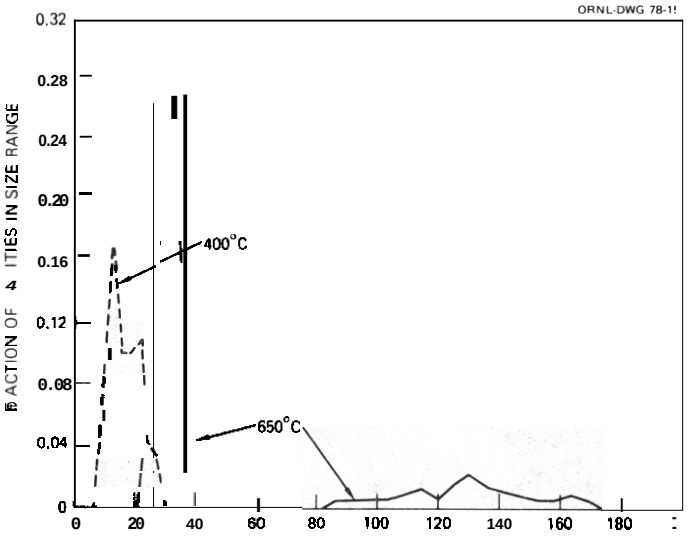

YE-11574

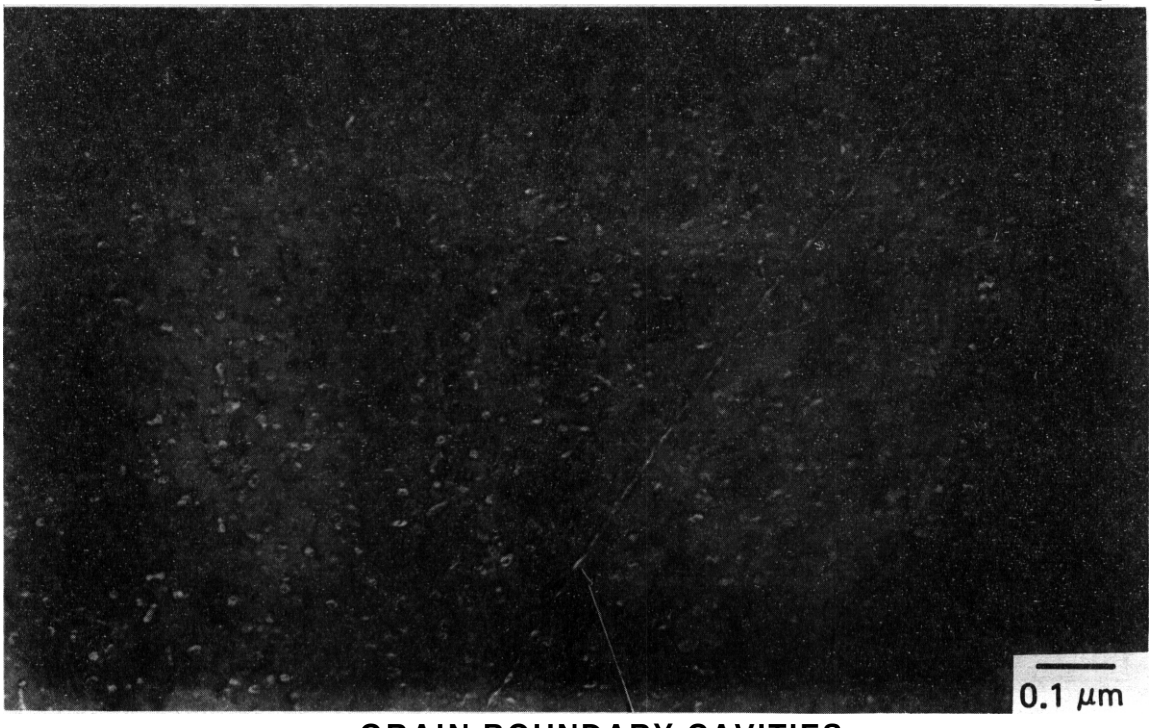

GRAIN BOUNDARY CAVITIES

Fig. 4.1.2. Grain Boundary Cavities in PE-16 After Irradiation in HFIR at 400°C (4.4 dpa, 370 at. ppm He).

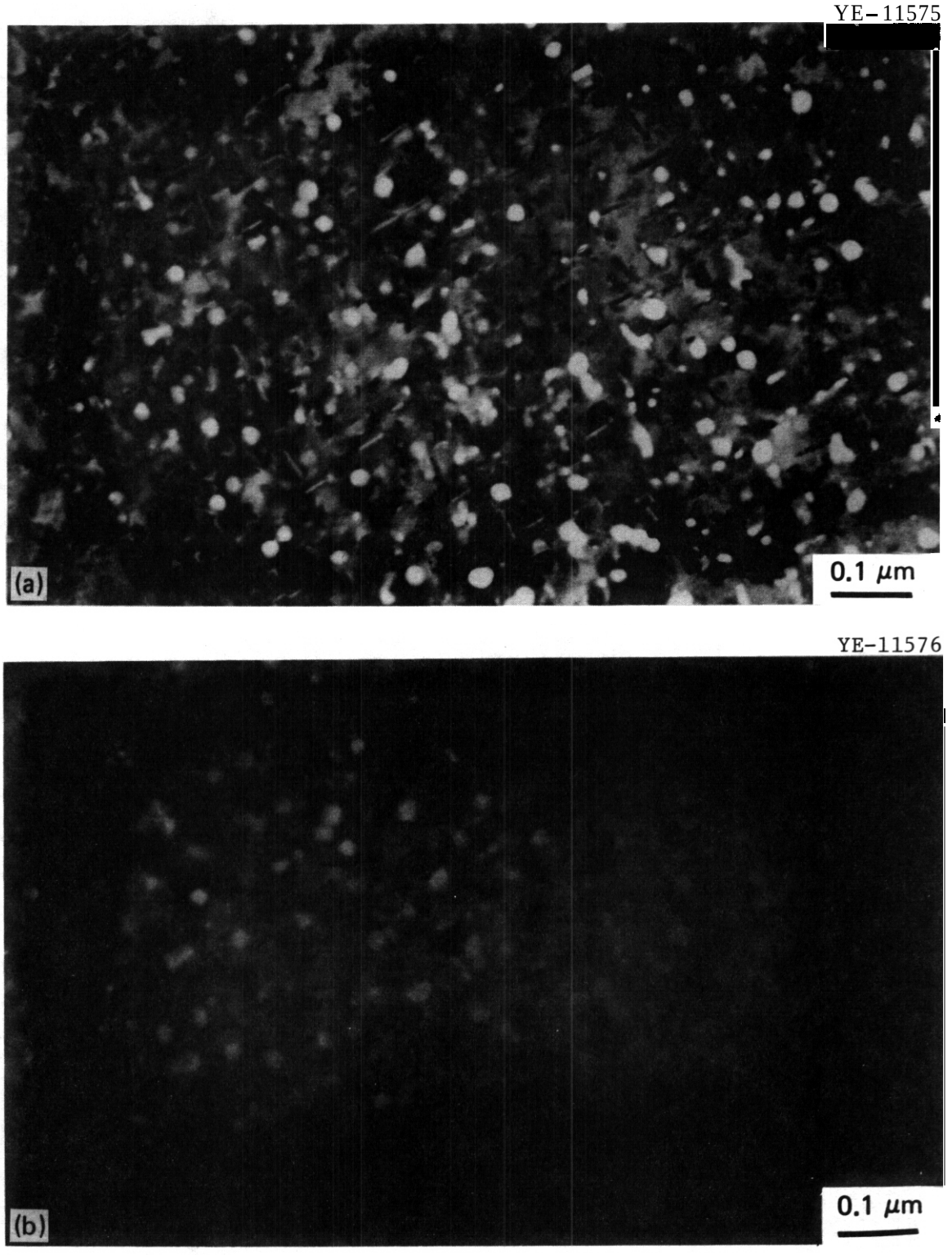

Fig. 4.1.3. Cavities in PE-16 After Irradiation in HFIR at 400°C (4.4 dpa, 370 at. ppm He) Viewed in (a) Bright Field, and (b) Dark Field With a (110) γ' Reflection. This shows that the cavities were coated with γ'.

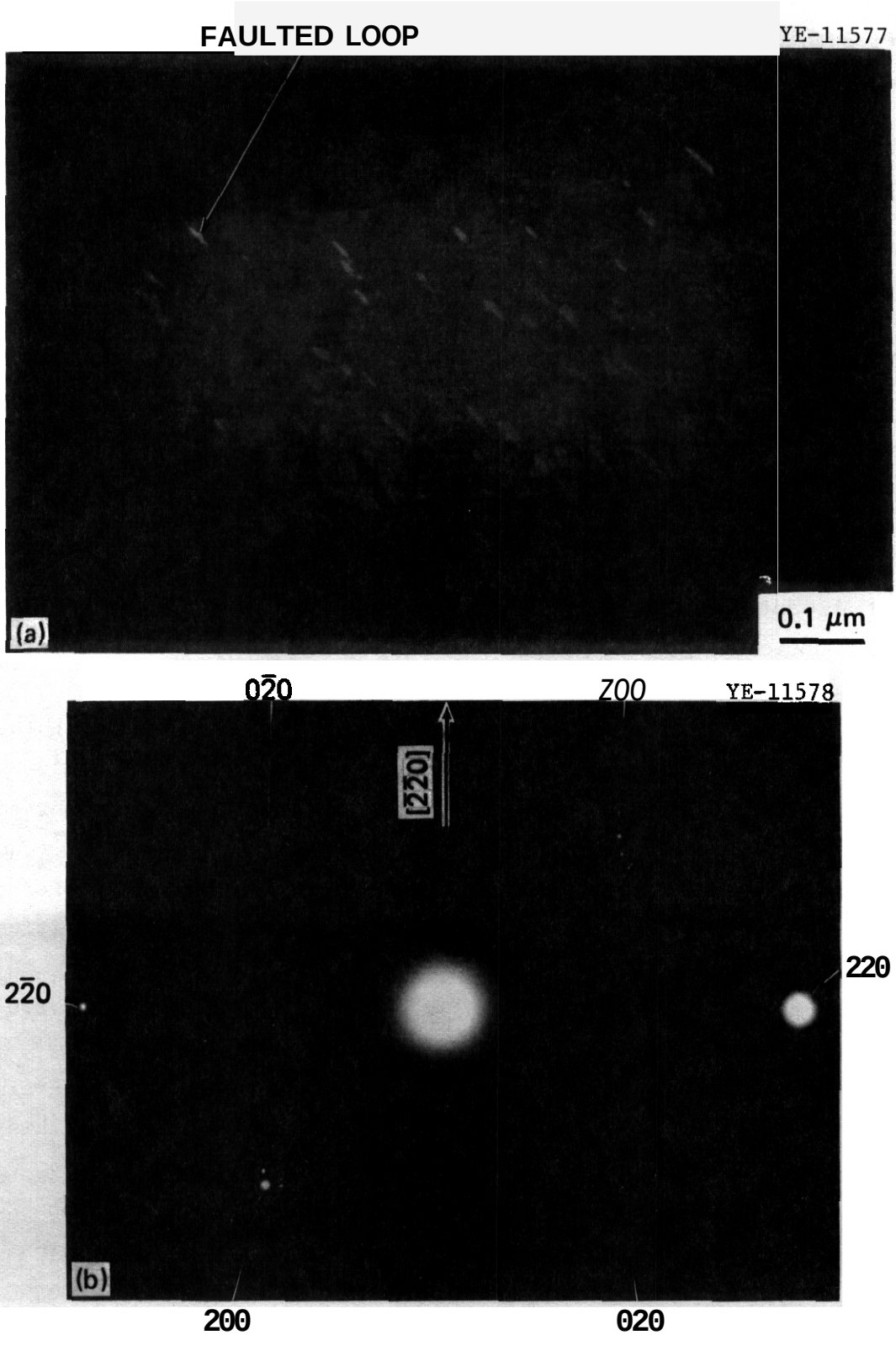

Fig. 4.1.4. Faulted Loops in PE-16 After Irradiation at 400°C (4.4 dpa, 370 at. ppm He). (a) Imaging with a satellite spot near a (111) reflection under weak-beam dark-field conditions shows that loops lie on {111} planes. (b) Selected-area diffraction pattern showing streaking due to faulted loops in [220] directions at matrix reflections.

under such conditions along with the SAD pattern for the area. The streaking at the matrix spots in the [220] directions was due to the faulted loops that had formed on {111} habit planes. We did not observed any γ' particles associated with the faulted loops.

The second specimen examined was irradiated at 650°C to a higher fluence and developed a considerably greater helium content (see Table 4.1.1). The microstructure contained a bimodal cavity distribution shown in the size distribution plots in Fig. 4.1.1 and the micrographs in Fig. 4.1.5. The average diameters for the small and large cavity distributions were 31.3 and 124.0 nm, respectively. Both small and large cavities were coated with γ', as demonstrated by the bright field-dark-field series in Fig. 4.1.5. Large precipitate particles on the grain boundaries are shown in Fig. 4.1.6. The precipitates were identified as $M_{23}C_6$ by SAD. Large irregularly shaped cavities were also found at various points along grain boundaries and especially at triple point junctions. No loops were observed for this irradiation temperature, and virtually all the γ' was located on the cavities.

The observation of cavities coated with γ' is consistent with the observations of Sklad et al.,[1,2] who found γ'-coated voids in PE-16 irradiated in EBR-II. Sklad found γ' on dislocations, and we observed this — but only at the lower irradiation temperature. Sklad also found γ' on large, perfect loops, while the HFIR irradiation at 400°C produced faulted loops without γ' attached. Therefore, while some similarities are seen in microstructural response of PE-16 to EBR-II and HFIR irradiation, many differences are also clearly seen. This is not too surprising since the HFIR irradiation produced much more helium. Significantly, large quantities of $M_{23}C_6$ precipitated out in the grain boundaries at 650°C. This is believed to be the first time that this carbide has been observed in irradiated PE-16. The bimodal cavity distribution at 650°C is also an important observation. It is too early to speculate on the mechanisms causing these changes in PE-16 during irradiation, but upcoming experiments should help shed some light on them.

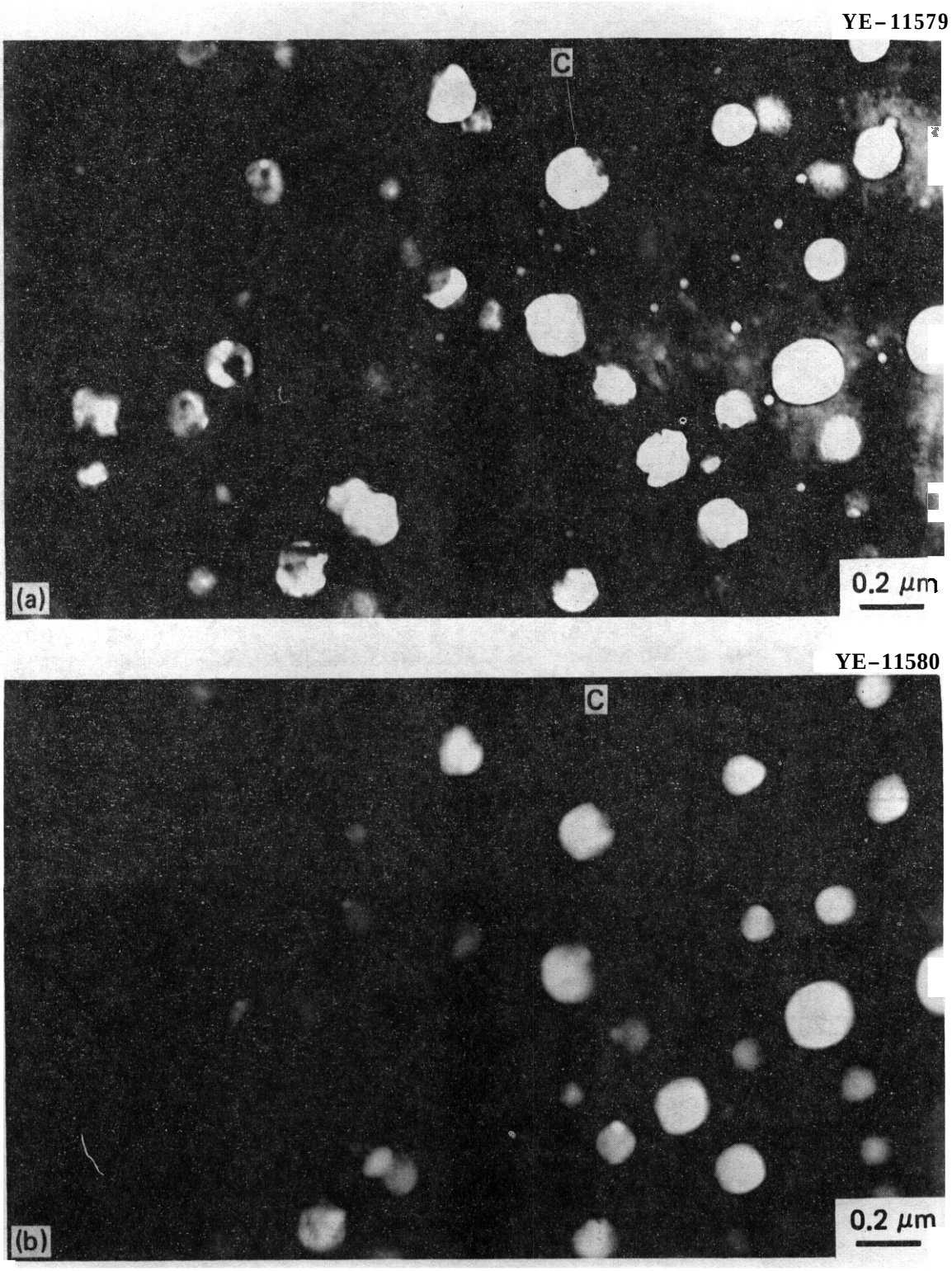

Fig. 4.1.5. Cavities in PE-16 After Irradiation in HFIR at 650°C (8.7 dpa, 1030 at. ppm He). (a) Bright field view. (b) Dark field imaged with a (110) γ' reflection, showing that the cavities were coated with γ'. C = reference point.

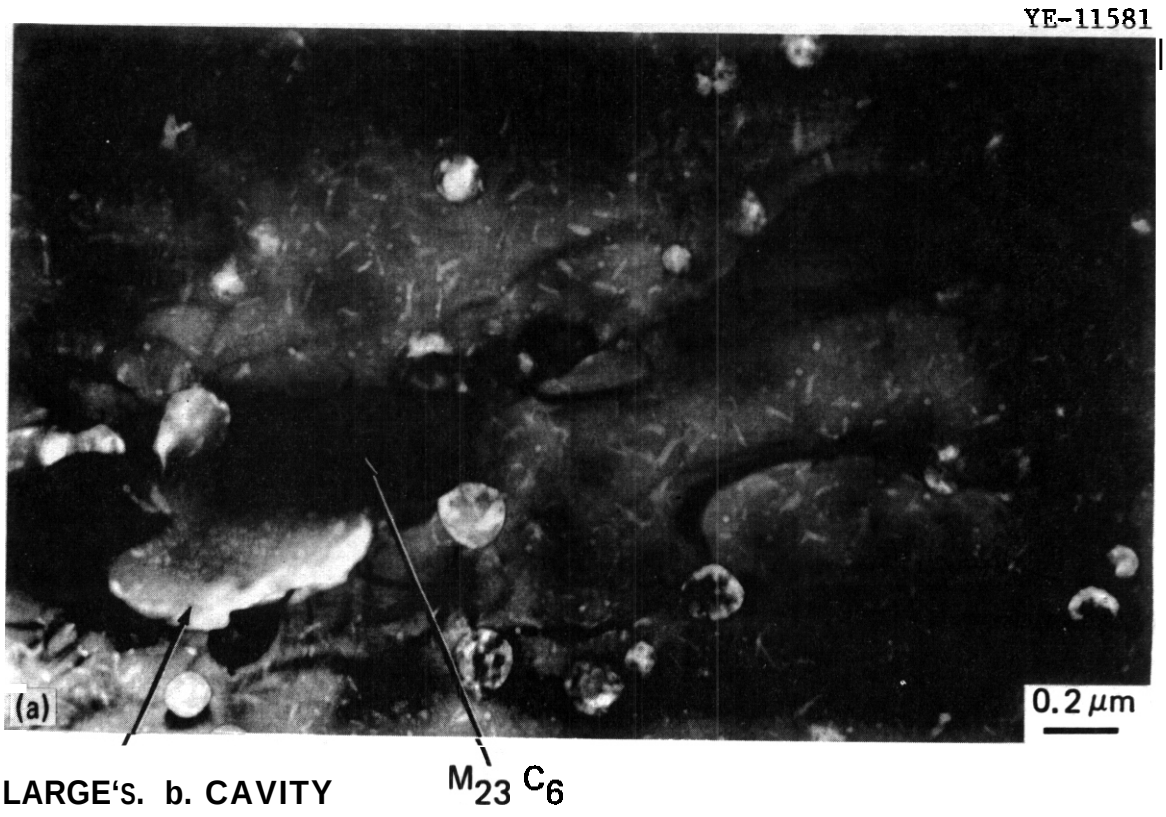

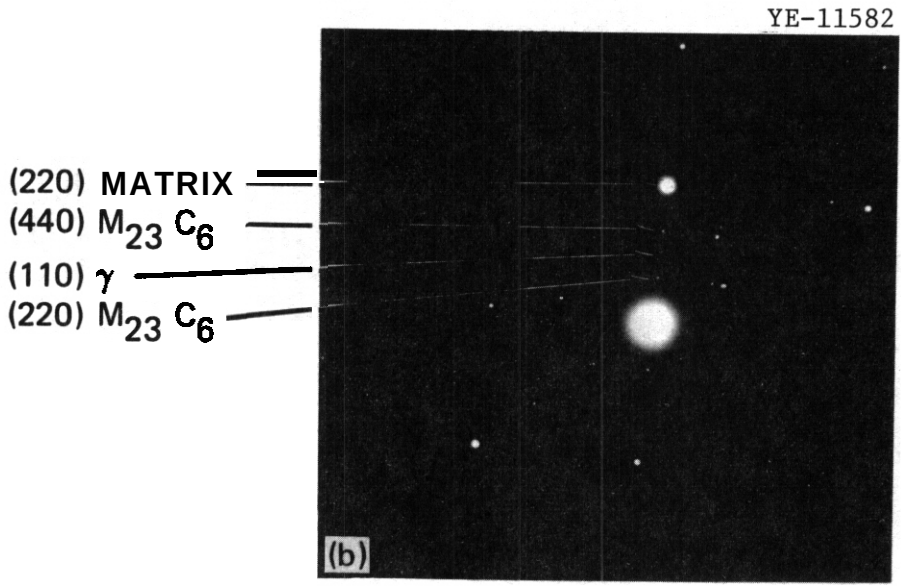

Fig. 4.1.6. Large Irregular Cavity and $M_{23}C_6$ Precipitate in Grain Boundary of PE-16 After Irradiation in HFIR (8.7 dpa, 1030 at. ppm He). Selected area diffraction pattern of area shows matrix, $M_{23}C_6$, and γ' reflections.

The cavity properties measured by transmission electron microscopy lead to a calculated swelling of 0.35% for irradiation at 400°C and 2.59% for irradiation at 650°C. Immersion density measurements on the same samples gave swelling values of 0.32 and 0.51%, respectively. The agreement for the sample irradiated at 400°C is excellent. For the sample irradiated at 650°C, we have not yet been able to resolve the source of the discrepancy. Measurement of the length change produced by the irradiation of the sample indicated only a small amount of swelling in this sample, less than 0.1%. The relative agreement of the density and geometry measurements indicate that the problem is in the quantitative microscopy. More work will be required to sort out this discrepancy.

4.1.5 Conclusions

1. Irradiation of PE-16 in HFIR at 400 and 650°C produced cavities coated with γ' phase.

2. A single cavity size distribution with an average diameter of 16.5 nm was produced at 400°C, while a bimodal distribution with average sizes of 31.3 and 124.0 nm was produced at 650°C.

3. Faulted loops with a {111} habit plane were produced at 400°C, but none were found after irradiation at 650°C.

4. During irradiation at 650°C, $M_{23}C_6$ precipitated out on the grain boundaries of PE-16. The carbide was not observed after irradiation at 400°C.

4.1.6 References

1. P. S. Sklad, R. E. Clausing, and E. E. Bloom, "Effects of Neutron Irradiation on Microstructure and Mechanical Properties of Nimonic PE-16," pp. 139-55 in *Effects of Radiation on Structural Materials, Spec. Tech. Publ.* 611, American Society for Testing and Materials, Philadelphia, 1976.

2. P. S. Sklad and J. Bentley, "Changes in the Distribution and Morphology of γ' Precipitate in Neutron Irradiated PE-16," pp. 602-03 in *34th Ann. Proc. Electron Microscopy Soc. Amer.*, G. W. Bailey, ed., Claitor's Publishing Division, Baton Rouge, LA, 1976.

5. PATH C ALLOY DEVELOPMENT — REACTIVE AND REFRACTORY ALLOYS

Two distinct and separate subgroups fall under the broad classification of path C alloys. These subgroups are conveniently classified as "reactive metal alloys" and "refractory metal alloys." Analyses of the properties required for performance of materials in high-flux regions of fusion reactors and assessments of the known and extrapolated properties have identified titanium alloys of the reactive metal alloys and vanadium and niobium alloys of the refractory metal alloys as having the most promise for fusion reactor applications. For both the reactive and refractory alloys, there is an extreme lack of data that are relevant and necessary for selection of specific alloy types for development (i.e., solid solution, precipitation strengthened, single or multiphase). In the case of titanium alloys, the most critical deficiency is the lack of data on the response of these alloys to high-fluence neutron radiation. For vanadium and niobium alloys, while the effects of radiation on mechanical behavior are not adequately known, perhaps the most alarming deficiency is the near total lack of base-line information on the effects of cyclic (fatigue) loading on mechanical performance. Precisely because of these deficiencies in the data base and overall metallurgical experience, these alloys are still in a "scoping study" phase of their evaluation as candidates for fusion reactor first-wall materials.

The ADIP task group has selected four titanium alloys, three vanadium alloys, and two niobium alloys for the scoping phase of the development program. Titanium alloys are generally classified according to the relative amounts of α (hcp) and β (bcc) phases that they contain. The titanium alloys selected represent the three alloys (types α plus β, α rich, and β rich). Vanadium and niobium alloys are not in commercial use as are the other alloy systems in the program. Selection of the scoping alloys was based primarily on results of previous programs on vanadium cladding development for LMFBRs and high-temperature alloys for space power systems. The three vanadium alloys are V—20% Ti, V—15% Cr—5%Ti, and Vanstar 7. The binary has relatively good fabricability, and appears to be swelling resistant in fast-reactor irradiations but is rather weak. The tern-ary V—15% Cr—5% Ti and precipitation--strengthened

Vanstar 7 alloys are significantly stronger. The Nb–1% Zr binary alloy is included as a reference material, since a significant amount of data exists for this alloy irradiated in fast reactors. The alloy Nb–5% Mo–1% Zr is much stronger than the binary and can be developed for applications near *800°C.*

Near-term activities on path C alloys will focus on obtaining data on the unirradiated mechanical properties, corrosion and compatibility, and the effects of irradiation on physical and mechanical properties. Fission reactor irradiation with and without helium preinjection, high-energy neutron sources, and charged-particle irradiations will be used in the development of techniques to approximate the effects of the fusion reactor neutron spectrum (He/dpa production). The objective is to develop sufficient understanding of the behavior of path C alloy systems (Ti, V, and Nb alloys) to allow selection of path C base research alloys. The effects of composition and microstructure on alloy performance will then be investigated in the base research alloys.

5.1 SELECTION OF TITANIUM ALLOYS FOR PATH C SCOPING STUDIES -

J. W. Davis (McDonnell Douglas Astronautics Company - St. Louis).

5.1.1 ADIP Task

Tasks 1.B.3, 1.B.7, 1.B.11, 1.B.15, 1.C.4, and 1.C.8 collectively to provide basic understanding of fatigue crack propagation (FCP), strain controlled fatigue (SSCF), stress rupture resistance (SR), tensile strength and ductility, swelling, and irradiation creep of Path C alloy.

Task 1.D.1 - To provide a stock pile source of common material to be used in all phases of the Office of Fusion Energy Research Program.

5.1.2 Objective

To select representative titanium alloy systems and heat treatments for the Path C scoping studies.

5.1.3 Summary

Titanium alloys offer potential for use as fusion reactor structure based on their strength, low thermal stresses, and coolant compatibility. However, little or nothing is known about the mechanical property response of titanium alloys *to* radiation damage. To provide more information, titanium alloys were included as part of the Path C Refractory/Reactive metal scoping studies. The objective of these studies is to assess the general response of the Path C materials to the radiation environment.

In selecting the titanium alloys to be included in these studies, a wide variety of compositions and heat treatments were carefully examined before the final 6 alloys/heat treatments were selected. The alloys selected are Ti-6242s (Ti-6Al-2Sn-4Zr-2Mo-0.09Si), Ti-5621s (Ti-5Al-6Sn-2Zr-1Mo-0.25Si), Ti-38-6-44 (Ti-3Al-8V-6Cr-4Mo-4Zr) and Ti-6A1-4V. They are representative of the three major classes of titanium alloys, identified by their primary phase constituent, alpha, beta, and alpha plus beta. Since the metallurgical condition may affect the radiation damage response, three different heat treatments (which produce three distinct microstructures) were selected for the alpha plus beta alloy Ti-6Al-4V.

After the alloys and their compositions were identified, a letter describing the requirements for the titanium alloys, along with the

selected alloys and heat treatments was sent to various laboratories, industries, and universities soliciting their comments. In general, there is concurrence with the alloys selected and no significant disagreements have surfaced. As a result, a titanium inventory has been established containing 0.8–1.2 mm sheet of the four alloys and six heat treatments.

5.1.4 Progress and Status

Titanium alloys are one class of materials that are currently being considered for fusion reactor first wall and blanket structure. However, little is known about the relative resistance of titanium alloys to radiation damage, especially at the fluence and temperature levels of interest. The purpose of these studies is to assess the general response of the Path C metals to the radiation environment, then at a later date, specific alloys and systems will be selected for base research studies.

Over the past 20 years a considerable effort has been devoted to developing titanium alloys for aerospace applications. These studies have revealed that specific phases or microstructure present in titanium can affect properties, such as creep, fatigue and tensile strength. It is for this reason that the microstructural changes brought about by alloying are the basis for the classification of titanium alloys into alpha (HCP), beta (BCC) or alpha–beta groups. In general, the single phase and near single phase alpha alloys (these alloys have a small amount of beta phase present) exhibit good weldability and are not heat treatable. They have medium strength, good notch toughness and creep resistance at elevated temperatures, especially if they contain silicon which enhances the creep strength of this type of alloy. Near alpha or super alpha type of alloys were developed for stability and strength at elevated temperatures (400–500°C). The alloys that consist largely of the beta phase on air-cooling from the solution treating temperature are referred to as beta alloys. Beta or near–beta alloys are not considered as weldable, however, there are some exceptions. They are highly heat treatable and are capable of high strengths, fair creep resistance, and good formability. These alloys are generally not stable for long times above 400°C.

The alpha-beta alloys usually contain 10-50%beta phase at room temperature. They are heat treatable and are usually weldable if the amount of beta phase is kept below ***20%.*** They have good fabrication characteristics, high room temperature strength and moderate elevated temperature strength. The creep strength of these alloys is usually not as high as the near alpha alloys.

Since representative alloys of each of these types have properties or characteristics which offer advantage in the fusion application, without an indication on how the mechanical properties might change during irradiation, it is impossible to make a judgement regarding which alloys or type of alloys, offer the most potential. As a result, the titanium alloys, for the scoping studies should include alloys which are representative of a broad range of promising compositions and microstructures. Towards this end it was determined that alloys representative of the alpha, beta, and alpha plus beta classes of titanium alloys should be included in the scoping studies.

5.1.4.1 Alpha Alloy Selection

At the present time there are a large number of alpha or near alpha alloys that are commercially available or have been developed to the extent that they have a reasonable data base behind them. These alloys range from the simple ternary (Ti-3Al-2.5V) ***to*** the higher strength complex alloys such as Ti-11 (Ti-6Al-2Sn-1.5Zr-1Mo-0.35 Bi-0.1Si). Of these alloys, two appear to offer a good combination of strength and weldability. These alloys are Ti-6242s (Ti-6Al-2Sn-4Zr-2Mo-0.09Si) and Ti-5621s (Ti-5Al-6Sn-2Zr-1Mo-0.25Si). The Ti-6242 alloy was developed for high temperature jet engine service. As such it possesses better elevated temperature strength and stability than previously developed alloys for temperatures up to 550°C. The Ti-5621s alloy was developed, to achieve higher creep strength than Ti-6242 in the temperature range of 450-500°C. This is largely accomplished by the addition of silicon which is a solid solution strengthener. Early evaluation of this alloy indicated good retention of ductility (stability) for air exposures of >1000 hours at 480°C, under a stress to yield 0.1% deformation. Above 500°C the alloy began to lose ductility (reduction in area decrasing from 24 to 10%) for

5000 hours at 0.1% creep strain. There is a question, however, whether or not this loss in ductility was a result of phase instability because of the combined high levels of aluminum, tin, and silicon or promoted by the presence of oxygen from the high temperature oxidation. Since this alloy has good stability up to 500°C and will not be in an oxidizing environment, it was recommended to include it as part of the scoping studies. In addition, the lower concentration of molybdenum (0.5-0.9%) than Ti-6242 (1.75-2.25%) results in a slight reduction in radioactivity and may give insight into the effect of eliminating molybdenum from titanium. Subsequent to the development of Ti-5612S, a similar silicon addition was made to Ti-6242 with the resultant improvement in creep strength. With the improvement in creep strength of Ti-62425 and the larger data base than Ti-5621S, it was also recommended for the scoping studies.

Even though the alpha alloys are not heat treatable, the small amounts of beta phase present in the near or super-alpha alloys allows some response to heat treatment. These heat treatments which are modifications of the annealing cycle help to enhance certain properties such as creep or fracture toughness. Possible heat treatments consist of single (mill), duplex, triplex and beta anneals. Of these 4 anneals the duplex condition is the one most commonly used because it provides a reasonable balance between elevated temperature strength, stability, and fracture toughness. The triplex anneal primarily improves room temperature strength and since most of the fusion reactor designs are not room temperature strength limited there does not appear to be any advantage in using this heat treatment. The beta anneal has been recommended by the people at the Naval Research Laboratory (NRL) in place of the duplex anneal.[1] This recommendation is based on flaw growth data developed by NRL on Ti-6Al-4V which shows that the growth rate is decreased by an order of magnitude below that of a mill anneal.' Subsequent to the NRL meeting a series of discussions were held with titanium research personnel and the titanium suppliers.[3,4] These discussions considered proposed operating environments, property requirements and heat treatment. Based on these discussions both TIMET and RMI independently recommended that the Beta anneal only be evaluated in conjunction with the duplex anneal.

However, if only one heat treatment can be considered, (the case for the scoping studies) they recommended the duplex anneal. Their chief concern over the beta anneal is that it reduces the ductility which may be a problem after irradiation. As an alternate they proposed a modified duplex anneal which consists of solution treating 15–30 degrees below the beta transus followed by a stabilization treatment. It is their opinion that this heat treatment will improve the flaw growth characteristics without degrading the ductility. Based on their recommendation, it was concluded that the modified duplex anneal heat treatment be used for Ti–5621s and Ti–6242s.

5.1.4.2 Beta Alloy Selection

The current beta alloys do not appear to have the stability or the strength for the long term service at temperatures >400°C. However, the beta alloys are of interest because of a concern that the h.c.p. structure of titanium may experience the same anisotropic growth that occurs in irradiated zirconium. Since the beta alloys have a higher percentage of beta phase (bcc) than the alpha alloys, this growth should be minimized if it occurs. Of the available beta alloys, the Beta III (Ti–11.5Mo–6Zr–4.5Sn), Ti–38–6–44 (Ti–3Al–8V–6Cr–4Mo–4Zr), and Ti–15–3 (Ti–15V–3Cr–3Al–3Sn) appear to have good stability. The Ti–38–6–44 alloy appears to have a slightly more beta stabilized composition than the Beta III. Both the Beta III and the Ti–38–6–44 have a fairly well developed data base. The Ti–15–3 is a relatively new alloy and as such does not appear to have as good a data base as either Ti–38–6–44 or Beta III. After reviewing the available information on the beta alloys, and their availability, it was recommended that the Ti–38–6–44 alloy in the solution treated and over–aged condition be used in the scoping studies.

5.1.4.3 Alpha Plus Beta Alloy Selection

Of the available alpha plus beta alloys, Ti–6Al–4V appears to be the best alloy for the scoping studies. This alloy was first developed in 1954 and is representative of an all purpose alloy.

It has been and is still being extensively used in the aerospace industry. It is commercially available in standard mill forms, is weldable and has a large data base. Several grades are currently produced which differ from one another primarily in interstitial and iron content. Because impurities can influence the fracture toughness of titanium alloys, the extra low interstitial grade (ELI) is preferred even though the strength will be lower than the more conventional grades.

Since Ti-6Al-4V is a heat treatable alloy, there are a variety of different heat treatments available, each of which produces a different microstructure and improves a different property. The mill anneal (typically 2 hours at 730°C followed by air or rapid furnace cool) essentially results in moderate strength but good ductility. The low temperature anneal in the alpha plus beta region produces a microstructure consisting of equiaxed alpha and intergranular beta (See Figure 5.1.1a). This heat treatment and the resultant properties are well characterized and covered by various military and aerospace handbooks and specifications.[5,6,7] For higher tensile strengths and improved fracture toughness, specialized annealing treatments have been developed such as the recrystallization anneal, the duplex anneal, and the beta anneal. The recrystallization anneal usually consists of 4 or more hours at 925°C, followed by a furnace cool to 760°C, a rapid cool to 350°C, and air cooling to room temperature. The higher temperature anneal in the alpha plus beta region also produces a microstructure similar to the mill anneal material, equiaxed alpha and intergranular beta (see Figure 5.1.1.b). The duplex anneal consists of 10 minutes at 940°C, followed by air cooling and a stabilization of 4 hours at 675°C, and air-cooling to room temperature. By solution treating the material just below the beta transus and air or rapid cooling, produces a microstructure consisting of primary alpha in a matrix of transformed beta; this latter constituent is referred. to as acicular alpha. The subsequent aging or stabilizing at a lower temperature in the alpha plus beta field stabilizes the microstructure by allowing the super saturated alpha phase to achieve equilibrium through the precipitation of beta (see Figure 5.1.1.c). The beta anneal is accomplished by solution treating'at 1040°C for 30 minutes, followed by air cooling and over-aging at 730°C for 2 hours and air cooling to room

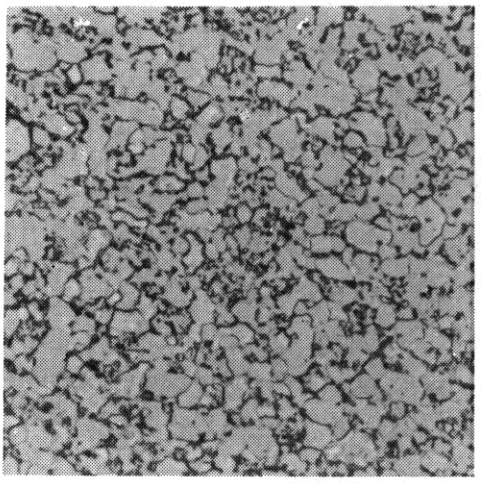

400 X

(a) MILL ANNEAL

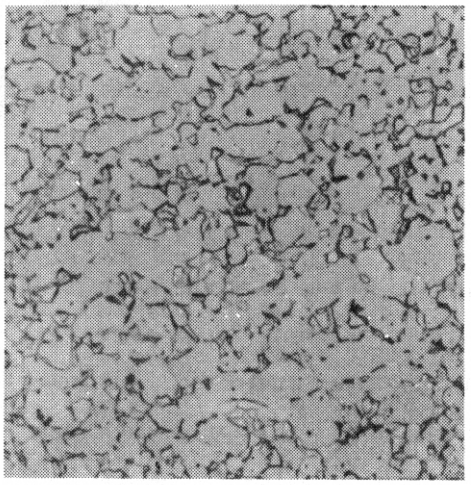

400 X

(b) RECRYSTALLIZATION ANNEAL

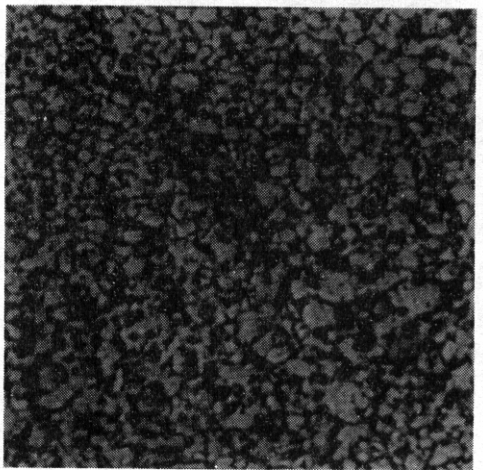

400 X

(c) DUPLEX ANNEAL

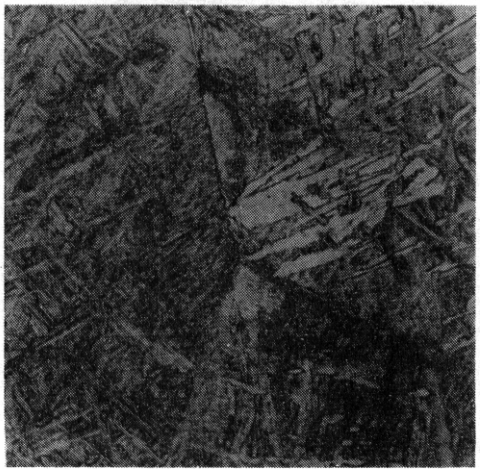

200 X

(d) BETA ANNEAL

13–1437

Figure 5.1.1 Microstructures of Ti–6Al–4V After various Heat Treatments

temperature. Solution treatment above the beta transus eliminates the primary alpha constituent in the microstructure and leaves an acicular alpha (transformed beta) structure, with alpha at the prior beta grain boundaries. On aging, this structure is stabilized through the precipitation of minor amounts of beta (see Figure 5.1.1.d). This structure differs from the duplex annealed structure in that no primary alpha is present. For the highest tensile strength, there is a heat treatment

referred to as solution treat and age (STA), however, this heat treatment tends to lower toughness and ductility and as a result was not considered.

Studies on the life limiting failure modes of typical first walls, revealed that the most likely failure was crack-induced coolant leakage.[8,9,10] Therefore, flaw growth will be an important parameter in selecting titanium alloys and heat treatments. To evaluate the effect of irradiation on the mechanical properties of Ti-6Al-4V (and to gain an understanding of microstructure-irradiation effects relationships) it was recommended that at least two flaw growth resistant heat treatments be included in the scoping studies. The two selected were the beta anneal and the duplex anneal. To serve as a reference the mill anneal was also recommended.

5.1.4.4 Coordination with Titanium Community

Subsequent to the above recommendation of titanium scoping alloys and heat treatments, a letter was sent to the various laboratories, titanium producers, and members of the titanium metallurgy committee of the AIME. In the letter the requirements of the titanium alloys, along with some of the rationale for their selection was described and their response or comments were solicitated. Of the people who responded, no significant disagreements were found with the exception of NRL's comments, part of which were discussed earlier. Their specific comments were to substitute a recrystallization anneal for the mill annealed condition of Ti-6Al-4V and a beta anneal in place of the duplex anneal of Ti-6242s. They recommended that the Ti-5621s alloy be eliminated in favor of Ti-6211 (Ti-6Al-2Cb-1Ta-0.8Mo). Subsequent to that meeting they withdrew the recommendation for Ti-6211 and instead suggested Ti-662 (Ti-6Al-6V-2Sn) as a substitute.[11] The response to the recommended substitution of heat treatments was discussed earlier. With respect to the substitution of 662 for Ti-5621S, the 662 is a heat treatable titanium alloy of the alpha plus beta class. It is similar to the Ti-6Al-4V alloy except that it is not classified as a weldable alloy even though some welds have been successfully made. Since it is not a near alpha alloy and does not have the elevated temperature creep strength of Ti-5621S, its' substitution for Ti-5621S is not advantageous. Since it is not a weldable alloy, it did not appear feasible to substitute it for the other alpha plus beta alloy Ti-6Al-4V.

With respect to the substitution of the recrystallization anneal for the mill anneal, after careful consideration, the mill anneal was selected. The recrystallization anneal primarily increases fracture toughness and two other heat treatments that improve fracture toughness are already included. The second reason is that the properties of specific mill annealed material are well documented and in several design handbooks[6,7] whereas the recrystallization anneal is not.

5.1.4.5 Titanium Inventory

In order to fulfill the requirements of the various experiments, a titanium inventory has been established. This inventory contains all of the recommended scoping alloys and their respective heat treatments. While the majority of the alloys are in the form of 0.8-1.2 mm sheet, heavier gauges are being added such as 2.5 and 5 mm Ti-5621s and 3.2 mm Ti-6242s. In order to accommodate the pressurized tube tests, rod stock has been ordered for all of the alloys with the exception of Ti-6242s which will not be available in time for the planned EBR-I1 irradiation tests.

5.1.5 Conclusions

The recommended titanium alloys for the Path C scoping studies and their respective heat treatments are presented in Table 5.1.1. These recommendations are based on careful consideration of the comments and suggestions of people from the national laboratories, titanium industry, and other experts in the field of titanium.

Table 5.1.1 Recommended Titanium Alloys and Heat Treatments for Scoping Studies

ALLOY DESIGNATION	COMPOSITION % BY WEIGHT	CONDITION
Ti-6-4	Ti-6Al-4V	MILLANNEAL DUPLEX ANNEAL BETA ANNEAL
Ti-62425	Ti-6Al-2Sn-4Zr-2Mo-0.09Si	DUPLEX ANNEAL
Ti-56215	Ti-5Al-6Sn-2Zr-1Mo-0.25Si	DUPLEX ANNEAL
Ti-38644	Ti-3Al-8V-6Cr-2Mo-4Zr	SOLUTION TREAT AND AGE

5.1.6 References

1. R. W. Powell, Minutes of Meeting on the DOE/OFE-NRL Workshop on Titanium Alloy Research and Technology, Germantown, Maryland, December 15, 1977.
2. G. R. Yoder, L. A. Cooley, and T. W. Crooker, A Micromechanistic Interpretation of Cyclic Crack-Growth Behavior in a Beta-Annealed Ti-6Al-4V Alloy, Naval Research Laboratory, NRL Report 8048, 1976.
3. Personal Communication, P. A. Russo, RMI Titanium, to J. W. Davis, McDonnell Douglas Astronautics Company - St. Louis, February 17, 1978.
4. Personal Communication, H. W. Rosenberg, Titanium Metals Corporation of America, to J. W. Davis, McDonnell Douglas Astronautics Company - St. Louis, February 28, 1978.
5. J. Wolf, Editor, Aerospace Structural Metals Handbook, Mechanical Properties Data Center, AFML-TR-68-115, Volume 4 (Revised: December, 1977).
6. R. A. Wood, and R. J. Favor, Titanium Alloys Handbook, Metals and Ceramic Information Center, MCIC-HB-02, 1972.
7. Department of Defense, Military Standardization Handbook, Metallic Materials and Elements for Aerospace Vehicle Structure, MIL-HDBK-5B, Volume 2 (Revised 1975).
8. B. A. Cramer, Structural Analysis for High Temperature Performance, ANS Transactions, Volume 26: p.207 (June 1977).
9. M. Abdou, et al., The Establishment of Alloy Development Goals Important to the Commercialization of Tokamak-Based Fusion Reactors, Argonne National Laboratory and McDonnell Douglas Astronautics Company - St. Louis, ANL/FPP/TM-99, 1977.
10. G. M. Fuller, Fusion Reactor First Wall/Blanket Systems Analysis Tokamak Concepts, Electric Power Research Institute, EPRI ER-582, 1977.
11. Personal Communication, L. R. Hettche, Naval Research Laboratory, to J. W. Davis, McDonnell-Douglas Astronautics Company - St. Louis, February 2, 1978.

5.2 TECHNICAL ASSESSMENT OF VANADIUM-BASE ALLOYS FOR FUSION REACTOR APPLICATIONS — R. E. Gold, D. L. Harrod, R. L. Ammon, R. W. Buckman, Jr., and R. C. Svedberg (Westinghouse Electric Corporation)

5.2.1 ADIP Tasks

I.A.l. Define material property requirements (Path C)

I.A.2. Define test matrices and procedures (Path C)

I.A.3. Chemical/metallurgical compatibility analyses (Path C)

5.2.2 Objective

The available literature and technical data on vanadium and vanadium-base alloys were compiled, reviewed and summarized for the purpose of establishing an informed, current basis of understanding of the mechanical, chemical and irradiation response characteristics of vanadium-base alloys in the context of their potential application to fusion reactor development. Specific objectives included identification of critical vanadium alloy data needs for life assessment models used in parametric systems and design studies, and the development of the rationale and criteria appropriate to the selection of alloy compositional/metallurgical variables, the evaluation of alloy performance, and recommendations for laboratory/reactor test requirements and controls.

5.2.3 Summary

A large data base has been compiled on vanadium-base alloys but the data base on any one alloy is quite limited. Great flexibility exists in the composition-microstructure-property relationship and this facilitates alloy optimization to meet diverse property requirements. Tensile properties and creep properties of existing alloys exceed likely requirements. Fatigue strength, including crack growth rate, is probably the most critical material property but no data exists for vanadium alloys. Swelling and irradiated ductility behavior look promising but require further evaluation. Vanadium alloy-liquid metal compatibility, particularly interstitial mass transfer, may be equally as critical as fatigue behavior; viability cannot be established with the existing data base.

Fabricability must be given early consideration in alloy selection to guard against potentially serious problems in subsequent scale-up and production.

5.2.4 Progress and Status

Fusion reactor systems/design studies have suggested promising performance from the use of vanadium-base alloys as the structural material for the first-wall/blanket assembly. More recent first-wall material life assessments of the type performed at MDAC-E and ANL give further support to the potential superiority of vanadium-base alloys over stainless steels. In fact, these assessments show that stainless steel has severe life limitations. The stainless steel results are based on a rather large data base covering all likely modes of failure. The potential superiority of vanadium-base alloys, by contrast, rests upon a very limited data base covering only a few modes of failure. Moreover, the failure mode found to be life limiting in stainless steel, namely fatigue crack growth, was not evaluated in the vanadium alloy assessments because of a complete lack of data. Yet, this mode of failure might also be life limiting in vanadium-base alloys. Additionally, the use of vanadium-base alloys requires careful consideration of various factors which are not normally accounted for in conventional laboratory tests; factors such as liquid metal corrosion, gas-metal interactions and fabricability, for example.

In order to improve the vanadium alloy data base a literature search was made which resulted in a substantially broader data base than previously existed in a single compilation. This new data base, in conjunction with the existing life assessment analytical methodology, provides a reasonably sure identification of the current critical data needs.

The final report describing this work was presented in two volumes. Volume 1 contains a summary of the literature review, an assessment of information and data needs, and recommendations for future research and development efforts. Volume 2 contains the results of the literature review which covers mechanical properties of unirradiated vanadium and

vanadium-base alloys, irradiation effects, liquid metal corrosion/compatibility, gas-metal reactions and fabricability. Only a synopsis of the results are given here.

5.2.4.1 Radiation Effects

Radiation effects in vanadium and vanadium-base alloys can be separated into the following categories:

- Radiation anneal hardening (RAH)
- Void swelling, precipitation, and other microstructural features
- Mechanical property characterizations
- Ion irradiation-simulations.

Radiation anneal hardening (RAH) is a phenomenon unique to the bcc metals and certsin of their alloys, and just as the name implies, describes an additional hardening or strengthening which occurs due to post-irradiation annealing. It is a low fluence phenomenon which saturates at $\sim 10^{20}$ n/cm^2. Maximum strengthening occurs after annealing at ~160°-200°C where strengthening increments of up to 30 ksi have been observed in impure vanadium.

The mechanism for RAH appears to be the migration and subsequent trapping of interstitial impurity elements at radiation-produced defect sites. Hence, alloying elements which affect the level of interstitial impurity in solution will also affect RAH. The only study to date on a vanadium alloy (a V-Ti binary) revealed no RAH. Hence, this factor and the saturation at low fluence suggest RAH phenomena are of little technological significance to high temperature reactor design.

Void formation and void-related swelling in unalloyed vanadium follows the same general trends as other pure metals, with void concentrations and sizes dependent on both dose and irradiation temperature. For fluences up to $\sim 10^{22}$ n/cm^2 (E_n>0.1 MeV), peak swelling is about 2% and occurs for irradiations at 550°-600°C. Binary alloys containing more than about 3% Ti are virtually completely resistant to swelling. Ternary V-Ti-Cr alloys, VANSTAR-7 (V-Cr-Fe-Zr-C), VANSTAR-9 (V-Fe-Nb-Zr-C), and V-Cr binary alloys are also quite resistant to swelling for irradiation temperatures up to 600°C. The maximum neutron induced void

swelling yet observed in these alloys is only ∿1% (for V-10Cr irradiated at 700°-800°C).

Void swelling results from energetic ion irradiation experiments are generally consistent with those of neutron irradiations. Peak swelling of up to *3%* in unalloyed vanadium occurs at irradiation temperatures of 650°-750°C but this swelling is virtually suppressed by Ti additions.

Low temperature (50°-100°C) neutron irradiation of vanadium-base alloys produces significant radiation hardening with an associated decrease in ductility. Elevated temperature tensile tests indicate recovery of the irradiation damage begins at a temperature of about 400°C and is complete at 650°-750°C. Irradiation at elevated temperatures yields somewhat different behavior. In V-Ti and V-Ti-Cr alloys no hardening was observed in subsequent room temperature tensile tests, whereas marked hardening was observed in VANSTAR-7. In all alloys, hardening is observed in tests conducted at elevated temperatures near that of the irradiation. Little change in ductility is associated with this elevated temperature hardening. The temperature for complete recovery following elevated temperature irradiation is much higher than the recovery temperature of 650°-750°C observed for low temperature irradiations.

5.2.4.2 Unirradiated Mechanical Properties

The tensile properties of vanadium, including interstitial effects, are quite well defined. Though not extensive, sufficient creep data exists to characterize the general behavior of vanadium. Fatigue data is extremely limited; only one study at room temperature has been conducted. Elastic properties and diffusion data (self and interstitial) are satisfactorily defined. In order to reinforce the data base in support of alloy development efforts, there is need only for, (1) additional fatigue testing at elevated temperatures, and (2) further evaluation of interstitial and environmental effects on high temperature creep and fatigue.

The spectrum of vanadium-base alloys has been surveyed experimentally and composition and mechanical property behavior trends established for tensile and creep properties. No fatigue data has been reported for any vanadium-base alloy. The solutes Cr, Ti, Mo, Fe, Ni, Nb, W and Ta are all potent solid solution hardeners. Their relative strengthening effect is somewhat uncertain but perhaps increases in the order listed (Cr least, Ta greatest). Precipitation or dispersion hardening effects are not well defined, nor have they been studied in any detail. Cold work or thermal/mechanical processing can produce extremely high strength levels in short time tests at temperatures below the recrystallization temperature.

The range of tensile and creep properties attainable is very large. Even for nominally solid solution alloys the existing range of properties is too large to be accounted for in terms of kind and amount of substitutional solute. Precipitation, substitutional-interstitial solute interactions and other microstructural features have significant effects but these effects are not yet sufficiently well understood to be controlled and utilized in large scale commercial alloys. Titanium, as an alloy addition, has dominated the development of vanadium-base alloys. The so-called Ti weakening effect in creep is now well known; the mechanism of this effect is important to the future development of vanadium-base alloys.

The great flexibility in the composition-microstructure-mechanical property relationship in vanadium-base alloys offers considerable potential for alloy optimization for radiation response, liquid metal corrosion, gas-metal reactions and fabricability.

5.2.4.3 Corrosion and Compatibility

Conceptual fusion reactor designs to date have employed both liquid alkali metals and high pressure helium as the coolant. Of the liquid alkali metals, lithium offers the dual advantage of being an excellent neutronic breeder of tritium as well as an excellent heat transfer fluid. The use of a single working fluid to achieve both the cooling and breeding functions of the blanket'has obvious advantages.

In addition to lithium, the alkali liquid metal sodium has also been suggested for the blanket coolant. The major advantages of sodium over lithium are related to its slightly lower corrosive properties, although most of this advantage applies more to the austenitic stainless steels or nickel-base alloys than to the refractory metals.

High pressure helium has also been suggested as a blanket coolant. While this gas is nominally inert, trace concentrations of active impurities, which are always present and essentially impossible to monitor and control, will react unfavorably with vanadium alloys at the temperatures of interest (to 650°C). It is generally recognized that blanket/first wall designs of systems employing high pressure helium will not be designed with refractory metal alloys. Hence, no review or discussion of these compatibility concerns was conducted.

Little experimental data concerning the compatibility of vanadium alloys with lithium have been reported. The most profound effects on the corrosion behavior of vanadium and vanadium alloys that have been revealed experimentally are attributed to interstitial-solute interactions. These results have come primarily from experiments which utilized small capsules with tests conducted for relatively short times; <1000 hours. Only one forced convection loop experiment has been reported. Many questions regarding the effects of interstitial impurities in a vanadium alloy/lithium system operating for an extended time, on the order of several years, at a peak temperature of 650°C, remain to be answered.

Consideration of the equilibrium distribution coefficients for oxygen, carbon, and nitrogen in vanadium/lithium systems indicate oxygen transport will be from vanadium to lithium whereas carbon and nitrogen will proceed in the opposite direction. This implies that oxygen-enhanced corrosion will most likely not occur in these systems. Rather, a more pertinent concern is the question of the change in mechanical properties which will result due to the loss of oxygen from the alloys. The implications of carbon and/or nitrogen pickup by the alloy are very important because they could lead to embrittlement.

The substitutional solutes such as Ti, Nb, Mo, and Cr do not alter the direction of interstitial mass transfer in Li systems, but may alter

the rate of transfer, the interstitial solute distribution (solid solution or precipitate), and features of grain boundary penetration, formation of surface layers of interstitial compounds, and spalling.

Vanadium and vanadium alloys behave differently in sodium than in lithium at elevated temperatures. The most important factor influencing this difference is the fact that oxygen is absorbed from sodium, while it is lost to lithium. At 650°C, the partitioning of oxygen is *so* pronounced in the direction of vanadium that a 1 ppm oxygen level in liquid sodium leads to an equilibrium oxygen concentration in vanadium of about 5000 ppm. Maintaining the oxygen concentration in sodium at less than 1 ppm is not trivial, even on a laboratory scale. For a reactor-size coolant, heat-exchange system, the difficulties are enormous.[2]

The transport of nitrogen and carbon has not been as thoroughly investigated as oxygen. However, these elements can harden and embrittle vanadium to an extent comparable with oxygen and therefore must be carefully controlled as well. Carbon accumulations may be particularly crucial in view of the much lower solubility of this element in vanadium relative to oxygen and nitrogen.

To an extent, alloying additions can modify the compatibility of vanadium with sodium. For example, titanium, zirconium, and aluminum additions to vanadium have been shown to increase the rate and level of oxygen picked up by vanadium. In addition, these elements can produce a subsurface hardened zone which can drastically affect mechanical properties, particularly the ductility. The levels of these elements which can be tolerated has not been determined. Elements such as Cr, Mo, Fe, Nb, and Ta appear to lower the apparent solubility of oxygen in vanadium and should therefore enhance the performance of vanadium in sodium systems.

A dominant element affecting the overall compatibility of structural alloys within liquid metal systems is the choice of materials for the balance of the coolant-heat exchange subsystem. The selection of materials and components, including the hot or cold trapping methods and other features of the heat exchange subsystem, will ultimately control

the level and identity of interstitial impurities present in the recirculating liquid metal. Therefore, even if substantial progress can be realized in modifications of the primary structural alloy, the ultimate success of these efforts will require attention to the system as a whole.

5.2.4.4 Data Needs and Recommendations

The only material property data required to establish stress/temperature loading conditions for the design of fusion reactor structural components are thermal conductivity, thermal expansivity, elastic constants and yield strength. Yield strength is needed only to set an upper limit on allowable thermal stresses. In the designs studied to date, the thermal stresses are much less than the yield strength of many candidate vanadium alloys; hence, yield strength poses no limitation. On the contrary, the more important problem is to define the maximum yield strength that is needed so that alloy selection can be based on optimization of other properties.

For structural material/wall-life analyses, specific mechanical property data are necessary, i.e. fatigue, creep, etc. Numerous vanadium-base alloys have creep strength in excess of what will likely be required. Here too, the problem is to determine the maximum creep strength needed so that still other properties can be optimized.

Irradiation effects on mechanical properties constitute one of the critical data needs.. All of the existing data base suggests that swelling and irradiated ductility problems will be manageable. The very limited data on post-irradiation thermal creep behavior is also promising.

No fatigue data exists for vanadium-base alloys, yet this will likely be the life-limiting property. Fatigue life and fatigue crack growth rate data constitute the current most critical property need; both unirradiated and irradiated data are needed.

Next to fatigue, the most critical need is for additional information and data on the compatibility of vanadium-base alloys with Li and Na liquid metals. Interstitial mass transfer is particularly important. A major difierence between Li and Na is that Li getters orygen from vanadium while vanadium removes oxygen from Na. Of the two, it is better

for the vanadium alloy to lose oxygen than to gain it. Yence, Li might be preferred on this simple argument. Vanadium getters carbon and nitrogen from both Li and Na and possible embrittlement due to excessive pickup of these interstitials poses serious concern. Alloying elements affect the kinetics of interstitial mass transfer but do not change the direction of transfer.

Gas-metal environmental interactions may be important in actual fusion reactor applications. They are certainly important in laboratory/reactor property evaluations and in alloy consolidation and fabrication, and extreme care must be exercised in their control.

The very high strength levels attainable in some vanadium-base alloys could lead to serious fabrication problems. It is essential in alloy selection that early emphasis be given to fabricability. A low bend-ductile-brittle-transition-temperature accompanied by little or no change due to gas-tungsten-arc welding is suggested as a suitable criterion of good fabricability.

5.2.5 Conclusions

The viability of vanadium-base alloys for fusion reactor first-wall/blanket assembly structural components cannot yet be proved if consideration is given to all possible failure modes. Conversely, no part of the existing data base shows vanadium alloys to be deficient for these applications. Vanadium-base alloys, therefore, still hold forth great promise. Tensile property and creep property requirements are easily met. Fatigue behavior, irradiation effects and liquid metal compatibility represent the most critical areas of data needs. No present need exists for a conventional alloy development program wherein broad ranges of new compositions are explored for mechanical property behavior trends. Rather, the present need is for more detailed evaluations of select existing alloys in the critical property areas.

5.3 16 MeV PROTON CREEP IN A Ti-6AL/4V SPECIMEN - E. K. Opperman, (Hanford Engineering Development Laboratory)

5.3.1 ADIP Task

Task I.C.8, Irradiation Creep of Reactive and Refractory Alloys (Path C).

5.3.2 Objective

The overall objective of this study was to develop and utilize a proton accelerator-based creep system for fusion materials research. The objectives of the work reported here are to determine the irradiation creep behavior of a titanium alloy (Ti-6AL/4V) and to compare these results with those from similarly irradiated AISI 20% CW 316 SS specimens.

5.3.3 Summary

A Ti-6AL/4V torsion creep specimen was irradiated with 16 MeV protons utilizing the isocronous cyclotron located at the Crocker Nuclear Laboratory in Davis, California. The wire specimen was stressed to 138 MPa (shear) throughout preirradiation thermal creep testing and the first 50 hours of irradiation creep testing. Following the first 50 hours of irradiation, the stress was reduced to zero for the subsequent 4 hours of irradiation. The test was conducted in a helium atmosphere at a nominal irradiation temperature of 325°C. The specimen received a total dose of 0.35 dpa (of which 0.31 was in a stressed condition) at a rate of approximately 2.4×10^{-6} dpa/sec.

Results of this single test indicate the presence of a primary irradiation creep regime followed by a "steady-state" regime in which the creep rate slowly decreased with dose. Below ~0.1 dpa the irradiation creep rate in Ti-6AL/4V was found to be 2-5 times that of similarly irradiated stainless steel specimens. By the end of the test (~0.31 dpa) the irradiation creep rate in Ti-6AL/4V was within a factor of two of that found in 20% CW Type 316 stainless steel.

Prior to the final 4 hours of irradiation testing the stress was reduced to zero. The results indicate a substantial amount of negative strain or reversal. The magnitude of this negative strain decreased with

dose and decreased significantly when the proton beam was turned off. A number of mechanisms are considered as possible explanations for the zero-stress strain recovery,

5.3.4 Progress and Status

An understanding of mechanical properties under irradiation conditions is fundamental to the development of materials for reactor structural components. The plastic deformation or creep of materials irradiated under stress is one such mechanical property receiving considerable attention in in-reactor studies aimed at fast breeder reactor materials development.

The development of fusion reactor structural materials, however, must presently rely on data from spectra considerably different from those predicted in fusion reactors. This report describes the results from an irradiation creep measurement of a Ti-6AL/4V alloy considered[1] a potential first wall material. The material was irradiated with 16 MeV protons. This particle produces the high energy portion of its primary knock-on spectra similar[2] to that produced by 14 MeV neutrons.

5.3.4.1 Experimental

Details of the apparatus development and experimental techniques can be found in Reference 3 and therefore only a brief summary of experimental features will be given here. The experiment consisted of irradiating a single Ti-6AL/4V specimen with a beam of 16 MeV protons to a maximum dose of 0.35 doa. The wire soecimen was loaded in torsion by the electrically controlled load cell shown in Figure 1. A jet of helium gas directed normal to the specimen removed the excess heat deposited into the specimen by the proton beam and provided temperature control. Specimen temperature was estimated using a 0.127 mm diameter thermocouple centered within the proton beam and positioned 1.0 mm from the irradiated specimen. The incident proton beam was collimated by four charge-sensitive tantalum tabs (Figure 1), before passing through the specimen and into the Faraday cup. Accurate collimation is necessary in order to determine beam location and to define the irradiated section of the specimen.

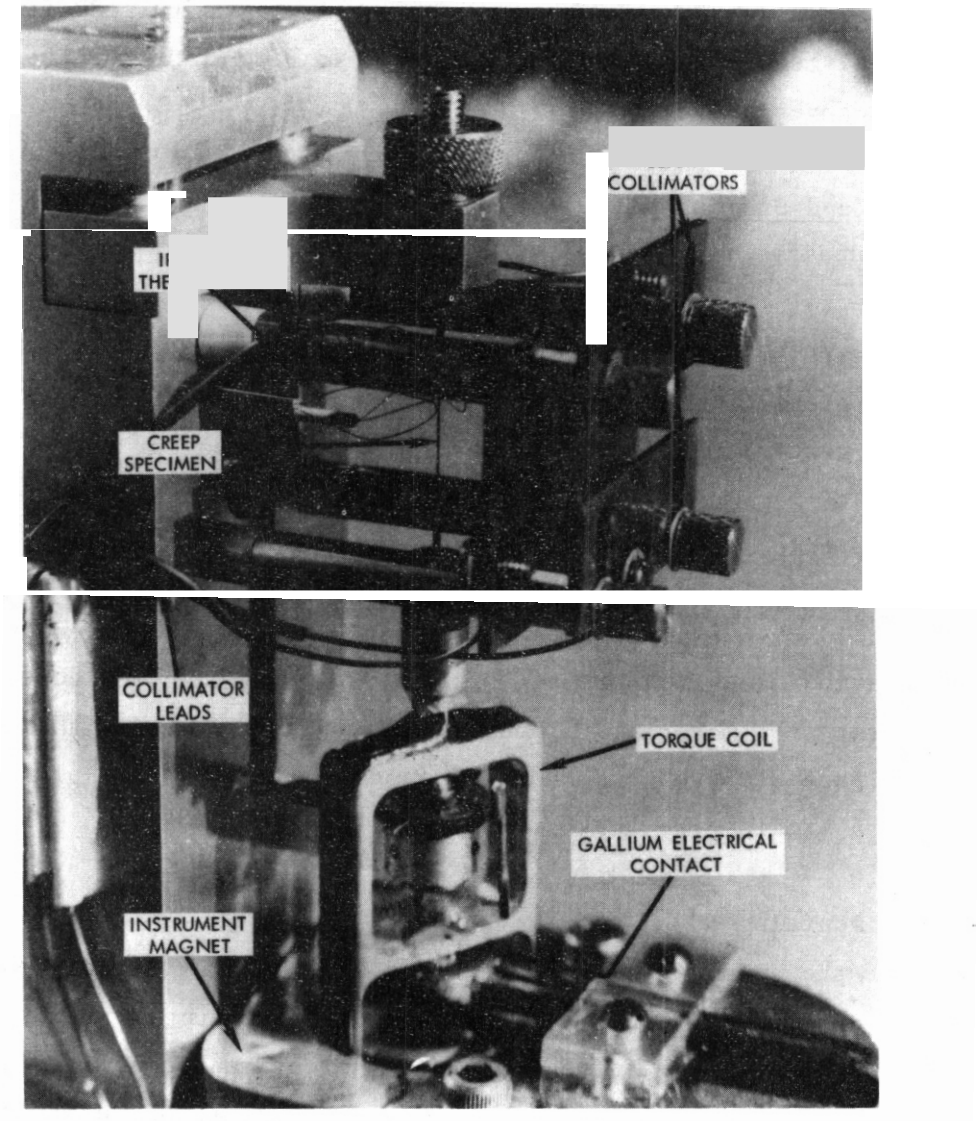

Fig. 1. Torsion Creep Loading System with Proton Beam Collimators.

The proton beam intensity was determined by a combination of two measurements. The first is the measure of the total charge passing through collimation tabs of a known area. The second measure of flux is determined by relating the output of the irradiated thermocouple (Figure 2) to the local beam intensity. The derived proton flux is shown in Figure 3.

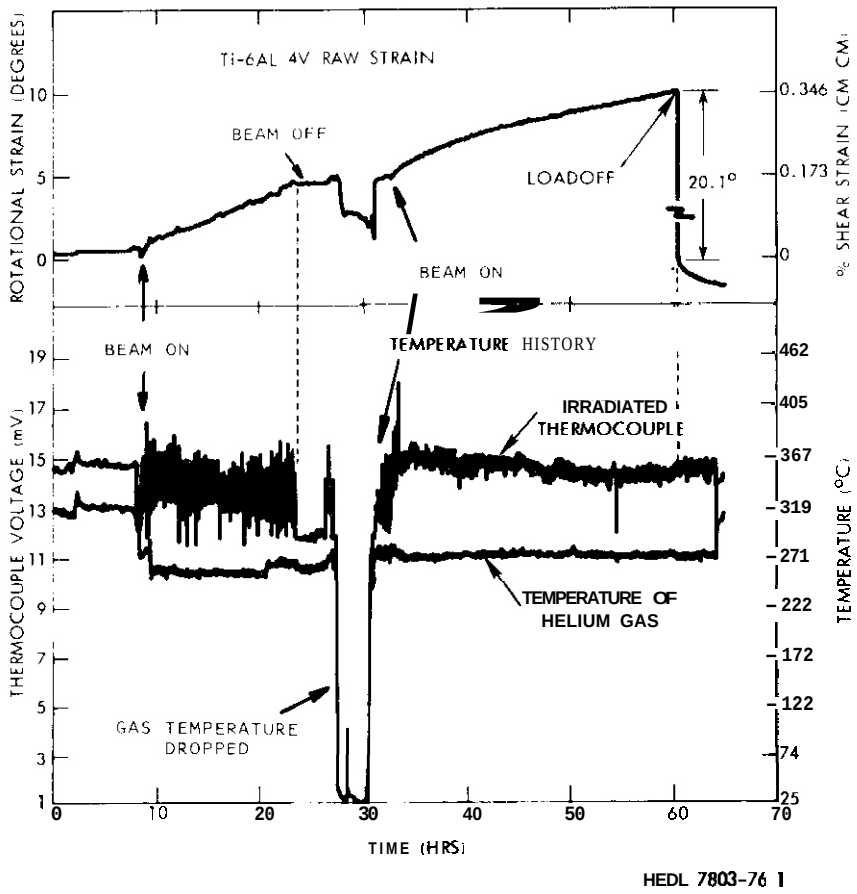

Fig, 2. Strain–time history of the Ti-6AL/4V irradiation along with the temperature history of the irradiated thermocouple and helium gas.

The creep specimen was fabricated from a 0.76 mm diameter wire by chemical milling so that the length of the axial region over which rotation occurs corresponds to the height of the collimated proton beam as illustrated in Figure *4*. The specimen diameter profile was measured by a commercially available laser diameter measuring system. Following the chemical milling procedure, the specimen was solution treated and aged. Solution treating was carried out at 927°C for approximately one-half hour in an inert atmosphere. This was followed by a quick cool with air to room temperature. The specimen was then aged at 525°C for *4* hours in a vacuum. This heat treatment results in an even distribution of the Beta phase (bcc) within the Alpha (hcp) matrix. The grain size was finer than ASTM 1/12.

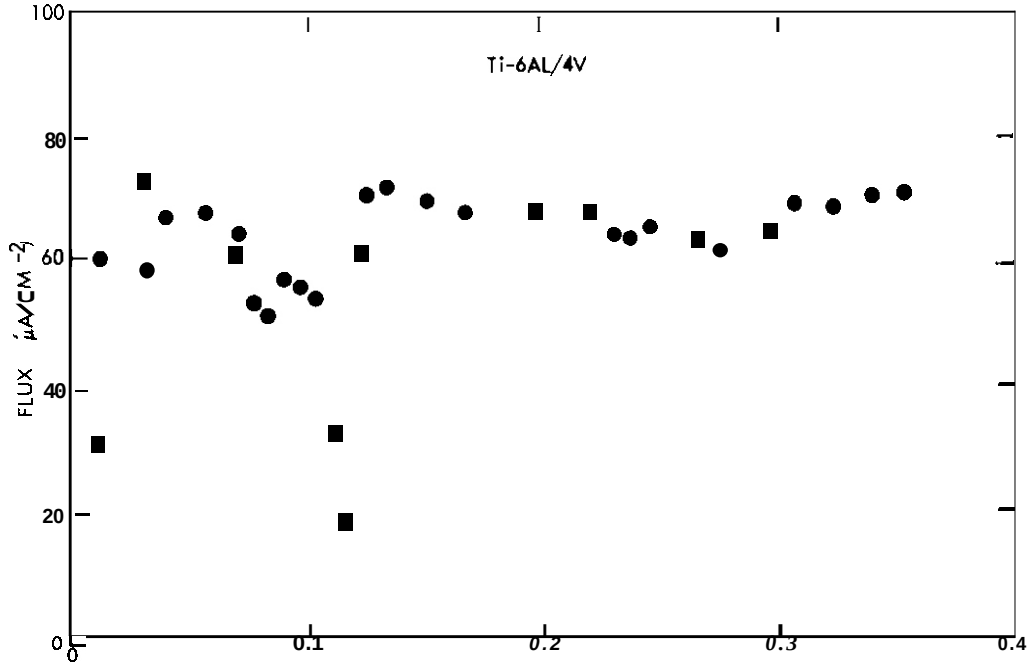

Fig. 3. 16 MeV Proton Flux Versus Dose.

Displacement rates were calculated[4] using a code developed by Logan[2] at the Lawrence Livermore Laboratory. The code calculates the damage energy when given the average proton energy within the specimen, which was 15 MeV in this case. To simplify calculations it was assumed the specimen was pure titanium. For the above conditions the calculated damage energy was 435 x 10^{-21} eV-cm^2, which corresponds to a displacement rate of 3.4 x 10^{-7} dpa/sec for a beam intensity of 10 μA/cm^2.

5.3.4.2 Results

The principle result of this test is the similarity of creep rates between solution treated and aged Ti-6AL/4V and 20% CW 316 SS. At 0.3 dpa the creep rate of the titanium specimen was within a factor of two of the averaged strain rates of five similarly irradiated stainless steel torsion specimens as shown in Figure 5. The strain rate data from stainless steel was obtained at temperatures from 240°C to 400°C and was normalized to a stress of 138 MPa and a flux of 50 μA/cm^2. Strain rate

linearity in both **flux** and stress were assumed. Initial transient strain rates were 2–5 times higher in titanium than in stainless steel, however, the strain rate in titanium decreased more rapidly than that of stainless steel with increasing dose. This resulted in strain rates of similar magnitude by the end of the test (Figure 5).

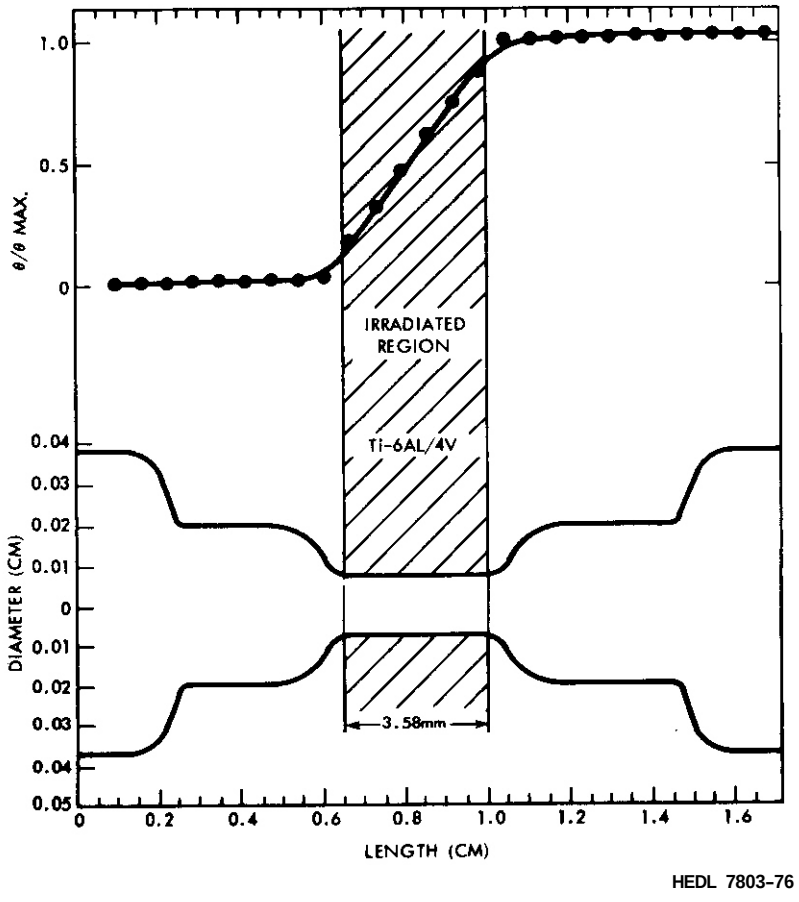

Fig. *4*. The specimen diameter profile showing the region where maximum rotation occurs and the irradiated region **of** the specimen.

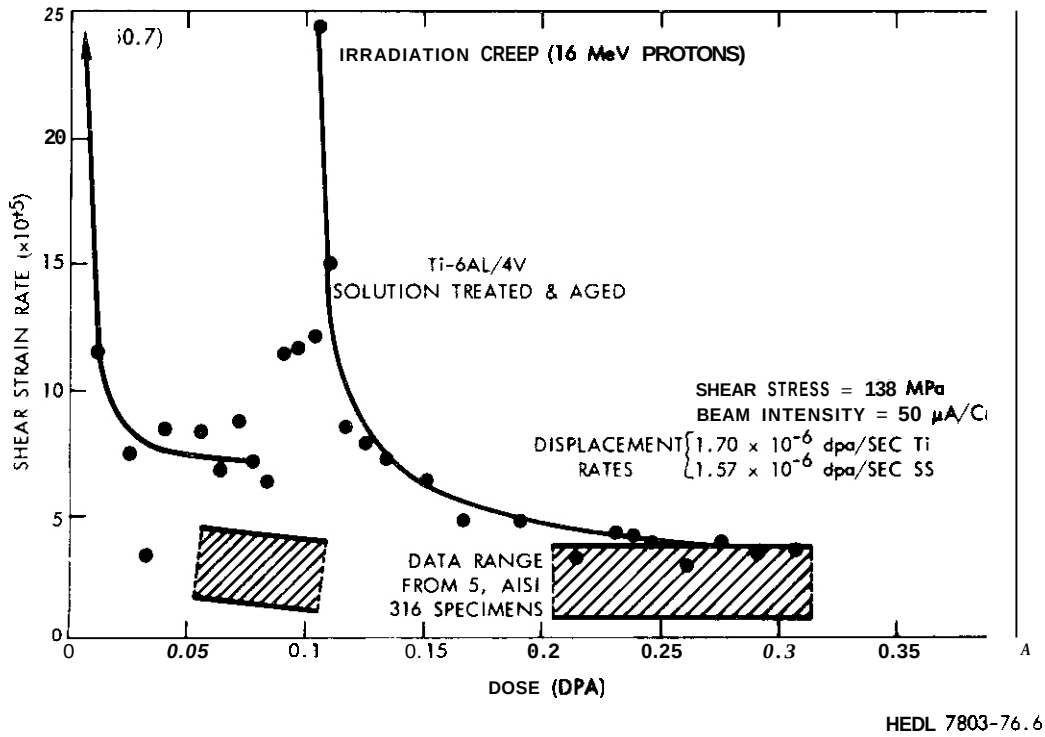

Fig. 5. Shear strain rate versus dose for irradiated Ti-6AL/4V and stainless steel. The second transient in the titanium data occurred after a system shutdown.

To investigate the effect of a stress change under irradiation conditions the load on the titanium specimen was reduced to zero after an accumulated dose of 0.31 dpa. The stress was reduced at a rate of 1 MPa per second while maintaining constant flux and temperature. Figure 2 illustrates the load reversal along with the output from the irradiated thermocouple a quantity proportional to beam intensity and specimen temperature. Figure 6 shows a strain versus time prior to and after the stress reduction. The total shear strain recovered during the four hours of zero stress irradiation was 0.052%. The magnitude of this strain is similar (within 20%) to that attained during the initial four hours of "load-on" testing indicating anelastic behavior. Upon turning the beam off, the zero-stress strain rate decreased abruptly as shown in Figure 6. This indicates the recovery is irradiation dependent.

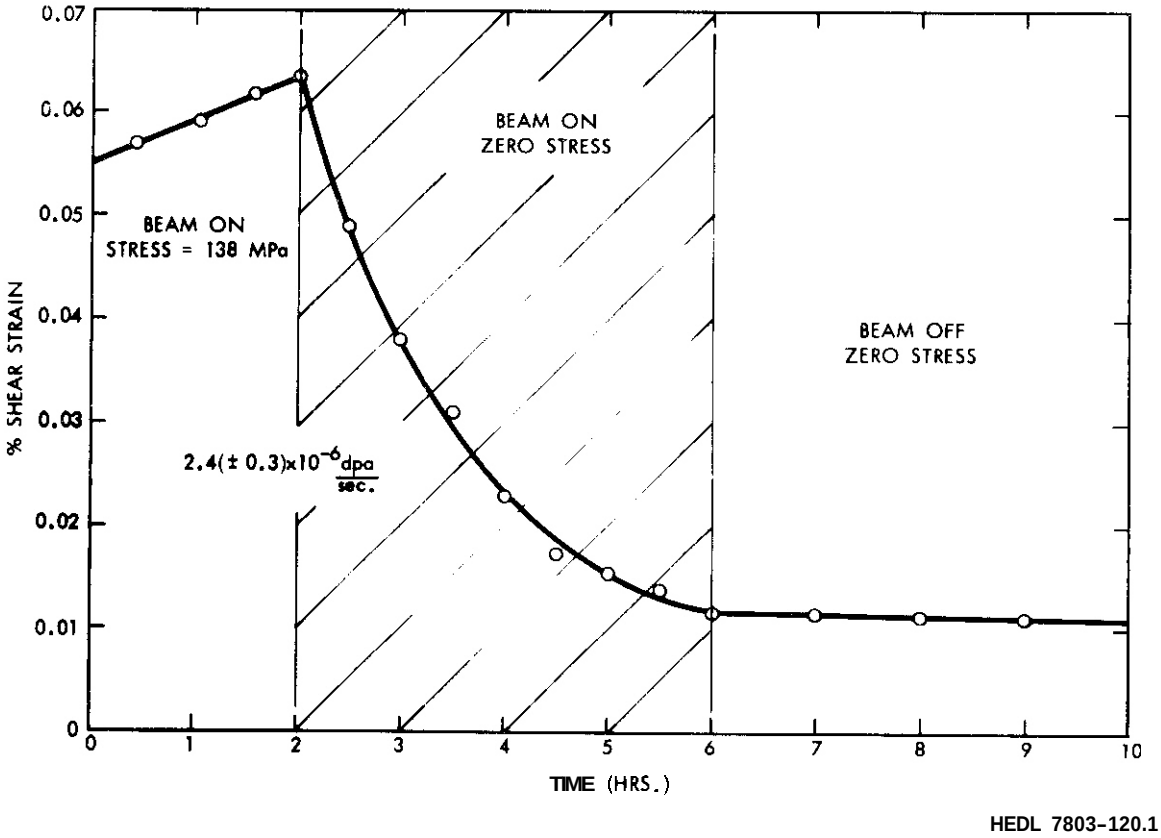

Fig. 6. Strain versus time illustrating the effect of a load change during beam-on conditions followed by beam-off conditions.

Figure 7 shows the preirradiation thermal creep curve from the titanium specimen. The thermal strain rate prior to beam-on was an order-of-magnitude less than the minimum strain rates during irradiation. The measured strain during irradiation were thus assumed to be the result of irradiation creep only.

5.3.4.3 Discussion

One of the key results of this experiment is the similarity in creep rates between the Ti-6AL/4V and 316 SS specimens. However, this discussion section will be devoted to models describing the anelastic behavior exhibited by the titanium specimen. Such behavior may not be particularly important in long-term steady-state testing. However, under the cyclic operating conditions expected in fusion reactors the magnitude of transient

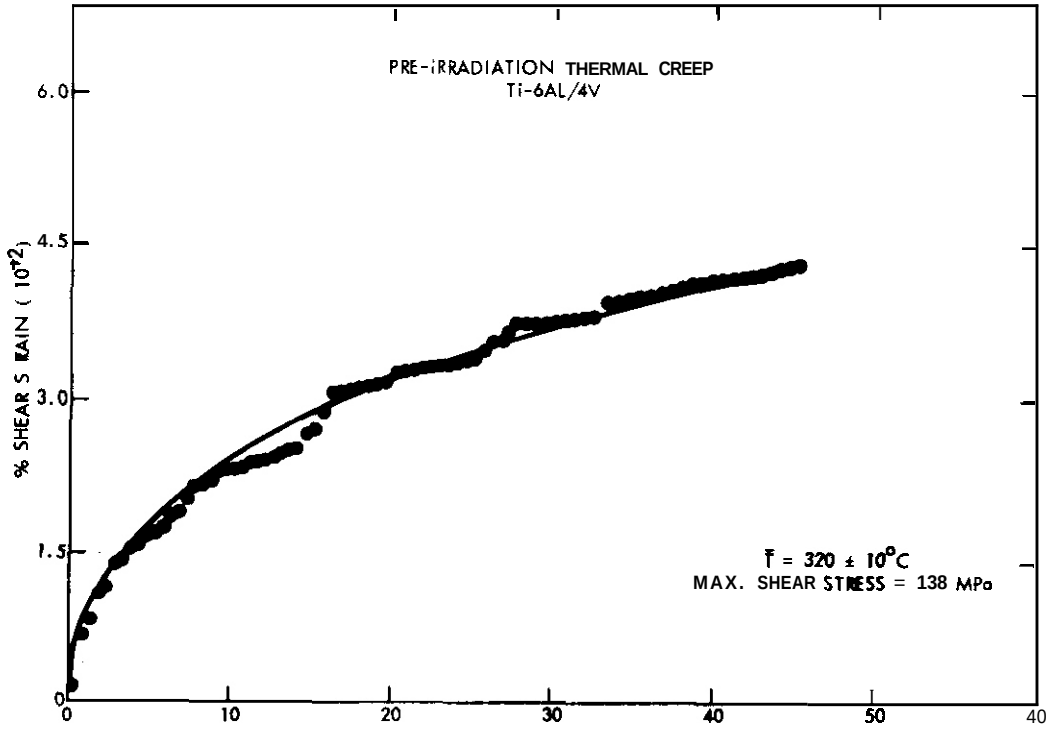

Fig. 7. Preirradiation thermal creep in Ti-6AL/4V.

strains following beam, temperature or stress changes may significantly affect the total deformation occurring in structural components. Even though insufficient test data are available at this time to isolate the source of this anelastic behavior a number of possible mechanisms will be explored.

Sophisticated models[5] of the SIPA[6,7] mechanism of irradiation creep indicate that a distribution of loops with preferred orientation should develop under an applied stress. After release of the stress, the oriented microstructure is gradually replaced by a new distribution that is more random in nature. This process, however, would not lead to strain recovery as the oriented distribution is not dissolved but is replaced by the growth of a new distribution.

The formation of vacancy loops as a result of cascade collapse may contribute to the anelasticity. Work by Lewthwaite[8] and Heald and Speight[5]

shows that stress assisted dissolution of cascade produced vacancy loops does not result in enhanced steady-state creep rates, however, it will add to transient deformation. A qualitative view of this effect may be obtained by considering a simple situation involving loops with only two possible orientations. To further simplify the situation it will be assumed that one orientation is such that the mechanical work done as vacancies are preferentially absorbed is the product of the stress multiplied by the atomic volume (Ω).

A rate equation for this model consists of a simple loop generation term G and a removal term C_L/τ. The rate equation is written as

$$\frac{d\,C_L}{dt} = G - C_L/\tau \qquad [1]$$

where C_L is the concentration of loops preferentially aligned to the stress and τ=loop lifetime. Under steady-state irradiation conditions the loop concentration is

$$C_L = \tau\, G \qquad [2]$$

The loop lifetime is estimated by dividing the loop size (number of vacancies) by the average dissolution rate of the vacancies from the loop. The dissolution rate may be considered as the sum of two parts:

$$\text{dissolution rate} = \psi + gD_s\, e^{-\sigma\Omega/KT}$$

where ψ is the net arrival rate of interstitials (e.g. interstitial arrival rate - vacancy arrival rate) and $gD_s\, e^{-\sigma\Omega/KT}$ is the dissolution rate due to thermal emission of vacancies, g = geometrical constant, D_s = vacancy self-diffusion coefficient, σ=external stress and Ω=atomic volume. τ may thus be expressed as:

$$\tau = \frac{N}{\psi + gD_s\, e^{-\sigma\Omega/KT}} \qquad [3]$$

where N=the number of vacancies in the loop. For small loops we assume thermal emission to be the dominant dissolution mechanism. This results in a simplified expression for τ which is written as

$$\tau = \frac{N}{gD_s\, e^{-\sigma\Omega/KT}} \qquad [4]$$

Having defined τ, G and C_L, the rate equation may be solved by integration. The resulting expression for the loop concentration is

$$C_\tau = G\tau(1-e^{-t/\tau})$$

which combined with the steady-state boundary conditions from Equation [2] gives

$$C_L = C_L^{ss}(I-e-t/\tau) \qquad [6]$$

Equation [6] is thus an expression for the transient build-up of preferentially aligned loops which contribute to transient strains. The build-up and decay of the loop concentration is illustrated in Figure 8. The shape of the curve illustrated in Figure 8 is similar to the measured anelastic recovery curve shown in Figure 6.

An estimate of the magnitude of strain resulting from the loop redistribution is obtained by considering the difference between the stressed (C_L^1) and zero stress (C_L^0) loop concentrations for steady-state conditions. The difference in loop concentration is

$$\Delta C_L = C_L^1 - C_L^0 = G\,(\tau_1 - \tau_0) \qquad [7]$$

which combined with the expression for τ (Equation *3)* becomes

$$\Delta C_L = \frac{GN}{gD_s}\,(e^{\sigma\Omega/KT} - 1) \qquad [8]$$

Since $\sigma\Omega << KT$ for the conditions of this experiment, Equation [8] may be simplified and written as

$$\Delta C_L = \frac{GN}{gD_s}\,\frac{\sigma\Omega}{KT} \qquad [9]$$

Equation [9] states that the transient strain. (ΔC_L) is a function of stress and temperature. The model thus predicts the magnitude of the transient strain to be dependent upon the stress change and inversely proportional to temperature. Since thermal emission is the dominant mechanism controlling recovery, this mode? does not predict a strong irrndiation dependence.

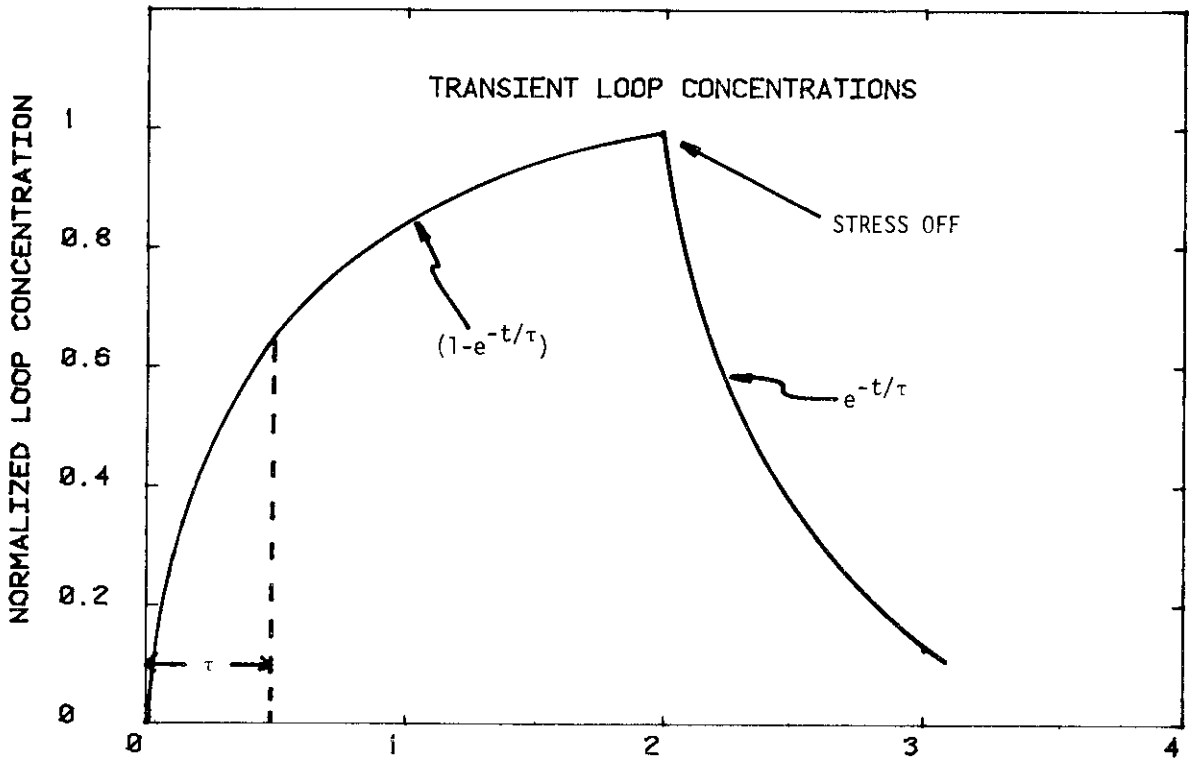

Fig. 8. An illustration of the loop concentration preferentially aligned to an external stress. The cycle illustrates the transient nature of the aligned loop concentration following loading and unloading.

Another mechanism[9] which may explain the anelasticity is based on the assumption that creep within individual grains is dependent upon the orientation of the grain with respect to the external stress. The Ti-6AL/4V used in this experiment is a two phase, polycrystalline material and it is assumed that grains, stressed in a preferred orientation, will creep at a higher rate than those oriented otherwise. This will result in a build-up of elastic stress within the non-creeping grains. Upon removal of the external stress, the non-creeping grains will produce a back stress within the material which drives the strain recovery. This residual stress mechanism also explains the decreased recovery rate that occurred when the beam was turned off. With the beam on, irradiation creep was able to relieve the internal stresses. When the beam was turned off, the internal stresses were locked in, resulting in a decreased strain recovery rate.

To further develop models describing transient phenomena additional experimentation will be required. The single stress change conducted during this test indicates the anelastic behavior to be beam related. However, a more definitive relation between irradiation effects and recovery would be obtained by terminating the irradiation earlier in the transient stage. Conversely, by extending the duration of the zero-stress conditions an estimate of the total amount of recovery could be made. Stress and temperature effects referred to in the model discussion also require experimental verification. If the residual stress model was the dominant mechanism one might expect grain boundary cavitation to occur under cyclic operating conditions. Electron microscopy could verify this.

5.3.5 Conclusion

Irradiation creep rates measured in a titanium alloy, Ti-6AL/4V (solution treated and aged condition), were the same order-of-magnitude as creep rates from similarly irradiated stainless steel specimens. The primary creep rates in titanium were 2-5 times higher than stainless steel for doses less than 0.1 dpa. The strain rate in titanium steadly decreased with increasing 16 MeV proton dose and by the end of the irradiation test (0.31 dpa) the titanium strain rates were within a factor of two of the stainless steel creep rates.

Strain measured during the final four hours of zero-stress irradiation indicates a substantial amount of strain recovery or anelasticity. The rate of anelastic recovery was similar to the transient creep rate that occured during the initial four hours of irradiation testing. The zero-stress strain rate abruptly decreased when the beam was turned off indicating an irradiation dependence. Two models, one based on the stress assisted dissolution of vacancy loops and the other based on residual stresses are considered as possible mechanisms describing this anelastic behavior.

5.3.6 References

1. McDonnel-Douglas Astronautics Company, *Assessment of Titanium for Use in the 1st Wall/Blanket Structure of Fusion Power reactors,* EPRI ER-386 (Project 472-1), April 1977.
2. C. M. Logan and J. D. Anderson, "Proton Simulation of Displacement Effects Induced in Metals by 14 MeV Neutrons,'' *J. Nucl. Mater.* 48, 223-232, (1973).
3. E. K. Opperman, J. L. Straalsund, G. L. Wire and R. H. Howell, *Proton Simulation of Irradiation Induced Creep,* HEDL-SA-1400, 1978.
4. Personal communication, R. H. Howell, Lawrence Livermore Laboratory to E. K. Opperman, Hanford Engineering Development Laboratory, January 1978.
5. P. T. Heald and M. V. Speight, "The Influence of Cascade Damage on Irradiation Creep and Swelling," *J. NucZ. Mater.,* 139-144 (1977).
6. P. T. Heald and M. V. Speight, "Steady-State Irradiation Creep," Phil. *Mag.* 29, 1075 (1974).
7. W. G. Wolfer and M. Ashkin, "Stress-induced Diffusion of Point Defects to Spherical Sinks," *J. Appl. Phys.* 46, 547 (1975).
8. G. W. Lewthwaite, "Vacancy Loops and Irradiation Induced Creep," *J. Nucl. Mater.* 61, 313-316 (1976).
9. Personal communication, W. G. Wolfer, University of Wisconsin, to E. K. Opperman, Hanford Engineering Development Laboratory, March 1978.

5.4 PLASTIC INSTABILITY IN NEUTRON-IRRADIATED NIOBIUM ALLOYS – F. W. Wiffen (OWL)

5.4.1 ADIP Task

ADIP Task I.B.15, Tensile Properties of Reactive and Refractory Alloys.

5.4.2 Objective

The objective of this work is to establish the mechanisms controlling plastic instability in neutron-irradiated niobium alloys and to examine the dependence of this instability on irradiation and test conditions.

5.4.3 Summary

Irradiation of niobium and Nb–1% Zr at about 70°C followed by tensile tests at about 35°C has shown no intrinsic difference in the tensile behavior of these two materials. The onset of plastic instability in both occurs at about 0.1 dpa, with strengthening continuing for irradiation beyond at least 0.36 dpa. Although the uniform elongation goes to near zero, the total elongation remains high, and the fracture mode is fully ductile. Ductility loss through plastic instability is related to deformation by dislocation channeling.

5.4.4 Progress and Status

5.4.4.1 Background

Plastic instability, for the present purpose, is defined as the type of tensile test in which the maximum load occurs at the yield point, with less than 0.5% uniform elongation, but with the total elongation remaining high. Earlier work' had shown that irradiation in the temperature range 390 to 460°C to fluences in the range 1.9 to 3.7 $\times 10^{26}$ n/m^2 (>0.1 MeV) resulted in plastic instability at the yield load in Nb–1% Zr, while unalloyed niobium retained appreciable uniform elongation. These earlier results are illustrated in Fig. 5.4.1. Low-fluence irradiation at reactor ambient temperatures (≥55°C) had not given any indication of plastic instability in niobium,' and higher fluence results[3] on both

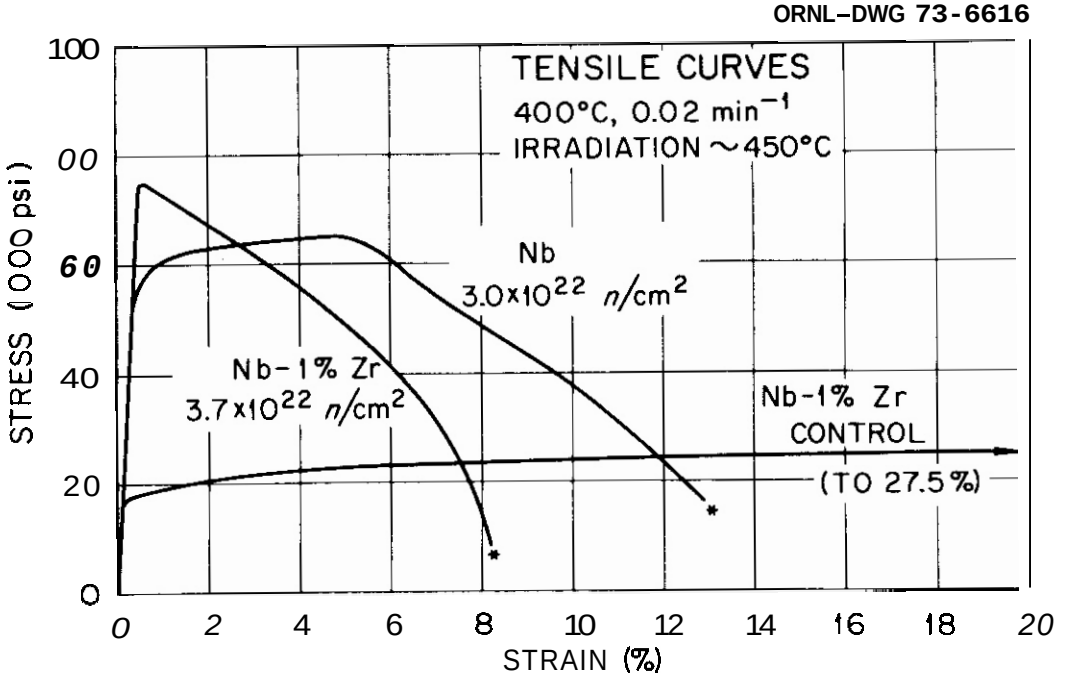

Fig. 5.4.1. Example of Plastic Instability in Nb–1% Zr but not in Niobium for Tensile Tests at 400°C After Irradiation at About 450°C. 1000 psi = 6.895 MPa.

the niobium and Nb-1% Zr showed small but nonzero uniform elongation, with some indication of plastic instability in the Nb–1% Zr only.

These experiments are directed at answering several questions related to plastic instability and ductility loss by other mechanisms in niobium alloys. These include:

1. Is the behavior of Nb–1% Zr intrinsically different than that of niobium after neutron irradiation?

2. What is the fluence dependence of the hardening and ductility loss in niobium and Nb–1% Zr for irradiation at reactor ambient temperature?

3. What is the mechanism of plastic instability?

4. Does a change in fracture mode reflect the onset of plastic instability?

5. Can a ductile–brittle transition temperature (DBTT) above room temperature result from neutron irradiation of niobium or Nb–1% Zr?

5.4.4.2 Tensile Properties

Two sizes of rod tensile specimens were used in these experiments. The larger specimen had a *25-mm-long* reduced gage section *3.2* mm in diameter; the smaller sample had a gage section 18 mm by *2* mm diam. Samples to be irradiated were sealed into aluminum irradiation capsules, one sample per capsule, with extra space filled with aluminum powder and helium at about 0.1 MPa (1 atm). These capsules were irradiated in the ORR or HFIR hydraulic tubes. The capsules were immersed in the reactor cooling water at about 55°C during irradiation. The specimen temperature during irradiations was estimated *to* be near *70°C.*

Postirradiation tests were conducted on an Instron machine. Strain values were calculated from the crosshead motion. All tests were conducted at hot cell ambient temperature, which is in the range *20* to 35°C.

The specimen materials were from commercially produced heats of niobium and Nb—1% Zr. All specimens were given a recrystallization anneal in vacuum before irradiation. The niobium was annealed 1 hr at 1150°C, and the Nb—1% Zr 1 hr at 1275°C.

5.4.4.3 Results

The results of tensile tests are given in Figs. *5.4.2* and *5.4.3.* The data are plotted as a function of dpa level achieved in the irradiation, calculated from the neutron spectrum at the irradiation position for an effective displacement energy of 60 eV. (The corresponding neutron fluence is indicated for reference at one point on the abscissa.)

Similar trends are shown for the strength increases of niobium and Nb—1% Zr with increasing dpa level. For the range of fluences available (up to *0.36* dpa) there is no indication of saturation of the strengthening effect of irradiation. Ductility values for both materials also show similar behavior with fluence. The uniform elongation drops to zero for both materials and the total elongation remains well above zero. There is some indication in the data that the total elongation may be approaching a lower bound, but higher fluence data would be required to verify this.

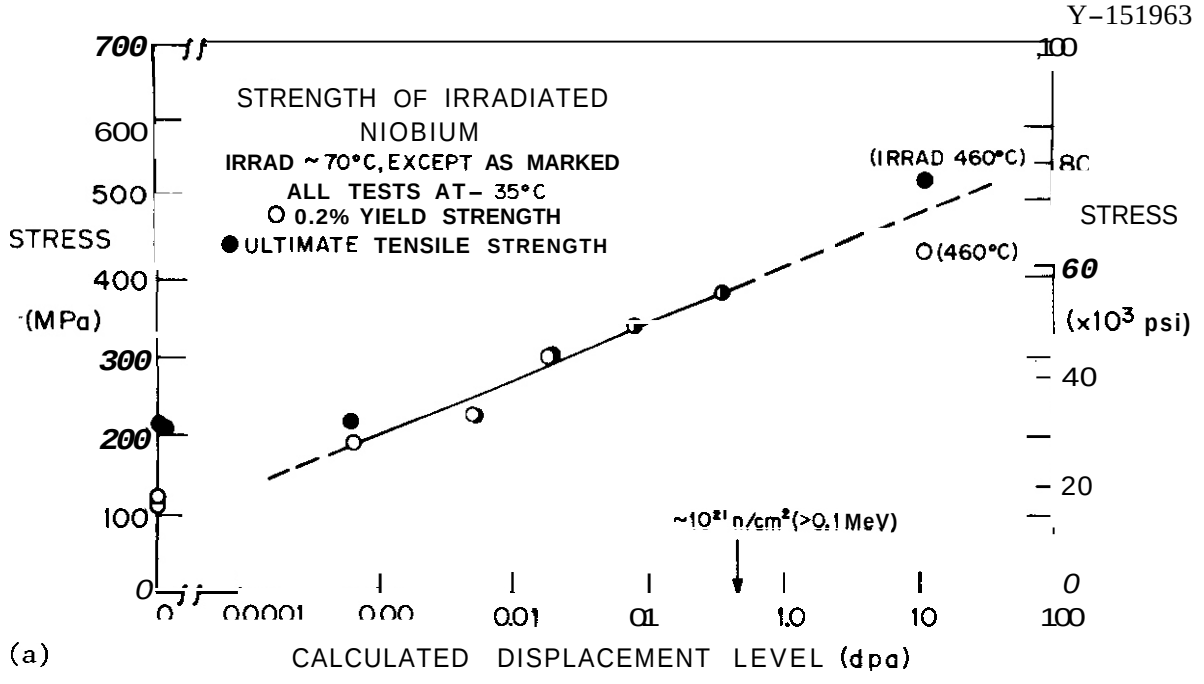

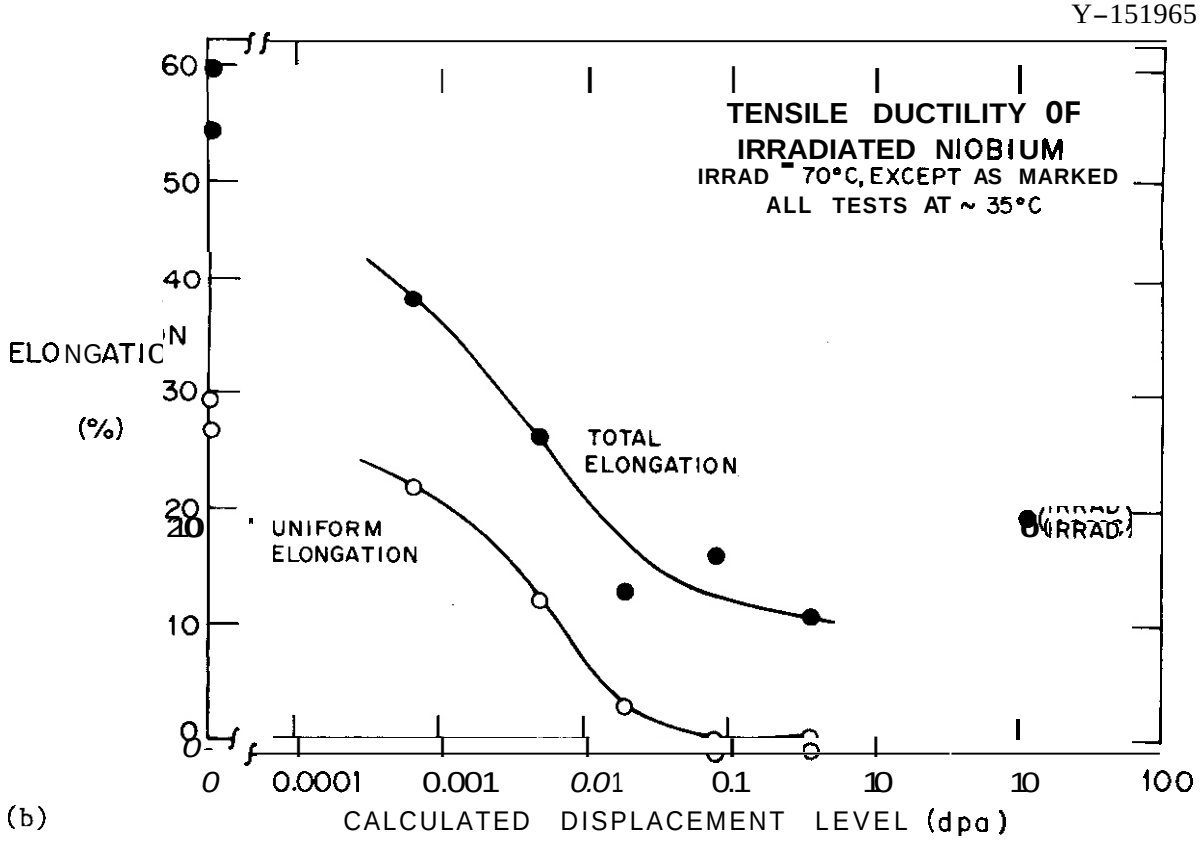

Fig. 5.4.2. **Tensile Properties of Niobium Irradiated at About 70°C and Tested at About 35°C. Values are plotted against displacement level for an effective threshold energy of 60 eV. (a) Strength. (b) Elongation.**

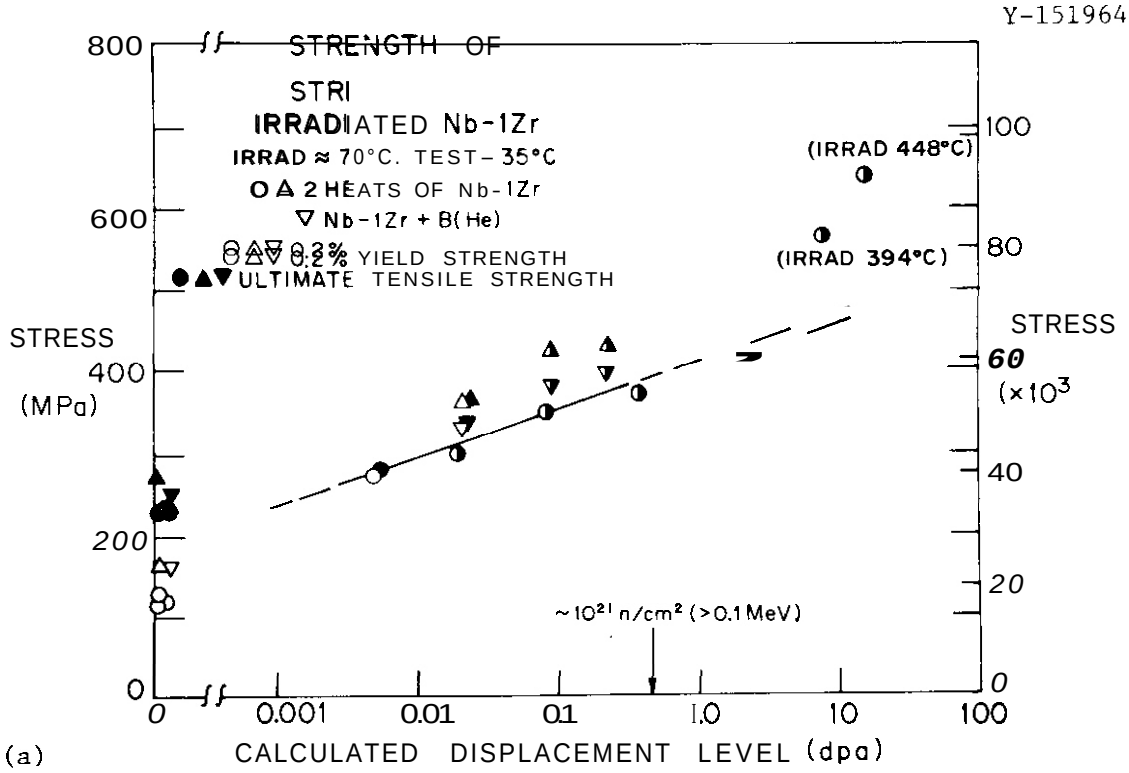

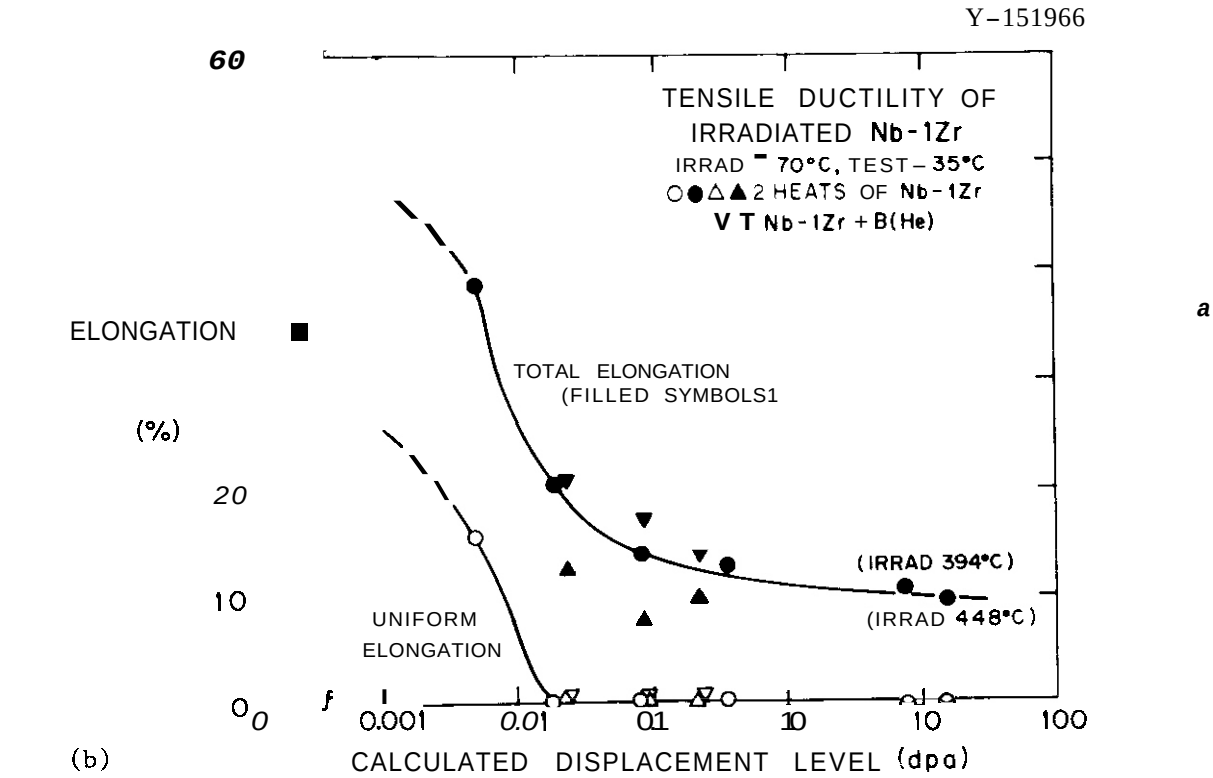

Fig. *5.4.3.* Tensile **Properties** of Nb—1% Zr Irradiated at About 70°C and Tested at About 35°C, Shown **as** a Function of Displacement **Level.** (a) **Strength.** (b) Elongation.

In irradiated niobium (Fig. 5.4.2) the strength increases as a smooth function of dpa level up to 0.36 dpa. The yield strength (YS) increases more rapidly than the ultimate tensile strength (UTS), with the two equal at about 0.1 dpa. The hardening rate for these irradiations at about 70°C extrapolated to higher dpa levels pass above the YS and below the UTS for the sample irradiated to 12.3 dpa at 460°C. The ductility values for these same samples show that zero uniform elongation is reached after irradiation to about 0.1 dpa. That is, the tensile behavior is plastically unstable at the yield point for 70°C irradiations producing at least 0.1 dpa. This figure also emphasizes that the higher temperature irradiation of niobium did not result in the same unstable behavior. The lowest total elongation measured in the niobium samples was about 10%. The scattered data suggests that this may be a lower bound.

The strength values for Nb-1% Zr are given in Fig. 5.4.3. Three heats of material tested show similar behavior, and the hardening rate with dpa level appears to be slightly lower than for the unalloyed niobium. As with the niobium, the YS and UTS become equal after irradiation to about 0.1 dpa. In contrast to the niobium, however, extrapolation of the hardening rate for the irradiation at about 70°C predicts much too low a strength level for irradiation of the same alloy to higher fluences at 394 and 448°C. Ductility values of all the Nb-1% Zr tested indicate similar behavior. The uniform elongation drops to zero for irradiations producing over 0.02 dpa. The total elongation remains at least 10% for all conditions tested. In the case of the ductility values of Nb-1% Zr, the higher fluence, higher temperature data fall on the extrapolation of the 70°C data.

Reduction of area at the fracture was high for all the samples tested. These results are not presented because of the large scatter produced by the difficulty of accurately measuring fracture diameters in tested samples.

5.4.4.4 Fracture Mode

Examination of selected fracture surfaces by scanning electron microscopy showed similar fracture appearance of unirradiated and irradiated samples. A typical fracture is shown in Fig. *5.4.4* for a sample that was plastically unstable at the yield. The sample had failed after extensive deformation with a well-formed neck, with an estimated *94%* reduction of area. The fracture surface shows only the dimples characteristic of ductile fractures, without any cleavage facets, grain boundary separations or the relatively flat channel fracture facets. None of the fractures examined showed any of the indications of the brittle or low-ductility fracture modes.

5.4.4.5 Deformation Mode

Examination of sections of selected samples by transmission electron microscopy showed that the only irradiation-produced defects in these samples appeared to be a very high concentration of small dislocation loops. After extensive deformation, as in the unnecked region of a sample that displayed extensive uniform elongation, Fig. *5.4.5*, there is little or no evidence of the irradiation-produced damage. It has been replaced by a fine scale network of dislocations resulting from the deformation. In regions that have experienced much less deformation, outside the neck on samples that displayed less than *0.5%* uniform elongation, all deformation has occurred by dislocation channeling. Figure *5.4.6* shows an example of this channeling behavior. The microstructure contains mainly areas of as-irradiated dislocation loops, separated by channels swept clear of the irradiation damage by the passage of multiple slip dislocations. This type of behavior has frequently been observed,[...] but there is not a fully accepted model of the processes occurring. The "map" of the deformation channels in Fig. *5.4.6* shows the traces of a number of the {110} and {112} slip planes in this sample. While many of the channels fit these expected slip planes, not all channels can be matched to these systems. A number of the channels also show significant curvature. These features indicate that a number of slip systems and cross-slip processes must have been operative in the deformation of this sample.

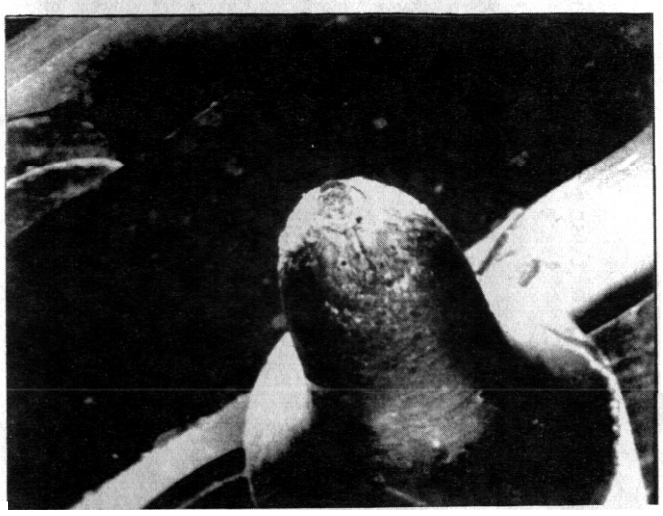

Fig. 5.4.4. Details of the Fracture Surface of an Nb–1% Zr Sample Irradiated and Tested to the Conditions Shown. Left views are at 12× and 40×.

0.22 dpa at ~70°C
[4.5×10^{20} n/cm^2 (>0.1 MeV)]

Tensile Test at ~35°C

0.2 % Uniform Elongation
9.6% Total Elongation

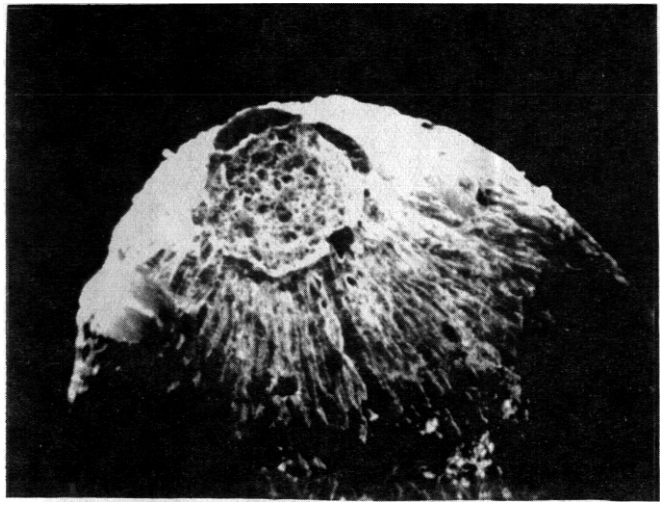

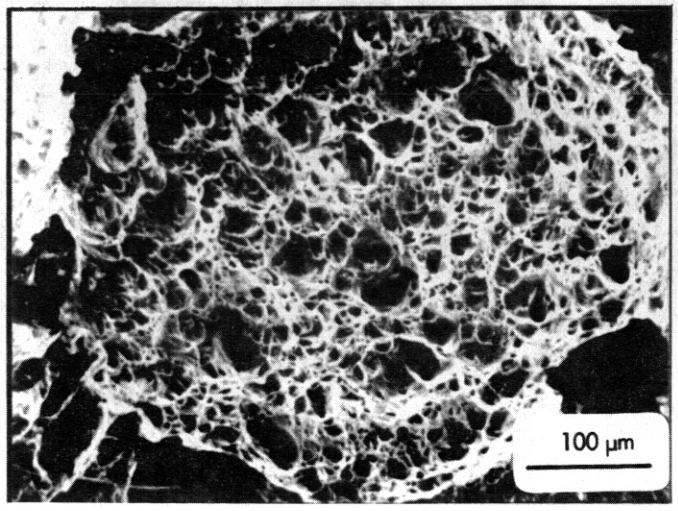

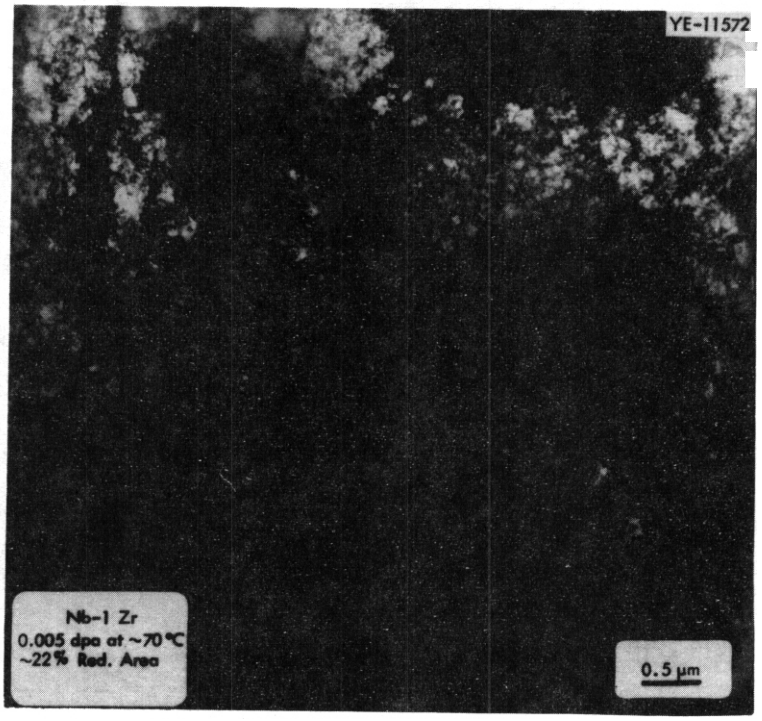

Fig. 5.4.5. Microstructure of an Nb–1% Zr Sample Irradiated to 0.005 dpa at About 70°C and Tensile Tested at About 35°C. Reduction of area of this sample section was about 22%.

5.4.5 Conclusions and Future Work

Irradiation at about 70°C followed by tensile tests at about 35°C showed:

1. The behavior of niobium and Nb–1% Zr is nearly identical.
2. Hardening continues beyond 0.36 dpa, and probably extends beyond 15 dpa.
3. Ductility loss by plastic instability is related to dislocation channeling. Slip dislocations clear swaths through the dislocation loops produced by irradiation.
4. Although *uniform* elongation goes to zero at about 0.05 dpa, *total* elongation remains high.
5. The fracture mode remains ductile.
6. The DBTT remains below room temperature for conditions investigated.

Future experiments are planned to establish the influence of strain rate during testing and of plastic strain before irradiation on the plastic instability behavior of Nb–1% Zr.

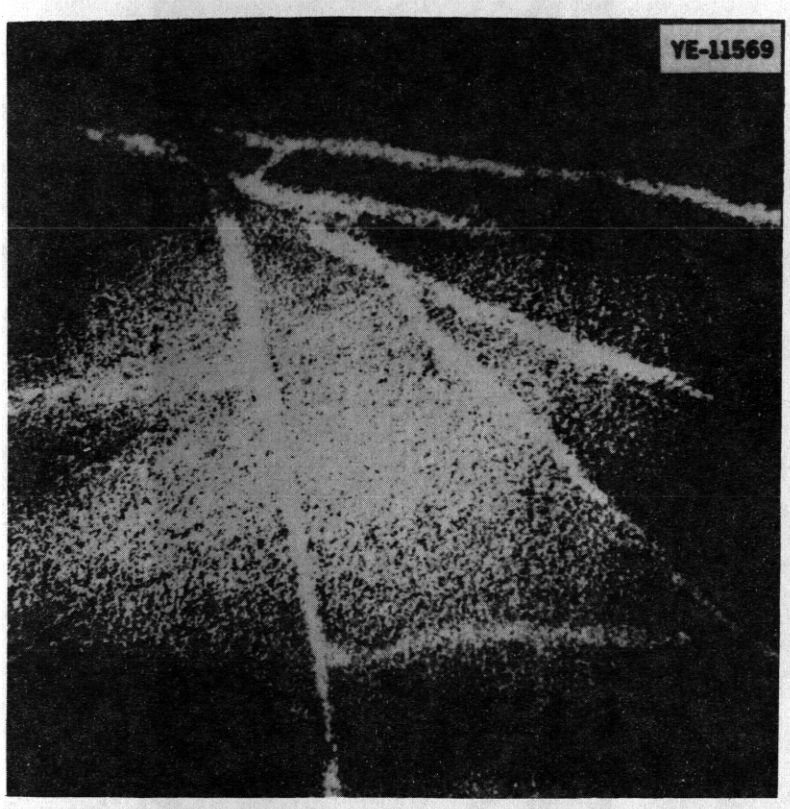

Fig. 5.4.6. Deformation by Dislocation Channeling. This sample of Nb—1% Zr was irradiated to 0.36 dpa at about 70°C and tensile tested at about 35°C. The sample exhibited 0.1% uniform elongation and 12.7% total elongation. Reduction of area at the section examined was about 1%.

5.4.6 References

1. F. W. Wiffen, "The Tensile Properties of Fast Reactor Neutron Irradiated BCC Metals and Alloys," pp. 176–97 in *Defects and Defect Clusters in B.C.C. Metals and Their Alloys*, National Bureau of Standards, Gaithersburg, Maryland, 1973.
2. R. P. Tucker, *Transmission Electron Microscopy and Plastic Deformation in Neutron-Irradiated Niobium*, ORNLITM-2480 (March 1969).
3. W. J. Stapp and A. R. Begany, *Seventh Annual Report — AEC Fuels and Materials Program*, GEMP-1004 (March 29, 1968), pp. 137–45.

5.5 MECHANICAL PROPERTY TESTING OF PATH C ALLOYS IN UNIRRADIATED CONDITION — K. C. Liu (ORNL)

5.5.1 ADIP Task

ADIP Task I.B.3, Fatigue Crack Growth in Reactive and Refractory Alloys.

5.5.2 Objective

Fatigue and crack growth behavior are among the most important properties of an alloy to be used in a fusion reactor. There is essentially no information on these properties for refractory metal alloys. The objective of this work is to develop base-line information for the path C refractory metal scoping alloys in the unirradiated condition.

5.5.3 Summary

Equipment for conducting tensile, fatigue, and crack growth tests on refractory scoping alloys in vacuum is currently being assembled at ORNL.

5.5.4 Progress and Status

A multipurpose tension-torsion biaxial testing system with closed-loop servo-control capabilities, as shown in Fig. 5.5.1, will be used to determine the mechanical properties of a scoping set of unirradiated reactive and refractory alloys. This is a complex-load tester, which can independently apply axial or torsional loading as well as a combined axial-torsional static and dynamic loading.

The atmosphere, oxygen in particular, will significantly influence the fatigue properties of alloys at elevated temperatures. Since these alloys will be used in the oxygen-free environment of a fusion reactor, samples must be tested in vacuum. The system available for conducting these tests presently lacks the capability for testing samples in controlled environments at elevated temperatures. An appropriate environmental chamber and associated equipment are currently being designed.

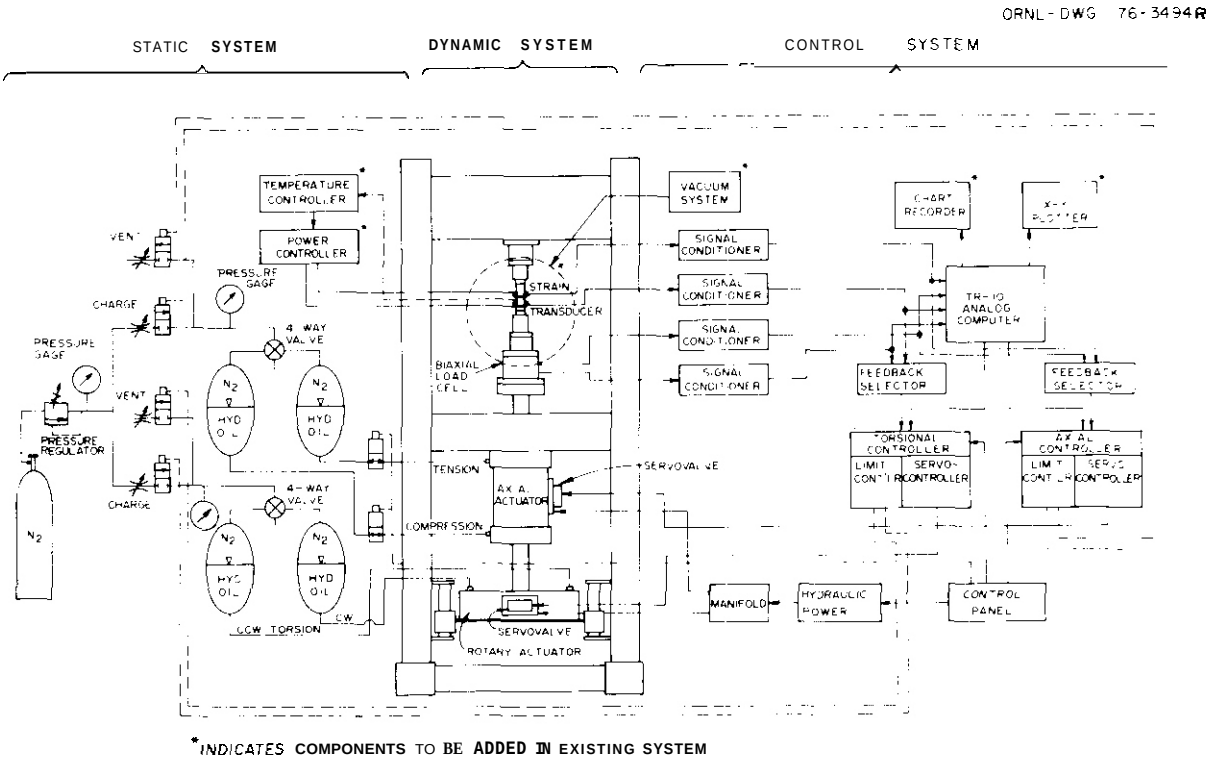

Fig. 5.5.1. Block Diagram for Multipurpose Biaxial Testing System.

The specimen design for various tests will be determined by the product form available and the desire to have these results serve as base-line data for irradiation effects studies. Only sheet material will be available, and restrictions imposed by the irradiation experiments dictate that the specimens be as small as possible. Figure 5.5.2 shows a sheet fatigue specimen designed by McDonnell-Douglas Corporation. This specimen has been designed with rounded shoulder fillets to minimize the strain concentration at the inception of the elliptical transition so that representative fatigue behavior and data can be observed at the gage section. A drawback to the sheet specimen design is that it permits fatigue loading in tension only to avoid buckling. Center-cracked sheet specimens will be used for crack growth studies.

Special specimen grips and strain measurement devices for use in the environment chamber are being developed.

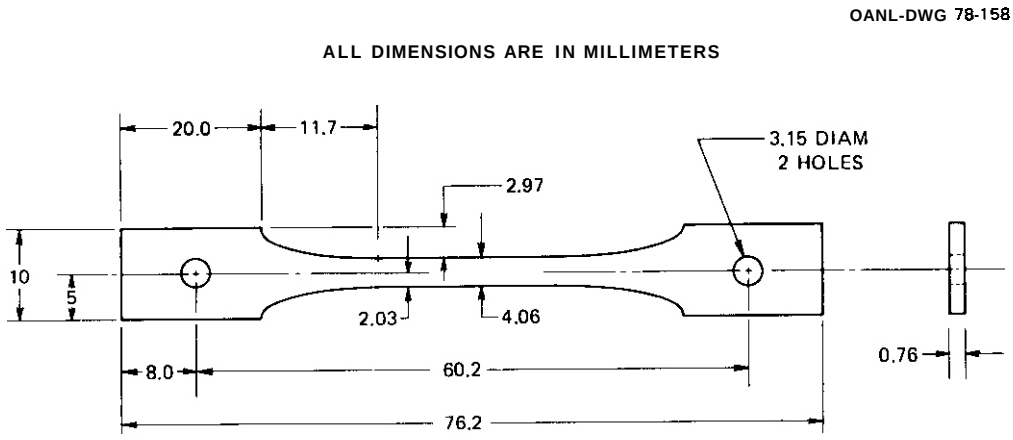

Fig. 5.5.2. Fatigue Specimen with Grodzinski Elliptical Fillet.

Path C scoping alloys identified by the Alloy Development Task Group include three vanadium alloys: V—20% Ti, V—15% Cr—5% Ti, and Vanstar 7; and two niobium alloys: Nb—5% Mo—1% Zr and Nb—1% Zr.

Because of the complete absence of data on the response of these alloys to cyclic loading, which is considered as the most damaging mode to the structural integrity of a fusion reactor, crack growth and fatigue tests will be emphasized. These will be supplemented by tensile tests. A tentative test matrix is shown in Table 5.5.1.

Table 5.5.1. Test Matrix of Path C (Vanadium, Niobium) Scoping Alloys

Material Property	Temperature (°C)	Test Parameters	Test Environments	Specimen	Test Conditions
Tensile	room 350 450 550 650 750	$\dot{\varepsilon}$ = 2%/min	inert	sheet	6
Fatigue	room 550 650	$\Delta\varepsilon$ = 2% 1 0.5 0.3	vacuum	sheet	12
Crack growth	room 550 650		vacuum	Center crack specimen	3

5.5.5 Conclusions

A tentative test matrix intended to provide base-line information on the fatigue, tensile, and crack growth properties of unirradiated refractory metal scoping alloys has been identified. Equipment for testing these alloys is being assembled and associated fixturing and instrumentation are being developed.

6. PATH D ALLOY DEVELOPMENT — INNOVATIVE MATERIAL CONCEPTS

Innovative material concepts are included as a path in the alloy development program because the fusion reactor environment is extremely demanding on materials in the high-flux region and the more conventional materials and metallurgical concepts may not be adequate. Novel approaches to alloy design, nonconventional material processing to tailor properties, or alternate materials such as structural ceramics and fiber composites will be considered.

6.1 DEVELOPMENT OF ALLOYS WITH LONG-RANGE ORDER* — C. T. Liu (ORNL)

6.1.1 ADIP Task

Task 1.B.16, Tensile Properties of Special and Innovative Materials, and Task 1.C.5, Microstructures and Swelling in Special and Innovative Materials.

6.1.2 Objective

The objective of this study is to determine the potential of alloys with long-range order (LRO) for high-temperature energy systems such as fusion reactors. These alloys have excellent high-temperature strength properties, and on the basis of electron and heavy ion simulation experiments appear to have good swelling resistance. Samples of LRO alloys will be included in alloy development irradiation experiments to assess the effects of irradiation on tensile properties and stability.

6.1.3 Summary

Two long-range ordered alloys with compositions 36.1% Fe—19.7% Ni—21.4% Co—22.8% V (LRO-15) and 46% Fe—31% Ni—23% V (LRO-16) were prepared and fabricated into 0.8-mm-thich sheets. Tensile tests indicate that these alloys are ductile, with elongation in excess of 35% at room temperature. The ordered alloys have very attractive high-temperature mechanical properties; that is, their strength increases with test temperature, instead of decreasing like that of conventional alloys. These two alloys will be irradiated in the ORR-MFE-2 experiment.

6.1.4 Progress and Status

Long-range ordered (LRO) alloys offer a significant advantage over the conventional or disordered alloys for high-temperature applications. This is because ordering reaction produces stronger binding and closer packing between atoms. As a result, any kinetic processes involving diffusion, such as creep or migration of point defects, are reduced.

*This work is entirely supported by the Nuclear Research and Applications Materials Programs sponsored by the Division of Advanced Systems and Materials, Department of Energy.

Also, unusual dislocation motion characteristics of the ordered lattice give the LKO alloys excellent high-temperature strength and fatigue resistance. Furthermore, recent electron irradiation and ion bombardment experiments have demonstrated[3,4] that alloys with LRO structure are more resistant to radiation-induced swelling. This provides incentive to examine the potential of LRO alloys for the potential fusion reactor applications.

One of the major obstacles to more widespread use of ordered alloys and intermetallic compounds is their brittleness. However, our recent work on the Co-Fe-Ni-V alloy system has demonstrated[5] that the ductility of the ordered alloys can be controlled by adjusting the composition and ordered structure. The alloys with controlled ordered structure have more than 40% elongation at room temperature. In this study, the alloy compositions are modified for nuclear power applications in the temperature range 300 to 700°C.

Two alloys with compositions 36.1% Fe—19.7% Ni–21.4% Co—22.8% V (designated as LRO-15) and 46% Fe—31% Ni—23% V (LRO-16) were prepared by arc-melting and drop casting. The ingots were wrapped in molybdenum sheet and then rolled to 0.8-mm-thick sheet at 1000 to 1100°C. The sheets have good quality with no indication of surface or edge cracks.

To characterize the ordering behavior and mechanical properties, tensile specimens were blanked from the LRO–15 and -16 sheets and then heat-treated at 600 to 1100°C to produce disordered (quenching from 1100°C) and ordered structures. Table 6.1.1 shows the room-temperature tensile properties of LKO–15 and –16 alloys. Formation of LRO significantly increases the work-hardening rate and tensile strength but only slightly affects the yield strength. As shown in the table, both alloys are ductile, and had 35 to 55% elongation in the ordered state.

Figure 6.1.1 shows the yield strength of LRO-15 and -16 alloys as a function of test temperature. The results are mainly obtained from consecutive testing in the temperature range 400 to 1000°C. The striking feature of this plot is that the yield strength of the ordered alloys increases with test temperature, instead of decreasing as that of conventional alloys (such as type 316 stainless steel). The ordered

Table 6.1.1. Room-Temperature Properties of LRO-15 and -16 In Ordered and Disordered States

Alloy	State	Strength, MPa		Elongation (%)
		Tensile	Yield	
LRO-15	**Disordered**	*881.2*	*394.1*	*51.1*
-15	**Ordered**	*1329.1*	*354.2*	*54.7*
LRO-16	**Disordered**	*858.5*	*392.7*	*48.0*
-16	**Ordered**	*1070.7*	*423.1*	*35.2*

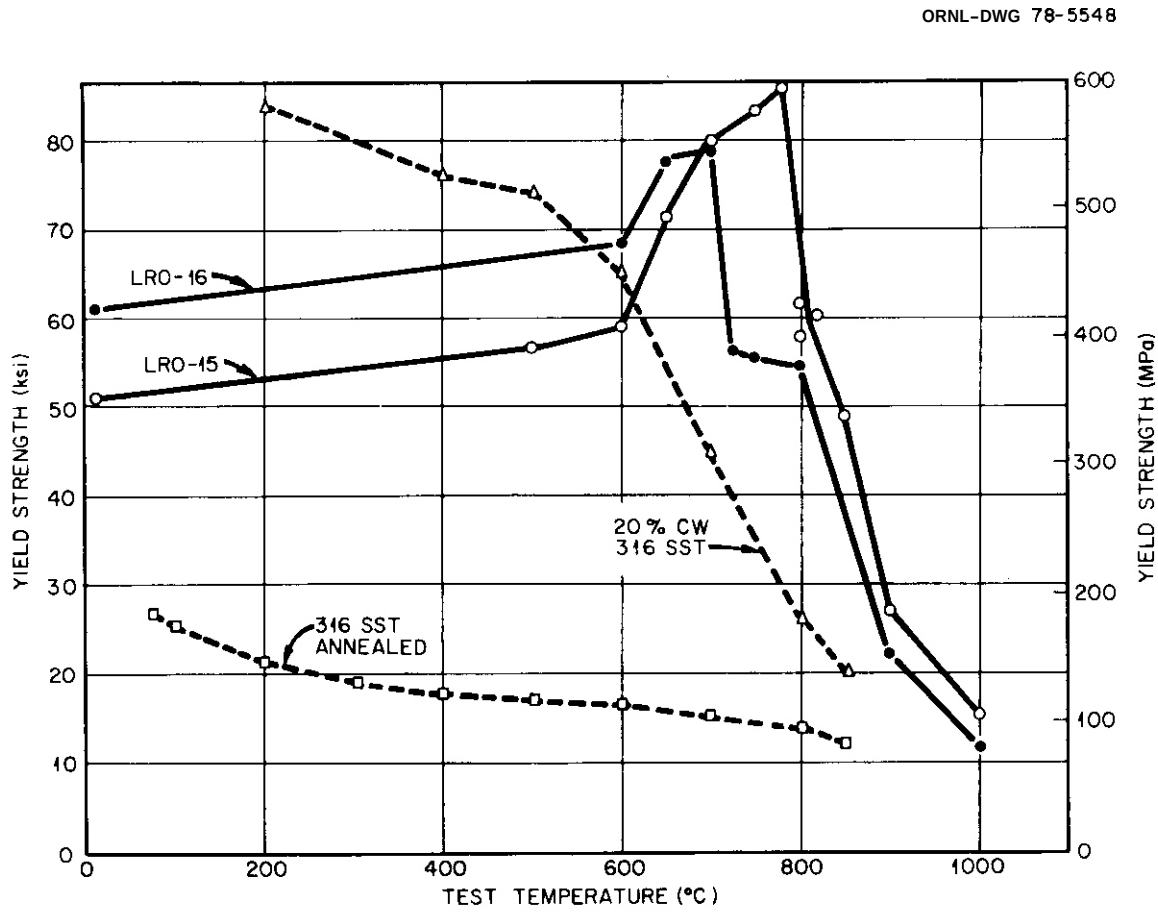

Fig. 6.1.1. Yield Strength as a Function of Test Temperature for the Ordered Alloys LRO-15 and -16 and for Type 316 Stainless Steel in the Annealed and 20%-Cold-Worked Conditions.

alloys are much stronger than type 316 stainless steel in the annealed condition and also stronger than the 20%-cold-worked 316 stainless steel at temperatures above 600°C. The yield strength of LRO-15 reaches 593 MPa at 780°C, which is 6 times that of annealed type 316 stainless steel and almost 3 times that of 20%-cold-worked type 316 stainless steel. The yield strength of the ordered alloys drops sharply beyond a critical temperature as a result of disordering. The critical ordering temperatures of the ordered alloys LRO-15 and -16 are estimated to be 790 and 710°C, respectively.

6.1.5 Conclusions and Future Work

Two-long range ordered alloys with compositions 36.1% Fe—19.7% Ni—21.4% Co—22.8% V (LRO-15) and 46% Fe—31% Ni–23% V (LRO-16) were hot rolled into sheets at 1000 to 1100°C. The alloys are ductile with tensile elongation in excess of 35% at room temperature. The alloys have very attractive high-temperature mechanical properties; that is, their strength increases with test temperature instead of decreasing as that of conventional alloys. The peak strength is located just below the critical ordering temperature, which is estimated to be 790 and 710°C for the alloys LRO-15 and -16, respectively. The yield strength drops sharply beyond these temperatures as a result of disordering.

6.1.6 References

1. N. S. Stoloff and R. G. Davies, "The Mechanical Properties of Ordered Alloys," *Prog. Mater. Sci.* 13(1): 1–84 (1966).
2. R. C. Boettner, N. S. Stoloff, and R. G. Davies, "Effect of Long-Range Order on Fatigue," *Trans. Metall. Soc.* 236: 131 (1966).
3. R. W. Carpenter and E. A. Kenik, "The Effect of Irradiation on Void Swelling and Chemical Order in Ni-Mo, Ni-V, and Ni-Ti Alloys," *Metallurgical* Transactions, in press.
4. G.J.C. Carpenter and E. M. Schulsen, "The Disordering of Zr_3Al by 1-MeV Electron Irradiation," paper presented in the 1977 TMS-AIME Fall Meeting, Chicago, Oct. 24—27, 1977.
5. C. T. Liu and H. Inouye, unpublished results.

7. STATUS OF IRRADIATION EXPERIMENTS

Irradiation experiments are presently being conducted in the ORR and HFIR, which are mixed-spectrum fission reactors, and in the EBR–II, which is a fast-spectrum reactor. Experiments are generally cooperative between several program participants. Experiment plans, test matrices, etc. are reviewed by the Alloy Development for Irradiation Performance Task Group.

7.1 STATUS OF ORR-MFE-1 AND -2 IRRADIATION EXPERIMENTS — J. W. Woods, A. F. Zulliger., and E. E. Bloom (ORNL)

7.1.1 ADIP Task

These two experiments support those tasks of the ADIP Program Plan that require neutron irradiations to accomplish their objectives. The experiments contain alloys from each alloy development path.

7.1.2 Objective

The ORR-MFE-1 and ORR-MFE-2 irradiation experiments are vehicles for irradiation of samples for postirradiation testing and examination (e.g., tensile, creep-rupture, and fatigue testing; measurement of irradiation creep; and microstructural examination). The objectives of these experiments from the viewpoint of alloy development are to examine:

1. effects of composition on the tensile properties of stainless steels with nominal compositions near that of type 316 stainless steel;
2. effects of preirradiation heat treatment on the tensile properties of type 316 stainless steel;
3. effects of irradiation on the tensile properties of type 316 and 16-8-2 stainless steel welds;
4. effects of irradiation on the tensile properties of representative path B alloys;
5. effects of irradiation on the tensile, creep-rupture, and fatigue properties and on the microstructures of representitative titanium alloys, vanadium alloys, and niobium alloys;
6. irradiation creep of type 316 stainless steel and Nimonic PE-16, path A and B alloys, respectively;
7. postirradiation fatigue properties of type 316 stainless steel, Nimonic PE-16, and high-nickel alloys X-750 and Inconel 600;
8. effects of irradiation on tensile and creep-rupture properties of alloys with long-range order (path D).

7.1.3 Summary

Irradiation of ORR-MFE-1 in position C-7 of the ORR began on February 8. This experiment contains microstructural and composition

variations on type 316 stainless steel (path A), several precipitation-strengthened Fe-Ni-Cr alloys (path B), and titanium alloys (path C). With the initial core configuration (fuel surrounding the experiment) the desired low irradiation temperatures, particularly 250 and 350°C, could not be attained. The core configuration was changed and control temperatures were raised. The experiment is now in the reactor. The irradiation time will be determined when neutron flux, spectrum, and damage production calculations are complete. Experiment ORR-MFE-2 is being redesigned for more efficient heat removal. Most of the original ORR-MFE-1 and -2 test matrices will be accomplished in the redesigned experiment. The ORR-MFE-2 schedule will be delayed about two months.

7.1.4 Progress and Status

7.1.4.1 Introduction

The number of times each atom is displaced from its normal lattice site (dpa) and the amount of helium produced by (n,α) transmutations are felt to be the most critical quantities for description of damage produced by a fusion reactor neutron spectrum. Mixed-spectrum fission reactors (those having high fluxes of both fast and thermal neutrons) provide an approximation of the damage created in a fusion reactor for materials containing nickel. Fast neutrons generate atom displacements, and thermal neutrons produce helium by the two-step reaction sequence

$$^{58}\mathrm{Ni} + n \rightarrow {}^{59}\mathrm{Ni} \ ,$$

$$^{59}\mathrm{Ni} + \mathrm{n} \rightarrow {}^{56}\mathrm{Fe} + {}^{4}\mathrm{He} \ .$$

By controlling the fast and thermal fluxes, the He-to-dpa production ratio can be matched to that in a fusion reactor. Since all path A and B alloys contain nickel, a good approximation of fusion reactor helium and dpa production can be obtained. For path C alloys the helium production rate in a fission reactor is much lower than in a fusion reactor. Without techniques to produce the needed helium [e.g., preinjection, doping with isotopes having desired (n,α) cross sections, etc.] fission reactors

provide only atom displacements. Until these techniques are developed and proven, fission reactors can provide only basic radiation effects data on path C alloys. These data are, however, important, particularly in the scoping phase of alloy development and as concerns elimination of unacceptable alloys, heat treatments, etc.

7.1.4.2 Status of ORR-MFE-1

This is the first experiment in support of fusion reactor materials development to be conducted in the ORR. The experiment vehicle is similar to that used in previous experiments on other materials development programs. The significant difference between ORR-MFE-1 and previous experiments was the position in the reactor. This experiment was placed in position C7 and had fuel elements on four sides [see Fig. 7.1.1(a)]. All previous experiments had been conducted in position B8 and generally had fuel only on two sides. It is desirable to maximize the amount of fuel around the experiment to increase the fast neutron flux and thus the displacement production rate. With the reactor core configuration shown in Fig. 7.1.1(a), temperatures in the experiment exceeded the desired control temperature by as much as 300°C with the reactor operating at 30 MW. Two actions were taken to maximize the usefulness of the experiment: (1) the core configuration was changed to that shown in Fig. 7.1.1(b), and (2) some control temperatures were raised. The final layout of the experiment and irradiation temperatures are shown in Table 7.1.1. Irradiation temperatures called for in the initial experiment planning are also shown. Alloy compositions and heat treatments included in the experiment are:

Type 316 Stainless Steel Microstructure Series. This series includes tensile samples from the MFE reference heat of type 316 stainless steel (composition given in Table 7.1.2). Microstructures were developed by the following heat treatments before sample fabrication:

annealed at 1050°C + 20% cold work
annealed at 1150°C + 20% cold work
annealed at 1050°C + 30% cold work
annealed at 1050°C + 50% cold work
annealed at 1050°C + 10 hr at 800°C
annealed at 1050°C + 10 hr at 800°C + 20% cold work
annealed at 1050°C + 20% warm work at 300°C
annealed at 1050°C

ORNL-DWG 73-6240

POOL

W

A-1 Be	A-2 Be	A-3 Be	A-4 154	A-5 253	A-6 153	A-7 Be	A-8 Be	A-9 Be
B-1 Be	B-2 Be	B-3 254	B-4 79	B-5 226	B-6 89	B-7 163	B-8 252	B-9 Be
C-1 Be	C-2 265	C-3 162	C-4 144	C-5 128	C-6 151	C-7 Exp	C-8 265	C-9 Be
D-1 Be	D-2 Exp	D-3 144	D-4 104	D-5 180	D-6 110	D-7 145	D-8 HT	D-9 Be
E-1 Be	E-2 137	E-3 143	E-4 127	E-5 181	E-6 127	E-7 180	E-8 143	E-9 Be
F-1 Be	F-2 Be	F-3 146	F-4 47	F-5 180	F-6 53	F-7 221	F-8 Be	F-9 Be
G-1	G-2	G-3	G-4	G-5	G-6	G-7	G-8	G-9 Be

S N

(a)

E

POOL

W

A-1 Be	A-2 Be	A-3 Be	A-4 154	A-5 253	A-6 153	A-7 Be	A-8 Be	A-9 Be
B-1 Be	B-2 Be	B-3 254	B-4 78	B-5 226	B-6 89	B-7 Be	B-8 Be	B-9 Be
C-1 Be	C-2 268	C-3 161	C-4 144	C-5 128	C-6 151	C-7 Exp	C-8 Be	C-9 Be
D-1 Be	D-2 Exp	D-3 143	D-4 104	D-5 179	D-6 110	D-7 Be	D-8 HT	D-9 Be
E-1 Be	E-2 172	E-3 175	E-4 173	E-5 121	E-6 172	E-7 179	E-8 174	E-9 Be
F-1 Be	F-2 271	F-3 145	F-4 47	F-5 180	F-6 53	F-7 220	F-8 Be	F-9 Be
G-1 Be	G-2 Be	G-3 Be	G-4 Be	G-5 Be	G-6 Be	G-7 Be	G-8 Be	G-9 Be

S N

(b)

E

Fig. 7.1.1. Fuel Element Loadings of the ORR for Experiment ORR-MFE-1. The experiment is in position C-7. The code in each lattice position is used as follows: HT = hydraulic tube, Be = beryllium element, Exp = experiment, number = loading in g ^{235}U in fuel element. (a) Loading at start of experiment. (b) Revised loading.

Table 7.1.1. Plan of ORR-MFE-1 Experiment, Showing Material Variables and Planned and Final Irradiation Temperatures

Level	Irradiation Temperature, °C, in Each Quadrant Final Control and (Planned)				Samples Irradiated (Quadrants)
	North	West	South	East	
1	350 (350)	450 (450)	550 (550)	650 (650)	Samples from damage analysis and fundamental studies programs (all)
2	350 (250)	450 (350)	550 (450)	650 (550)	Path B alloy series (all)
3	450 (250)	375 (350)	550 (450)	650 (550)	Samples from damage analysis and fundamental studies programs (all)
4	600 (350)	575 (450)	625 (550)	650 (650)	Samples from damage analysis and fundamental studies programs (all)
5	500 (450)	500 (350)	550 (450)	600 (550)	Ti alloys — fatigue samples (N) tensile samples (W,S,E)
6	525 (350)	575 (450)	575 (450)	650 (550)	Type 316 stainless steel composition series (all)
7	525 (350)	475 (350)	575 (450)	650 (550)	Type 316 veld samples (all)
8	500 (450)	450 (350)	550 (450)	600 (550)	Ti alloys — fatigue samples (N) creep samples (W) tensile samples (S,E)

Table 7.1.2. Composition of MFE Reference Heat of Type 316 Stainless Steel, Heat X-15893'

	Content, wt %							
	Ni	Cr	Mo	Mn	Si	C	P	S
Mill analysis	12.4	17.3	2.1	1.8	0.65	0.05	0.03	0.02
Vendor overcheck	12.8	17.5	2.2	1.8	0.64	0.05	0.03	0.02
ORNL overcheck	12.4	17.3	2.1	1.7				

[a] Titanium not reported.

Type 316 Stainless Steel Composition Series. This series includes tensile samples of alloys having the nominal composition of type 316 stainless steel with systematic variations in Si, Mo, Ti, C, and P. All samples are in the 20%-cold-worked condition. These alloys were supplied by the Breeder Reactor Cladding and Duct Materials Development Program supported by the Division of Reactor Research and Technology, Department of Energy.

Type 316 Stainless Steel Weld. This series consists of tensile samples from welds made with type 316 and 16-8-2 stainless steel filler metal on type 316 stainless steel plate. It includes both longitudinal samples, which are all weld metal, and transverse samples. which include weld metal, heat-affected zone, and base metal.

Path B Alloy Series. The path B alloy series consists of tensile samples of Nimonic PE-16 in three heat treatment conditions and four developmental precipitation-strengthened alloys, also supplied by the Breeder Reactor Cladding and Duct Materials Development Program of the Division of Reactor Reasearch and Technology.

Titanium Alloys. The titanium alloy test matrix is summarized in Table 7.1.3. The alloys and heat treatments were selected to explore a-rich, β-rich, and (α + β) structures. Tensile, creep-rupture, and fatigue samples are included.

Table 7.1.3. Test Matrix for Titanium Alloys in ORR-MFE-1

Alloy Designation	Heat Treatment	Relative Neutron Flux	Irradiation Temperatures, °C		
			Tensile	Fatigue	Creep
Ti—6% Al—4% V (α + β Alloy)	Duplex Anneal	High	500, 550, 600	500	
		Low	450, 550, 600	500	450
	β Anneal	High	500, 550, 600	500	
		Low	450, 550, 600	500	450
	Mill Anneal	High	500, 550, 600		
		Low	450, 550, 600		
Ti—6242 S (α Rich)	Duplex	High	500, 550, 600	500	
		Low	450, 550, 600	500	450
Ti—5621 S (α Rich)	Duplex	High	500, 550, 600	500	
		Low	450, 550, 600	500	450
Ti-38644 (β Rich)	Stabilized	High	500, 550, 600		
		Low	450, 550, 600		

7.1.4.3 Description of Experiment ORR-MFE-1

An aluminum framework, constructed as shown by the sketch in Fig. 7.1.2 was used to position the heaters and specimens, as well as to support the heater leads and thermocouples. The length of the mounting frame was divided into eight levels, each containing four subassemblies. Each subassembly had a carousel-type spacing frame, which would hold up to 16 miniature sheet specimens. In some subassemblies a tube of electron microscopy specimens replaced three sheet specimens. Figure 7.1.3 shows the components of a typical subassembly.

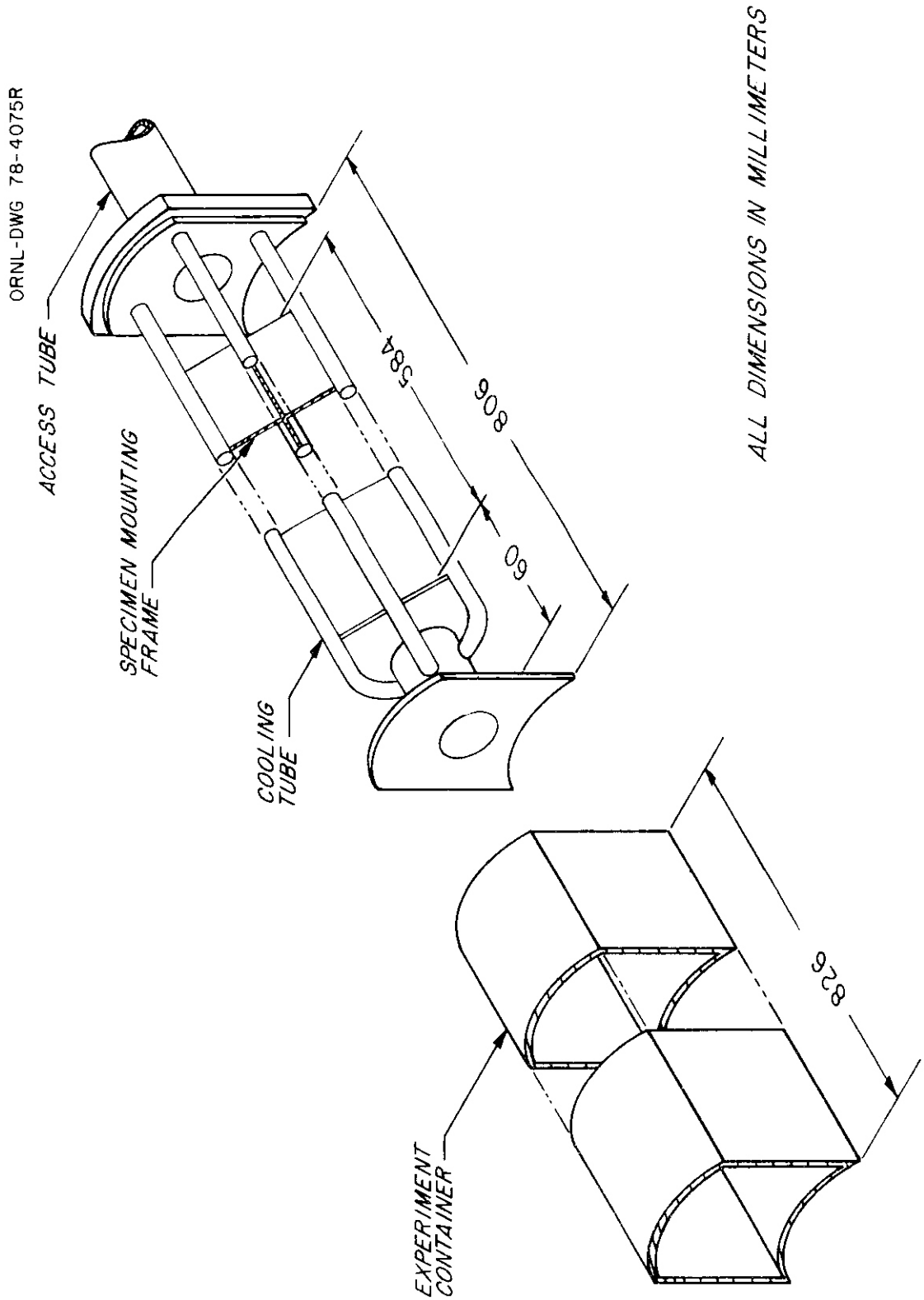

Fig. 7.1.2. Specimen Mounting Frame for ORR-MFE-1 Experiment.

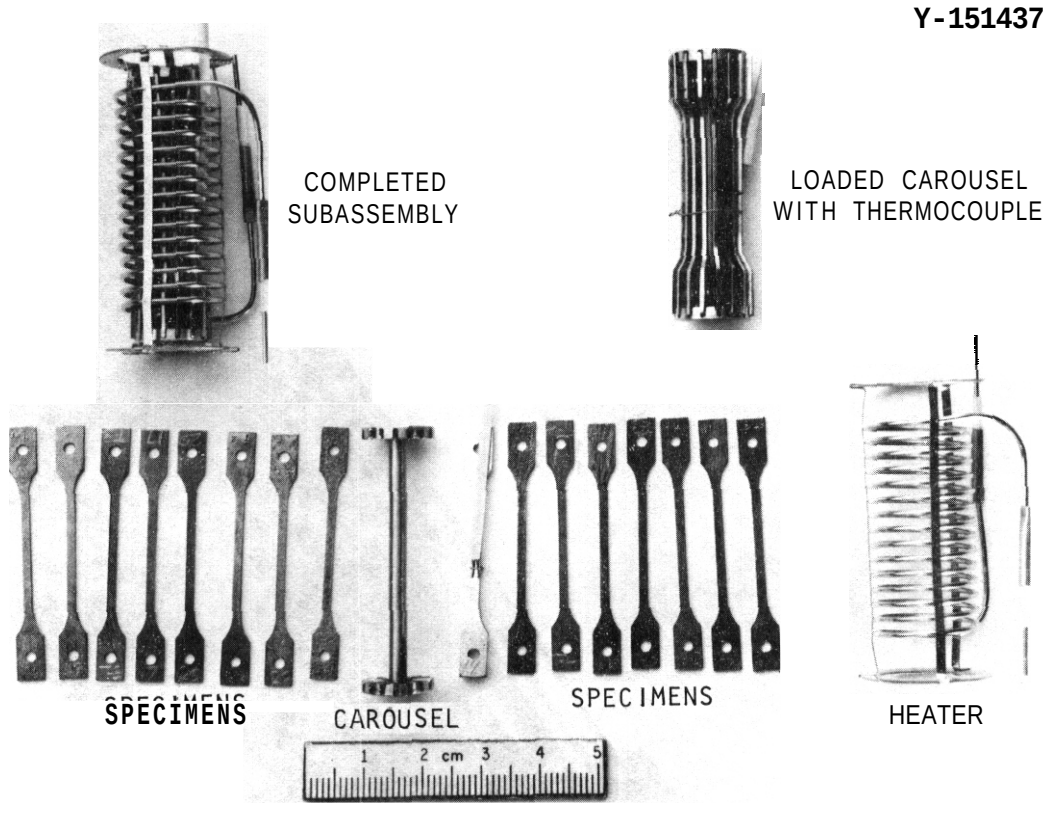

Fig. 7.1.3. Components of a Subassembly for ORR-MFE-1 Experiment.

The 32 subassemblies were positioned on the mounting frame, the heater ends were rigidly attached to it, and then connections were made to the heater and thermocouple leads. Figure 7.1.4 shows the assembled experiment. Figure 7.1.5 is a close-up of one subassembly.

After all the subassemblies were in place, the experiment container was positioned over the mounting frame and seal welded to the top and bottom plates. All electrical leads from the experiment were passed through the top plate to the access tube and finally terminated in the junction box located above the water at poolside. The output of one thermocouple in each subassembly was fed to a proportioning on-off controller, which adjusted the power input to that heater.

Neutron dosimetry for both ORR-MFE-1 and -2 was planned by L. R. Greenwood of Argonne National Laboratory. Plans include a short irradiation in the E-7 position for spectral mapping. For the long irradiations in both C-7 and E-7 positions, gradient wires of Fe, Co-Al,

ORNL-PHOTO 0644-78

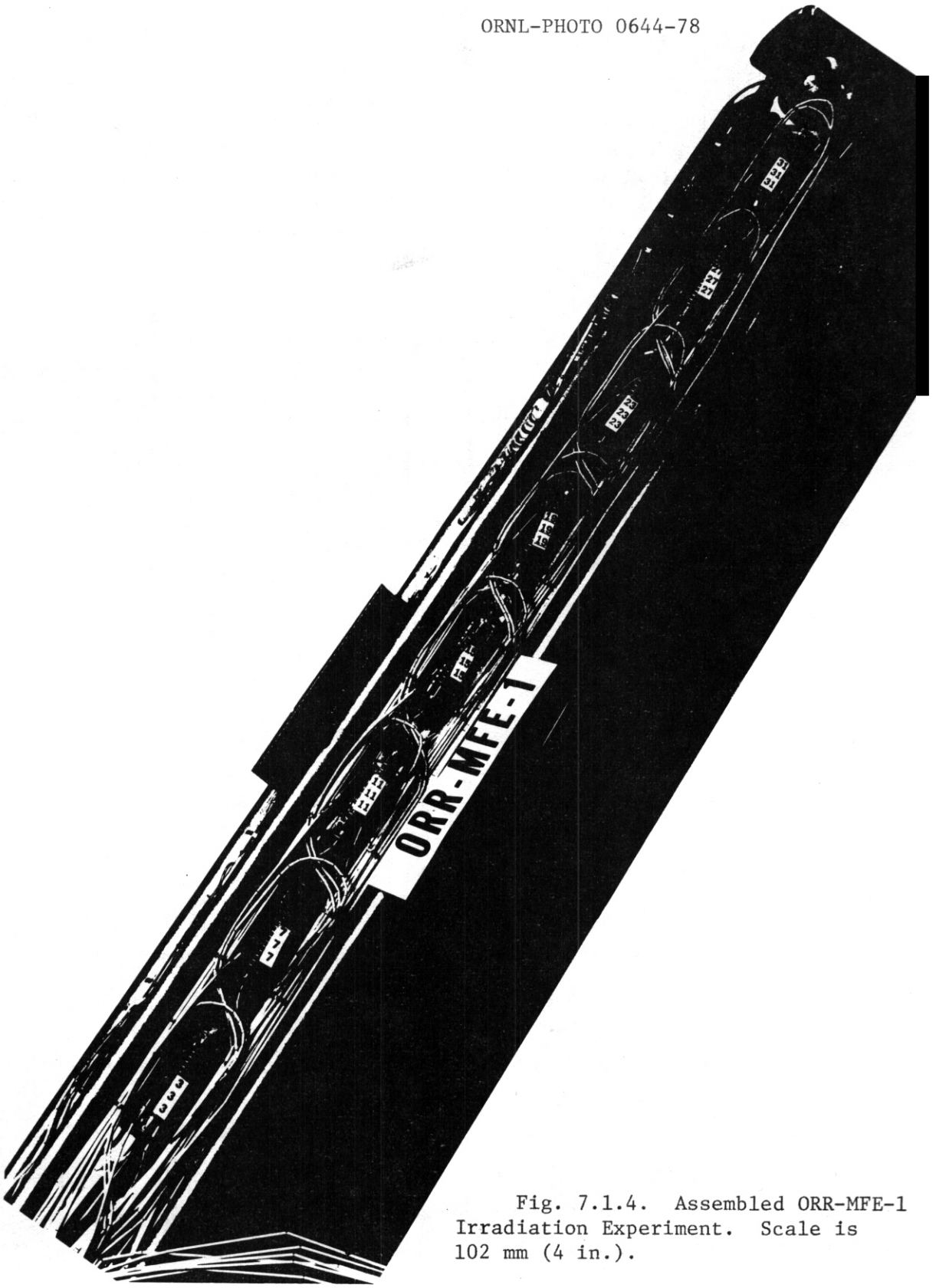

Fig. 7.1.4. Assembled ORR-MFE-1 Irradiation Experiment. Scale is 102 mm (4 in.).

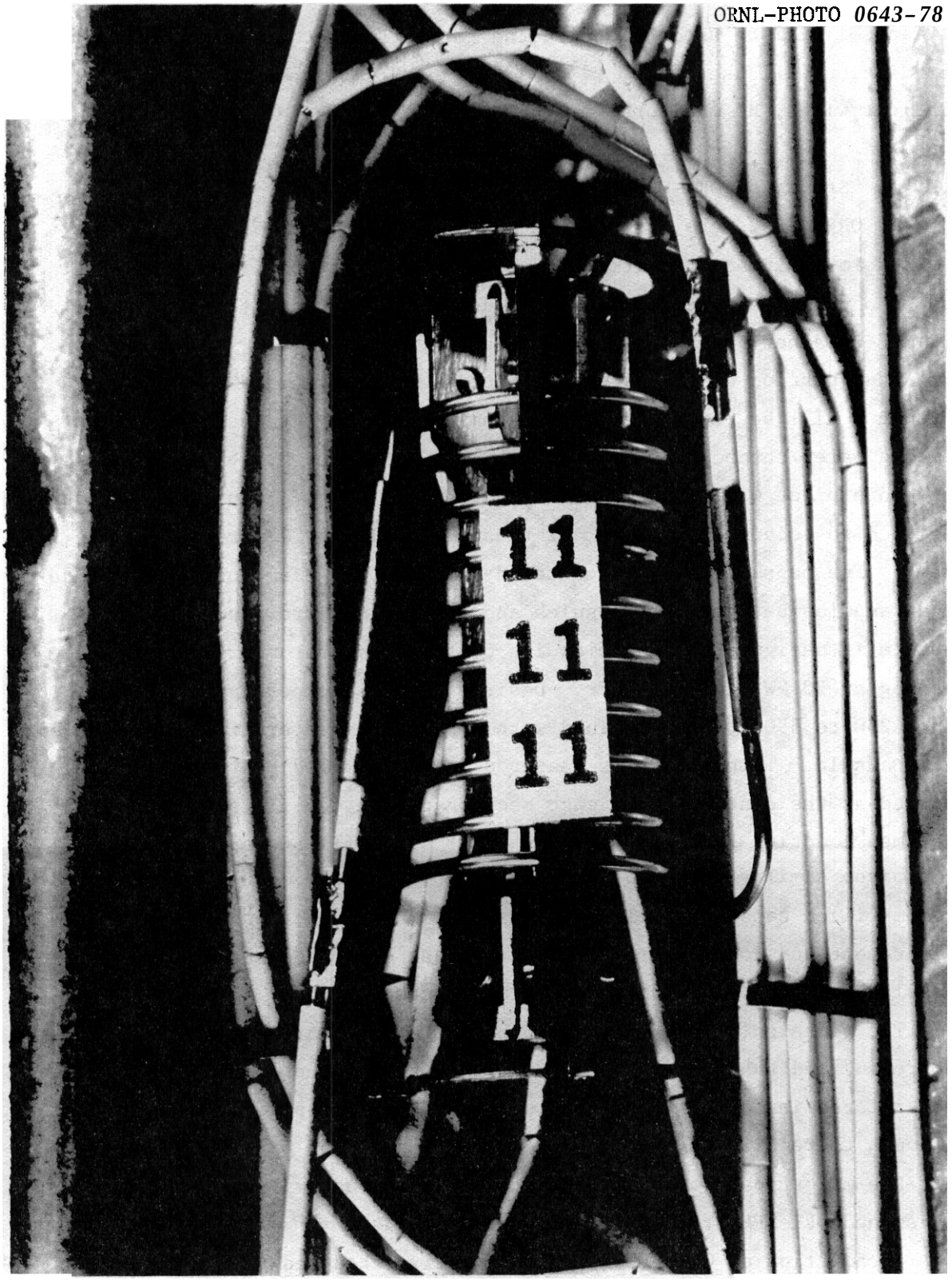

Fig. 7.1.5. Close-Up of Subassembly for ORR-MFE-1 Experiment.

Ni, and Ti will be used to obtain the total fluence. The spectral mapping irradiation will use ^{237}Np, ^{235}U, ^{238}U, and Sc monitors in addition to the gradient wires, He monitors, and bare and Cd-covered Au foils.

7.1.4.4 Status of ORR-MFE-2

If ORR-MFE-2 were of the same design as used for ORR-MFE-1, the desired lower irradiation temperatures could not be obtained unless the number of samples were drastically reduced. We decided to redesign ORR-MFE-2 rather than accept this penalty.

That portion of the specimen mounting frame occupied by levels 1 through 6 will be replaced with an aluminum core piece that contains cooling water channels as well as four 25-mm-diam by 0.31-m-long holes. This core piece will accommodate 16 gas-gap capsules. Capsules are being designed to accommodate either 22 tensile samples or 12 pressurized tubes. The capsules will be centered in the 25-mm-diam holes to provide a gas annulus between the capsules and the cooled core piece. Each capsule is designed to run below its control temperature with nuclear heating at 30 MW reactor power. Desired control temperatures, in the range 250 to 650°C, are attained with electrical heaters in the center of each capsule. Temperature is measured and controlled by thermocouples located at the center of the gage section of the tensile samples. The specimen mounting frame in levels 7 and 8 also will be replaced by a core piece similar to the one described above. Four doubly encapsulated sodium-filled capsules will be irradiated in this section. Temperature measurement and control are similar to those described above. These capsules will contain refractory metal specimens.

The redesign of ORR-MFE-2 enables us to irradiate 432 sheet specimens, 48 pressurized tubes, and up to 1000 TEM disks at the desired test temperatures instead of 352 sheet specimens as were placed in ORR-MFE-1. Although there will be some modification of the test matrix, we believe that the major goals of ORR-MFE-1 and -2 can be accomplished with the redesigned ORR-MFE-2.

Irradiation of ORR-MFE-2 was originally scheduled to begin March 27, 1978. As a result of the necessary redesign, irradiation of the experiment is now planned to begin with Cycle 145, June 2, 1978.

7.1.5 Conclusions and Plans for Future Work

The high temperatures in the ORR-MFE-1 irradiation experiment resulted from nuclear heating rates higher than had existed for the core configurations and in the particular core position in which experiments of this design were previously used. Estimated neutron energy spectrum and helium and displacement production rates for the present core configuration will be calculated, and recommendations for proceeding with ORR-MFE-1 will be developed. When an experiment of this design is surrounded with fuel, temperatures at the lower part of the range of interest are very difficult to obtain. Rather than drastically reduce the number of samples in the experiment, an action required to reach the low temperatures with the present design, we decided to design an experiment with more efficient heat removal. This design is now well under way and will be used. In ORR-MFE-2 the more efficient heat removal will allow irradiation of about 432 sheet tensile samples and 48 pressurized tube samples. Nearly all the original ORR-MFE-1 and -2 test matrix can thus be accomplished in the redesigned ORR-MFE-2. The experiment will be delayed about two months by this action.

7.2 CAPSULE DESIGN FOR IRRADIATION OF FATIGUE CRACK PROPAGATION SPECIMENS IN ORR - H. E. Watson, J. A. Sprague, and D. J. Michel (Naval Research Laboratory)

7.2.1 ADIP Task

The work described in this report is being performed as part of the following ADIP Program Plan Tasks: I.A.2, Define Test Matrices and Test Procedures; I.B.1, Fatigue Crack Growth in Austenitic Alloys (Path A); I.B.2, Fatigue Crack Growth in High Strength/High Temperature Fe-Ni-Cr Alloys (Path B); I.B.3, Fatigue Crack Growth in Reactive/Refractory Alloys (Path C).

7.2.2 Objectives

The objective of this work is to design a capsule for irradiation of compact-tension geometry fatigue crack propagation specimens at controlled elevated temperatures in the high-flux regions of ORR.

7.2.3 Summary

The capsule has been designed to allow the irradiation of fatigue crack propagation specimens with the 0.5T compact tension (0.5T CT) geometry at elevated temperatures in the high-flux region of the ORR core. Temperature control will be achieved by a balance between gamma heat generation in the specimens and heat loss to the reactor cooling water through an externally controlled variable gas gap. The design of the ORR capsule has been derived from NRL capsules used to irradiate reactor pressure vessel steels in a number of research reactors, with modifications to the geometry to allow for the high gamma heating rate encountered in the core of ORR. The first assembly of this design will be irradiated as experiment MFE-3, scheduled for insertion in ORR by the end of FY 78.

7.2.4 Progress and Status

7.2.4.1 Introduction

The first wall structure of a magnetic-confinement fusion reactor (MFR) is expected to experience combined cyclic-static loading at elevated temperatures, while being subjected to intense neutron and ion irradiation. Under those conditions, the propagation of cracks from flaws is expected to be an important potential failure mechanism. The high helium concentrations and high displacement damage levels projected for first-wall materials may adversely affect their crack propagation resistance by the combined effects of matrix hardening and weakening of the grain boundaries. It is, therefore, important to use the high helium generation rates available for nickel-bearing alloys in high-flux mixed-spectrum reactors such as OF3 to simulate the effects of fusion reactor irradiation on fatigue crack propagation. It is important also to include titanium-base alloys in these experiments at an early date, since no baseline data exist on their irradiation performance. To fulfill these goals, a capsule has been designed to allow the irradiation of small fracture-mechanics-type crack propagation specimens at controlled elevated temporatures in the core of ORR.

7.2.4.2 Capsule Design Considerations

In designing an irradiation capsule for these experiments, several requirements of the specimen type, the irradiation environment, and the experiment matrix had to be considered. The principal specimens were to be 0.5T CT crack propagation specimens of the WOL design, which have a cross-section of 40.64 mm (1.60 in.) x 30.5 mm (1.2 in.) and a thickness of 12.7 mm (0.5 in.). Some thickness-effect specimens were also to be included with the same cross-section, and thicknesses of 2.5 mm (0.1 in.), 5.0 mm (0.2 in.), 7.5 mm (0.3 in.), and 10.2 mm (0.4 in.). The mass of a full 0.5T specimen ranges from ∿50 gm for Ti-base alloys to ∿90 gm for Fe-Ni-Cr alloys. The irradiation environment in the E-3 position of ORR, to be used for the MFE-3 experiment, is characterized by a peak thermal neutron flux of ∿2 x 10^{14} n/cm^2-sec, peak fast neutron flux (>0.18 MeV) of ∿3 x 10^{14} n/cm^2-sec, a gamma heating rate of ∿8 watts per gm, and

cooling by low pressure water at 60°C. The proposed experiment matrix called for irradiation for approximately one year at temperatures between 350 and 550°C.

Of the above considerations, the size of the specimens and the high gamma heating rate have the strongest implications for the capsule design. For 0.5T CT specimens to operate at a constant temperature, 720 watts must be removed from each Fe-Ni-Cr specimen, and 400 watts from each Ti-alloy specimen. Because of this high heat input from gamma heating, it was decided to control the experimental temperatures by regulating the heat loss to the reactor cooling water. Based on previous experience with elevated temperature irradiations in water-cooled reactors, the variable gas gap (vgg) method of temperature control was chosen.

In principal, the operation of a vgg capsule is quite simple, as illustrated in Fig. 7.2.1. The capsule is constructed with a flexible

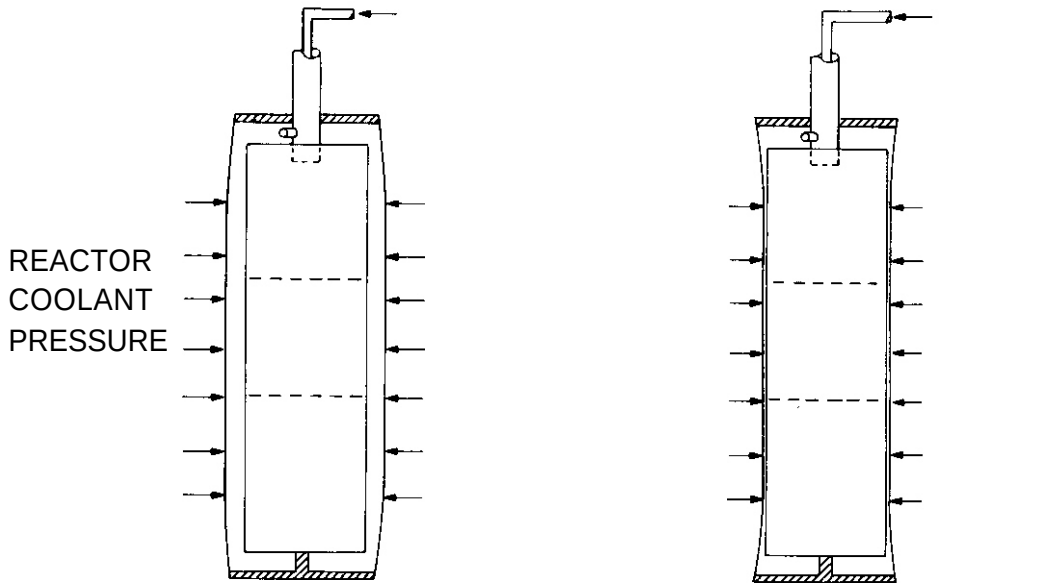

Fig. 7.2.1 Schematic illuatration of the operating principle of the variable gas gap irradiation capsule. The width of the gap, and thus the heat transfer to the cooling water, is controlled by a balance between the pressures of the reactor coolant and the control gas.

outer sheath, and the spnce between this sheath and the specimens is connected to a controlled-pressure gas source outside of the reactor. The width of the gas gap between the outer and inner skins is controlled by the balance between the gas pressure and the pressure of the reactor cooling water. This gap acts as a variable heat leak, since the thermal conductivity of the gas (5×10^{-4} to 3×10^{-3} watts/cm ^{o}K) is much lower than that of the metal specimens and capsule components ($\sim$0.2 watts/cm ^{o}K for stainless steels). An increase in the width of the gap (shown greatly exaggerated in Fig. 7.2.1), therefore, causes an increase in the equilibrium operating temperature of the experiment. The experiment control console permits the use of a single gas or the mixing of two gases to improve the heat removal rate.

The high gamma heating in the E-3 position of ORR required that the experiment be designed for maximum available heat transfer to the cooling water. The irradiation assembly was therefore designed with three subcapsules, each one of which is the thickness of one 0.5T CT specimen. This allows the heat to be removed from both side faces of each specimen. For this geometry, the temperature rise as a function of gas gap width could be approximated by assuming one-dimensional heat flow normal to the specimen faces.

Figure 7.2.2 shows this temperature rise calculated for 316 SS and Ti-6Al-4V, with 8 watts/gm gamma heating and He control gas (.0028 watts/gm ^{o}K thermal conductivity). Three design implications are apparent from these plots. First, the small values of the gap width imply that a very sensitive control system will be required to avoid undesirable temperature fluctuations. Second, great care will be required in the design and assembly of the subcapsules to avoid large temperature gradients. Finally, the Fe-Ni-Cr and Ti-alloy specimens will have to be separated into different subcapsules to avoid their running at much different, unplanned temperatures.

The high gamma heating rate causes an additional problem that is fundamental to the specimen geometry and cannot be solved by capsule design. Since the heat is generated fairly uniformly through the thickness of a specimen, and it is removed at the surfaces, the temperature distribution across the thickness will be approximately parabolic. In the worst

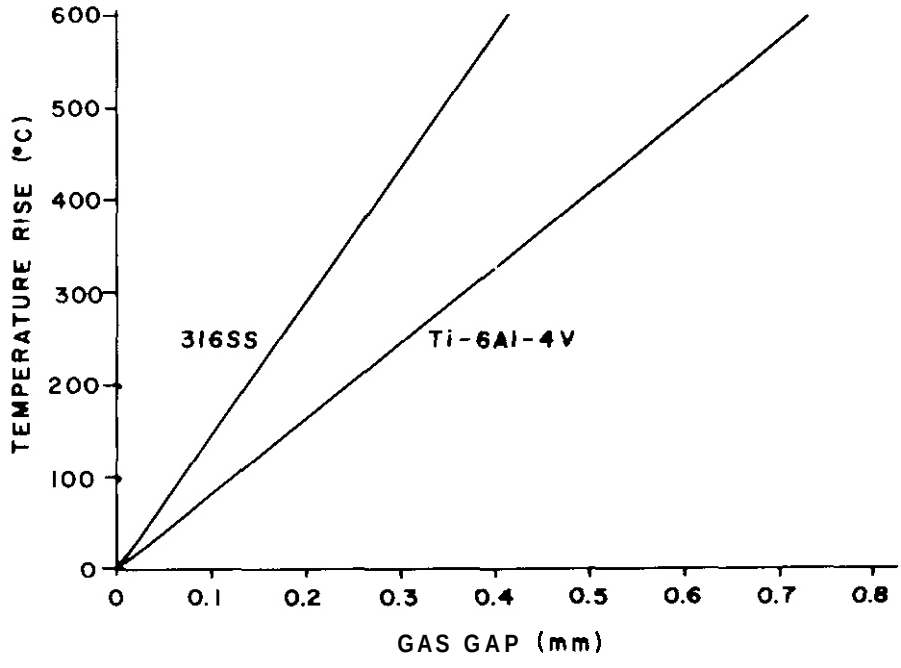

Fig. 7.2.2 The temperature rise across a helium gas gap calculated for 316 SS and Ti-6Al-4V 0.5T CT specimens in the MFE-3 capsule design. A gamma heating rate of 8 watts per gram was assumed.

case, assuming uniform 8 watts/gm gamma heating, the temperature at the center could be as much as 50°C higher than that at the surfaces. Due to self-shielding by the specimens, the actual gradients may not be this large, but discussions are in progress with the ORR staff to attempt to tailor the E-3 position somewhat to reduce the gamma heating rate in the E-3 position as much as possible. The specimen-center temperatures during irradiation will be monitored by thermocouples embedded in test blocks in each of the subcapsules.

7.2.4.3 Description of Capsule Design

The above criteria led to an irradiation assembly for MFE-3 that consists of three subcapsules, each containing the equivalent of 12 0.5T CT specimens. A plan of one of these subcapsules is shown in Fig. 7.2.3. The specimens are laid flat in two rows, with a central open channel left for gas tubes and thermocouple wires. The thinner specimens are to be

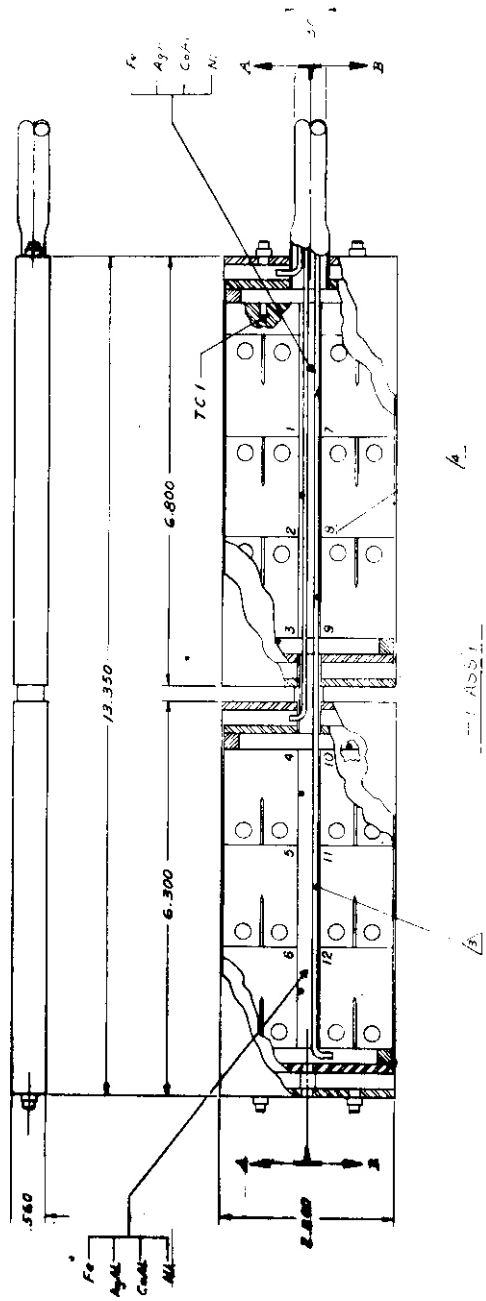

Fig. 7.2.3 Design for each of three subcapsules for the MFE-3 experiment. The subcapsule is divided into two independently controlled sections, each holding the equivalent of six 0.5T CT specimens.

stacked in pairs to give the same total thickness at each specimen position. To improve the temperature uniformity, the subcapsule is divided vertically into two sections, giving a total of six independently controlled sections in the complete assembly. Temperatures will be monitored at several positions in each section.

Before loading into the subcapsules, specimens will be ground to a uniform thickness. Following welding of the inner skin, it will be shrunk onto the specimens in a high pressure chamber to assure good thermal contact. The subcapsule assembly will then be completed by welding on the outer skins. The three subcapsules will be welded together into an assembly to hold them in the proper position in the ORR core piece, and will then be shipped to Oak Ridge for final assembly to a standard ORR lead tube and core 'piece.

7.2.5 Conclusions

An assembly has been designed for the irradiation of 0.5T CT crack propagation specimens at controlled elevated temperatures in the high-flux core region of ORR. The assembly will contain the equivalent of 36 0.5T CT specimens in three subcapsules, with a total of six independently controlled sections. Temperature control in each section is maintained by varying the width of a gas gap using pressure control. The assembly has been designed to allow the maximum possible heat removal from the 0.5T CT geometry to account for the high gamma heating rate encountered in the core-center positions in ORR. The first exper-ment using this design will be irradiated as experiment MFE-3, scheduled for insertion in ORR by the end of FY 78.

7.3 IRRADIATION EXPERIMENT SCHEDULE

Experiment Designation	Major Objective
A. Oak Ridge Research Reactor	
ORR-MFE-1 ORR-MFE-2	Experiments to scope the effects of composition and microstructure on the tensile, fatigue, and irradiation creep of representative path A, B, and C alloys.
ORR-MFE-3	Effects of irradiation on postirradiation fatigue crack growth in representative path A, B, and C alloys.
ORR-MFE-4	Effect of irradiation on tensile, fatigue, and irradiation creep of path A PCA (Prime Candidate Alloy) and path B base research alloys. Spectral tailoring to maintain correct He/dpa ratio. Irradiation on continuing basis.

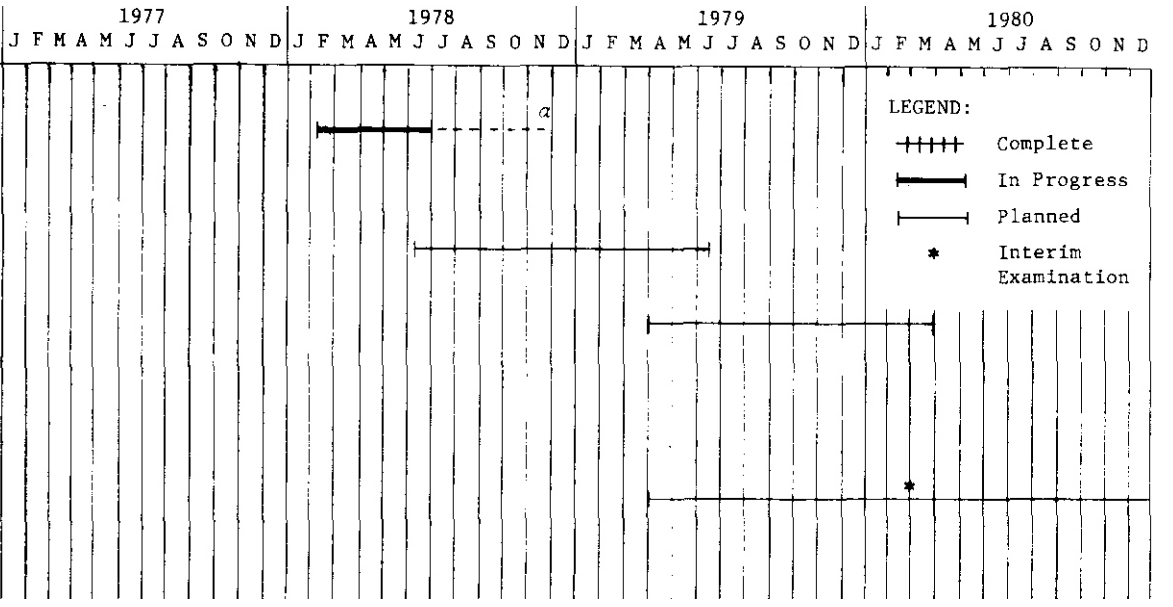

[a]Initially scheduled for 1 year irradiation; this will be reduced because of temperature control problems.

Experiment Designation	Major Objective
ORR-MFE-5	In-reactor fatigue crack growth experiment
Experimental Breeder Reactor II	
Subassembly X 264	Effect of preinjected helium (2–200 at. ppm) on microstructure and tensile properties of 316 SS, PE-16, V and Nb alloys. Fluence $\leq 2.3 \times 10^{26}$ n/m^2, 500–825°C.
Subassembly X 287	Effect of preinjected helium (2–200 at. ppm He) on microstructure and tensile properties of 316 SS, PE-16, V and Nb alloys. Fluence $\leq 4 \times 10^{26}$ n/m^2, 400–700°C.
Subassembly X 217D	Stress relaxation Ti Alloys
Planned, Subassembly Designation not available	Effect of irradiation on swelling, tensile, fatigue, and crack growth properties of Ti scoping alloys. 370, 450, and 550°C, position in reactor not finalized, therefore no fluence estimate

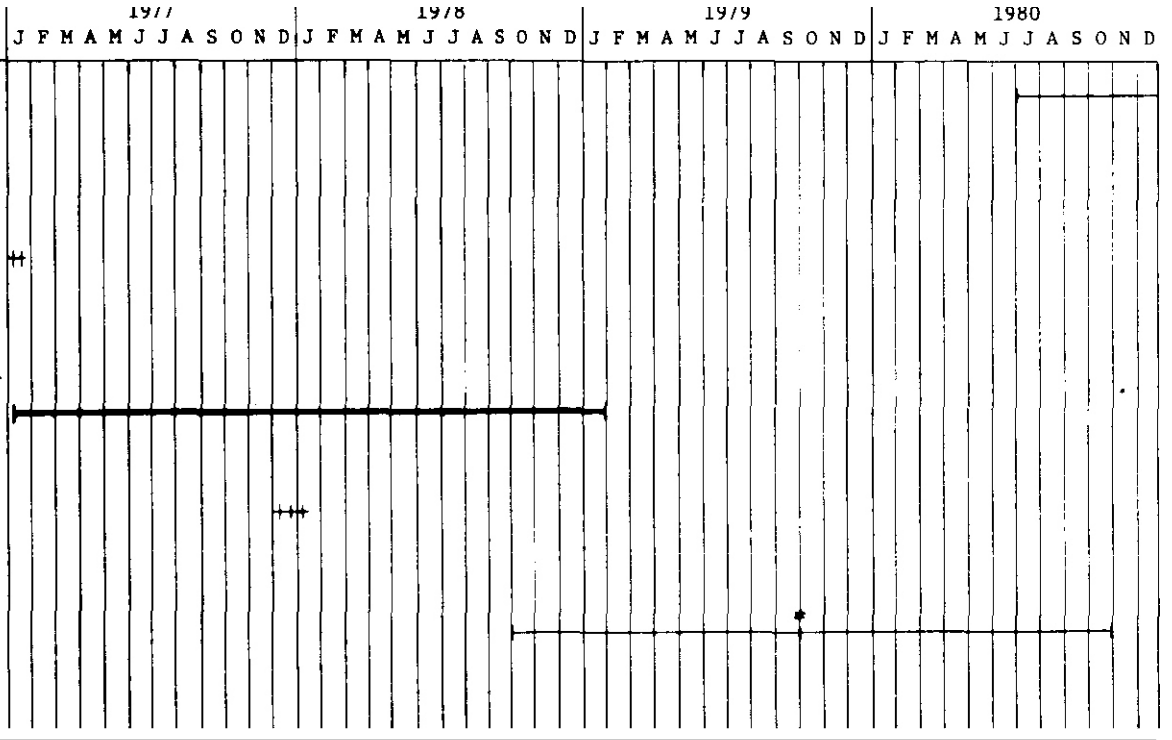

Experiment Designation	Major Objective
Not available	Effect of Irradiation on swelling, tensile, fatigue, and crack growth properties of V and Nb scoping alloys. 370, 450, 550, and 650°C. Position in reactor not finalized, therefore no fluence estimate.
C. High Flux Isotope Reactor (HFIR)	
HFIR-CTR-4	PE-16 for swelling and tensile properties, 300–700°C 2.2–4.5 dpa, 100–350 at. ppm He
HFIR-CTR-7	PE-16 for swelling and tensile properties, 300–700°C 9–18 dpa, 1250–3000 at. ppm He
HFIR-CTR-8	duplicate of -7
HFIR-CTR-9	316 and 316 + Ti for swelling and tensile properties, 280–680°C, 9–18 dpa, 400–1000 at. ppm He

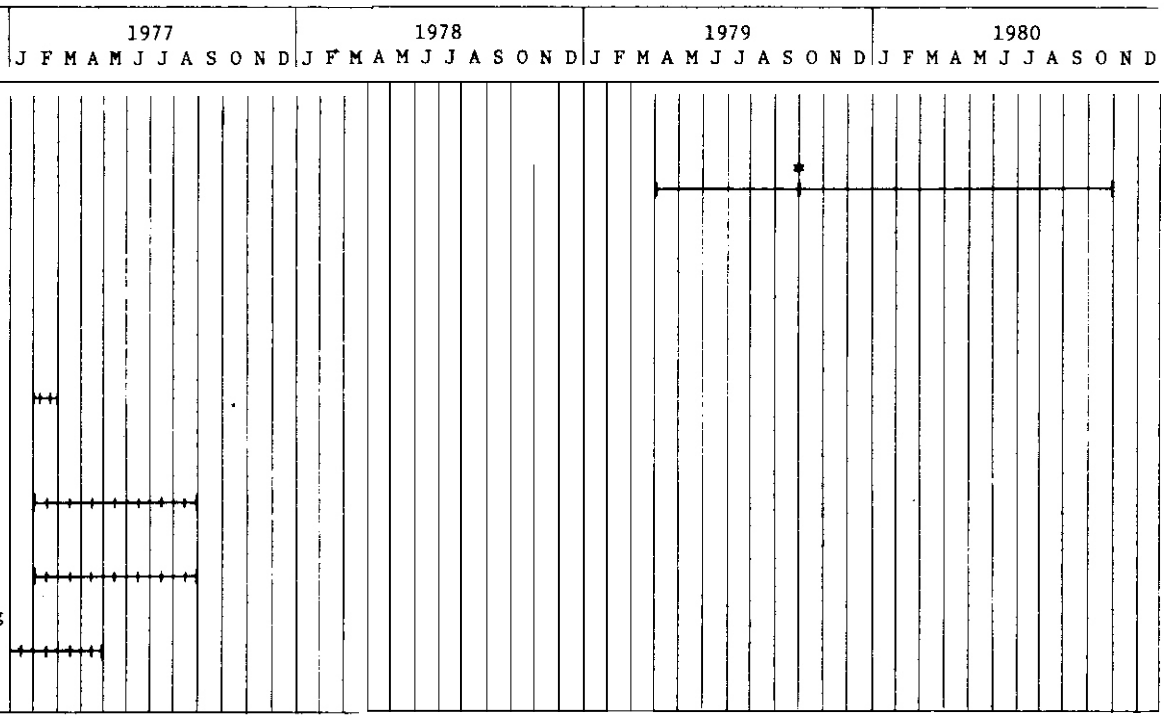

Experiment Designation	Major Objective
HFIR-CTR-10	duplicate of -9
HFIR-CTR-11	
HFIR-CTR-12	316 and 316 + Ti for swelling and tensile properties, 280–680°C, 5.5–11 dpa, 200–500 at. ppm He
HFIR-CTR-13	duplicate of -12
HFIR-CTR-14	20%-CW 316 for fatigue testing 300°C. 9–18 dpa, 400–1000 at. ppm He
HFIR-CTR-15	20%-CW 316 for fatigue testing 500°C, 5.5–11 dpa, 200–500 at. ppm He
HFIR-CTR-16	316, welds, PE-16, and Inconel 600 for swelling and tensile properties, ~55°C, 5.5–11 dpa, 150–2700 at. ppm He (depending on alloy)
HFIR-CTR-17	Type 316 welded with 16-8-2 filler metal for tensile properties and failure analysis, 280–620°C, 6.7–13 dpa, 180–460 at. ppm He in weld metal

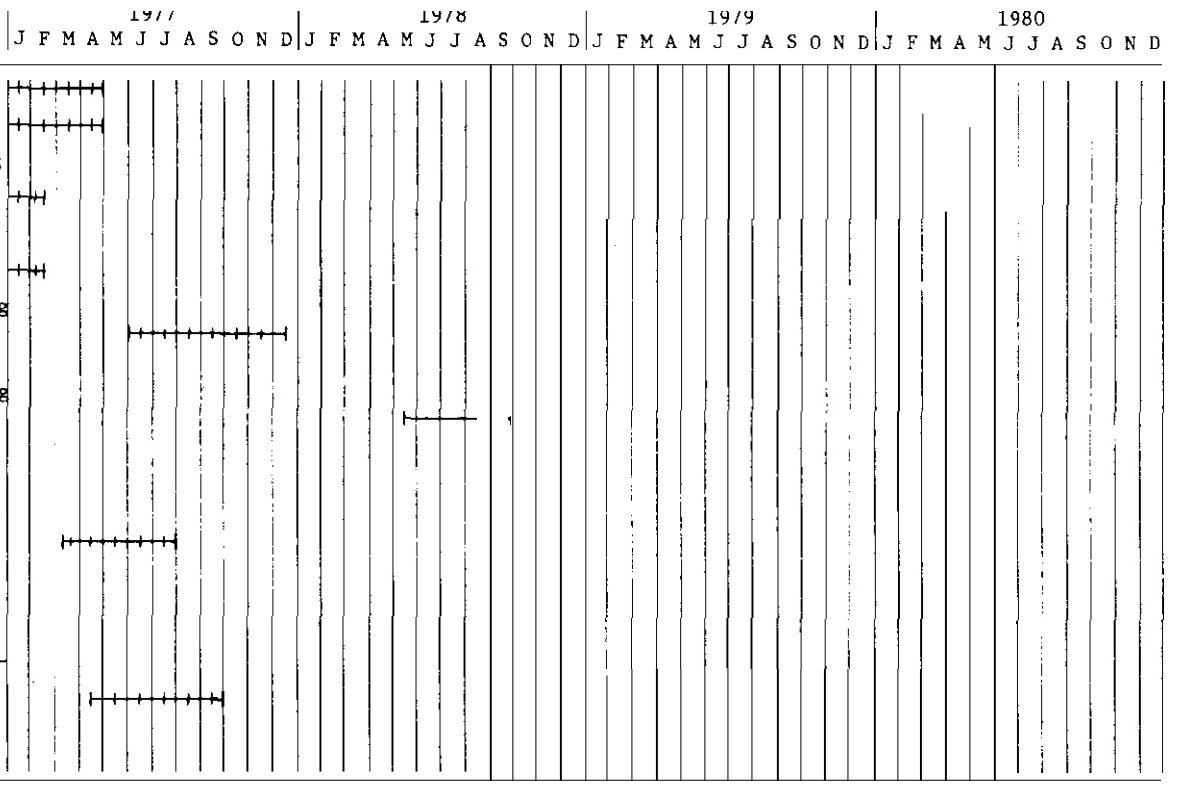

Designation	Major Objective
HFIR-CTR-18	PE-16 and 20%-CW type 316 for swelling and tensile properties, 280–700°C, PE-16: 17–27 dpa, 3400–5600 at. ppm He 316: 27–34 dpa, 1600–2100 at. ppm He
HFIR-CTR-19	316 welded with 316 filler metal for tensile properties, 280–620°C, 5.5–11 dpa, 200–500 at. ppm He
HFIR-CTR-20	20%-CW 316 for fatigue testing, 300°C, 5.5–11 dpa, 200–500 at. ppm He
HFIR-CTR-21	20%-CW 316 for fatigue testing, 500°C, 9–18 dpa, 400–1000 at. ppm He
HFIR-CTR-22	duplicate of -20
HFIR-CTR-23	PE-16 for fatigue testing, 300°C, 4.4–9 dpa, 370–1000 at. ppm He

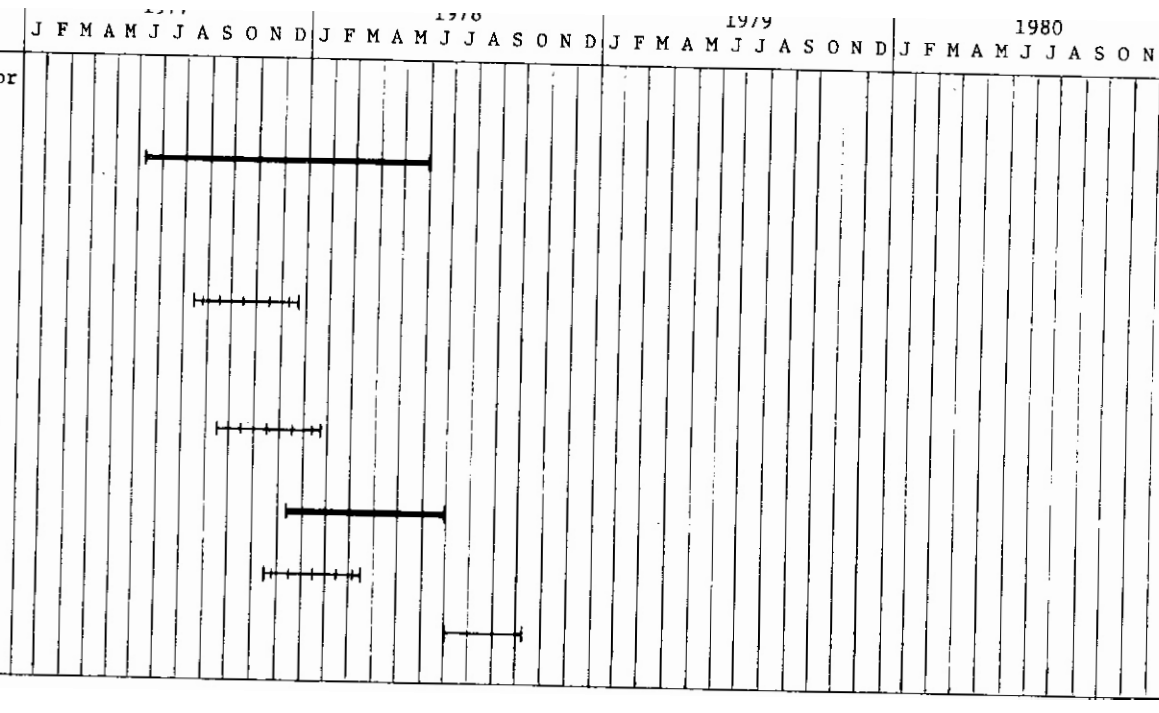

Experiment Designation
Major Objective
J F M A M J J A S O N D J F M A M J J A S O N D J F M A M J J A S O N D J F M A M J J A S O N D
(2 future expts.)
Path A PCA for phase stability, swelling, tensile properties, 280–620°C, 10 dpa, 570 at. ppm He (max)
(2 future expts.)
Path A PCA for phase stability, swelling, tensile properties, 280–620°C, 34 dpa, 2400 at. ppm He (max)
(4 future expts.)
Path B base research alloys, various conditions
(4 to 6 future expts.)
Path C Ti alloys, various conditions

8. CORROSION TESTING AND HYDROGEN PERMEATION STUDIES

Corrosion, erosion, and mass transfer are processes that may degrade mechanical properties, alter heat transfer characteristics of heat transport systems, and present maintenance problems when radioactive nuclides are involved. The importance of hydrogen permeation and the behavior of hydrogen in the alloy systems under development is clear from consideration of tritium inventory, containment, etc. In the early stages of the development program, base-line information is required to define compatible or noncompatible alloy systems and coolants. As optimized alloys are developed, more detailed data on effects of adjustments in alloy composition or structure may be required. Extensive engineering compatibility data will be required on the final optimized alloys.

8.1 CAPSULE TESTS OF IRON-BASE ALLOYS IN LITHIUM — J. H. Devan and J. R. DiStefano (ORNL)

8.1.1 ADIP Task

Task 1.A.3, Perform Chemical and Metallurgical Comptability Analyses.

8.1.2 Objective

The purpose of this program is to determine the chemical compatibility of iron-base alloys with metallic lithium. Structural steel specimens are exposed to static lithium containing selected solute additions to identify the kinetics and mechanisms that govern the corrosion of steels by lithium. Specific program objectives are (1) to determine the effects of N, C, H, and O on apparent solubilities of stainless steel components in lithium; (2) to determine the C and N partitioning coefficients between stainless steels and lithium; (3) to determine the effects of soluble (Ca, Al) and solid (Y, Zr, Ti) active metal additions on corrosion of stainless steels by lithium; and (4) to determine the tendencies for dissimilar-metal mass transfer between stainless steel and Mo, Nb, and Co.

8.1.3 Summary

Data on the mechanisms and kinetics of the corrosion of stainless steels by lithium were obtained from a series of 150 capsule tests at temperatures from 500 to 700°C and for times to 10,000 hr. One of the primary objectives of the program was to evaluate the effects of N, O, C, and H on compatibility and to determine if impurity getters will successfully inhibit impurity effects.

Base-line capsule tests conducted to 10,000 hr showed no measurable corrosion of type 316 stainless steel in lithium up to 700°C. Nitrogen in lithium strongly promoted the corrosion of type 316 stainless steel at 500, 600, and 700°C. At 500°C calcium, a soluble getter in lithium, effectively inhibited corrosion by nitrogen but was relatively ineffective at 600 and 700°C. Yttrium, a solid, relatively insoluble getter, was ineffective at inhibiting corrosion by nitrogen at all temperatures.

8.1.4 Progress and Status

8.1.4.1 Introduction

For reasons discussed in Sect. 8.2.4.1, compatibility with liquid lithium is an important property in the development of path A and B alloys. The degree to which these alloys will resist corrosion by lithium is a function of both the alloy composition and the purity of the lithium. Thus the interaction of naturally occurring impurities in lithium with components of path A and B alloys and the partitioning of minor and major alloying elements to the lithium must be determined in order to achieve alloy compositions that are optimized for lithium service.

Static capsules of the type shown in Fig. 8.1.1 are being used to study impurity-induced reactions of austenitic stainless steels in lithium. Sheet specimens identical in composition to the capsule wall

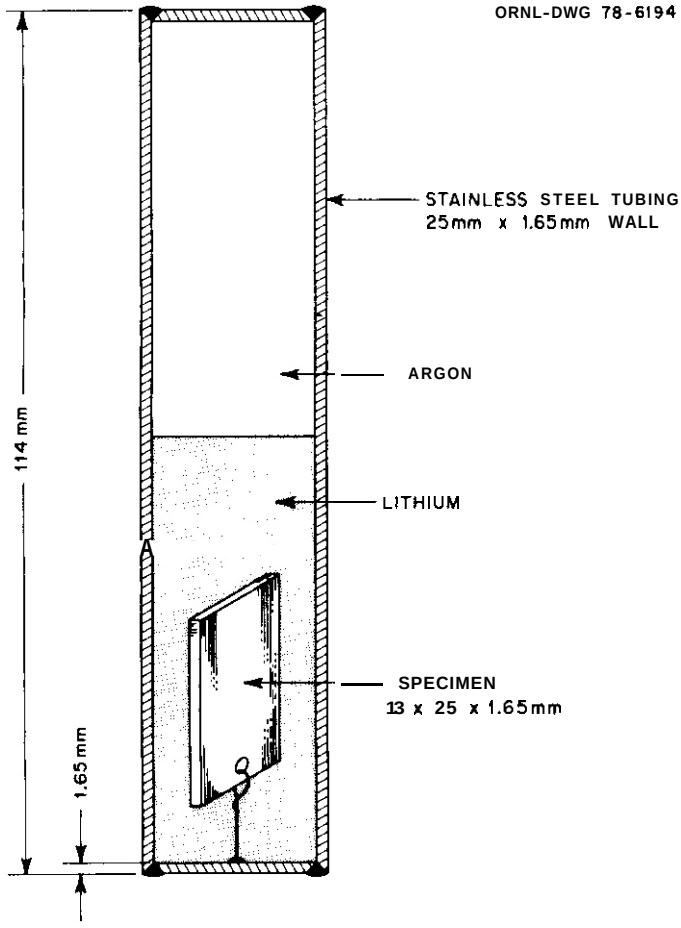

Fig. 8.1.1. Static Capsule Used for Testing Austenitic Stainless Steels in Lithium.

are included within the capsule to facilitate weight change and magnetic permeability measurements. A measured weight of solid lithium is placed in the capsule along with any impurity additions before the top end cap is welded. The filling operation and final weld are conducted under an inert atmosphere. Singly and doubly encapsulated test systems have been used to determine that diffusion of nitrogen through the capsule wall is not a factor in any of the tests.

8.1.4.2 Results

Previous work on the compatibility of iron-base alloys with lithium was reviewed' before this program started. A capsule test matrix based on this backgound is summarized in Table 8.1.1. Over

Table 8.1.1. Summary of Capsule Tests of Stainless Steels in Lithium at 500, 600, and 700°C for Times from 1000 to 10,000 hr

Capsule Material	Addition to Lithium	Objective
316 SS	None	Base-line corrosion data
316L SS *304L* SS 310 SS 321 SS	None None None None	Base-line corrosion tests to compare several stainless steels
316 SS	Li_3N, LiH, Li_2O, C	Effect of interstitial impurities on corrosion
316 SS	Li_3N + Y, Li_3N + Ca, Li_3N + Ti, Li_3N + Zr, Li_2O + Y	Effect of interstitial impurity getters on corrosion
316 SS	Y, Ca, Al, Ti, Zr, Si, Mg, Mn	Effect of active metals on corrosion
316 SS	Pb, Sn, In	Effect of heavy metals on corrosion
316 SS	Nb, Mo, *Co*	Dissimilar-metal mass transfer determination

150 capsule tests were conducted in the temperature range 500 to 700°C. Base-line corrosion tests and tests of additions of nitrogen and nitrogen getters are essentially complete, and these will be discussed below. A report summarizing the results from all the tests is now in preparation.

Specimens from these tests were examined primarily for weight change and metallographic appearance. Table 8.1.2 summarizes the weight changes in type type 316 stainless steel after exposure to lithium that had been gettered with zirconium before test, Li + Li_3N, Li + Li_3N + Y, and Li + Li_3N + Ca. In these base-line tests, the weight changes were very small and there was little or no evidence of grain boundary attack (Table 8.1.3 and Fig. 8.1.2). Adding about 5% Li_3N to lithium markedly increased the weight loss in type 316 stainless steel at all temperaure-time combinations. When 19% Y was added along with the 5% Li_3N, the results were almost unchanged.

Table 8.1.2. Effect of Nitrogen and Nitrogen Getter on Weight Change in Type 316 Stainless Steel Exposed to Lithium

Temperature (°C)	Time (hr)	Weight Change, g/m^2			
		Base line	Li_3N	Li_3N + Y	Li_3N + Ca
500	1000	+0.3	−51.5	−41.1	+6.9
	2000	0	−49.8	−48.5	+5.5
600	1000	−0.1	−39.0	−30.9	−2.9
	2000	-0.1	−43.0	−31.8	−5.0
700	1000	−0.3	−51.0	−39.7	−5.1
	2000	−0.7	−44.8	−30.3	−5.6

However, adding about 13% Ca resulted in small weight gains at 500°C and small weight losses at 600 and 700°C. Samples exposed to Li + Li_3N and Li + Li_3N + Y at 500°C had a 25-μm (1-mil) surface layer (Fig. 8.1.3), which x-ray analysis indicated to be α-iron with nitrogen in solution. Nitrogen in lithium appears to increase the solubility of chromium and nickel, thereby depleting a near-surface zone of these elements. Calcium, which is soluble in lithium, inhibited attack by nitrogen

Table 8.1.3. Effect of Nitrogen and Nitrogen Getters on Metallographic Appearance of Type 316 Stainless Steel Exposed to Lithium

Temperature (°C)	Time (hr)	Metallographic Appearance			
		Base Line	Li_3N	Li_3N + Y	Li_3N + Ca
600	1000	No attack	Surface layer and grain boundary attack	Surface layer and grain boundary attack	Very slight grain boundary attack
	2000	No attack	Surface layer and grain boundary attack	Surface layer and grain boundary attack	Very slight grain boundary attack
	1000	No attack	Thin surface layer and grain boundary attack	Surface layer and grain boundary attack	Rough surface and boundary attack
	2000	No attack	Thin surface layer and grain boundary attack	Surface layer and grain boundary attack	Rough surface and boundary attack
700	1000	No attack	Heavy grain boundary attack	Heavy grain boundary attack	Heavy grain boundary attack
	2000	Very slight grain boundary attack	Heavy grain boundary attack	Surface layer and heavy grain boundary attack	Heavy grain boundary attack

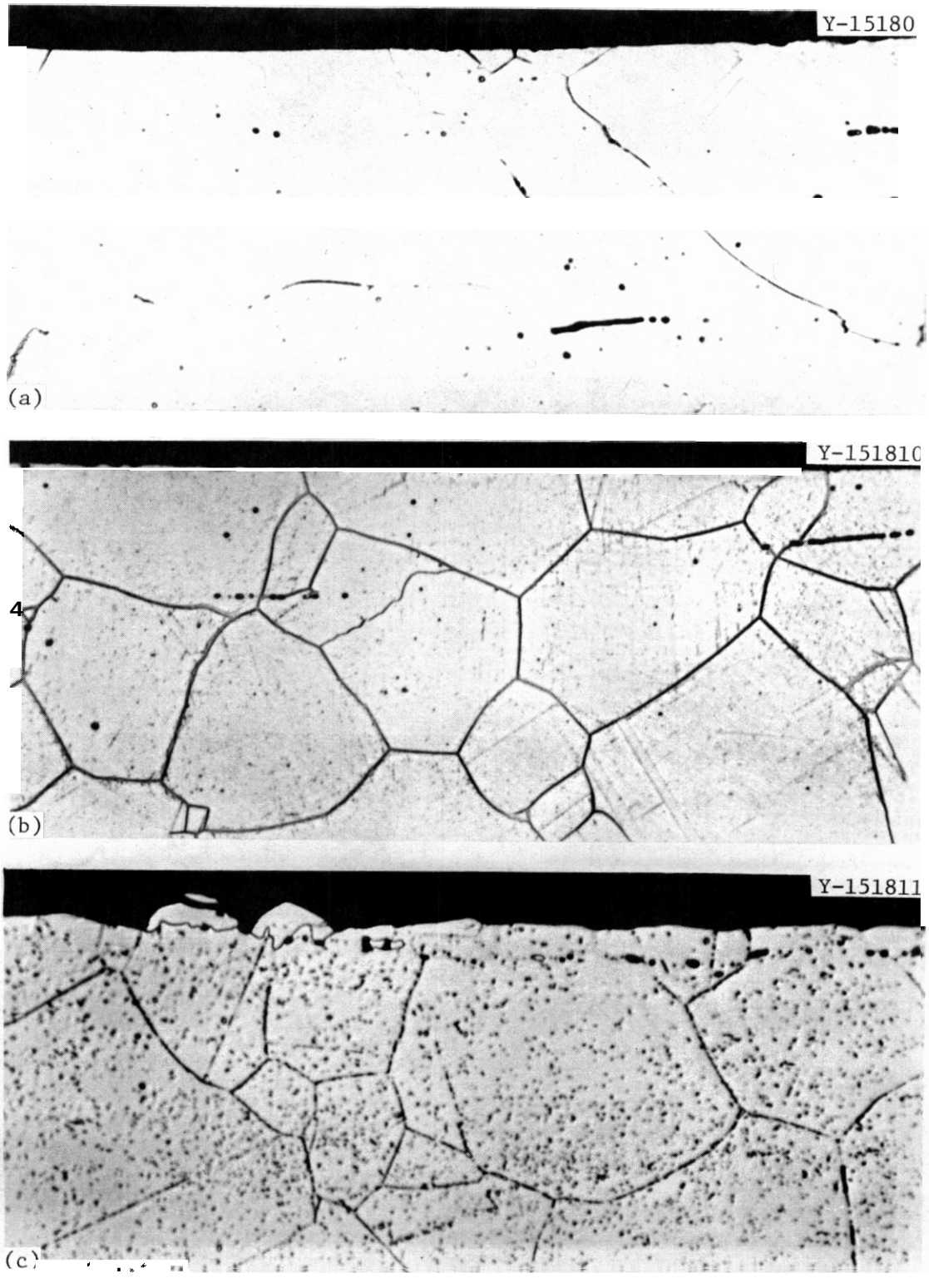

Fig. 8.1.2. Type 316 Stainless Steel After Exposure to Lithium for 10,000 hr. (Base-line capsule tests.) 500×. Exposed at (a) 500°C, (b) 600°C, (c) 700°C.

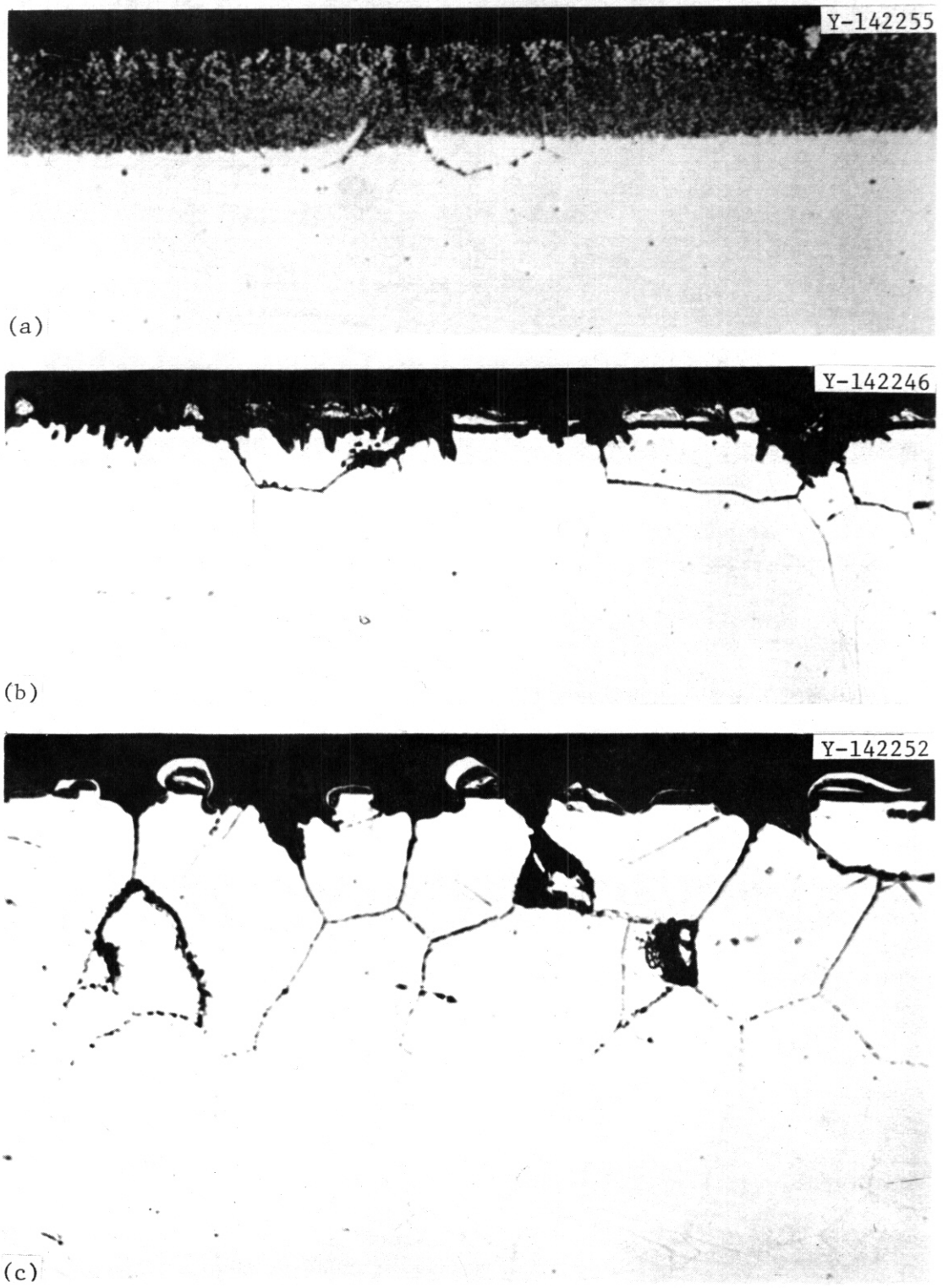

Fig. 8.1.3. Type 316 Stainless Steel After Exposure to Li—5% Li_3N for 2000 hr at (a) 500°C, (b) 600°C, and (c) 700°C. 500×.

at 500°C, but solid yttrium did not (Fig. 8.1.4). At 600°C the addition of Li_3N resulted in a very thin surface layer, and all specimens showed evidence of grain boundary attack (Fig. 8.1.3). Specimens exposed to Li + Li_3N + Ca at 600°C showed less evidence of grain boundary penetration than those exposed to Li + Li_3N or Li + Li_3N + Y. At 700°C, the surface layer observed at the lower temperatures was no longer visible, and calcium did not limit grain boundary penetration. All the samples at 700°C showed heavy grain boundary attack to depths of 50 to 80 μm (2–3 mils). as indicated by Fig. 8.1.3. In general the depth of attack and weight changes after 1000- and 2000-hr exposures were similar. The reaction of nitrogen with stainless steel appears to be relatively rapid, and in our closed system, the attack had reached an end point during the shortest test time.

Analyses of lithium from the base-line corrosion tests showed that the stability of nitrogen in lithium increases relative to stainless steel components over the range 500 to 700°C (Table 8.1.4). At 500°C the lithium was either unaffected or slightly purified with respect to nitrogen level. At 600°C lithium picked up small amounts of nitrogen, and at 700°C the lithium picked up significant nitrogen from the stainless steel. This, of course, occurred with relatively low initial concentrations of nitrogen in lithium. When Li_3N was added to the lithium as discussed above, the final concentration of nitrogen in the lithium was always much lower than the initial concentration.

8.1.5 Conclusions

Evaluation of the test data from capsule tests of type 316 stainless steel in lithium has led to the following conclusions:

1. Up to 700°C. type 316 stainless steel shows no perceptible weight change or grain boundary penetration in static lithium that has been purified by reaction with zirconium before test.

2. Nitrogen increases the corrosion of type 316 stainless steel by lithium at 500, 600, and 700°C.

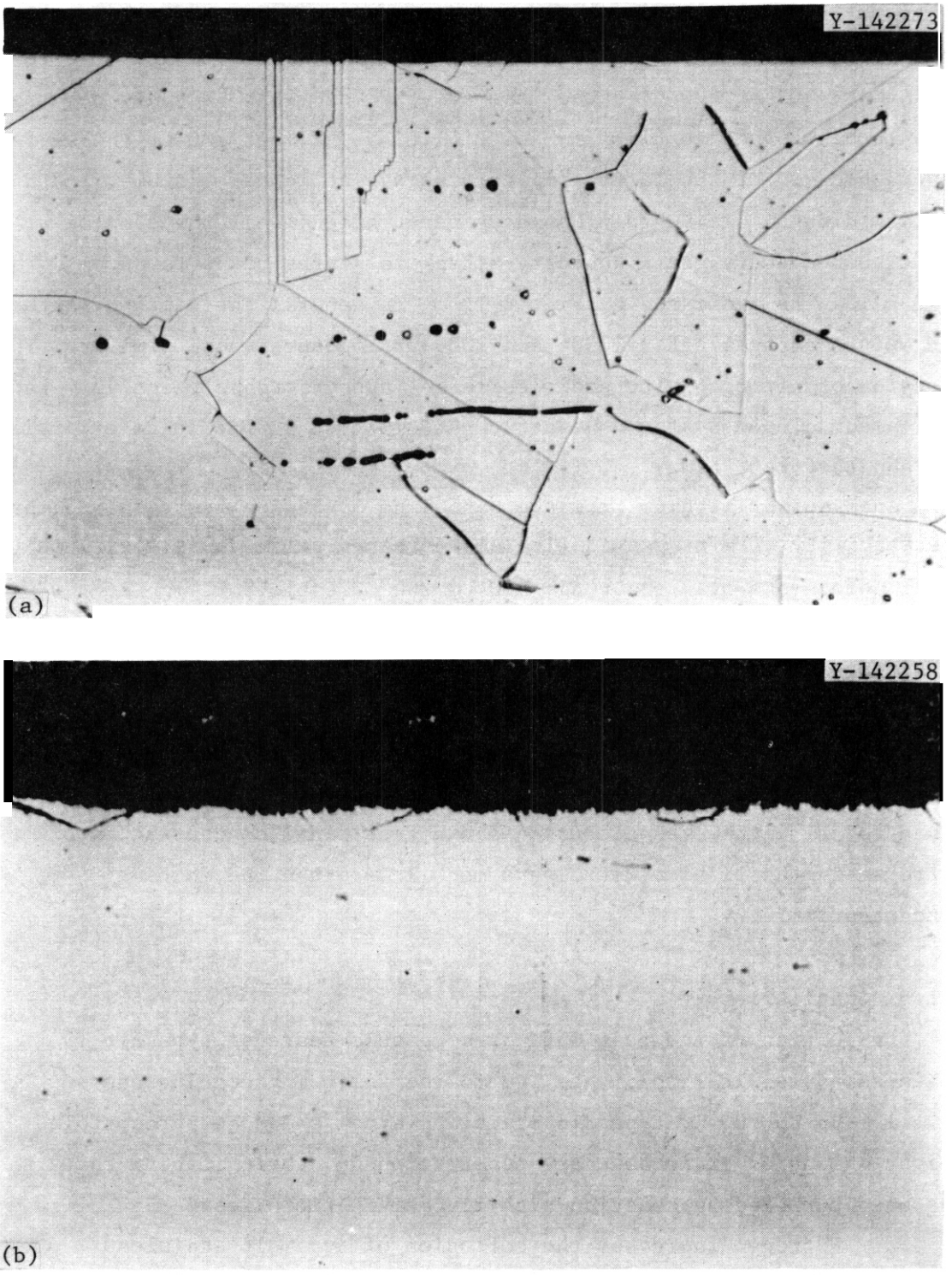

Fig. 8.1.4. Type 316 Stainless Steel After Exposure to Lithium and Li_3N for 2000 hr at 500°C. 500×. (a) Calcium inhibited corrosion. (b) Yttrium did not.

Table 8.1.4. Nitrogen in Lithium After Exposure to Type 316 Stainless Steel in Base-Linea Corrosion Tests

Temperature (°C)	Time (hr)	Nitrogen in Lithium[b] (ppm)
500	2,000	<10
	10,000	<20
600	2,000	48
	10,000	37
700	2,000	185
	10,000	170

[a] ~15–25 ppm N in lithium before test.

[b] Each capsule contained about 5 g Li. Capsules were 16 mm diam × 100 mm long. Surface area of capsule/volume of lithium was approximately 500/m.

3. Calcium effectively inhibits nitrogen corrosion at 500°C, does less so at 600°C, and has little effect at 700°C. Yttrium does not inhibit corrosion by nitrogen at 500, 600, or 700°C.

4. The partitioning of nitrogen between stainless steel and lithium results in an increasing concentration of nitrogen in lithium as temperature increases from 500 to 700°C.

8.1.6 Reference

1. J. H. DeVan, J. E. Selle, and A. E. Morris, *Review of Lithium Iron-Base Alloy Corrosion Studies*, ORNL/TM-4927 (January 1976)

8.7 THERMAL-CONVECTION LOOP TESTS OF TYPE 316 STAINLESS STEEL IN LITHIUM – J. H. DeVan and J. R. DiStefano (ORNL)

8.2.1 ADIP TASK

Task I.A.3, Perform Chemical and Metallurgical Compatibility Analyses.

8.2.2 Objective

The purpose of this task is to evaluate the corrosion resistance of candidate first-wall materials with molten lithium in the presence of a temperature gradient. Corrosion rates (in terms of both dissolution and deposition) are measured as functions of time, temperature, and lithium flow parameters.

Corrosion rate measurements are combined with chemical and metallographic examination of specimen surfaces to establish the mechanisms and rate-controlling processes for dissolution and deposition reactions.

8.2.3 Summary

Thermal-convection loops are being used to determine the corrosion properties of systems of lithium with stainless steel at low flow velocities. Small loops of iron-base alloys with fixed corrosion specimens have been operated at lithium temperatures between 500 and 650°C for times up to 10,000 hr. The test results have provided quantitative information on the microstructural changes in 300-series stainless steels caused by thermal gradient mass transport in flowing lithium. The corrosion rate of type 316 stainless steel increased with temperature in accordance with an Arrhenius relation. Addition of 5% Al to the lithium strongly inhibited the mass transport of iron, chromium, and nickel at 600°C. Stainless steels and path A alloys in lithium are being tested further in larger type 316 stainless steel thermal-convection loops, which contain accessible insert specimens.

8.2.4 Progress and Status

8.2.4.1 Introduction

Presently conceived D-T fusion power reactors produce their own tritium fuel supply by reacting neutrons, borne of the fusion reaction, with lithium atoms. Accordingly, in such reactors the plasma containment wall is surrounded by a lithium-containing, neutron-absorbing blanket. Most design concepts have used liquid lithium for this purpose.

The composition of the material selected for the plasma containment wall of a fusion reactor will obviously strongly influence the viability of the liquid lithium-absorber concept. For path A and B alloys, metallic mass transfer in recirculating lithium systems competes with radiation damage considerations in setting the useful operating temperature of the plasma containment wall, Thus the determination of corrosion mechanisms and temperature limitations with respect to lithium containment becomes a critical factor in assessing developmental path A and B alloys for fusion first-wall applications.

8.2.4.2 Results

Our initial studies of the mass transfer of iron-base alloys in flowing lithium compared the corrosion rates of stabilized (type 321) and unstabilized (type 304L) stainless steels with stabilized 2 1/4 Cr-1 Mo steel. Results of these tests were reported at the International Conference on Liquid Metal Technology' in May 1976. Tests of the same general type have now been completed on type 316 stainless steel under the conditions listed in Table *8.2.1.* All these tests used a small thermal-convection loop of the design pictured in Fig. *8.2.1.* Flow was induced in these loops by heating one vertical leg and cooling the other. Interlocking sheet specimens were contained in the two vertical legs of the loops to provide weight change data along the heated and cooled sections. Each loop operated without interruption for 3000 or 10,000 hr and was then destructively examined. Additional loops of this design are being fabricated of Incoloy alloy *800,* Inconel alloy *600,* and Inconel alloy *718* to determine the resistance of higher nickel alloys to thermal gradient mass transfer in lithium at about *500°C.*

Table 8.2.1. Test Conditions of Initial Type 316 Stainless Steel Thermal-Convection Loops Operated with Lithium at a Velocity of About 20 mm/s

T_{max} (°C)	ΔT (°C)	Time (hr)	Test Variable
600	200	3,000	Base line
600	200	3,000	1700 ppm N in Li
600	200	10,000	Time
550	200	3,000	Hot-leg temperature
650	200	3,000	Hot-leg temperature
500	150	3,000	Hot-leg temperature
600	200	3,000	Al addition

Currently we are testing austenitic stainless steels in flowing lithium with larger thermal-convection loops shown in Fig. 8.2.2. This loop is maintained as a permanent test fixture, and corrosion processes in the loop are followed by periodically withdrawing tubular specimens for weight change and metallographic examinations. Using stand-pipes located directly above the two vertical legs of the loop, we can lower sheet specimens into and remove them from the legs while the loop is operating. Using similar stand-pipes in conjunction with the surge tanks, we can make controlled additions to the lithium, insert active metal getters, and remove lithium samples for analysis at any selected time without otherwise affecting loop operation. Three such loops, constructed of type 316 stainless steel, have been in operation with lithium under the conditions shown in Table 8.2.2. Two additional type 316 stainless steel loops have been fabricated to permit the testing of path A alloys as they become available.

This report reviews some of the significant findings derived from the series of type 316 stainless steel loops shown in Table 8.2.1. This test series was designed to provide corrosion rate information in lithium as a function of hot-leg temperature and operating time. One loop was also operated with aluminum added to the lithium. With the test time fixed at 3000 hr, loops of identical geometries were operated

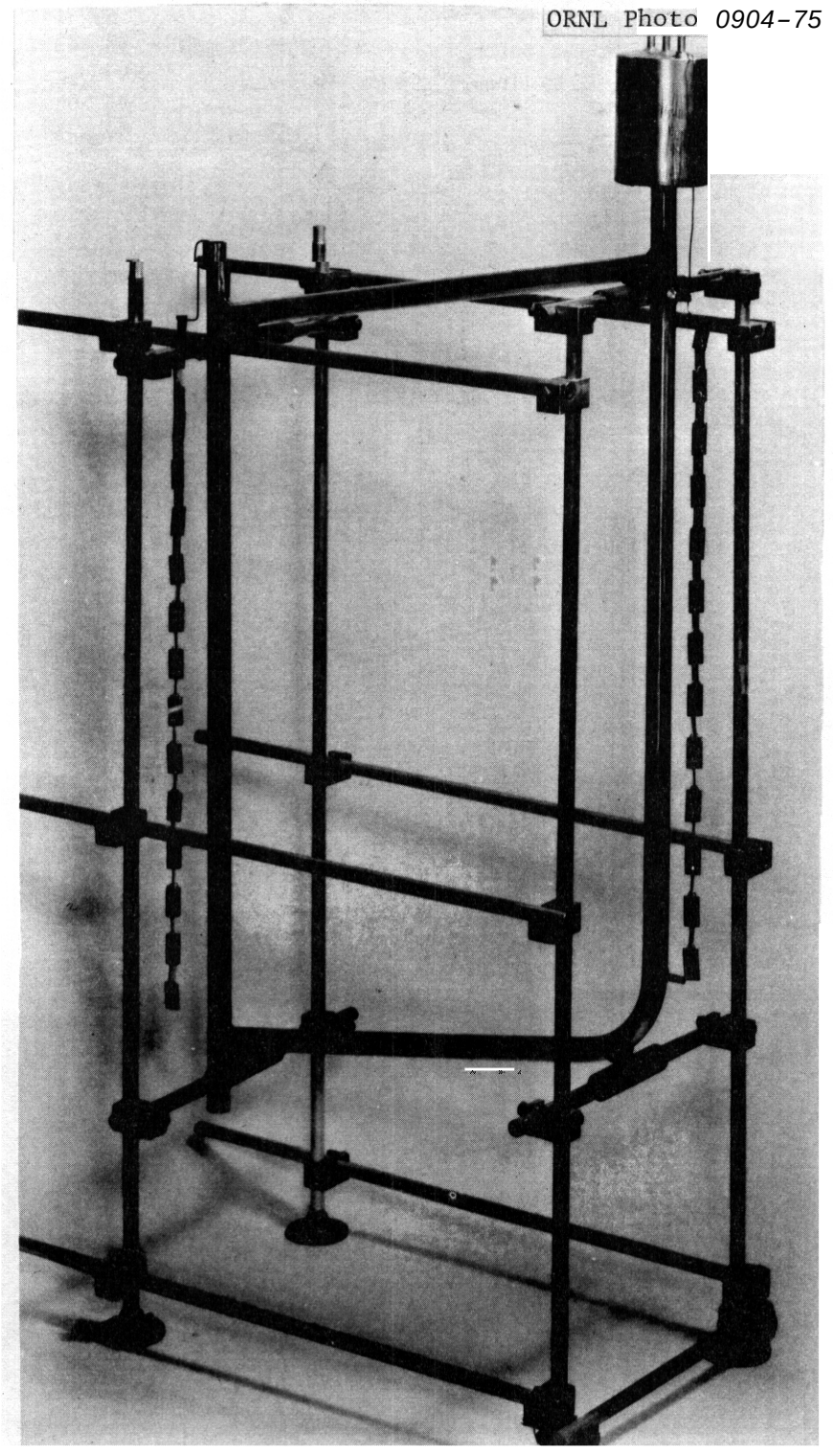

Fig. 8.2.1. Thermal-Convection Loop Used for 3000- and 10,000-hr Tests of Type 316 Stainless Steel in Lithium (Loop Height ≈ 0.7 m).

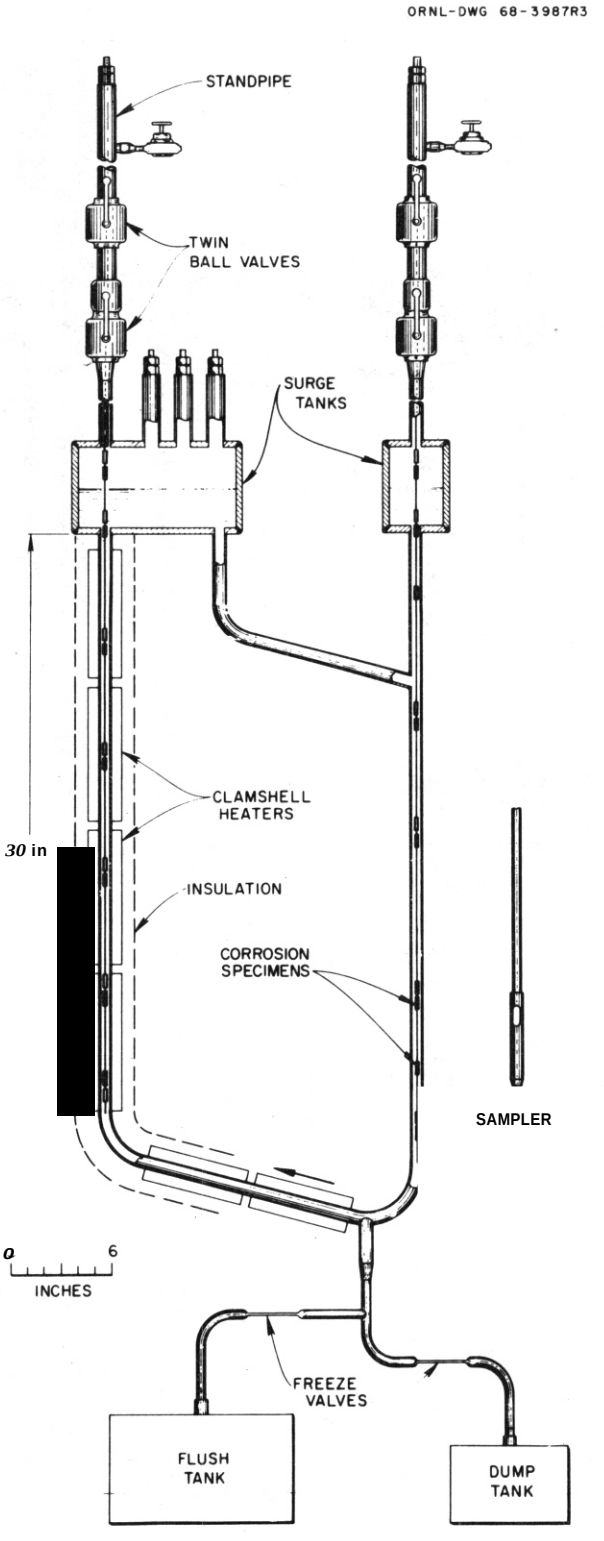

Fig. 8.2.2. Schematic of Type 316 Stainless Steel Thermal-Convection Loop with Accessible Test Coupons. Scale is 0.15 m; heated section is 0.76 m.

Table 8.2.2. Test Conditions of Type 316 Stainless Steel Thermal-Convection Loops with Accessible Insert Specimens, Lithium Velocity About 30 mm/s

T_{max} (°C)	ΔT (°C)	Operating Time (hr)	Test Variable
600	95	1675[a]	Preliminary evaluation of loop performance with lithium
600	115	4370[b]	Base-line loop
600	115	100[b]	Effect on Li_3N addition to lithium

[a]Loop terminated.
[b]March 31, 1978.

at maximum temperatures of 500, 550, 600, and 650°C. Weight losses recorded at the point of maximum temperature increased with temperature according to the Arrhenius plot shown in Fig. 8.2.3.

A 10,000-hr loop test was also operated at a maximum temperature of 600°C, and the maximum weight losses from this test and the 3000-hr test are compared in Fig. 8.2.4. The two test times are not sufficient to derive an accurate time relationship for the corrosion rate. However, it is evident that the rate averaged over the 3000-hr interval is about double that averaged over the 10,000-hr interval.

The microstructure of corrosion specimens from the point of maximm weight loss was also identical for the two time periods, as shown in Fig. 8.2.5. The most significant metallographic feature is the development of a ferritic surface layer. The constant thickness of this layer (15 μm) at the two time periods is consistent with the "steady-state, moving boundary" model' developed for ferrite layer growth on type 316 stainless steel in sodium. If this model is assumed, then the mass transfer rate of type 316 stainless steel in lithium stays constant with time at 3000 hr and beyond.

The addition of aluminum to lithium in a 3000 hr test at 600°C dramatically changed the mass transfer pattern from that of a base-line

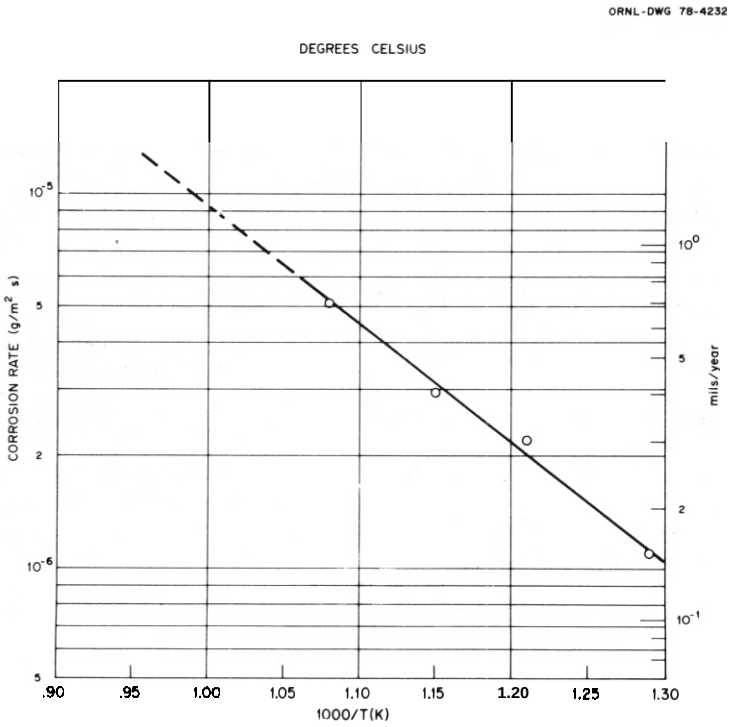

Fig. 8.2.3. Effect of Maximum Loop Operating Temperature on Maximum Weight Loss of Type 316 Stainless Steel in Lithium.

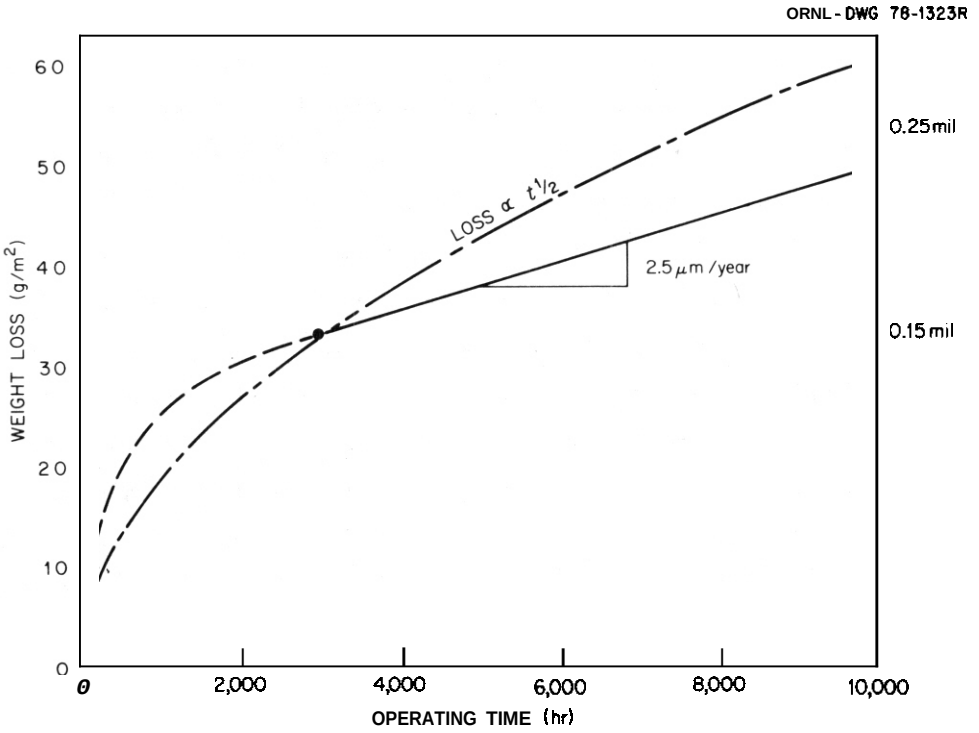

Fig. 8.2.4. Weight Loss of Type 316 Stainless Steel at 600°C Loop Position After 3000 and 10,000 hr.

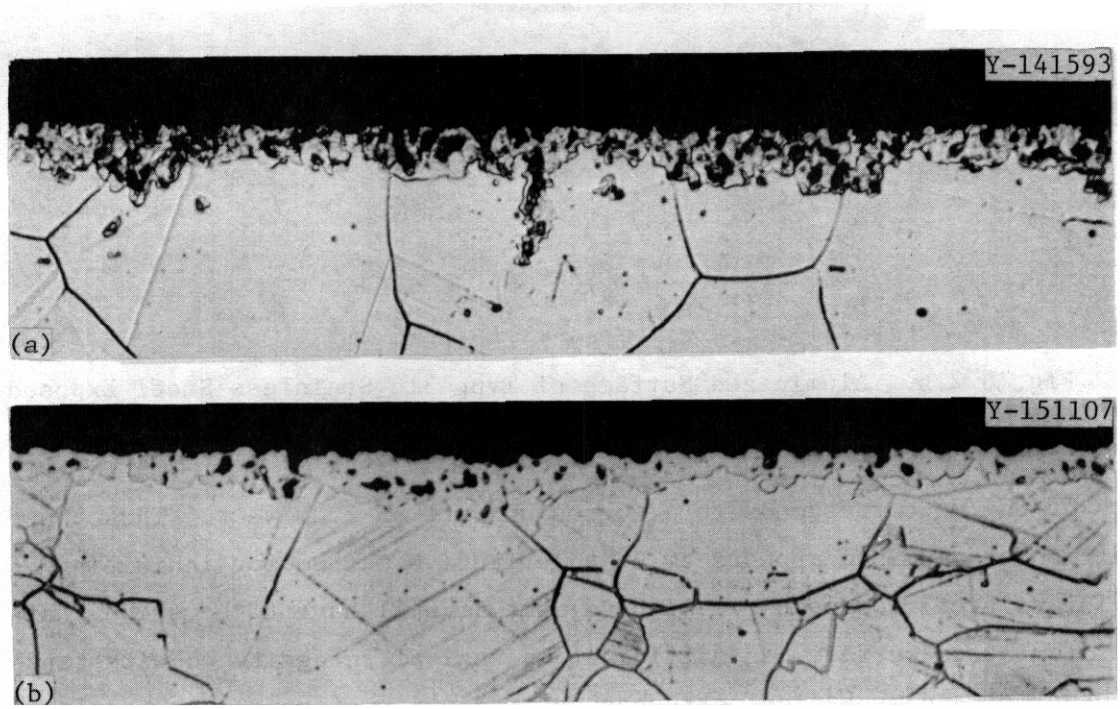

Fig. 8.2.5. Microstructure of Type 316 Stainless Steel Specimens at 600°C Loop Position After (a) 3000 and (b) 10,000 hr. 500×. Etchant: 40 HNO_3, 60 H_2O (Electrolytic).

test at the same time and temperature. The 1100 aluminum was added to the loop in the form of 16-mm-diam (1/16-in.) wire, which was wrapped on the hot-leg specimen holder (Fig. 8.2.1). The weight of wire added was 5% of the weight of lithium charged into the loop. We found no traces of the wire at the end of test, although the aluminum content of the after-test lithium was less than 0.1%. This suggests that almost all the aluminum transferred to the stainless steel. Metallographic examinations of stainless steel specimens and loop surfaces confirmed the presence of an aluminized surface layer, which increased in thickness with the lithium temperature. The heaviest layer, measured at 600°C, is shown in Fig. 8.2.6 and is seen to be about 10 μm in total thickness. The layer was almost imperceptible at 400°C, and no bulk aluminum was deposited anywhere in the loop. Only four specimens in the loop, all located near the heater exit, showed any perceptible weight loss, the largest loss being 6 g/m^2. In the base-line loop the maximum weight loss occurred at the same specimen position but was more than five times as great (33 g/m^2). Averaged over the 3000-hr test period, a weight

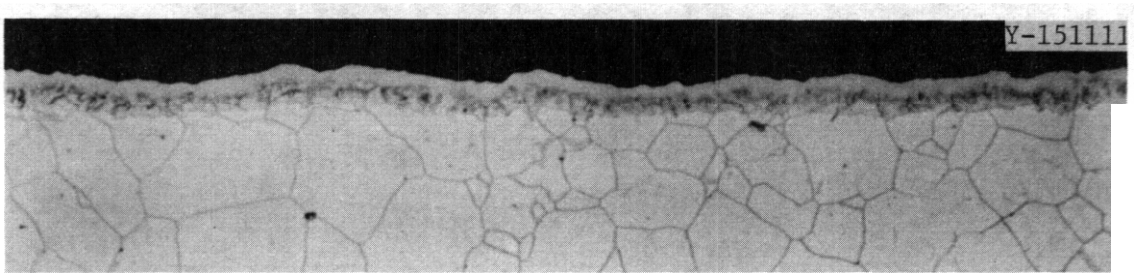

Fig. 8.2.6. Aluminized Surface of Type 316 Stainless Steel Exposed to Lithium + 5% Aluminum at 600°C.

loss of 6 g/m^2 corresponds to a corrosion rate of 2 μm/year. Thus the addition of aluminum appears to be an effective method for inhibiting stainless steel corrosion in lithium, but it will have to be shown that the aluminized surface has sufficient mechanical integrity to withstand the thermal and mechanical stresses and radiation effects expected for fusion reactor service.

8.2.5 Conclusions

1. The maximum rate of weight loss of type 316 stainless steel exposed to lithium for 3000 hr increased from 1 $\mu g/m^2 s$ (2.5 μm/year) in 500°C loop tests to 5 $\mu g/m^2 s$ (18 μm/year) in 650°C loop tests.

2. In loop tests at 600°C, the maximum corrosion rate of type 316 stainless steel averaged over a 3000-hr run was double that averaged over a 10,000-hr run. Metallographic examinations of hot-leg specimens suggest that the corrosion rate is constant between 3000 and 10,000 hr.

3. The addition of aluminum to lithium in a 3000-hr loop test at 600°C lowered the mass transfer rate of type 316 stainless steel to about 2 μm/year (0.08 mil/year).

8.2.6 References

1. J. E. Selle, "Corrosion of Iron-Base Alloys by Lithium," *International Conference on Liquid Metal Technology in Energy Production*, M. H. Cooper, ed., CONF-760503-P2, pp. 453–61.

2. E. G. Brush, *Sodium Mass Transfer. XVI, The Selective Corrosion Component of Steel Exposed to Flowing Sodium*, GEAP-4832 (March 1965).

8.3 COMPATIBILITY STUDIES OF TYPE 316 STAINLESS STEEL AND HASTELLOY N IN KNO_3-$NaNO_2$-$NaNO_3$ — J. H. DeVan and J. R. Keiser (ORNL)

8.3.1 ADIP TASK

Task I.A.3, Perform Chemical and Metallurgical Compatibility Analyses.

8.3.2 Objective

A nitrate-based heat transfer salt (HTS) is a possible coolant for a fusion reactor in which a solid or static liquid breeding blanket is used. The purpose of this work is to study the corrosion behavior of potential fusion reactor structural materials in HTS under conditions where a temperature gradient exists.

8.3.3 Summary

The nitrate-based fused salt mixture KNO_3-$NaNO_2$-$NaNO_3$ *(44–49–7* mol %) has been widely used as a heat transport fluid and for metallurgical heat-treating. We have measured the corrosion rate of this salt in the presence of a temperature gradient for an iron-base material, type 316 stainless steel, and a nickel-base material, Hastelloy N. Corrosion rates were measured with maximum loop temperatures of *431* and 504°C. Measured corrosion rates were in all cases less than 8 μm/year.

8.3.4 Progress and Status

A nitrate-based heat transfer salt (HTS) [KNO_3-$NaNO_2$-$NaNO_3$ *(44–49–7* mol %)] is being considered as a possible coolant for a fusion reactor in which a solid or static liquid breeding blanket is used. Since the purpose of the coolant would be to transfer heat from the blanket to a power generating system, the coolant must be liquid (or gaseous) at operating temperatures and must have good heat transfer capabilities. Other requirements for the coolant are compatibility with the container material, compatibility with the blanket (in the event of a failure of the container), and adequate stability under neutron irradiation.

We are using a thermal-convection loop to study the compatibility of type 316 stainless steel and the nickel-base alloy Hastelloy N with

HTS. As has been described elsewhere,' 16 specimens are exposed to the circulating salt over a range of temperatures listed in Table 8.3.1.

Table 8.3.1. Operating Conditions for HTS Loop

Time Interval After Loop Startup (hr)	Maximum Temperature (°C)	Temperature Difference (°C)
0–3,000	431	70
3,000–9,000	505	81
9,000–10,000	432	78

As can be seen in Fig. 8.3.1, both the stainless steel and Hastelloy specimens lost weight at the maximum temperature position at 431°C during the first 1000 hr, but showed very little change during the following 2000 hr. The specimens had a black oxide layer after the first 1000 hr. Because the corrosion rate was very low after the first 3000 hr, the maximum temperature was raised to 505°C to determine the corrosion rate under more demanding conditions. Figure 8.3.1 shows that over the next 6000 hr, weight losses increased for both alloys. The corrosion rates calculated from the weight change data are given in Table 8.3.2. In the case of type 316 stainless steel, the corrosion rate at 505°C *increased* as a function of time, and in the final 2000 hr at 505°C the rate was about 8 μm/year (0.3 mil/year).

Photomicrographs (Fig. 8.3.2) show that a surface film was formed on both stainless and Hastelloy specimens. Electron microprobe examination is being performed to determine the composition of the surface layers. Photomicrographs of etched specimens (Fig. 8.3.3) suggest that a depleted layer exists beneath the surface layer. Table 8.3.3 shows that the concentration of chromium in the salt increased significantly with time, presumably as a result of chromium removed from the specimens. Thus, we expect microprobe analysis to indicate that chromium is depleted near the surface.

Table 8.3.2. Corrosion Rates in HTS Loop[1]

Maximum Loop Temperature (°C)	Corrosion Rate, g/m^2 year	
	Type 316 Stainless Steel	Hastelloy N
431	2.6	2.6
505	64.5	40.6

[1]Does not include initial 1000-hr exposure. For stainless steel, 10 g/m^2 year = 1.25 μm/year ≈ 0.05 mil/year. For Hastelloy N, 10 g/m^2 year = 1.12 μm/year ≈ 0.04 mil/year.

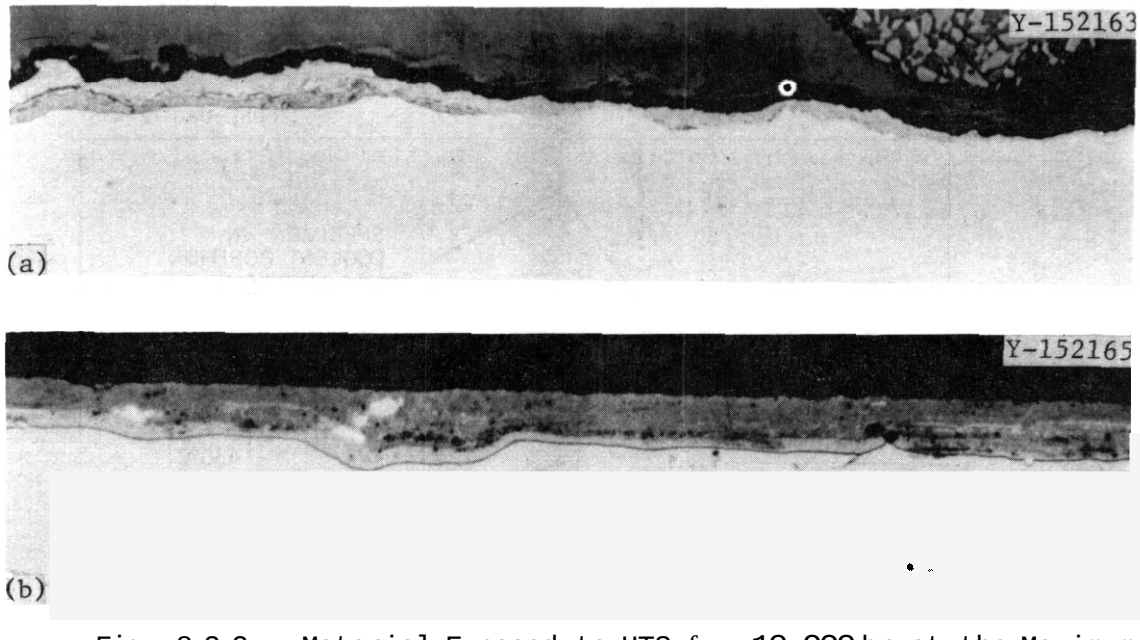

Fig. 8.3.2. Material Exposed to HTS for 10,000 hr at the Maximum Temperature for Conditions Given in Table 8.3.1. As polished. 500×. (a) Type 316 stainless steel. (b) Hastelloy N.

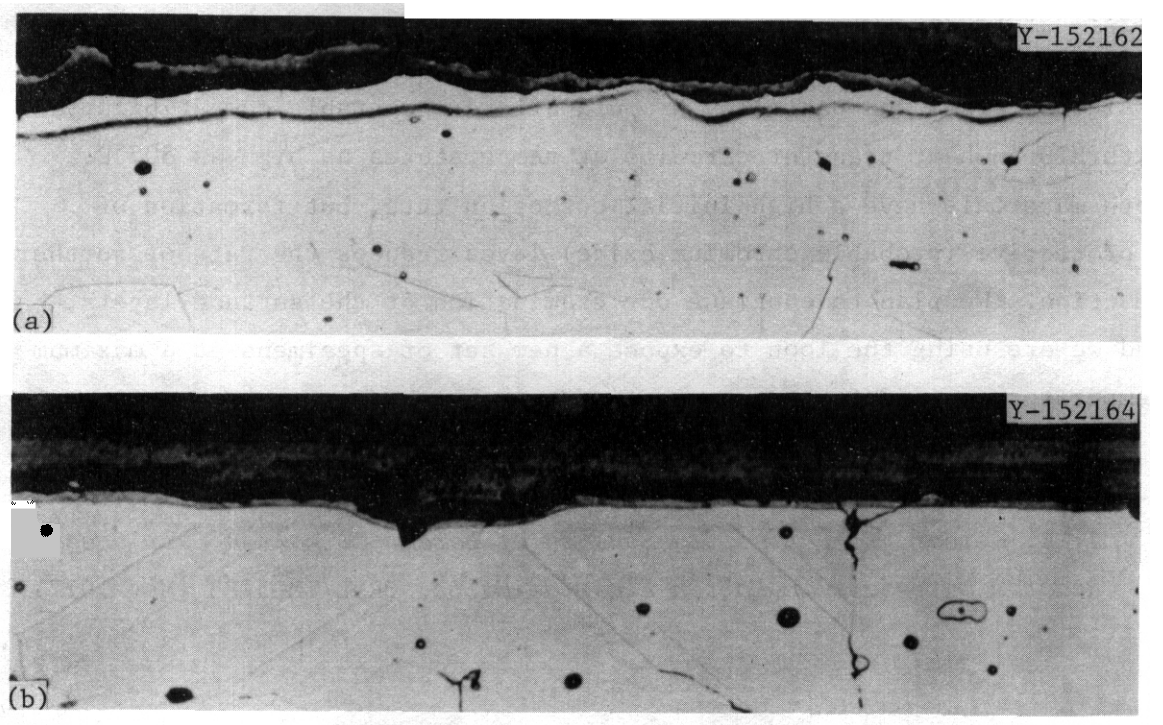

Fig. 8.3.3. Material Exposed to HTS for 10,000 hr at the Maximum Temperature Conditions Given in Table 8.3.1. Etched. 500×. (a) Type 316 stainless steel. (b) Hastelloy N.

Table 8.3.3. Results of Chemical Analysis of HTS

Operating Time (hr)	Concentration, ppm		
	Fe	Ni	Cr
1000	17	12	52
2000	10	<5	70
4000	7.2	<1	93
7000	1.4	<0.1	163

For the final 1000 hr exposure, the maximum loop temperature was reduced to its initial value of about 430°C and the initial corrosion rate at that temperature was reestablished (Fig. 8.3.1).

8.3.5 Conclusions

From the data we have obtained, we can conclude that both type 316 stainless steel and Hastelloy N would afford acceptable compatibility with HTS in heat transfer circuits at temperatures as high as 505°C. Both materials have a high initial corrosion rate, but formation of a protective (probably chromium oxide) layer reduces the rate of further reaction. We plan to continue our examination of the surface layers, and we are using the loop to expose a new set of specimens at a maximum temperature of 550°C.

8.3.6 Reference

1. J. R. Keiser, *Compatibility Studies of Potential Molten Salt Breeder Reactor Materials in Molten Fluoride Salts*, ORNL/TM-5783 (May 1977).

8.4 HYDROGEN PERMEATION OF TYPE 316 STAINLESS STEEL – V. A. Maroni and E. H. Van Deventer (Argonne National Laboratory).

8.4.1 ADIP Task

Hydrogen Dissolution and Permeation Effects. This task is being considered for addition to the ADIP program plan. The results presented in this section contribute to Subtask I.E.1.1., Milestone I.E.1.a. The above assigned title and numbering are tentative, pending approval by the ADIP Task Group.

8.4.2 Objective

The objective of the work described in this contribution is to examine the base-line hydrogen permeation characteristics of 316-stainless steel (SS) over the range of temperatures and hydrogen driving pressures anticipated in fusion reactor applications. The selection of 316-SS for this study is predicated on its role as a representative Path A alloy. The results of this study will provide a basis for evaluating the effectiveness of permeation barrier methods that are currently being developed for 300-series stainless steels.

8.4.3 Summary

Under conditions of high hydrogen purity (low oxygen potential), the hydrogen permeability of 316-SS was found to be bulk-diffusion limited over ranges of temperature and hydrogen pressure that are pertinent to most projected fusion reactor applications for this material. A half-power dependence on hydrogen pressure was retained down to the present experimental limit of the ANL permeation apparatus (*i.e.*, 10^{-3} Pa). The presence of a 1 mCi source of 1 MeV gamma radiation in the upstream compartment had no effect on measured hydrogen permeation rates.

8.4.4 Progress and Status

This section reports the results of hydrogen permeation studies carried out on 316-SS over the temperature range from 150 to 800°C,

using hydrogen driving pressures in the range from 10^{-3} to 10^{4} Pa (10^{-5} to 10^{2} Torr). Details of the experimental procedures used in these studies were generally the same as those described in two previous publications.[1,2] Additional features incorporated into the permeation apparatus in recent months now permit us to monitor and control (to some extent) gas compositions in the upstream compartment.

During the measurements reported herein, continuous monitoring of the upstream gas composition (using a partial pressure analyzer) revealed that at low upstream hydrogen pressures, water, carbon monoxide/nitrogen,* argon, and helium can combine to make a significant contribution to the total pressure in the upstream compartment. In some cases, the molecular hydrogen partial pressure was found to constitute *as* little as *20%* of the total pressure. It became evident from this observation that a total pressure measurement does not necessarily represent an accurate determination of the molecular hydrogen activity when the upstream pressure is relatively low (*i.e.*, <1 Pa). By applying continuous, slow evacuation using a throttled ion pump (with hydrogen makeup to maintain the H_2 pressure), it was possible to effect a moderate reduction of the fractional contribution of impurities to the total pressure. Use of a liquid nitrogen cold trap on the upstream Compartment was somewhat less effective in this regard. Best results in terms of achieving a high purity hydrogen environment were obtained using a temperature-controlled uranium hydride bed (to regulate H_2 pressure) in combination with a throttled ion pump. The presence of uranium metal in the upstream system caused a substantial reduction in the active gases (*e.g.*, H_2O, O_2, N_2/CO) while the throttled ion pump helped to remove the inert gases (*e.g.*, He, Ar). Many of the simulated environments used during the course of these experiments were considered to be representative of plasma chamber exhaust-gas compositions for near-term fusion devices.

*It is not possible to distinguish between N_2 and CO (both mass 28) with the partial pressure analyzer. Both are known to be present from other tests.

Permeation data obtain for 316–SS as a function of temperature are shown in Fig. *8.4.1* and the least-squares-refined permeation curve derived from these data is given by equation (1):

$$\Phi_{316\text{-}SS} = 0.158 \exp(-15{,}148/RT) \qquad (1)$$

where Φ is in units of $cm^3(STP)/m \cdot s \cdot kPa^{\frac{1}{2}}$, R is equal to 1.987, and T is in K. The data employed to derive equation (1) were collected under conditions where hydrogen constituted a major fraction of the gas-phase species present. Also, no changes in permeation rate were observed for 316-SS when a 1 mCi gamma source was place inside the upstream compartment in close proximity to the upstream surface of the sample. This result implies that an ionizing radiation environment (*e.g.*, as in the vicinity of a fusion reactor first wall) may not affect permeation rates that are controlled by bulk diffusion mechanisms.

A plot of the relationship between permeation rate and hydrogen partial pressure in the upstream compartment obtained for 316–SS is given in Fig. *8.4.2.* The data presented in this figure were collected under conditions where hydrogen was the major species in both upstream and downstream gas-phase environments. Under these conditions, a near-to-half-power dependence on driving pressure was observed over the entire pressure range of the study. In cases where oxygen bearing species dominated the gas phase in the upstream compartment, measureable deviations toward first-power dependence on upstream hydrogen pressure were observed at the lower end of the pressure range (*i.e.*, 10^{-3} to 1 Pa). The small departures from an exact half-power dependence in Fig. 8.4.2 are probably due in part to experimental uncertainty and in part to factors attributable to impurity interactions with the surfaces of the permeation samples.

8.4.5 Conclusions

The principal conclusions drawn from this study are that in pure (or nearly pure) hydrogen environments, the permeability of 316-SS is

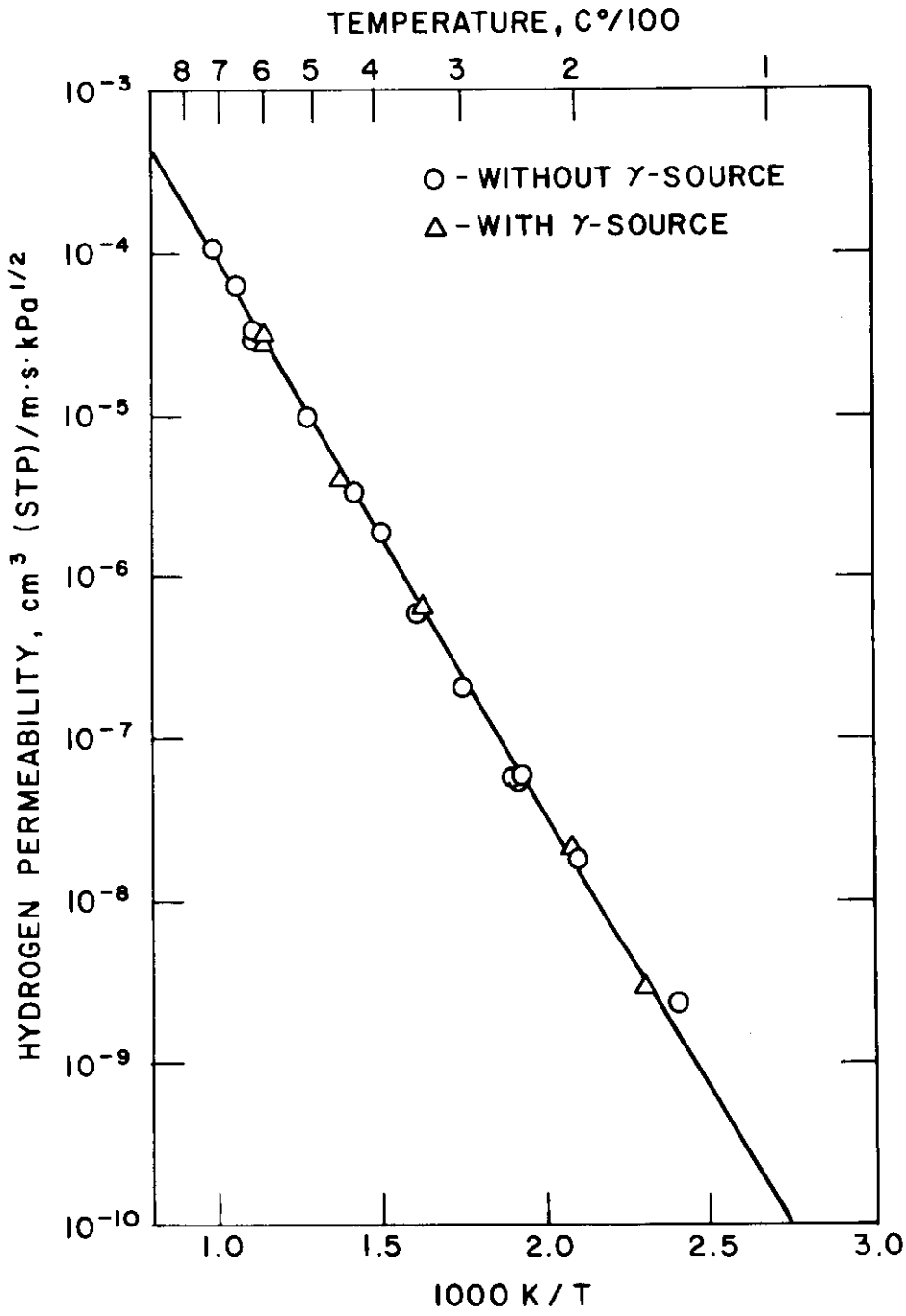

Fig. 8.4.1 Hydrogen Permeability of 316-stainless steel as a function of temperature.

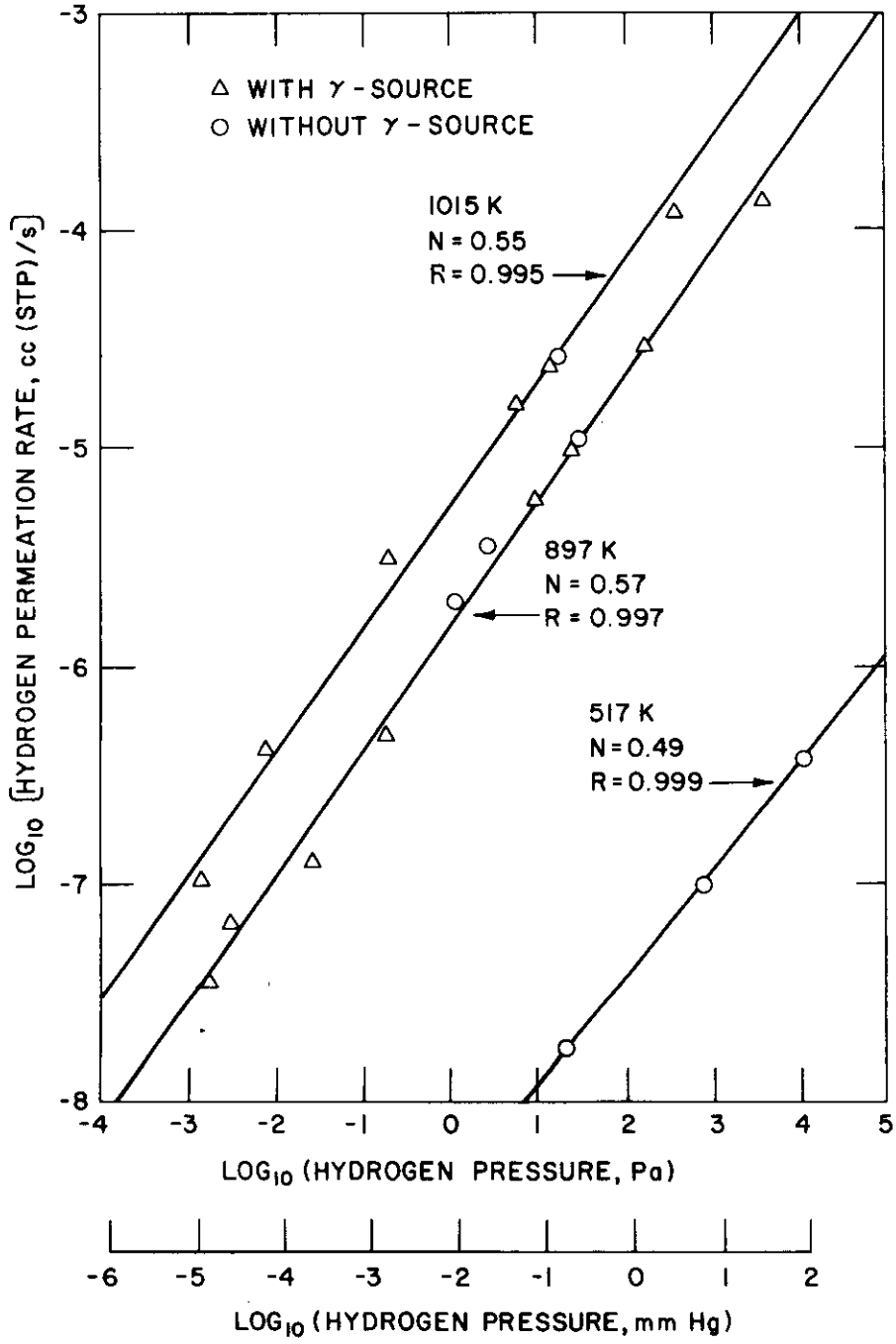

Fig. 8.4.2 Hydrogen permeation rate versus hydrogen driving pressure for 316 stainless steel (N = slope, R = correlation coefficient).

bulk-diffusion limited to pressures as low as 10^{-3} Pa. (This conclusion can probably be extended to pressures considerably lower than 10^{-3} Pa, without reservation.) Also, the presence of ionizing radiation (as described in section 8.4.4) in close proximity to the surfaces of permeation samples, did not have a detectable effect on the permeation rate in the bulk-diffusion-limited regime. This latter result should not be unequivocally extrapolated to reflect effects that are likely to occur in a fully representative fusion reactor radiation environment.

8.4.6 References

1. E. H. Van Deventer, "Hydrogen Permeability of Haynes Alloy-188." *J. Nucl. Mater.* 66(3): 325-328 (1977).

2. E. H. Van Deventer, T. A. Renner, R. H. Pelto, and V. A. Maroni, "Effects of Surface Impurity Layers on the Hydrogen Permeability of Vanadium," *J. Nucl. Mater.* 64(3): 241-248 (1977).

8.5 HYDROGEN PERMEATION OF INCONEL 625 – V. A. Maroni and E. H. Van Deventer (Argonne National Laboratory).

8.5.1 ADIP Task

Hydrogen Dissolution and Permeation Effects. This task is under consideration for addition to the ADIP program plan. The results presented in this section contribute to Subtask I.E.1.1., Milestone I.E.1.a. The above title and assigned numbering are tentative, pending approval by the ADIP Task Group.

8.5.2 Objective

The objective of the work described in this contribution is to provide base-line hydrogen permeation data for Inconel-625. These data will be useful to at least one near-term physics device (*e.g.*, Doublet III), and will serve as a basis for evaluating the effectiveness of subsequently developed permeation barrier methods for Inconel-type Path B alloys.

8.5.3 Sumnary

The hydrogen permeability of Inconel-625 was measured over a range of temperatures and hydrogen pressures that included values relevant to the Doublet III experiment (Inconel-625 is being used as the vacuum vessel material for Doublet III). The permeation rate obeyed a half-power dependence on hydrogen pressure down to the lowest pressure studied (10^{-1} Pa). The activation energy and permeation coefficient were in good agreement with published data for other Inconel-type alloys. These results will also be useful as a standard for comparison of the effectiveness of permeation barrier methods applied to Path B alloys.

8.5.4 Progress and Status

This section reports the results of hydrogen permeation studies carried out on Inconel-625 over the temperature range from 150 to 800°C, using hydrogen pressures in the range 10^{-1} to 10^{4} Pa (10^{-3} to

10^2 Torr). The experimental methods employed in this study are the same as those described and referred to in section 8.4.4 of this report.

Permeation data obtained for Inconel-625 as a function of temperature are shown in Fig. 8.5.1 and the least-square-refined permeation curve derived from these data is given by equation (1):

$$\Phi_{\text{Inconel-625}} = 0.198 \exp(-14{,}371/RT) \qquad (1)$$

where Φ is in units of cm^3 (STP)/m·s·$kPa^{\frac{1}{2}}$, R is equal to 1.987, and T is in K. All of the data used to develop equation (1) were collected under conditions where hydrogen constituted >98% of the gas phase species present in the upstream compartment. (The downstream partial pressure of hydrogen is always at least three orders of magnitude lower than the upstream pressure in these types of permeation experiments; consequently, hydrogen back-pressure effects are negligible.) A plot of the relationship between hydrogen permeation rate and hydrogen pressure is shown in Fig. 8.5.2. The near-to-half-power dependence on pressure provides confirmation that the rate is indeed bulk-diffusion limited over the pressure range studied.

The permeation data in Fig. 8.5.1 are in reasonably good agreement with recently published results' for a related alloy, Inconel-718. The permeability of Inconel-625 is roughly a factor of two lower than that of pure nickel.[2]

8.5.5 Conclusions

Hydrogen permeation of Inconel-625 is controlled by bulk diffusion in hydrogen environments typical of those anticipated for fusion plasma chambers (*i.e.*, >98% hydrogen). The permeability data for Inconel-625 are close in value to those of related Path B alloys.

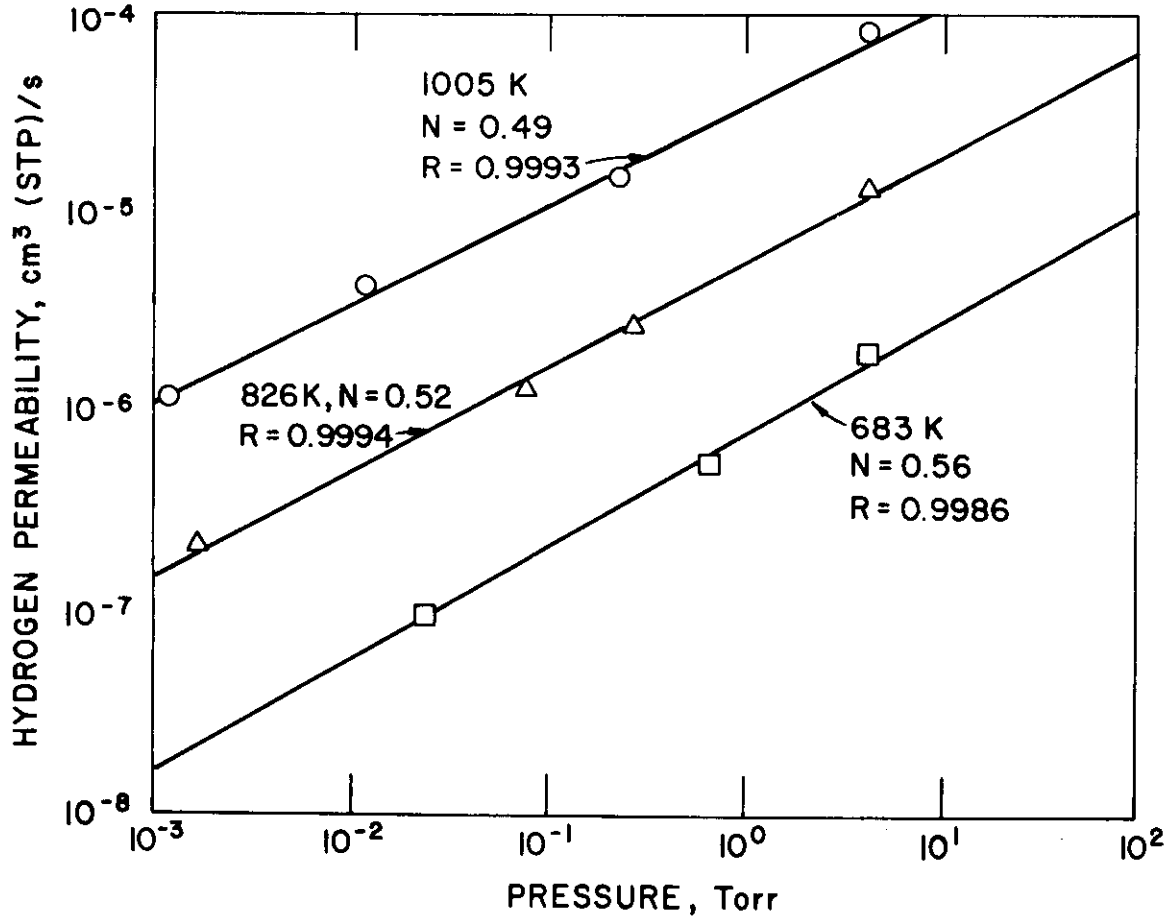

Fig. 8.5.1 Hydrogen Permeability of Inconel-625 as a function of temperature.

8.5.6 References

1. W. M. Robertson, "Hydrogen Permeation and Diffusion in Inconel 718 and Incoloy 903," *Metall. Trans.* 8A(11):, 1709-1712 (1977).

2. M. R. Louthan, Jr., J. A. Donovan, and G. R. Caskey, Jr., "Isotope Effects on Hydrogen Transport in Nickel," *Scr. Metall.* 8(6): 643-650 (1974).

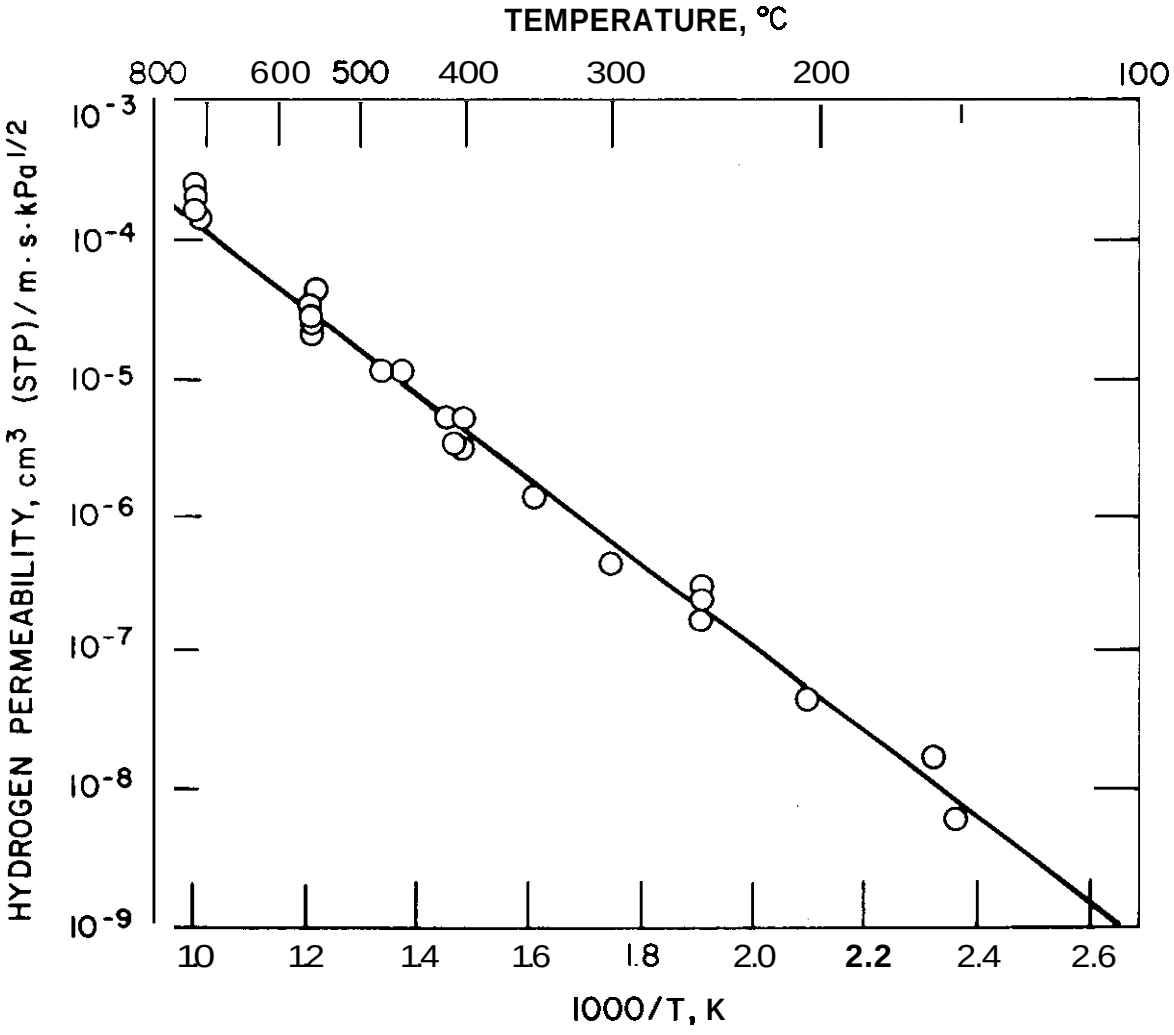

Fig. 8.5.2 Hydrogen permeation rate versus hydrogen driving pressure for Inconel-625 (N = slope, R = correlation coefficient).

DISTRIBUTION

1. uc-20
2. UC-20c
3. Additions by name

Argonne National Laboratory, 9700 South Cass Avenue, Argonne, IL 60439

Director, Materials Science Division
L. Greenwood
V. Maroni
D. L. Smith
H. Wiedersich

Battelle-Pacific Northwest Laboratory, P.O. Box 999, Richland, WA 99352

J. L. Brimhall
D. Dingee

Carnegie-Mellon University, Schenley Park, Pittsburgh, PA 15213

J. C. Williams

Department of Energy, Technical Information Center, Office of Information Services, P.O. Box 62, Oak Ridge, TN 37830

For distribution as shown in TID-4500 Distribution Category, UC-20 (Magnetic Fusion Energy), and UC-20c (Reactor Materials)

Department of Energy, Office of Fusion Energy, Washington, DC 20545

M. M. Cohen
C. R. Finfgeld
T. C. Reuther, Jr. (5 copies)

Department of Energy, Oak Ridge Operations Office, P.O. Box E, Oak Ridge, TN 37830

Director, Research and Technical Support Division (2 copies)

General Atomic Company, P.O. Box 81608, San Diego, CA 92138

S. M. Rossenwasser

Hanford Engineering Development Laboratory, P.O. Box 1970, Richland, WA 99352

R. E. Nygren
E. C. Opperman
R. W. Powell
J. L. Straalsund

Lawrence Livermore Laboratory, P.O. Box 808, Livermore, CA 94550

C. Gatroosis
M. Guinan
C. M. Logan
R. R. Vandervoort

Massachusetts Institute of Technology, Cambridge, MA 02139

D. J. Rose

McDonnell Douglas Astronautics Company, East, P.O. Box 516, St. Louis, MO 63166

D. L. Kummer

Naval Research Laboratory, Washington, DC 20375

Superintendent, Materials Science and Technology Division
J. A. Sprague
H. Watson

Oak Ridge National Laboratory, P.O. Box X, Oak Ridge, TN 37830

Central Research Library (2 copies)
Document Reference Section
Laboratory Records Department (2 copies)
Laboratory Records, ORNL RC
ORNL Patent Office
E. E. Bloom (20 copies)
D. N. Braski
T. A. Gabriel
M. L. Grossbeck
M. R. Hill
K. C. Liu
P. J. Maziasz
C. J. McHargue
S. Peterson
T. C. Roche
J. W. Woods

University of Virginia, Department of Materials Science, Charlottesville, VA 22901

W. A. Jesser
D. Wilsdorf

University of Wisconsin, 1500 Johnson Drive, Madison, WI 53706

K. Conn
P. Wilkes
W. G. Wolfer